Study of Negative Magnetization and Tunable Exchange Bias Behavior in Nanostructured Double Perovskites

A Thesis Submitted
by

K Pushpanjali Patra

Roll Number - 186121011

In Partial Fulfillment of the Requirements for the Award of the Degree of

Doctor of Philosophy in Physics

Department of Physics
Indian Institute of Technology Guwahati
Guwahati-781039, India

July, 2023

Statement

The work presented in my thesis, titled "**Study of Negative Magnetization and Tunable Exchange Bias Behavior in Nanostructured Double Perovskites**" has been conducted under the guidance and supervision of Prof. S. Ravi, Department of Physics, Indian Institute of Technology Guwahati. I confirm that the research work presented in this thesis is original and has not been submitted elsewhere for the award of any degree. The data, results, and conclusions presented in this thesis are the outcome of my independent research work, and no part of this thesis has been copied from any other sources, except where due reference has been made. I acknowledge all the sources used in the preparation of this thesis. This thesis complies with the guidelines and regulations of the Indian Institute of Technology Guwahati.

July, 2023

K Pushpanjali Patra
Department of Physics
Indian Institute of Technology Guwahati
Guwahati – 781039, India

Certificate

It is certified that the work contained in the thesis entitled "**Study of Negative Magnetization and Tunable Exchange Bias Behavior in Nanostructured Double Perovskites**" by Ms. K Pushpanjali Patra, a PhD student of the Department of Physics, Indian Institute of Technology Guwahati for the award of the degree of *Doctor of Philosophy* has been carried out under my supervision. This work has not been submitted elsewhere for the award of any degree.

July, 2023

Prof. S. Ravi
Professor, Department of Physics
Indian Institute of Technology Guwahati
Guwahati – 781 039, India

Dedicated

to

My Family

Acknowledgements

I am delighted to present this thesis as the culmination of my research conducted at IIT Guwahati from 2018 to 2023. I am deeply grateful to everyone who provided me with direct or indirect support during this journey, which has been both enlightening and rewarding.

Firstly, I would like to express my heartfelt gratitude to my thesis supervisor Prof. S. Ravi, for accepting me as his Ph.D. student and providing me with the opportunity to conduct my research in a well-established experimental lab. I am indebted to him for his unwavering support, guidance, encouragement, and valuable insights throughout my doctoral journey that helped shape my research. His expert guidance and valuable advice helped me navigate through all the stages of my research. I would not have been able to achieve what I have in my research career. His compassionate nature, gentle demeanor and patience have always been an inspiration to me and served as a great source of motivation for me throughout this journey. Furthermore, his vast knowledge and experience in this field provided me with valuable insights into various technical concepts, which proved to be immensely helpful in resolving issues that arose during my experiments. I feel fortunate to have the privilege of working under him.

I would like to express my heartfelt appreciation to my doctoral committee members, Prof. D. Pal (chairperson), Prof. D. Pamu, and Prof. S. Kanagaraj, for their valuable support, insightful feedback, and encouragement throughout my thesis work. Their thoughtful suggestions and diverse perspectives have helped me to deepen my understanding of the subject and improve the quality of my research. I am thankful to Dr. U. N. Maiti and Prof. Pugazhenthi for being in my Viva Voce board and both Indian and abroad examiners Prof. P. N. Santhosh, Prof. Z. Cheng for recommending the award of Ph.D.

I would like to extend my sincere gratitude to the present Head of the Department of Physics, Prof. A. Perumal, and the former HOD, Prof. S. Ghosh, for their kind cooperation and for providing me with the necessary instrument facilities during the course of my Ph.D. thesis. I am also grateful to all the administrative staff and technical personnel of the Department of Physics for their support, assistance and providing the necessary infrastructure and equipment, without which this research would not have been possible.

I would like to thank my lab-mates whose presence has made the work environment interesting, engaging, and fruitful. I am deeply thankful to all the present and former members of my research group, including Dr. Vishwajit M. Gaikwad, Dr Junmoni Barman, Dr. Bibhuti B. Das, Dr. Pratap Behera, Dr. Akansha, Dr. Riupan Borah, Mahananda Brahma, Debabrata, Shalini, Deepak and Nibedita for their valuable assistance, advice, and cooperation. My special thanks to Dr. Vishwajit M. Gaikwad for his guidance and support during my initial period of PhD. I would also like to give a special thanks to Dr. Akansha and Dr. Riupan Borah for their help and discussions. I feel fortunate to had the opportunity to work alongside such talented and knowledgeable researchers. Their contributions, feedback, and ideas have been invaluable in enhancing the quality of my research work.

I am thankful to all my 2018 batch-mates, Specially, Pushpesh, Sayan, Shubhangi, Suchit, Sourav, Sumit, Mandira, Akanshu, and Bhargabi for having very good friendship and providing me with their unwavering support, constructive criticism, and thought-provoking discussions that helped me expand my knowledge and refine my ideas.

I am thankful to my seniors as well as juniors of the department, Subrat bhaiya, Gajendra bhaiya, Manisha dii, Prajna, Pragya dii, Sumouna dii, Alok, Harekrishna, Koushik for their continuous support and encouragements.

Moreover, I am grateful to my parents and family for their constant support, encouragement, and understanding throughout my research.

I am thankful to Central Instrumental Facility (CIF), IIT Guwahati, for enabling us to avail several sophisticated instruments to perform the experiments during my Ph.D.

Finally, I would like to extend my sincere appreciation to all those who have directly or indirectly contributed to this research, for their valuable assistance and encouragement.

I acknowledge the Department of Science and Technology (DST), Fund for Improvement of S&T Infrastructure (FIST), New Delhi for providing the facilities of Vibrating sample magnetometer, TTRAX III X-ray diffractometer, Physical properties measurements system. Last but not the least, I am grateful to Indian Institute of Technology Guwahati and Ministry of Human Resource and Development for giving the financial support to carry out the present thesis work.

K Pushpanjali Patra

IIT Guwahati, India, July 2023

Abstract

Magnetic materials are anticipated to exert a considerable influence on shaping the landscape of future electronic devices and circuits. Not only do the type and concentrations of charge carriers serve as key controlling factors in electronic circuits, but also the magnetic spins. This increased degree of flexibility should lead to improvements in non-volatile memory, speed, efficiency, miniaturization, and power usage. Researchers are putting in significant efforts to create novel materials that surpass the performance of current materials, while also striving to deepen their understanding of diverse physical properties. The mixed valence perovskite manganites are an intriguing collection of compounds with numerous possible uses. It shows a broad spectrum of conductivity spanning from strongly conducting metallic state to insulating state demonstrates their flexibility for electrical uses. It also has possible uses in magnetic switches, sensors, magnetic refrigerator and storage devices. Likewise, the remarkable characteristics of magnetic orthochromites, such as their high magnetization reversal, exchange bias behavior, and exceptional electronic conductivity, signify their immense potential for diverse electronic applications. The discovery of large magnetization reversal and tunable exchange bias behavior in orthochromites has paved the way for their promising utilization in spintronics, magnetic storage, multiple memory elements, and magnetic switches.

The recent scientific focus on R_2CoMnO_6 (R is trivalent rare earth element) stems from its intriguingly complex magnetic behavior, which has opened up a diverse range of potential applications. They are mostly found in monoclinic structure with $P2_1/n$ space group, the super exchange interactions across Co^{2+}-O^{2-}-Mn^{4+} networks lead to FM ordering. The compounds such as La_2CoMnO_6, Sm_2CoMnO_6, Nd_2CoMnO_6, Tb_2CoMnO_6, Er_2CoMnO_6, Y_2CoMnO_6 etc., exhibit metamagnetic behavior, magneto-electric coupling, multiferroic behavior, spin-phonon coupling, magnetization reversal (MR) and tunable exchange bias behavior, magnetocaloric effect, low-temperature magnetic frustration and large magneto-resistance like properties. Few research groups have been started working on Ho_2CoMnO_6, and reported a FM T_C around 77 K, with a large magnetic entropy (ΔS_m) of value ~ 12 J/kg.K at a 7 T field. This feature makes this material applicable for magnetic refrigeration.

R_2FeCrO_6 are also an important family of magnetic double perovskites, mostly found in orthorhombic structure with space group - Pbnm, Pnma, R3c etc. The magnetic ordering is

determined by the super exchange interaction between Fe^{3+}-O^{2-}-Fe^{3+}, Cr^{3+}-O^{2-}-Cr^{3+}, and Fe^{3+}-O^{2-}-Cr^{3+} networks. It generally shows a canted G-type AFM structure with a weak FM component. In Fe-Cr based perovskites such as $LaFe_{0.5}Cr_{0.5}O_3$, $YFe_{0.5}Cr_{0.5}O_3$ and $YFe_{1-x}Cr_xO_3$ ($0 \leq x \leq 1$) shows MR. The MR observed in the aforementioned samples are ascribed to the competition between the single ion anisotropy (SIA) and Dzyaloshinsky-Moriya (DM) interaction. $YFe_{0.5}Cr_{0.5}O_3$ shows normal and inverse magnetocaloric effects at around 260 K. This property makes this material applicable in spintronics and magnetic refrigeration. While Fe-Cr based perovskites have been extensively studied, there has been relatively limited exploration of Fe-Cr based double perovskites. Bi_2FeCrO_6 compounds has been the subject of extensive investigation for its multiferroic properties. However, structural instability at high temperatures is a major issue. Pr_2FeCrO_6, which exhibits exceptional structural stability up to 1500 K, represents a promising addition to the A_2FeCrO_6 family, possessing a type-I multiferroic nature that has been sought after. It shows a magnetic entropy change ($-\Delta S_m$) = 2.06 J kg^{-1} K^{-1} at 14 K for H = 9 T. Double perovskite Y_2FeCrO_6, shows magneto-dielectric behavior.

After going through the above literature survey on Co-Mn and Fe-Cr based DP, we found that, there are just a few reports on Ho_2CoMnO_6, and Y_2FeCrO_6 DPs. Thus, a thorough investigation into the magnetic interactions present in the aforementioned two compounds is still needed for a comprehensive understanding. Hence, our current research is centred on exploring the magnetic DP materials based on Co-Mn (Ho_2CoMnO_6) and Fe-Cr (Y_2FeCrO_6), with the primary objective of tuning and comprehending their magnetic properties in this direction. To the best of our understanding, there hasn't been much study done on nanostructured Ho_2CoMnO_6 and Y_2FeCrO_6 DPs, despite their high interest. In this work we have synthesizing nanostructured Ho_2CoMnO_6 and Y_2FeCrO_6 DPs and emphasis on the investigation of their structural and magnetic characteristics.

For the present thesis work, we have synthesized the following nanostructured double perovskite compounds.

1) Nanocrystalline $(Ho_{1-x}Sm_x)_2CoMnO_6$ for x = 0.0 to 0.5
2) Nanorods of Ho_2CoMnO_6
3) Nanocrystalline $Ho_2CoMn_{1-x}Ni_xO_6$ for x = 0 - 0.4
4) Nanocrystalline $Ho_2CoMn_{1-x}Cr_xO_6$ for x = 0 - 0.5
5) Nanoparticles of Y_2FeCrO_6

The present thesis consists of six chapters, namely

Chapter - 1 :- Introduction

Chapter - 2 :- Synthesis and Characterization Techniques

Chapter - 3 :- $(Ho_{1-x}Sm_x)_2CoMnO_6$ series and Ho_2CoMnO_6 Nanorods

Chapter - 4 :- $Ho_2CoMn_{1-x}M_xO_6$ (M = Ni and Cr) Series

Chapter - 5 :- Nanoparticles of Y_2FeCrO_6 Double Perovskite

Chapter - 6 :- Conclusions

Chapter - 1 deals with a brief introduction to crystal structure of DPs, crystal field effect and Jahn-Teller distortion, various magnetic ordering types, interactions, and frustrations arising from competing interactions. A literature review on DPs, emphasizing crystal structure and magnetic properties like, the discovery of magnetization reversal (MR) and exchange bias (EB) phenomena.

Chapter - 2 stands for synthesis of the materials and discussion on their characterization techniques. The working principle of various equipment such as X- ray diffractometer, Raman Spectroscopy, Field Emission Scanning Electron Microscope, Energy Dispersive X-ray Spectroscope, Transmission Electron Microscope, X-ray Photoelectron Spectroscope and Physical Properties Measurement System are discussed.

Chapter - 3 deals with the detailed analysis of structural and magnetic properties of nanocrystalline Ho_2CoMnO_6 system substituted by Sm at Ho site and Ho_2CoMnO_6 flat nanorods.

Single phase nanocrystalline samples of double perovskite $(Ho_{1-x}Sm_x)_2CoMnO_6$ (x = 0-0.5) (HSCMO) were prepared by auto combustion method. The samples are crystalized into a monoclinic structure with space group $P2_1/n$. The lattice parameters along with the unit cell volume are found to increase with Sm concentration. The average bond angle among the transition metal (TM) ions is also found to increase with Sm concentration which lead to strengthen the super exchange interaction and hence increases the ferromagnetic (FM) T_C. Temperature variation of magnetization (M-T) measurements show that all the prepared samples exhibit FM transition with transition temperature (T_C) increasing from 83 K for x = 0.0 to 115 K for x = 0.5. The FM transition is attributed to the super-exchange interaction in Co^{2+}-O - Mn^{4+} networks. A secondary rise in magnetization is observed for T < 50 K and is attributed to FM interaction between rare-earth (RE)

and TM ions. The M-H loops recorded at 5 K with an applied field of ± 9T show a saturation magnetization (M_S) in the range of 11.64 μ_B/f.u. for x = 0.0 to 7.86 μ_B/f.u. for x = 0.5 and it indicates the contribution of RE ions to the net FM moment. All the prepared samples show EB behaviour which is increasing from 30 Oe for x = 0.0 to 237 Oe for x = 0.5 sample at 5 K. The origin of EB in this system is attributed to competition between FM moment of TM ions and the spin canted magnetic moment of RE ions.

The nanorods of Ho_2CoMnO_6 were prepared by the hydrothermal method and are formed in pure monoclinic phase (space group: $P2_1/n$). The lattice parameters are found to be higher compared to its bulk counterpart which leads to unit cell expansion. FESEM and FETEM examination revealed a clear image of HCMO nanorods and the average width of rod is determined to be 71 (±3) nm. The M-T measurement reveals that unlike the single FM transition in the bulk HCMO sample, here three transitions corresponding to FM, antiferromagnetic (AFM) and re-entrant spin glass (SG) ordering at 182, 97 and 31 K respectively. The FM transition (T_C) which is much higher than the bulk (79 K) is due to the higher bond angles of HCMO nanorods as compared to the bulk sample which depict the FM super exchange interaction in Co^{2+} -O- Mn^{4+} networks are getting stronger and it leads to increase the FM T_C. The AFM transition is due to exchange interactions across Co^{2+}- O - Co^{2+} and Mn^{4+}- O - Mn^{4+} networks, as well as due to the presence of Co^{3+} and Mn^{3+} ions. The presence of this spin-glass phenomena is further confirmed by the magnetic relaxation phenomena and aging effect at different fields. A low value of coercivity (H_C) and saturation magnetization (M_S) is observed for HCMO nanorods (8.52 μ_B/f.u) as compared to that of bulk (14.9 μ_B/f.u). It may be due to the presence of higher oxidation states of ions as well as the introduction of AFM ordering and frustration in the system. The maximum value of magnetic entropy ($-\Delta S_m$) is recorded as 12.4 J/kg.K from the magnetocaloric studies.

Chapter - 4 contains the study of magnetic properties of nanocrystalline Ho_2CoMnO_6 double perovskite by Ni and Cr substitutions at Mn site.

The polycrystalline samples of $Ho_2CoMn_{1-x}Ni_xO_6$ (x = 0.0 - 0.4) (HCMNO) and $Ho_2CoMn_{1-x}Cr_xO_6$ (x = 0.0 - 0.5) (HCMCO) were prepared by auto combustion method. Structural studies reveals the single-phase formation of the compounds which belongs to a monoclinic structure and adopt the $P2_1/n$ space group. A drop in the lattice parameters including unit cell volume are noticed with Ni substitution. The M-T measurements shows a single FM transition in

the parent compound at 83 K (T_{C1}). However, it is turned into two FM transitions (T_{C1}, T_{C2}) after Ni substitution, where T_{C2} arises due to possible super exchange interaction in Co^{2+} - O^{2-} - Ni^{4+} networks. One FM transition (T_{C1}) is decreasing from 83 K for x = 0.0 to 78 K for x = 0.4 sample. However, another FM transition (T_{C1}) is increasing from 82 K for x = 0.1 to 88 K for x = 0.4 sample. A MR has been observed in higher Ni concentrated samples such as x = 0.3 and 0.4 in the field cooled state with a compensation temperature (T_{comp}) of 4.4 K and 10 K respectively. This MR is attributed to the competition between the FM moment of the TM ions and the polarization of magnetic moments of RE ions at low temperatures. A typical bipolar switching of magnetization has been demonstrated for x = 0.3 and 0.4 sample in order to confirm the MR. At 5 K, the M-H loops demonstrate a decrease in saturation magnetization (M_S) and coercivity (H_C) value after Ni substitution. However, the observed M_S value of the order of 11.60 to 10.27 μ_B/f.u. (for x = 0.0 to 0.4) at 5 K is attributed to some visible contribution related to the polarization/ordering of Ho moment with the net magnetic moment of TM ions. From the EB studies, we have observed an interesting property, i.e., the FC M-H loop for x = 0.0 is shifting towards the negative field direction, while for Ni substituted compounds it shifts towards positive field direction. The EB field value is increasing with Ni substitution and a maximum value of 230 Oe is obtained for x = 0.4 sample at 5 K. It is due to the competition between the spin canted magnetic moments of RE ions and the FM moments of TM ions.

Nanocrystalline samples of $Ho_2CoMn_{1-x}Cr_xO_6$ (x = 0.0 - 0.5) are also prepared by auto combustion method and are comes under monoclinic structure with space group $P2_1/n$. The lattice parameters along with unit cell volume are found to decrease with Cr concentration. Magnetic analysis reveals a single FM transition (T_{C1}) at 83 K for $x \leq 0.2$. Whereas, for $x \geq 0.3$, we observed two transitions namely T_{C1} and T_{C2}. Here T_{C2} is attributed to the result of AFM interactions in Cr^{3+}- O^{2-} - Cr^{3+} and/or Cr^{3+}- O^{2-} - Mn^{4+} networks. T_{C2} decreases from 77 K for x = 0.3 to 63 K for x = 0.5 sample, whereas no appreciable variation in T_{C1} is observed. In addition, the intermediate compounds such as x = 0.2 and 0.4 show another transition at 120 K and is attributed to the charge ordering temperature (T_{CO}). A MR has been noticed at 50 Oe applied field for x = 0.5 sample with a T_{comp} of 7 K. The competition between the paramagnetic (PM) moment of Ho^{3+} ions under the influence of the negative internal field caused by AFM ordered ions and the FM components of Co^{2+} and Mn^{4+} ions is attributed to this MR. In order to confirm the MR, at 4 K, a bipolar switching of magnetization is demonstrated for x = 0.5. The drop in the values of saturation magnetization

(M_S) is ascribed to the replacement of Mn^{3+} ions having higher magnetic moment (4 μ_B/ion) with the Cr^{3+} ions having lower magnetic moment (3 μ_B/ion). From the EB studies, we have observed a sign reversal of the EB field with Cr doping. the FC M-H loop for x = 0.0 to 0.2 are shifting towards the negative field direction, while for x = 0.3 to 0.5 it shifts towards the positive field direction. EB field of - 114 Oe and + 208 Oe are observed for x = 0.0 and 0.5 samples respectively. They are attributed to the competition between canted magnetic moments of RE ions and FM moments of TM ions, where, the former one is dominating for x = 0.5 and vice versa for x = 0.0 samples.

Chapter - 5 describe the structural and magnetic properties of nanoparticle Y_2FeCrO_6 (YFCO) double perovskite.

Here the technique used for the preparation of YFCO is auto combustion. It is found to be in single phase form which comes under orthorhombic structure with Pnma space group. FESEM image reveals an average particle size of 67 nm (±2). M-T measurements reveals an AFM transition (T_N) at 327 K. The super-exchange interactions in Cr^{3+}-O-Cr^{3+} and Fe^{3+}-O-Fe^{3+} networks are responsible for this transition. Both zero field cooled (ZFC) and field cooled (FC) curves show MR with T_{comp} = 192 K. In addition, a small hump like structure is noticed in both ZFC and FC curves at T~30 K, which is ascribed to the spin reorientation transition (T_{SR}). Further raising the field towards 5 kOe a reduction in T_{comp} value and suppression of spin reorientation has been observed. The study of magnetic Hysteresis loops in both ZFC and FC condition shows a shift towards the field axis. That is, the system has both spontaneous exchange bias (SEB) and conventional exchange bias (CEB) behavior. The maximum absolute values of SEB H_{EB} is found to be 431 Oe at 55 K. However, the sign of the SEB H_{EB} is changing from positive to negative in the vicinity of T_{SR} and then decreases with rise in temperature and it is almost vanishing from T_{comp} to 300 K. Similarly, the maximum value of CEB H_{EB} is found to be 2.1 kOe at 5 K, which is 10 times higher than the SEB value at 5 K. It also shows a sign reversal in the vicinity of T_{comp}. The competition between single-ion anisotropy and the Dzyaloshinsky Moriya interaction is found to be responsible for the above behaviors.

Chapter - 6 deals with a brief summary of results obtained from the measurement and analysis of experimental data of Chapter - 3, 4, and 5 respectively.

List of Abbreviations used in this Thesis

1. **FM** …… Ferromagnetic
2. **FIM** …….. Ferrimagnetic
3. **AFM** …… Antiferromagnetic
4. **PM** …… Paramagnetic
5. **HP** …… High-pressure
6. **DP** …… Double Perovskite
7. **MR** …… Magnetization reversal
8. **NM** …… Negative magnetization
9. **EB** …… Exchange Bias
10. **SE** …….. Super Exchange
11. **SR** …… Spin Reorientation
12. **MCE** …… Magneto-Caloric Effect
13. **TM** …… Transition Metal
14. **RE** …… Rare Earth
15. **ASD** …….. Antisite Defect
16. **APB** …….. Antiphase Boundary
17. **J-T** …… Jahn-Teller
18. **CFT** …….. Crystal Field Theory
19. **CFSE** …… Crystal Field Splitting Energy
20. **DE** …… Double Exchange
21. **DM** ……... Dzyaloshinsky -Moriya
22. **NPD** …… Neutron Powder Diffraction
23. **CO** ……... Charge Ordering
24. **SG** …… Spin Glass
25. **ZFC** …… Zero-Field Cooled
26. **FC** …… Field Cooled
27. **TRM** …… Thermoremanent Magnetization
28. **TAM-RAM** …….. Thermally Assisted Magneto Resistive Random Access Memory

29. SIA ……... Single Ion Magnetic Anisotropy

30. RCP ……. Relative Cooling Power

31. SOPT …….. Second Order Phase Transitions

32. FOPT …….. First Order Phase Transitions

33. RT ……... Room Temperature

34. CTAB ……. Cetyltrimethyl Ammonium Bromide

35. XRD …… X-ray diffraction

36. CCD …… Charge Couple Device

37. FESEM ……... Field Emission Scanning Electron Microscope

38. EDS ……. Energy Dispersive X-ray Spectroscopy

39. TEM ……... Transmission Electron Microscope

40. XPS …… X-ray Photoelectron Spectroscopy

41. PEE ……. Photoelectric effect

42. PPMS …….. Physical Properties Measurement System

43. VSM …… Vibrating Sample Magnetometer

44. HCMO/HSCMO/HCM(N/C)O/YFCO ……

Ho_2CoMnO_6/$(Ho_{1-x}Sm_x)_2CoMnO_6$/ $Ho_2CoMn_{1-x}(Ni/Cr)_xO_6$ /Y_2FeCrO_6

45. FWHM …… Full width at half maximum

46. CWL …… Curie-Wiess Law

47. RSG ……. Re-entrant spin glass

48. LAS ……. Law of approach to saturation

Contents

List of Figures

Chapter 1: **Page No.**

Chapter 2:

Chapter 3:

Chapter 4:

Chapter 5:

List of Tables

Chapter 1: Page No.

Chapter 3:

Chapter 4:

Chapter 1

Introduction

Materials with decreased dimensions, such as thin films, wires/rods, and nanoparticles, whose properties differ from those of bulk materials, have piqued the interest of researchers because they add functionality to a wide range of applications. The success of technological advancement in developing smart and nano magnetic materials over the last few decades for applications in memory devices, data storage processing, spintronic devices, sensors, biotechnology, magnetic refrigeration, etc. has piqued the interest of many people in magnetic materials. Carbon nanotube discovery in 1991 was a watershed moment in nanomaterials research [1]. After the ground-breaking discovery was made public, the number of researchers working in the field has increased dramatically. The magnetoelectronic based on transition metal oxide is rapidly emerging as a future viable technology. There are various applications of them in electronics, medicine, technology, catalysis, alternative energy, etc., [2].

1.1 Historical Overview

Because of their intriguing physical properties and technological applications, transition metal oxide-based materials with perovskite structures are attracting the attention of physicists, materials scientists, etc. [2]. Oxide perovskite with ferromagnetic (FM) behavior around room temperature was first reported in 1950 in manganite by Jonker and Van Santen [3]. Zener proposed that the presence of mixed valence in Mn results in this FM behavior due to the double exchange FM interaction in Mn^{3+}-O^{2-}-Mn^{4+} networks [4]. In order to get higher FM ordering temperature, this discovery prompted subsequent research on mixed valanced TM oxides. As partial substitution is a very common method in order to tailoring the structural and magnetic properties of any system. By continuing this discovery, in 1961 FM ordering was observed at 401 K in $SrFe_{0.5}Re_{0.5}O_3$ and 538 K in $CaFe_{0.5}Re_{0.5}O_3$ having perovskite structure [5]. In addition to this, perovskites possess potential applications in spintronic devices, magnetic storage, magnetic sensors, magnetic switches, oxygen sensors and magnetic refrigeration etc. [6]. The fact that perovskites exhibit a wide range of conductivity ranging from highly conducting metallic state to insulating state

demonstrates their versatility for electronic applications. Because of their intriguing magnetic and magneto transport properties, these materials have technological applications [7-13]. A highly popular technique for altering the characteristics of perovskite compounds is partial cation substitution. This replacement might happen in several ways at either the A or B site. The scenario in which precisely half of the B-site cations are replaced with another cation, has garnered a lot of attention in recent years. The two distinct cations, *B* and *B'*, can either stay disordered at the B site or order, yielding a B-site ordered double-perovskite, $A_2BB'O_6$. The majority of the $A_2BB'O_6$-type perovskite compounds reported in the literature were made at ambient pressure. High-pressure (HP) synthesis has also yielded various novel $A_2BB'O_6$ compounds.

It is noteworthy that many $A_2BB'O_6$ compounds exhibit a diverse range of characteristics, including semiconducting, metallic, half-metallic, dielectric, ferroelectric, thermoelectric, and possibly even superconducting properties. Several semiconducting substances, like La_2NiFeO_6 and Sr_2CoIrO_6, have electrical resistivities that are on the range of 10^{-3}-10^{-4} Ωcm. Contrarily, the resistivity values of La_2CoMnO_6 exhibit wide fluctuations [14,15]. There have been reports of metal-insulator transitions (MITs) in Sr_2CoTiO_6 around 700 K [16], $YNiO_3$ around 580 K [17], and Ca_2MnMoO_6 at 209 K [18]. The halfmetallicity present in substances like Sr_2FeMoO_6 (B = Fe/Cr) [19,20] is the most remarkable characteristic of the $A_2BB'O_6$ perovskites. The most extensively researched half-metallic perovskites are A_2FeMoO_6 with A = Ca, Sr, and Ba. Even at ambient temperature, they are all half-metallic materials with a strong metallic conductivity and noticeable negative tunneling magnetoresistance behavior [19,21]. Takata and Kageyama [22] investigated a series of $A_2BB'O_6$ compounds, where A = Ca, Sr, or Ba; B = La, Nd, Sm, or Yb; and B' = Nb or Ta. They discovered a number of compounds with dielectric constant $k > 20$ and either positive or negative temperature coefficients of resistance. Similar to this, various A_2BWO_6 compounds [23] have been reported with significant *k* values and negative temperature coefficients of resistance where A is Sr or Ba and B is Co, Ni, or Zn. For La_2CuTiO_6 [24], La_2NiRuO_6 [25], and La_2BMnO_6 with B= Mg, Co, or Ni [26,27,28], high values of k have been recorded. La_2GaMnO_6 has a thermal conductivity of around 2 W/m K [29]. Similarly, Sr_2CoReO_6 (0.9 W/m K), Sr_2BRuO_6 compounds with B = Y or Er have demonstrated extremely low thermal conductivities of 0.2 W/m K at 300 K [30]. In contrast, the conductivity of the $Sr_{2-x}A_xFeMoO_6$ series, where A is either Ba or La, fluctuates between 0.6 and 1.0 W/m K [31]. Sr_2MgMoO_6 was shown to be a suitable anode material for solid oxide fuel cells [32,33]. Sr_2FeMoO_6 [34] and Ba_2FeMoO_6 [35] have also been discovered

to have strong fuel-cell performance and to be highly conducting. A_2BMoO_6 with A = Sr or Ba and B = Mn, Co, or Ni has been demonstrated to function as a solid oxide fuel-cell anode [32,35,36]. Samples of quenched La_2NiMnO_6 that have undergone B-site disordering exhibit frustrated magnetic behavior [37]. In R_2BMnO_6, with B = Co or Ni, FM arises as a result of the coexistence of vacant $Mn^{4+}e_g$ orbitals and partially filled $Co^{2+}/Ni^{2+}e_g$ orbitals [38-40]. The FM interaction, can be weakened by AFM interactions across *Co-O-Co, Ni-O-Ni,* or *Mn-O-Mn* networks as cation disorder is widespread in these compounds [2]. The FM $A_2BB'O_6$ perovskites often have very low T_C values that are below room temperature (RT). The multiferroic characteristics may be discovered in a variety of $A = Bi^{3+}$ compounds and one of them is Bi_2NiMnO_6 [41]. Sr_2FeCoO_6 exhibits two interesting phenomena: exchange bias and spin glass behavior. Even after 50% replacement of strontium atoms with lanthanum atoms, these properties still persist [42,43]. Antisite disorder is attributed for the above behavior.

Jia et.al. reported a second order FM transition in the range of 70 K – 96 K for R_2CoMnO_6 (*R = Dy, Ho, Er*), with a maximum value of the magnetic entropy of 10.5 (Dy), 11.5 (Ho), and 11.8 (Er) $Jkg^{-1}K^{-1}$ at low temperature for 7 T applied field [44]. Similarly, in Gd_2NiMnO_6 and Gd_2CoMnO_6 DPs, maximum value of the magnetic entropy (ΔS_m) of 35.5 J/kg K and 24 J/kg K are reported at 10.5 K and 6.5 K at H = 7 T respectively [45]. These features make these materials applicable for low temperature magnetic refrigeration. In 2014 it was found that Y_2CoMnO_6 exhibited a multicaloric behavior that is with $\Delta S_m \sim 7.3$ J/kg K and an electric field driven entropy change (ΔS_e) of 0.26 $Jm^{-3}K^{-1}$ [46]. Multiferroics provide interesting prospects for electric-field control of magnetism. Hence, people from experimental as well as theoretical group work on multiferroic Bi_2FeCrO_6 compound in order to tune and enhance its property [47,48,49]. Nasir et. al. gave a comparative study on structural and magnetic properties of R_2NiMnO_6 (*R = La, Pr, Nd, Sm, Gd, Tb, Dy, Y,* and *Ho*) based on ionic size and antisite disorder [50]. Similarly, in 2016, Kumar et. al. reported exchange bias in Nd_2NiMnO_6 with a multi magnetic phase [51]. Ferroelectricity is also noticed in Y_2NiMnO_6 by Su et. al. [52]. Colossal magnetodielectric behavior has been observed in La_2NiMnO_6 at RT [53]. Many interesting properties have been observed in *Co/Mn* based DPs, including multi magnetic phase, magnetocaloric behavior, multiferroic behavior with magneto-electric coupling, negative magnetization (NM), exchange bias (EB) behavior, metamagnetism, spin phonon coupling, Griffith phase, spin glass and colossal magneto-resistance [54-70]. Ho_2CoMnO_6 shows competing magnetic interactions, NM as well as a large

magnetic entropy (ΔS_m) of the order of 12 J/kg K at 10 K for 7 T field [44,63,71]. Orthochromites and orthoferrites have been the most researched compounds over the last two decades due to their fascinating underlying physics such as temperature-induced magnetization reversal (TMR), EB, spin reorientation (SR), and potential applications in information storage, thermomagnetic switches, spintronics, resistive memory devices, multiferroic materials, etc. [72-85]. The intriguing properties of *Fe/Cr* based perovskite structures inspire researchers to work on *Fe-Cr* based DPs (R_2FeCrO_6, *R*- rare-earth element) [86-91].

1.2 Crystal structure

The crystal structure of a solid substance is of considerable fundamental interest. Numerous significant physical characteristics of the material, such as electrical, magnetic, optical properties, can also be impacted by the crystal structure. Therefore, understanding the crystal structure is frequently necessary in order to anticipate or predict the material characteristics. Perovskite oxides are compounds with the general chemical formula ABO_3, where *A* is rare earth (RE) and *B* is transition metal (TM) ions. The structure of ideal cubic perovskite is shown in Figure.1.1 (a). The oxygen ions occupy the face cantered position with the B-cations at the centers of the cube, while the A site ions are located at the vertices of the cube. When the formula unit of a perovskite structure is doubled, it results in the formation of $A_2B_2O_6$. However, if one of the B-cations in the formula, which is octahedrally coordinated, is replaced entirely by a different B' cation, then a new type of double perovskite (DP) oxide structure is formed with the general chemical formula $A_2BB'O_6$. The ideal cubic DP structure is shown in Figure.1.1 (b). Unlike the simple perovskite structures with one A cation and one B cation site, DP compounds with two different TM elements at B sites (B, B') and the presence of either RE or alkaline earth elements at A sites offer even more flexibility and degrees of freedom to the compound. Because of this adaptability, DPs can accept nearly all of the elements in the periodic table. On each of the three sites of the structure, it is also possible to make partial substitution. The perovskite compounds are more complex and adaptable because of the potential for cation ordering. Furthermore, the presence of two distinct B-site cations permits the synthesis of unique and intriguing combinations of diverse elements, including main group elements and TMs in the 3d, 4d, or 5d oxidation states, lanthanides, and actinides. Due to the fact that the B-site cations usually control the most intriguing aspects of perovskites, including their electrical conductivity and magnetic properties, the possibility of

different elemental combinations and cation ordering opens up a world of intriguing and potentially practical new materials.

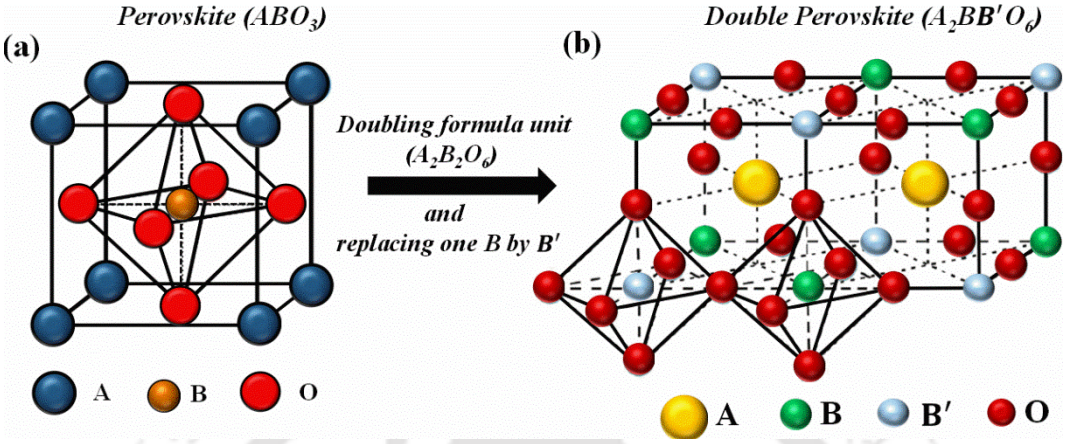

Fig. 1.1: Ideal cubic crystal structure of (a) perovskite and (b) double perovskite.

In DPs, the cations at the octahedral site can order in three different ways, as shown in Figure.1.2 (a-c) [92,93]. The most common case is that alternate arrangement of cations in 3-D and the resulting rock-salt type structure (Figure.1.2 (a)). Similarly, when the cations alternate in 2-D and 1-D they give rise to columnar (Figure.1.2 (b)) and layered type (Figure.1.2 (c)) DPs.

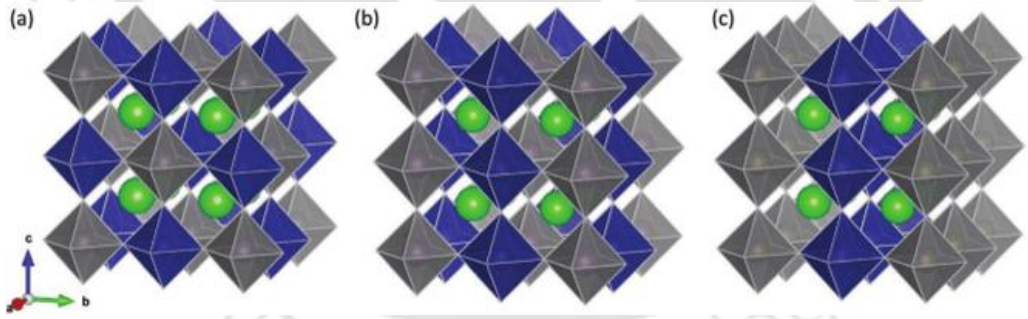

Fig. 1.2: Different types of double perovskites based on ordering of *(B/B') O_6* octahedral (a) rock salt, (b) columnar and (c) layered structures. Reproduced image from ref [2].

Cation Size Mismatch

For an ideal cubic perovskite structure, the bond length $A - O = \sqrt{2} * (B - O)$. However, DP compounds generally deviate from ideal cubic structure due to lattice distortion caused by a variety of factors such as ionic size mismatch, crystal field effect, Jahn-Teller effect, and so on [2]. It is very rare that the ionic radii of A and B should match perfectly. So, the Goldschmidt tolerance

factor *t* [94] is often used to define a large mismatch in the ionic radii of A and B / B' site cations in DPs. Where, *t* is defined as;

$$t = \frac{r_A + r_O}{\sqrt{2}[\frac{r_B + r_{B'}}{2} + r_O]} \quad (1.1)$$

Here, r_A, r_B, $r_{B'}$ and r_O are the ionic radii of *A*, *B*, *B'* and oxygen ion respectively. An ideal cubic structure should have *t* = 1. If the value of *t* is differing from 1 then, a structural distortion from the ideal cubic phase is expected [94]. For *t* < 1, the ionic size mismatch can be compensated by tilting the BO_6 octahedra in perovskite structure. Whereas, in $A_2BB'O_6$ DPs the mismatch can be compensated either by changing the bond lengths or by tilting the octahedra.

Phase Formation of Double Perovskite

Generally, it is quite difficult to get a typical DP phase at ambient pressure [98]. Some of the compounds form at high pressure [99], whereas a few compounds could not even form at 80 kbar [100]. It was often found as a mixed phase such as pyrochlore, spinel and hexagonal phases while trying to get a perovskite structure [101,102]. Ramesha et. al. found that, at 550^0 C it is possible to get a DP structure at ambient pressure but when the temperature is raised to 600^0 C they got a pyrochlore phase [103]. Once the DP is formed, depending on the crystallographic site occupation of TM ions, the structure and space group can be defined. Most common type of *B/B'* ordering in perovskite and/or DPs is the rock salt type. An alternating periodic arrangement of TM ions gives rise to monoclinic structure, while a random arrangement of TM ions leads to an orthorhombic structure. As shown in Figure. 1.3, there are several ways that the B-site cations might become disordered. The antisite disorder (ASD), in which B and B' cations merely swap locations. The antiphase boundary (APB), which divides two ordered domains with reversed B and B' site occupancies, and it is another typical form of defect. This can be thought of as the gath-

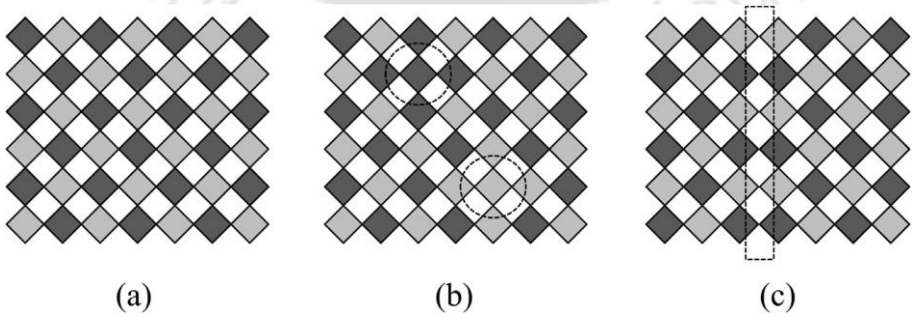

Fig. 1.3: Types of B-site cation disorders: (a) completely ordered, (b) antisite disorder and (c) antiphase boundary. Reproduced image from ref [2].

ering of ASD in a particular area, which causes the correct periodicity of the ordered phase but in the reverse order [104]. These APBs have actually been discovered quite often in the $A_2BB'O_6$ perovskites [2].

Some compounds, primarily those with B' = *Fe*, appear to undergo structural transitions connected to magnetic ordering, and the interaction between the magnetic and structural degrees of freedom results in a reduction of symmetry. The well-known halfmetallic and FM material, Sr_2FeMoO_6, undergoes a structural change at T_C = *400* K, i.e., changing from tetragonal to cubic with rising temperature [14,126]. Similar to this, Ba_2FeMoO_6 is said to undergo transition from tetragonal *I4/mmm* structure to a cubic $Fm\bar{3}m$ structure at T_C = 320 K [21]. At 305 K, Ba_2FeReO_6 undergoes a phase transition from *I4/mmm* to $Fm\bar{3}m$, and magnetic peaks are also seen at the same temperature [127]. With *B' = Mn, Ti, or Rh*, the $A^{3+}{}_2Cu^{2+}B'^{4+}O_6$ compounds are all disordered and lack a cooperative J-T effect. Finally, several B' = *Co* compounds have also shown a mild J-T effect.

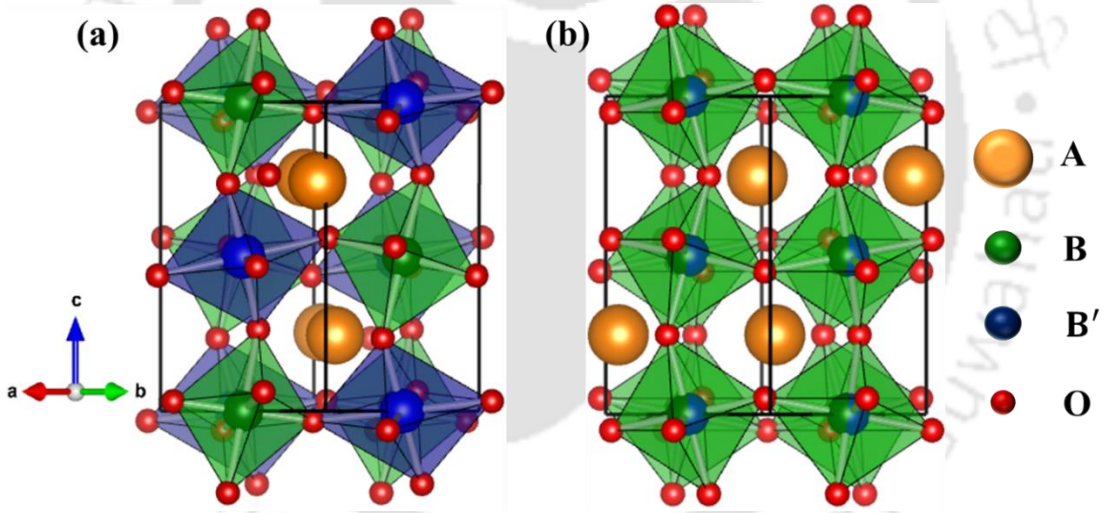

Fig. 1.4: Crystal structure of double perovskites in (a) monoclinic and (b) orthorhombic symmetry.

The CoO_6 octahedra in Sr_2CoFeO_6 appear to have a small J-T distortion [128]. This was explained by the presence of Co^{3+} ions (J-T active). Short annealing periods can result in two-phase coexistence, making it difficult to determine the structure [129]. The temperature of the orthorhombic to rhombohedral phase transition in La_2CoMnO_6 is dependent on the cooling rate during synthesis, which is quite intriguing. In a slow-cooled sample, the oxidation states appear to be Co^{2+} and Mn^{4+} or very near to it, but in quenched samples, the Valancy is shifted toward Co^{3+} and Mn^{3+}. The monoclinic and orthorhombic structure of DPs are shown in Figure.1.7 (a) and (b)

respectively. The crystal structure of A_2CoMnO_6 *(A = Ho, Tm, Yb, Lu)*, $LaSrFeCoO_6$, R_2NiMnO_6 [43,50,55,57,64,66,68-71] comes under monoclinic structure with space group $P2_1/n$. On the other hand, the perovskite structure $AFe_{0.5}Cr_{0.5}O_3$ (*A = Y, Dy*) and the DP Y_2FeCrO_6 come under Orthorhombic phase with space group *Pnma* [91,133, 134].

Table 1.1: Atomic position of elements in R_2CoMnO_6 having monoclinic phase with $P2_1/n$ space group (from Ref. [57]).

Atoms	Site	x, y, z
R	4e	0.018(x), 0.071(y), 0.250(z)
Co	2d	0, ½, 0
Mn	2c	½, 0, 0
O1	4e	0.298(x), 0.316(y), 0.051(z)
O2	4e	0.317(x), 0.293(y), 0.444(z)
O3	4e	0.605(x), 0.965(y), 0.256(z)

Table 1.2: Atomic position of elements in $YFe_{0.5}Cr_{0.5}O_3$ having orthorhombic phase with *Pnma* space group (from Ref. [133]).

Atoms	Site	x, y, z
Y	4c	0.066(x), ¼, 0.983(z)
Fe	4b	½, 0, 0
Cr	4b	½, 0, 0
O1	4c	0.463(x), ¼, 0.107(z)
O2	8d	0.304(x), 0.055(y), 0.692(z)

1.3 Crystal Field Theory (CFT)

The crystal field is the average electric field experienced by an atom (ion) due to other atoms (ions) in the crystal [136]. Crystal Field Theory (CFT) is a model that explains the electronic structure of TM ions in complex compounds based on their interaction with the electric field of surrounding ligands. Magnetism in transition elements is caused by the partially filled d orbital. The d orbital has five degenerate energy levels, so electron can enter into any of the energy levels.

These energy levels are again divided into sub orbitals as e_g ($d_{x^2-y^2}$, d_{z^2}) and t_{2g} (d_{xy}, d_{yz}, d_{zx}) respectively. The complete configuration of the *d* orbital is shown in Figure.1.5. The case where the lobes of the *d* orbital present in between the axis such as xy, yz, zx, are named as t_{2g} orbitals with sub orbitals d_{xy}, d_{yz}, d_{zx}. Whereas, when the lobes are present along the axis it is named as e_g orbitals with sub orbitals d_{z^2} and $d_{x^2-y^2}$ respectively.

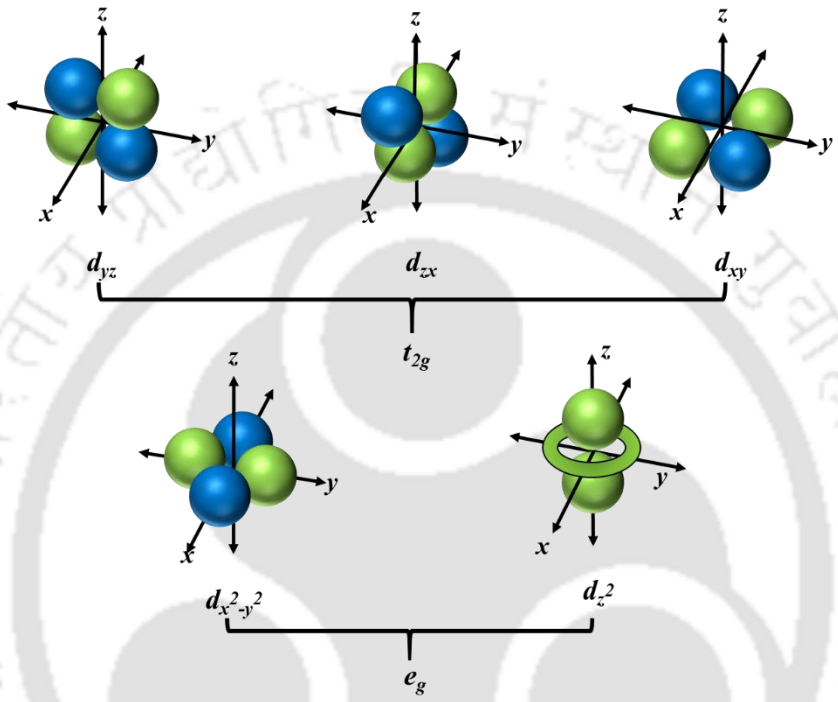

Fig. 1.5: Electronic distribution of 3d orbitals.

To explain the CFT let us take an example of CrO_6 and MnO_4 compounds [136,137]. So, here, Cr/Mn are metal ions with *d* orbitals, and the oxygen ion approaches the metal to form the compounds. As Cr/Mn has d orbital electrons, and Oxygen also has a lone pair of electrons. When these ligands approach the metal, they will experience repulsion from the metal's *d* orbitals, causing the *d* orbitals to lose degeneracy. These non-degenerate d orbitals have now been divided into two sub orbitals, e_g and t_{2g}. Because lobes are present along the axis in e_g orbitals, ligand approaches along the axis in octahedral compounds, raising the energy of e_g. Because the t_{2g} lobes are located between the axes, they experience very little repulsive force and thus in smaller energy state. The difference in energy between these two sets of degenerate orbitals is known as crystal field splitting energy (CFSE) or crystal field stabilization energy (CFSE). This CFSE is denoted by the symbol Δ (Δ_t, Δ_o). The letters *t* and *o* stand for tetrahedral and octahedral compounds,

respectively. In the case of tetrahedral compounds, ligands approach between the axes, hence, t_{2g} orbitals experience more repulsive forces and move to the higher energy state, whereas e_g orbitals experience less force and hence lower energy. Figure 1.6 depicts the splitting of energy levels in tetrahedral and octahedral environments.

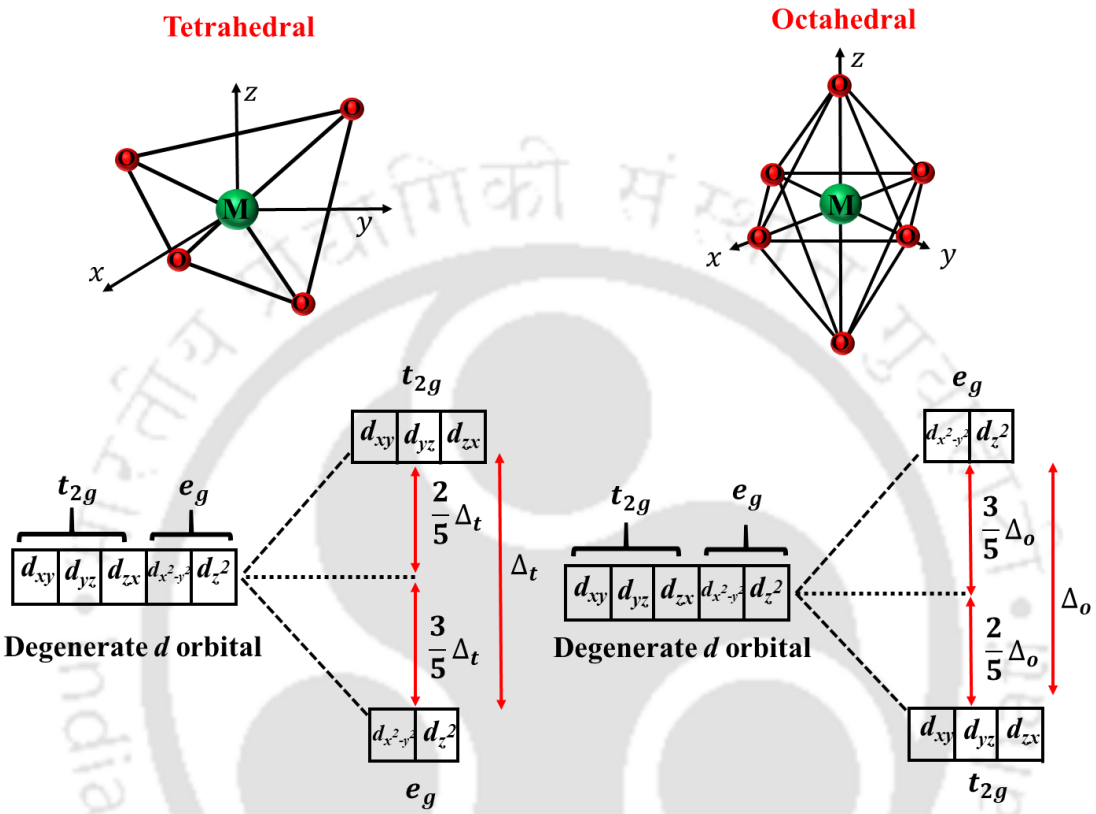

Fig. 1.6: Crystal field effect in tetrahedral and octahedral environments.

The formula used to calculate the magnitude of effective magnetic moment (μ_{eff}) of an ion is: $\mu_{eff} = g\sqrt{J(J+1)}\ \mu_B$, ($J$ is the total angular quantum number). But sometimes it does not correspond to experimental values for the majority of transition elements. This is due to the large crystal field effect in 3d transition elements, which dominates over the Hund's spin-orbit coupling energy and, in such case, the orbital angular momentum is quenched. As a result, the relation for μ_{eff} is reduced to $\mu_{eff} = g\sqrt{S(S+1)}\ \mu_B$ (S is the spin quantum number). The RE series, which derives its magnetism from the 4f shell, is another intriguing series of elements with strong magnetic moments. In contrast to transition elements, the 4f orbitals here are deep inside from the outermost orbital with negligible overlapping with the electronic configuration of neighboring

ions, and thus they do not exhibit any crystal field effect. The general relation $\mu_{eff} = g\sqrt{J(J+1)}$ μ_B can be used to calculate μ_{eff} for rare earth ions.

Jahn-Teller distortion

According to the JT theorem, any nonlinear molecules or ions in a degenerated electronic ground state will be distorted in order to remove its degeneracy [137]. When electrons are occupied in orbitals asymmetrically, they experience distortion. The JTD is a geometrical distortion that reduces the symmetry and energy of a nonlinear molecular system. This distortion is most common in octahedral complexes, where the two axial bonds can be shorter or longer than the equatorial bonds. The JTD is generally present for octahedral complexes of d^9 and high spin d^4 ions.

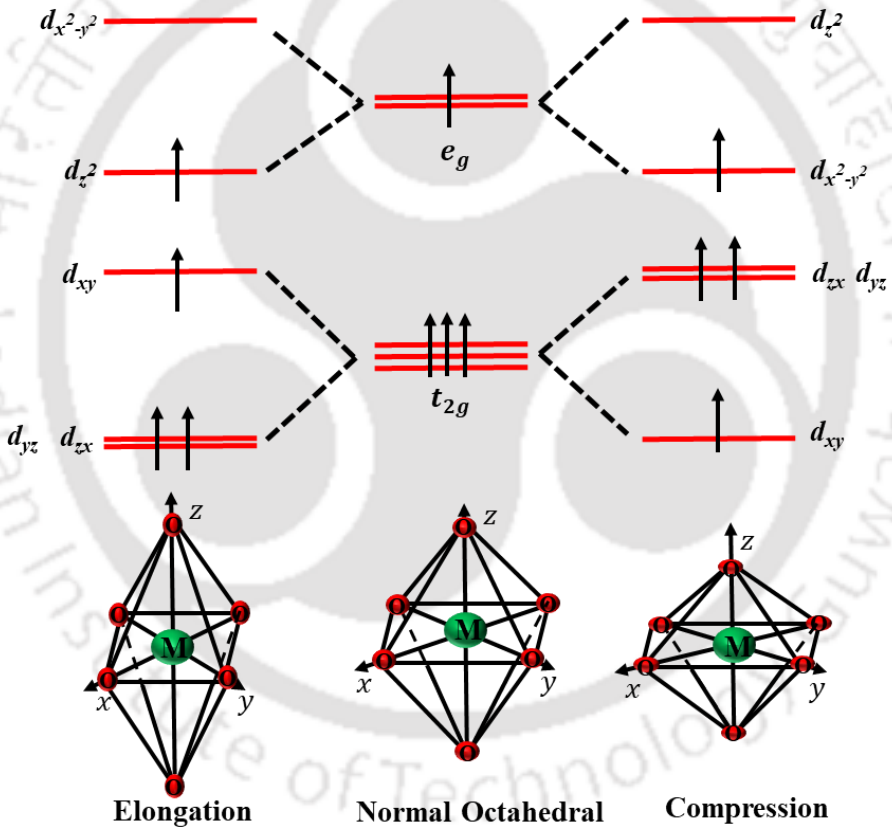

Fig. 1.7: The splitting of sub orbitals t_{2g} and e_g in Mn^{3+} ion at octahedral site due to JTD.

In octahedral compounds, two types of distortion are commonly observed: elongation and compression. If e_g electron is in the d_{z^2} axis, the two ligands along the axis feel more repulsion, causing axial elongation. If e_g electron is in the $d_{x^2-y^2}$ axis, the four ligands along the equatorial feel more repulsion, causing equatorial elongation. Consider the Mn^{3+} ion in an octahedral site

with a d^4 configuration. Its three electrons occupy t_{2g} orbitals, while the fourth electron has orbital degeneracy in e_g orbitals. To remove the degeneracy, the octahedra stretch along the Z-axis, resulting in a lower energy of d_{z^2} compared to $d_{x^2-y^2}$. As a result, the fourth electron will occupy the d_{z^2} orbitals. Similarly, in the t_{2g} orbital, the d_{xy} level is elevated above the d_{yz} and d_{zx} levels. However, in some other systems, the energy is reduced by octahedral compression. As a result, the $d_{x^2-y^2}$ energy level is reduced, and the fourth electron occupies the $d_{x^2-y^2}$ orbital [138] and the d_{yz} and d_{zx} levels are lifted up in comparison to the d_{xy} level in the t_{2g} orbital. Figure 1.7. depicts a schematic diagram of this phenomenon. JTD is also observed in tetrahedral site, however, in this case t_{2g} orbitals have a higher energy and JTD distortion is seen for both the high spin configurations (d^3, d^4, d^8, d^9) and the low spin configurations (d^5, d^6, d^8, d^9).

1.4 Magnetic Interactions

In the solids, when we move to atomic or sub atomic level, the only interaction we have is the electromagnetic interaction. The electrostatic interaction is a quantum mechanical phenomenon between the spins, proposed by Heisenberg in 1928, popularly known as exchange interaction [136]. According to Heisenberg model, the Hamiltonian for two spin interactions can be written as;

$$H_{SE} = -\sum_{ij} J_{ij}\vec{S}_i.\vec{S}_j \qquad (1.2)$$

Here, J_{ij} is the exchange constant, $\vec{S}_i, \vec{S}_j$ are the interacting spins due to two different atomic sites. For any system, the spins try to align and interact to other spins in such a way that it should acquire a minimum energy. Based on this, for parallel (FM) alignment of the spins, $J_{ij} > 0$, and for antiparallel (AFM/FIM) alignment of the spins, $J_{ij} < 0$, such that the system will get a minimum energy [136]. Here we will be discussing some of the important exchange interactions.

1.4.1 Double Exchange (DE) Interaction

This interaction is found in the oxides where the magnetic ion must have a mixed valency [136]. The oxides having magnetic elements such as *Fe* (Fe^{2+}/Fe^{3+}), and *Mn* (Mn^{3+}/Mn^{4+}) are the most common example of this interaction. It is an indirect exchange interaction, that means the interaction can't be taken place between the cations directly. They need a nonmagnetic anion in between them to make this interaction possible. This mechanism was first introduced by Zener in 1951 hence it is also known as Zener DE interaction [4,139]. The name is DE, because here the

exchange of electron takes place simultaneously twice. That is, first from the magnetic cation having lower oxidation state to nonmagnetic anion then second from anion to higher oxidation state cation.

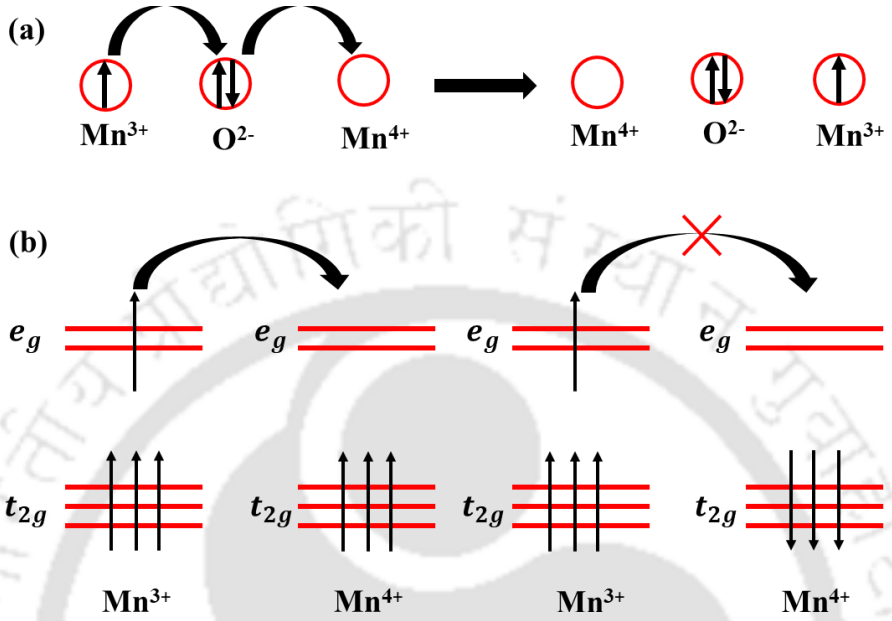

Fig. 1.8: Schematic diagram for DE mechanism between Mn^{3+} and Mn^{4+} ions via Oxygen.

To explain this interaction, we have taken Mn^{3+} and Mn^{4+} ions as magnetic ions and O^{2-} as nonmagnetic ion in the octahedral site as shown in Figure 1.8 (a, b). In the first step, one up spin electron hops from e_g state of Mn^{3+} to O^{2-}, simultaneously, in the second step, the up spin of O^{2-} jumps to e_g state of Mn^{4+} ion. As a result, now Mn^{3+} changes to Mn^{4+} and Mn^{4+} ion changes to Mn^{3+}. This interaction is only possible when the electrons in the t_{2g} orbital of Mn^{4+} are parallel to the electrons in the *d*-shell of Mn^{3+} as shown in Figure 1.8 (a). Whereas, the antiparallel spin structure of t_{2g} level in Mn^{4+} does not allow this interaction as per the Hund's rule as shown in Figure 1.8 (b) [136].

1.4.2 Super exchange (SE) interaction

It is also an indirect exchange interaction however; the mechanism is different than that of DE interaction. Based on the electronic distribution, here both FM and AFM interaction can be possible. Similar to DE interaction, here also two magnetic ions are interacting via a nonmagnetic ion. SE interactions are crucial in determining the magnetic ordering, magnetic transition temperatures, and magnetic properties of materials. In Fig.1.9 (a), Mn^{4+} -O - Mn^{4+} pair is presented.

When magnetic cations have antiparallel core spins, and there are empty higher energy levels available through a non-magnetic ion like oxygen, the strong Hund's coupling results in to AFM interaction. In order to satisfy the Hund's rule, one of the valence electrons of oxygen spends some time with the cation having the same spin orientation (up-up), while the other valence electron (down spin) spends time with the cation having the down spin configuration. This results in each cation-anion pair having a FM alignment of electrons, while the overall interaction between cations is AFM.

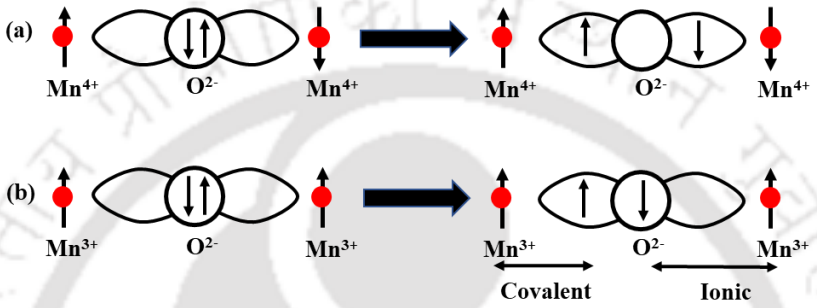

Fig. 1.9: Schematic diagram for super exchange mechanism in Mn-O-Mn network showing (a) AFM and (b) FM ordering.

Figure 1.9 (b) shows the interaction between Mn^{3+}-O-Mn^{3+} network, which leads to a FM ordering. In this case, the core spins of the cations are aligned in parallel to each other. Here, a covalent bond is created when the up-spin of the O^{2-} ion points in the direction of the up-spin of the Mn^{3+} cation (left side). On the other hand, the down spin of O^{2-} ion directed away from Mn^{3+} cation (right side) forming an ionic bond. As a result, the network as a whole experience an FM interaction. The SE interaction between Co^{2+}-O^{2-}-Mn^{4+} and Fe^{3+}-O^{2-}-Fe^{3+} / Cr^{3+}-O^{2-}-Cr^{3+} networks lead to a FM and an AFM ordering in Ho_2CoMnO_6 and Y_2FeCrO_6 DPs [38,2].

1.4.3 Dzyaloshinsky - Moriya (DM) Interaction

The name itself says that this interaction is the result of the involvement of two scientist and the names are Igor Dzyaloshinsky and Toru Moriya [140,141]. The typical AFM interaction among the spins can be explained by the Hamiltonian containing the AFM superexchange term; $H_{SE} = -J_{ij}\vec{S}_i.\vec{S}_j$, where, $J_{ij} > 0$. While the explanation of weak ferromagnetism (WFM), due to the canting of antiparallel spins is explained by Dzyaloshinsky and Moriya which is known as DM interaction. Now the Hamiltonian for the interaction among the canted spins can be written as;

$$H_{DM} = \vec{D}.(\vec{S}_i \times \vec{S}_j) \quad (1.3)$$

Here, $\vec{D}$ is known as Dzyaloshinsky vector and $\vec{S}_i, \vec{S}_j$ are the two canted spins. This interaction tries to orient the spins perpendicularly. This interaction is very small as compared to Heisenberg exchange interaction, where the spins are perfectly colinear. If the anion mediating the two cation spins ($\vec{S}_i, \vec{S}_j$) is at the inversion center, it gives rise to a zero value for $\vec{D}$. Most common examples of the compounds which shows this interaction is the Fe/Cr based perovskites [73,140,141].

1.5 Magnetism in Matter

The origin of magnetism in materials is found in orbital and spin motion of electrons, their interactions with one another, and how materials respond to external magnetic fields. Magnetic moment is the basic component of magnetism. Magnetic materials are typically defined as substances with a significant magnetic moment. There may not be any collective interaction of atomic magnetic moments in some materials, whereas in other materials there is a very strong interaction between atomic moments. Depending on the nature of response to the applied field and the nature of interaction among the magnetic dipoles present in the materials, the magnetic materials are classified into five types; (i) Diamagnetic, (ii) Paramagnetic, (iii) Ferromagnetic, (iv) Ferrimagnetic and (v) Antiferromagnetic.

1.5.1 Diamagnetic materials

In diamagnetic materials, there is no atomic dipoles, hence the net magnetic moment of each atom is zero. On application of external magnetic field, the electrons distribution get rearranged in an attempt to screen the applied field to some very small amount. This gives rise to weak negative moment or a small susceptibility of the order of -10^{-3} to -10^{-9}. In diamagnetic materials, the susceptibility (χ) is generally independent of temperature. When a diamagnetic material has N number of atoms per unit volume and Z number of fully filled electrons per atom then according to Langevin's theory [136], its susceptibility can be expressed as;

$$\chi = -\frac{N\mu_0 Ze^2}{6m}\bar{r}^2 \qquad (1.4)$$

Here, $\bar{r}^2$ is the mean square radius of the electron orbits, e, m, and μ_0 represent the charge and mass of single electron, and permeability in free space respectively of the electron. Few examples of these materials are He, Ne, Ar, H_2, N_2, NaCl etc.

1.5.2 Paramagnetic materials

Unlike diamagnetic materials, here, an atomic dipole exists because the net magnetic moment of every electron in the atom (Na = $1S^2$ $2S^2$ $2P^6$ $3S^1$) does not add up to zero. However, due to the random orientation of dipoles, it still has a zero net magnetic moment in the absence of an external magnetic field. The atomic dipoles partially align with the direction of applied external magnetic field. As a result, it has a small and positive value of susceptibility (10^{-4} to 10^{-6}). According to the Langevin's theory, its susceptibility can be expressed as [136],

$$\chi = \frac{N\mu_0\mu^2}{3k_BT} \tag{1.5}$$

Here, T and k_B are the absolute temperature and the Boltzmann constant respectively. μ is the magnetic moment of each dipole, and is also expressed as, $\mu = g^2\mu_B^2 J(J+1)$. Where g is the Landé g factor and μ_B is the Bohr magneton (eħ/2m). The PM susceptibility increases with decrease in temperature and the inverse susceptibility has a linear temperature dependence, such dependency is known as Curie law. Few examples of these materials are oxygen, aluminum etc.

1.5.3 Ferromagnetic (FM) materials

The atomic or ionic dipoles interact with each other in such a way that they spontaneously align in same direction in small volumes called as domains. It was first explained by Weiss in 1970 in terms of molecular field model. FM domains are quickly aligned along the external magnetic field. So, it has a large positive value for the susceptibility. Hard FM materials or permanent magnets are those whose magnetization persists even after the external magnetic field is removed. Soft FM materials are those in which magnetization disappears after the removal of an external magnetic field. On increasing temperature, FM moment decreases and above certain temperature called as Curie temperature it behaves as PM material. Above the Curie temperature, the magnetic susceptibility follows the following relation, [142];

$$\chi = \frac{C}{T-\theta_C} \tag{1.6}$$

This equation is known as Curie - Weiss law and here, C and θ_C are Curie constant and Curie temperature respectively. Here C can also be written as $C = \mu_0 N g^2\mu^2/3k_B$. In the case of DPs mostly the plot of inverse susceptibility versus temperature deviates from the linear behavior. As a result, they are unable to fit to the equation (1.6). In such case, the modified Curie-Wiess law (MCW) is used for extracting the magnetic data, which is given by [143];

$$\chi = \frac{C_{TM}}{T-\theta_{TM}} + \frac{C_{RE}}{T-\theta_{RE}} \quad (1.7)$$

Here, C_{TM} / C_{RE} and θ_{TM} / θ_{RE} are the Curie constants and Curie temperatures for TM and RE ions respectively. In such case, the interaction between TM and RE ions are treated as negligible. Hence, Curie constants and Curie temperatures are taken independently for TM and RE ions.

1.5.4 Antiferromagnetic (AFM) materials

AFM materials exhibit negative exchange interaction, resulting in antiparallel alignment of magnetic moments of adjacent magnetic ions leading to net zero magnetic moment. This AFM ordering is active below a certain temperature known as the Néel temperature (T_N), and it mostly behaves like a PM above the T_N, with susceptibility [142];

$$\chi = \frac{C}{T+T_N} \quad (1.8)$$

The AFM materials are Cr, NiO, CoO, Cr_2O_3, FeO, MnO etc.

1.5.5 Ferrimagnetic (FIM) materials

FIM materials are a type of AFM in which the magnetic moments are antiparallel but the overall magnetization is nonzero. Unlike AFM materials, the magnetic moments of the various magnetic sublattices in FIM materials are different in magnitude, which prevents them from cancelling one another out. Different sub-lattices in this case have different molecular fields. According to the molecular field theory, the inverse susceptibility in FIM for $T > T_C$ is [144,145];

$$\chi^{-1} = \left(\frac{(T-\Theta)}{C}\right) - \left(\frac{\xi}{(T-\Theta')}\right) \quad (1.9)$$

Here, Θ, ξ and Θ' represent asymptotic Curie temperature, the curvature in the inverse susceptibility plot and the characteristic temperature respectively. Spinel ferrites, spinel chromites, garnets, hexaferrites etc. comes under these materials

1.6 Magnetic Structure

The magnetic structure is the systematic configuration of the magnetic spins linked to each atom in a magnetic unit cell. The neutron powder diffraction (NPD) patterns provide the best insight to determine the three-dimensional magnetic structure, magnetic dipole orientation, and magnetic moment magnitude associated with each magnetic ion. Some selected magnetic structure based on the spin configurations in magnetic unit cell are shown in Figure. 1.10. In A-type structure, magnetic spins in each plane are aligned parallel, but spins in alternate planes are aligned

in opposite direction, resulting into a net AFM interaction in magnetic unit cell. As a result, the planes are interacting via AFM interaction. In C -type structure, the atoms are arranged parallelly in $(1\bar{1}0)$ and (110) planes. However, each atom has two parallel and four antiparallel nearest neighbours thus it results into a net AFM magnetic unit cell. In E-type the spins are not aligned parallelly in a particular plane perhaps they show some zig zag pattern. In F-type, all the spins in one plane as well as in adjacent planes are aligned parallelly and gives rise to a net FM interaction in the magnetic unit cell. However, in G-type each spin aligned antiparallelly to the six neighboring spins in a magnetic unit cell leads to an AFM ordering [136].

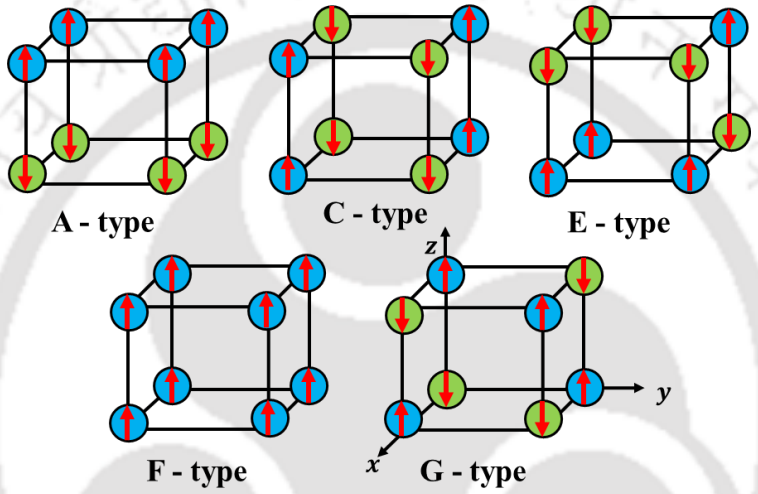

Fig. 1.10: Magnetic structures based on spin configurations in a magnetic unit cell.

The magnetic ordering of Ho_2CoMnO_6 is F-type and it gives rise to a net long-range FM ordering [57]. Where, the FM ordering in the ground state is taken place between the moments of Co^{2+} and Mn^{4+} cations. Blasco et.al. studied the neutron diffraction data at various temperature as shown in Figure 1.11 (a) [57]. At high temperature few peaks are observed, with lowering temperature the intensity of (110) reflection is getting rise along with that a few reflections ((020), (112), and (200)) are detected around 60 K. At 2 K, a hump like feature has been observed below 30 degree, which is considered as the short-range magnetic contribution from Ho^{3+} ion. Here, the spins of Co^{2+} and Mn^{4+} are ferromagnetically arranged in ac plane as shown in inset of Figure.1.11 (a). The net magnetic moment was found to be 2.92 μ_B/ atom at low temperature, which justifies that both the ions are at high spin state and aligned ferromagnetically. Similarly, $YFe_{0.5}Cr_{0.5}O_6$ perovskite shows a canted G-type AFM ordering at all the temperature below T_N [134]. Figure 1.11 (b) shows the neutron diffraction patterns at 6 K along with rietveld refinement for

$YFe_{0.5}Cr_{0.5}O_3$. Here, majority of the spins (Fe^{3+}, Cr^{3+}) are oriented along z axis with some canting along y axis (inset of Figure 1.11 (b)), this leads to a weak FM component along y axis. This canted structure is attributed to the effect of antisymmetric DM interactions.

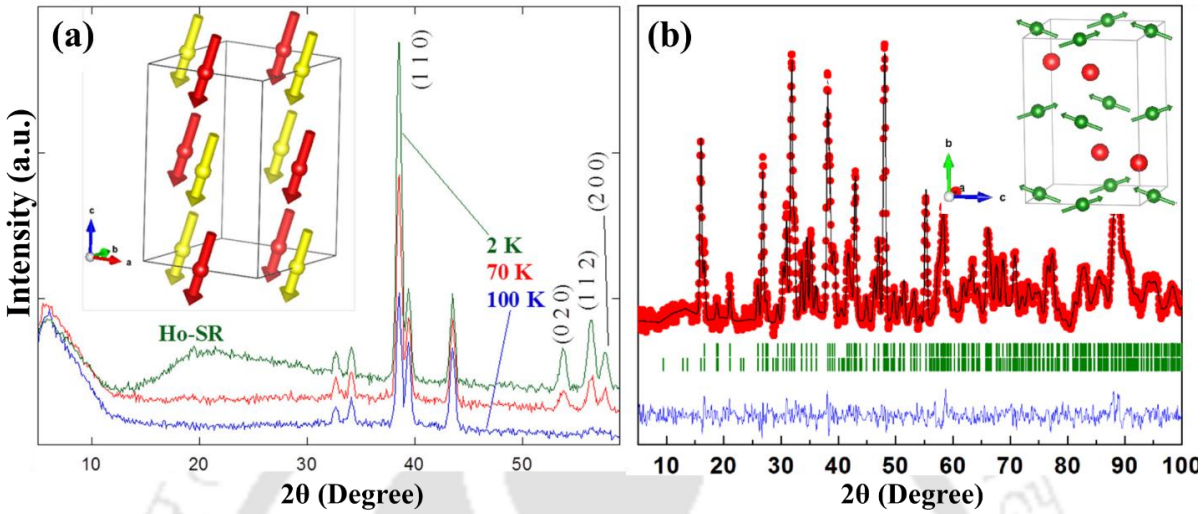

Fig. 1.11: (a) Temperature variation of neutron diffraction patterns for Ho_2CoMnO_6, (b) neutron diffraction patterns at 6 K along with rietveld refinement for $YFe_{0.5}Cr_{0.5}O_3$. Insets shows magnetic structure of the respective compounds. The arrows in yellow, red, and green stand for *Mn*, *Co*, and *Fe/Cr* moments, red and green spheres are stands for yttrium and *Fe/Cr* ions. Reproduced image from ref [57, 134].

1.7 Charge Ordering in Manganite

The ordering of cations with various charges on certain lattice sites is known as the charge ordering (CO), the evidence for this intriguing phenomenon, has been discovered in TM oxides [146-147]. In the charge ordered state, the electrons of the respective ions become localized in their particular sites. This localization possible because at this state the coulombs interaction dominates over the kinetic energy of the electrons to form a long-range charge ordered state. Around 0.5 to 1 eV is the range of energy that is associated with CO. Wollan and Koehler made the initial discovery of the charge ordering in $La_{1-x}Ca_xMnO_3$ [146], and Goodenough presented the qualitative theoretical work [38]. For $x < 0.5$, the concentration of Mn^{3+} and Mn^{4+} ions are not equivalent, hence they are dispersed randomly throughout the permitted Mn site. As a result, a FM DE interaction takes place across Mn^{3+}- O^{2-}- Mn^{4+} networks. However, for the 50% of Ca doping, Wollan and Koehler found a 1:1 ratio for Mn^{3+} and Mn^{4+} ions, leading to a charge ordering for

these ions below a particular temperature, which is shown in Figure 1.12. They discovered that the patterns observed could only be described with the help of a combination of *C*-type and *E*-type magnetic structures. The Mn^{3+} and Mn^{4+} ions are arranged in a regular pattern, occupying alternate positions, resulting in a zigzag chain composed of Mn^{3+} and Mn^{4+} ions. The intra chain magnetic moment of Mn^{3+} and Mn^{4+} ions are ordered ferromagnetically. while all the neighboring chains are ordered antiferromagnetically in ab plane (Figure 1.12). This ordering basically occurs below a particular temperature known as charge ordering temperature (T_{CO}). This ordering stops the DE FM interaction across Mn^{3+}-O^{2-}-Mn^{4+} networks and causes the material to behave like an insulator. As Mn^{3+} ions possess one electron in e_g state, so in order to minimize the electronic energy sometimes orbital ordering is also taking place.

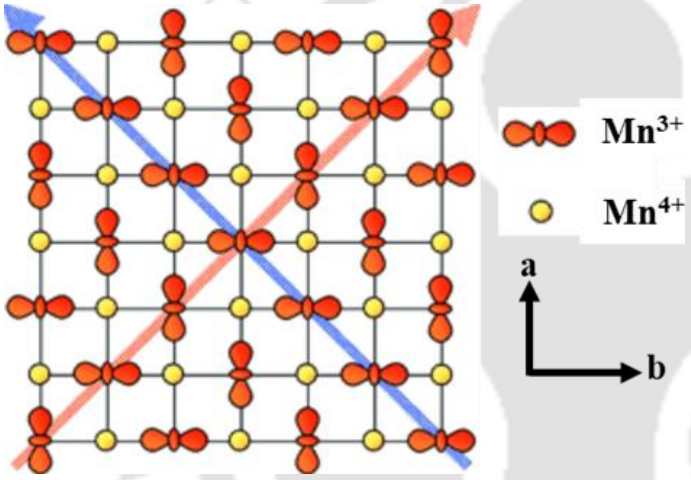

Fig. 1.12: Charge and orbital ordering of Mn^{3+} and Mn^{4+} in $La_{0.5}Ca_{0.5}MnO_3$. Reproduced image from ref [156].

The materials which show the charge ordering for the first time are *(La, Ca)-Mn-O* series [147,148]. Thereafter, several reports came of CO in $Pr_{1-x}Ca_xMnO_3$ [149], $Pr_{0.5}Sr_{0.5}MnO_3$ [150], and $Nd_{0.5}Sr_{0.5}MnO_3$ were reported [151]. By using an external magnetic field [152-155], pressure [156], exposure to x-ray photons [157], an electric field [158], and visible–infrared laser [159], the CO state may be transformed into a metallic FM state. It was also found that T_{CO} can be increased by decreasing the average ionic radii of rare earth ion in the A site [160]. Later on, some authors claimed that CO did not require a 1:1 ion ratio between Mn^{3+} and Mn^{4+} [161]. It has also been noticed that, a rise in magnetic field leads to a fall in T_{CO} [161]. So, it can't be denied that, the CO is crucial in determining the structural, electrical, and magnetic properties of a material.

1.8 Frustration in Magnetic Materials

Understanding magnetic ordering and phase transitions is a major focus of research. On numerous cases, it was discovered that the ordering could not be described by a single kind of magnetic interaction. In these situations, the concept of magnetic frustrations was introduced. Frustration is often caused by two causes in magnetic materials: geometry and disorder. In geometric frustration, the overall energy of a magnetic spin or group of spins in this situation could not be minimized by reducing each energy linked with its closest neighbor. The quantity of magnetic frustration is frequently measured using the frustration factor $f = |\theta_C|/T_C$, where θ_C is the Curie temperature and T_C is the transition temperature. In general, magnetic frustration would be present when $f > 10$ [162].

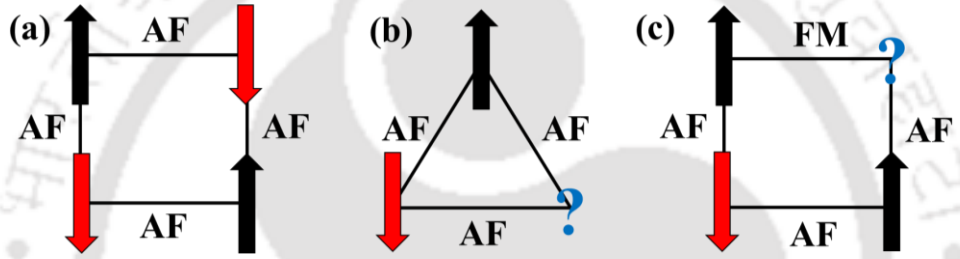

Fig. 1.13: (a) AFM spins that are not frustrated, (b) Equilateral triangle of geometrically frustrated AFM spins, (c) Spin-glass frustration from random FM interactions in (a).

The majority of $A_2BB'O_6$ perovskites exhibit noticeable cation disorder, and several of these materials exhibit spin-glass-like behavior [163-165]. Let's use an example where the conflicting magnetic interactions are the cause of the geometric frustration. To further comprehend this, let's assume that the given system has two spins, S_i and S_j and the exchange Hamiltonian is given by $H = -J\vec{S_i}.\vec{S_j}$, where J is the exchange constant. Consider a system, where all the interactions are FM, and the ground state has all spins aligned parallel to one another. In such case there will be no frustration. However, for a typical AFM interaction the spin configuration depends on the lattice structure. Figure 1.13 depicts the three cases; (a) unfrustrated system, (b) frustrated system and (c) spin glass frustration. If only the nearest neighbor interactions are considered and align two distinct spins in an antiparallel manner, there won't be any frustration observed (Figure1.13 (a)). In contrast, if the same case is taken in an equilateral triangle such that three spins are antiparallel to one another. If two spins are already aligned anti-parallel, then the third spin cannot be aligned anti-parallel with each of the other two spins since pointing up or down has the

same energy. Hence, it leads to a frustration in the system (Figure 1.13 (b)). Figure 1.13 (c) depicts the third case, in which three pair of spins are AFM ordered i.e. with adjacent spins and one pair ordering ferromagnetically. In this case the spin in one corner is frustrated, because the AFM interaction next to it wants the spin to point down, while another neighboring spin trying to align this spin ferromagnetically; this results in to frustration.

Spin Glass / Cluster Glass / Re-entrant Spin Glass State

Spin glass state is also known as spin freezing/frozen disordered state, where the spins got frozen in random direction in order to decrease the overall energy. Because they are unable to find a ground state by simultaneously reducing their energy with each neighboring spin. This state is completely different from the long range ordered FM/AFM/FIM states. Because, in FM/AFM/FIM states, a system changes from a disordered to an ordered state. On the other hand, in SG, the system undergoes transition from one disordered state to another. This property was first observed by Cannella et. al. in the year 1971 in gold-iron alloys [166]. The conventional SG states were observed in TM doped alloys, which is identified by ac susceptibility measurements [167,168]. One of the general identifications for SG state is, there should be a large bifurcation between the zero-field cooled (ZFC) and field cooled (FC) curves of dc susceptibility data at freezing temperature (T_f) [169]. There are laws to study the frequency dependence T_f, such as Arrhenius law and Vogel- Fulcher law [168]. The Arrhenius relation can be written as;

$$\tau = \tau_0 \, exp\left(\frac{E_a}{kT}\right) \tag{1.10}$$

Here, τ is the relaxation time (1/f), τ_0 is a time constant, E_a is the activation energy.
Similarly, the Vogel-Fulcher law can be written as;

$$\tau = \tau_0 \, exp\left[\frac{E_a}{k_B(T_f - T_0)}\right] \tag{1.11}$$

Here, T_0 represents the characteristic temperature.

The SG model can be used to develop algorithms for image restoration and machine learning [170,171], as well as to comprehend neural networks and protein folding [172,173]. A number of protocols have been developed in the last few decades to identify the SG state [174,175]. Such as relaxation of thermoremanent magnetization (TRM) that is decay of remanence magnetization with time. This relaxation process is explained by an exponential function, which can be written as [176];

$$M(t) = M_0 + M_{sg}\,[\exp(-(t/\tau)^{1-n})] \quad (1.12)$$

Here, M_0 stand for intrinsic FM component, M_{sg} magnetization contribution from spin glass component, and τ and n represents relaxation characteristic time and critical exponent respectively. As explained above, in conventional spin glass state, system changes its spin from one disordered PM spins state to another disordered metastable frozen state. However, in some material along with the ordered state like FM/AFM/FIM state, a spin frustration state has been observed at low temperature. In such case, the system undergoes transition from disordered PM state to ordered FM/AFM/FIM state then to another disordered metastable frozen state. Such type of spin frustration state is known as cluster glass/re-entered spin glass state. Because when a disordered (PM) to ordered (FM/AFM/FIM) state transition occurs in the system, then it reenters to the disordered spin frozen (spin glass) state. Some FM systems and few manganites with perovskite structure had shown this property [177-182]. Similarly, in single crystal of $Eu_{0.5}Sr_{1.5}MnO_4$, and perovskite $Eu_{0.5}Ba_{0.5}MnO_3$ shows SG behavior [183,184].

Aging Behavior

A general characteristic that can be investigated using thermoremanent magnetization versus time measurements $M(t, t_w)$ is the ageing behavior of a spin glass system. To achieve this, the system is field cooled below T_{sg} to a desired temperature and wait for a time t_w, then the magnetic field (H) was switched off. The response function produced by this is known as the spin relaxation rate (S), and it is defined as [185];

$$S(t) = \frac{d[-M(t,t_w)/H]}{d\ln(t)} \quad (1.13)$$

In this study, the S(t) versus ln (t) plots one can see a peak and this peak depends on the applied field value. Few authors demonstrated that applying a magnetic field in the spin frozen state reduces the height of the barrier or the depth of the trap [186]. Which is attributed to the reduction in Zeeman energy (E_Z), which aids spins to escape the trapped potential. E_Z can be calculated by using the relation $ln\,(t_{eff}/t_w) = -E_Z/K_BT$ [187], where t_{eff} is the time at which the peak is observed in S(t) versus ln (t) plots. By carrying out various ageing experiments, it is possible to investigate another feature of the SG system that is memory effects. Here the sample is zero field cooled through T_{sg} to a temperature, then an external magnetic field is applied after waiting for a time of t_w. An inflection points in the rate of evolution of magnetization at a time roughly equal to t_w, and

it suggests that SG remembers the waiting time. The slow spin relaxation, ageing effect, memory effects, and other magnetic characteristics of DPs make them more intriguing [187-189].

1.9 Magnetization Reversal (MR)

Magnetization reversal (MR) or negative magnetization (NM) is a very intriguing property of magnetic materials. It refers to a change in magnetization from a positive value to a negative value in a magnetization versus temperature measurement, under a fixed positive applied magnetic field. The particular temperature at which the net magnetization of the material vanishes (M = 0), and below this temperature magnetization becomes negative is called as compensation temperature (T_{comp}). This phenomenon was first observed by Neel in the year 1948 in FIM materials [144]. Afterwards MR has been observed in various FM and canted AFM materials [72,190-193], intermetallic alloys perovskites/DPs, and multilayers etc. [78]. Thermomagnetic switches, magnetic memory, spin valves, and thermally assisted magnetic random-access memory (TAM-RAM) are some possible technological applications of the materials [78,194]. There are several possible origins of MR in various materials; a few common ones are discussed below.

Temperature Dependent Antiferromagnetically Coupled Magnetization

This phenomenon was first explained by Neel in FIM materials [144]. It states that, if a system consists of temperature dependent sublattice moments which are antiferromagnetically coupled and placed at two distinct crystallographic sites. In this case, below a specific temperature, one sublattice magnetization dominate over the other, and vice versa at higher temperatures. As a result, at T_{comp} the material has a net magnetization of zero, due to the equivalent magnitude of magnetization value of two sublattices and their cancelation. Below the T_{comp}, system has negative value of magnetization. Menyuk et al. reported MR in the inverse spinel Co_2VO_4 in the year 1960 with T_{comp} = 70 K [195]. As an inverse spinel, it has Co in both tetrahedral (A) and octahedral (B) sites and V at octahedral site. The origin of MR in this compound is well explained by considering the various temperature dependences of the magnetic moments of A site and B site ions in accordance with the Neel's theory. Afterwards various compounds such as spinel ferrites $Co(Cr_{1-x}Fe_x)_2O_4$ [144], $Ni(Cr_{1-x}Fe_x)_2O_4$ [145], other spinels like Fe_2MoO_4 [142], $FeCr_{2-x}Al_xS_4$ [196], RE garnets [166] and Prussian blue analogues [197] show MR and are explained based on Neels model.

Competition between ferromagnetic moment and paramagnetic moments in negative internal magnetic field:

This feature is mostly found in perovskite compounds such as orthochromites and manganite [190,192,200,201]. MR is found in orthochromites $RCrO_3$ when the A site is partially or totally substituted by magnetic RE ions such as Pr, Ce, Yb, Gd, and so on. MR is caused by the negative internal magnetic field produced by the antiferromagnetically ordered Cr^{3+} ions and its impact on the PM moment of R and/or substituted ions. Then, under the influence of a negative internal field, the moments of the paramagnetic ions partially align themselves opposite to the applied field as well as FM moments and it leads to MR. Cook et. al. derived an expression for such compounds' net magnetization which can be written as [202].

$$M = M_{FM} + C \times \frac{(H_I + H_{ext})}{(T-\theta)} \tag{1.14}$$

Here, M_{FM}, C, H_I, H_{ext}, and θ stand for the total FM component present in the system, Curie constant, negative internal field, applied external field and the Curie temperature respectively. Based on these mechanism MR is explained in $Er(CoMn)O_3$ perovskite [200], epitaxial $Gd_{0.67}Ca_{0.33}MnO_3$ thin film, $GdCrO_3$ [190], $YbCrO_3$ [201], $LaCr_{0.85}Mn_{0.15}O_3$ [203] and $La_{1-x}Pr_xCrO_3$ (x = 0 - 1) [192] and R_2CoMnO_6 (R = Er, Ho) DPs [65,71].

Competition between Dzyaloshinskii-Moriya (DM) interaction and single ion anisotropy (SIA):

For some systems, competition between DM interaction and SIA leads to MR it is mostly found in AFM materials. Authors have attributed the MR in perovskite structures such as $YFe_{1-x}Cr_xO_3$ ($0 \leq x \leq 1$) [204], $BiFe_{0.5}Mn_{0.5}O_3$ [205], $Bi_{0.3}Ca_{0.7}Mn_{0.75}Cr_{0.25}O_3$ [68], $LaCr_{1-x}Fe_xO_3$ (x = 0.45 and 0.5) [206], and $LaFe_{0.5}Cr_{0.5}O_3$ [206,207] to competition among SIA and DM interactions. Ren et.al. said that tilting of VO_6 octahedra in YVO_3, display distorted perovskite structure, which results in to a canted spin structure [73]. The DM interaction and SIA are the results of this canted spin structure [73,140,141].

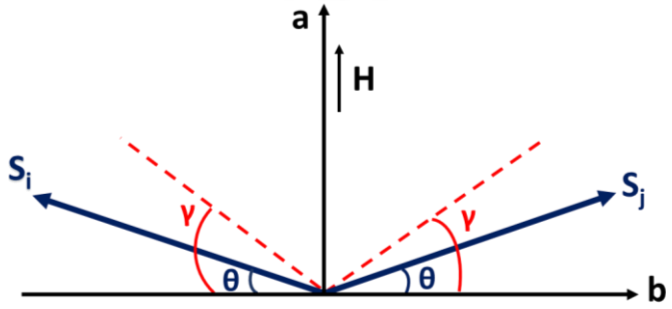

Fig.1.14. Canted spin structure of two sublattice spins S_i and S_j under SIA and DM interaction.

Due to structural distortion, the oxygen ions that mediate the SE interaction between the two nearest neighbors are not in the inversion center. As a result, the DM interaction, which is an antisymmetric interaction, occurs [140]. Additionally, the tilting of the VO_6 octahedra causes the V-O bonds to be staggered, which further causes the SIA axis to be staggered [141]. The schematic representation of two sublattice spins S_i and S_j is shown in Figure.1.14 with a canting angle of θ and SIA prefers the spins along the dotted line with a canting angle γ. For such system having contributions from SIA and DM interaction, the Hamiltonian in an external applied field can be expressed as;

$$H = H_S + H_A + H_e \quad (1.15)$$

Here, H_S contributes to the spin spin interactions, H_A represents the SIA and H_e is due to the external applied field. Hence, H_S = J $(S_i.S_j)$ + D. ($S_i \times S_j$), $H_A = -2AS_Z^2$ and $H_e = {}^{E_f}/_{N}$

Now, combining all these terms the net energy of the system can be written as [73,206],

$${}^{E}/_{N} = \text{J}\ (S_i.S_j) + \text{D}.\ (S_i \times S_j) - 2AS_Z^2 + {}^{E_f}/_{N} \quad (1.16)$$

Here, 1st term stands for Heisenberg exchange interaction with J as the exchange coupling constant. 2nd term stands for DM interaction and D is the Dzyaloshinsky vector. 3rd term stands for SIA and A as the anisotropy constant with the component of spins along the easy local easy axis S_Z. Similarly, last term stands for nearest neighbour (NN) FM interaction and is independent of canting angle. For a magnetic system and for single sublattice, the absolute value of magnetization can be written as,

$$M = Ng\mu_B|\langle S\rangle| \quad (1.17)$$

Here, $|\langle S\rangle| = \frac{g\mu_B\, S(S+1)B}{3k_BT}$ and B = μ_0H (H is the applied field). Now the equation. (1.16) can be written as,

$$E/N = -2AS^2\cos^2(\gamma - \theta) - J\,|\langle S\rangle|^2\cos(2\theta) + D\,|\langle S\rangle|^2\sin(2\theta) + E_f/N \quad (1.18)$$

After minimizing the energy equation. (1.18) can be reduced to,

$$2AS^2\cos(\theta-\gamma)\sin(\theta-\gamma) + J\,|\langle S\rangle|^2\sin(2\theta) + D|\langle S\rangle|^2\cos(2\theta) = 0 \quad (1.19)$$

By assuming θ - γ << 1, and using the Taylor expansion for sine and cosine functions, equation (1.19) can be reduced to,

$$\theta = \frac{2AS^2\gamma - D|\langle S\rangle|^2}{2AS^2 + 2J|\langle S\rangle|^2} \quad (1.20)$$

To reduce the number of variables, let us take $\xi = A/J$ and $\gamma_D = D/2J$, the above expression is reduced to,

$$\theta = \frac{S^2\xi\gamma - \gamma_D|\langle S\rangle|^2}{\xi S^2 + |\langle S\rangle|^2} \tag{1.21}$$

Now the net magnetic moment of the canted AFM system will be,

$$M_{net} = 2Ng\mu_B|\langle S\rangle| \sin(\theta)$$

$$= 2Ng\mu_B|\langle S\rangle|\,\theta \qquad (\because \theta \text{ is small})$$

$$= 2Ng\mu_B|\langle S\rangle| \frac{S^2\xi\gamma - \gamma_D|\langle S\rangle|^2}{\xi S^2 + |\langle S\rangle|^2} \tag{1.22}$$

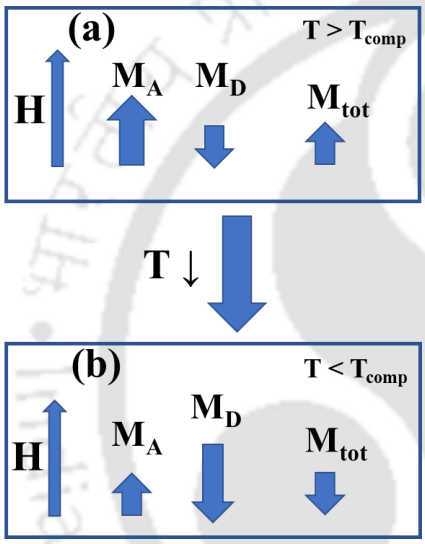

Fig.1.15. (a, b) Temperature dependency of the two sublattice magnetization due to SIA (M_A) and DM interaction (M_D).

Ren et.al. explained the MR, based on the competition between the temperature dependence SIA and DM interaction. Figure 1.14 shows the mechanism of this SIA and DM interaction below and above T_{comp}. SIA is stronger above T_{comp}, producing a net magnetic moment in the direction of the applied field (M_A). When the temperature drops from T_N, M_A will initially rise as a result of the development of the SE interaction and therefore, sublattice magnetization. When the sublattice magnetization increases, the DM interaction also increases, leading to the canting of the spins. The strength of SIA and DM interactions are equal at $T = T_{comp}$, resulting in zero magnetization. For $T < T_{comp}$, DM interaction takes over SIA and it leads to the magnetic moment opposite to the applied field (M_D). NM is thus shown below T_{comp}.

1.10 Bipolar Switching of Magnetization (BSM)

It is mechanism which is found in the material which shows the behavior of MR. When the strength of the applied magnetic field changes without affecting the direction of the field, the magnetization switches between positive and negative values and vice versa this is known as BSM.

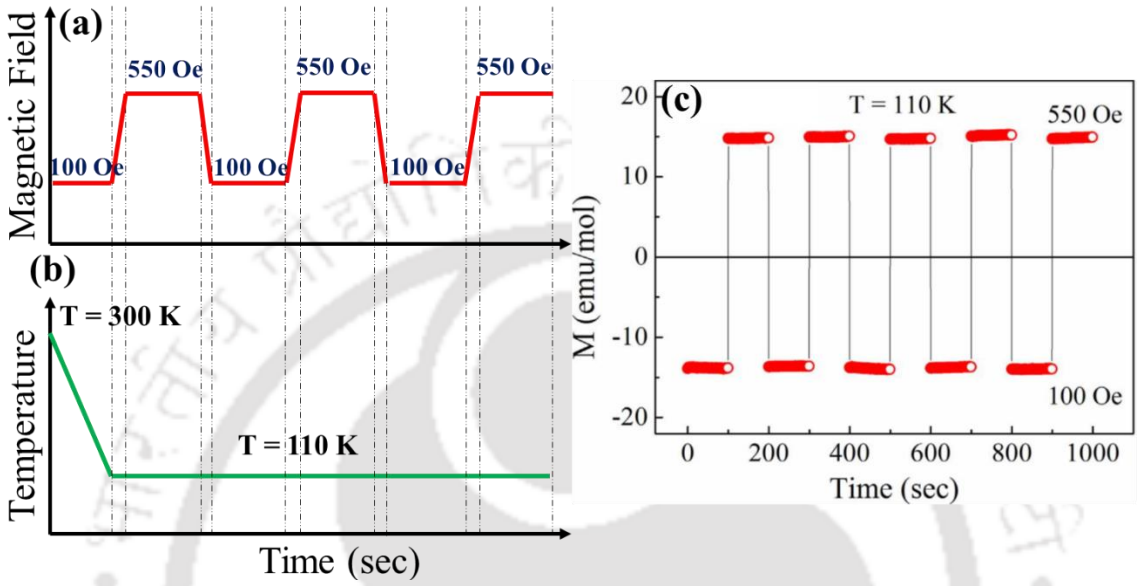

Fig.1.16. (a, b) Mechanism of Bipolar switching of magnetization for $GdCrO_3$ sample and (c) the result obtained for $GdCrO_3$ sample by following the mechanism. Reproduced image from ref [208].

In order to explain this, we have taken the help of magnetization versus time data provided by Bibhuti et.al. for $GdCrO_3$ compound [208]. The sample is initially FC to 110 K ($T < T_{comp}$) at a field of 100 Oe in order to get the switching behavior. After recording the magnetization for 100 seconds, it was discovered to be negative, as shown in Figure 1.16. Then by increasing the field to 550 Oe, the magnetization was recorded for 100 sec, here the magnetization switches to positive value. This procedure was performed multiple times varing the field from 100 to 550 Oe and back to 100 Oe and the BSM is consistent. This result indicates reproducible field induced bipolar switching of the magnetization. Bipolar magnetization switching in materials with temperature dependent MR has been reported [74,205]. These materials may thus be used in spintronics, thermomagnetic switches, TAM-RAM, and other multifunctional devices.

1.11 Exchange Bias (EB) Behavior

As a result of anisotropic exchange interactions at the interface between FM/AFM, FM/FIM, FIM/AFM, FM/SG, etc., give rise to the shift in the magnetic hysteresis loop from the

origin and this phenomenon is known as EB behavior [209-212]. This phenomenon was first discovered in 1956 by Meiklejon and Bean [213]. EB has now been found in a broad range of systems, including multilayers, core-shell structures, binary alloys, intermetallic alloys, oxide materials (manganite, cobaltite, chromite, ferrites) and so on [209-221]. This phenomenon has piqued the interest of many scientists because of its possible use in magnetic recording media, spintronics devices, spin valve, field sensor etc., The general formula used to calculate the shifting in the magnetic hysteresis loop along the field axis can be written as [79];

$$H_{EB} = \frac{H_+ + H_-}{2} \tag{1.23}$$

Similarly, the effective coercivity can also be calculated by using the relation;

$$H_C^{eff} = \frac{H_+ - H_-}{2} \tag{1.24}$$

Sometimes a vertical shift in the loop has also been observed along the magnetization axis and this can be calculated by using the relation;

$$M_{EB} = \frac{M_+ + M_-}{2} \tag{1.25}$$

Here, H_+ and H_- stands for the field values in ascending and descending branches of the loop for M = 0. Whereas, $M_+$and M_- represents the magnetization values for descending and ascending branch of loop where H = 0 Oe.

To explain this phenomenon, we have taken the help of Meiklejohn et. al. report [210, 213] as shown in the Figure 1.17. Here they have taken the layered AFM and FM structure to explain EB. The spins in the FM portion of a sample will align along field direction when it is cooled to a temperature that is below T_C but above T_N ($T_N < T < T_C$), while the spins in the AFM portion will stay in a random orientation (Figure 1.17 (a)). However, on further lowering the temperature below T_N ($T < T_N$), there should be two possibility of spin coupling at the interface. It is either parallel or antiparallel arrangement, here we have taken the case of parallel spins coupling at interfaces (Figure 1.17 (b)). When the field reaches to maximum value in the first quadrant, the FM spins are aligned themselves along the direction of field and the layer of AFM spins which is close to the FM layer is also aligned parallel to it at the interface. Whereas, rest of the AFM spins follow the usual AFM spin arrangement. Now, when we reverse the direction of field in the second quadrant, FM spins also try to reverse their spins to align themselves along the field direction. But here the AFM anisotropy is stronger than the FM one, as a result, AFM spins exert a torque on the FM spins at the interface to retain their previous spin configuration. Due to this torque, during the

descending branch of the loop, it required a large amount of field to demagnetize the system. Then at maximum negative field in the third quadrant, FM spins are aligned along the direction of the field and AFM spins are at the earlier state (Figure 1.17 (c)). Again, when the field changes its direction to positive value, FM spins easily flip their spins towards field direction, the favorable FM exchange anisotropy at the interface help the spin reversed. Hence, in the ascending branch of magnetization, it doesn't need a higher amount of field to align the spins in the field direction. This complete process in the magnetic hysteresis, leads to the shifting of the loop towards the negative field direction.

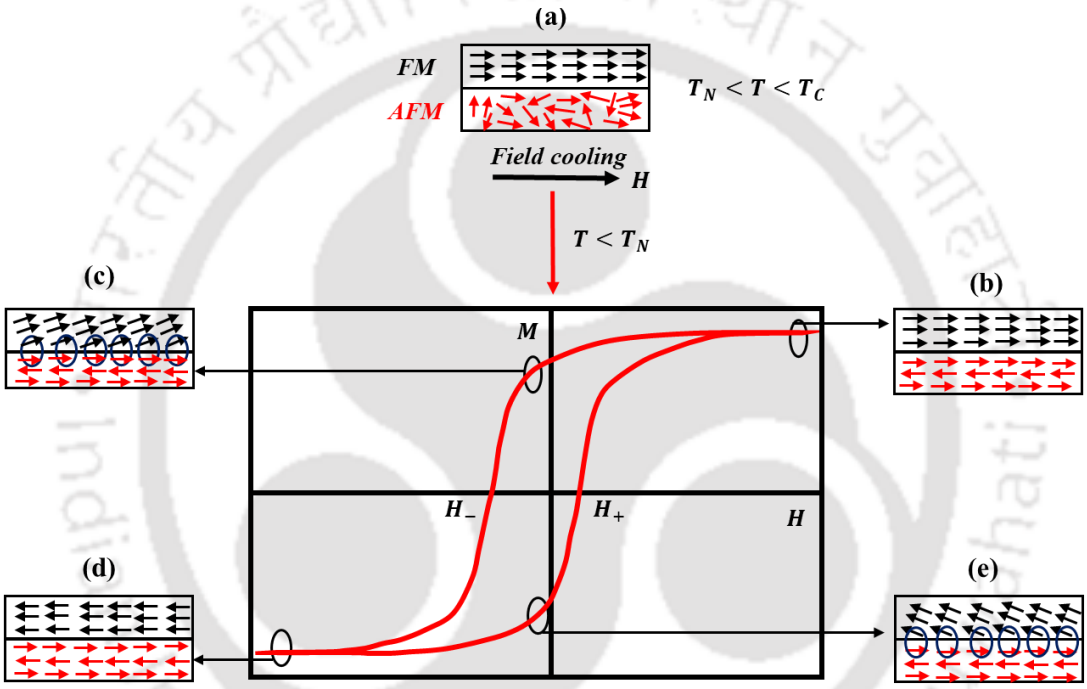

Fig. 1.17: Diagram showing FM-AFM coupling at various stages of a shifted hysteresis loop, including spin configuration at the interface.

The above explained loop is all about the conventional EB, where the system is cooled down in the presence of a field. Even without cooling by an external magnetic field, a spontaneous loop shift might be seen in some systems. This is known as the zero-field cooled EB or spontaneous EB effect. The SEB effect is very advantageous for electric field control of EB devices because it removes the need for an external magnetic field. At first, SEB was thought to be a minor loop effect or instrumental artefact [222]. Saha et. al. in 2007 disproved this presumption by demonstrating that it is an inherent characteristic of $Ni_{80}Fe_{20}/Ni_{50}Mn_{50}$ [223]. A number of authors have since reported SEB in a variety of systems, including nanocomposites, heusler alloys,

ceramics, films, perovskites, DPs etc., [223-230]. The existence of multi magnetic phases, spin glass-like phases, and FM/AFM phases is the most typical cause of such SEB.

In the above texts we have explained, in any material the MH loop shifts either to negative or positive field axis. But in certain systems, in a single compound the field dependent EB shows the sign reversal at a particular field [231,232]. Similarly, there are some systems which show a sign reversal in EB with respect to temperature [203,208,233]. Such sign reversal phenomenon of EB by field and/or by temperature is known as tunable EB behavior. Field induced tunable EB was observed in bilayer system such as *Ni/FeF_2* and *Fe/FeF_2*, and it is attributed it to the competition between the FM/AFM phase with the Zeeman energy [231,232]. Temperature induced tunable EB has been observed in 2009 by Kulkarni et.al in intermetallic system $Nd_{0.75}Ho_{0.25}Al_2$ across T_{comp} [234]. Later on, in $Sm_{0.98}Gd_{0.02}Al_2$ [235] and $Sm_{0.975}Gd_{0.025}Cu_4Pd$ [236] alloys, such behavior is also found. This characteristic behavior is generally observed in materials having temperature-induced magnetization reversal (TMR) property [203,208,233]. A system having the combined property of sign reversal in both temperature dependent MR as well as EB should be used in device applications such as thermomagnetic switches, TAM-RAM etc. [199,237]. Such behavior is observed by several authors in various materials such as, in nanoparticles of $La_{0.2}Ce_{0.8}CrO_3$ [199], perovskite structures of $YFe_{0.5}Cr_{0.5}O_3$ [238], $La_{1-x}Pr_xCrO_3$ [239], $NdCr_{1-x}Fe_xO_3$ (x = 0.05-0.20) [240], $LaCr_{0.85}Mn_{0.15}O_3$ [204], $NdMnO_3$ [240], solid solutions of $BiFeO_3$ – $BiMnO_3$ [241], DP of Sr_2YbRuO_6 [237] etc.

1.12 Magnetocaloric Effect (MCE)

The phenomena which describe the thermal reaction of a magnetic material to a varying magnetic field is known as the magnetocaloric effect (MCE). The domains of an adiabatic magnetic material attempt to align themselves along the field direction when an external magnetic field is applied to it, which results in a drop-in entropy at a given temperature. However, when an applied magnetic field is withdrawn under adiabatic conditions, the magnetic domains get randomised, causing a reduction in the temperature of the system. In order to use this approach for refrigeration, it is necessary to build a cycle that incorporates the two types of processes listed below: releasing heat to a high temperature heat sink and absorbing heat from a low temperature heat source. The Carnot magnetic refrigeration cycle, which combines the four processes of isothermal magnetization, adiabatic demagnetization, isothermal demagnetization and adiabatic magnetization is a typical example. The Maxwell equations of thermodynamics are considered to

determine the magneto caloric effect, which is characterized in terms of change in magnetic entropy ($-\Delta S_M$) as a function of temperature and magnetic field [242].

$$\Delta S_M(T,H) = \int_0^H \left|\frac{dM}{dT}\right| dH \tag{1.26}$$

The above equation can be written as,

$$\Delta S_M = \sum \frac{M_i - M_{i+1}}{T_i - T_{i+1}} \Delta H_i \tag{1.27}$$

Here, M_i and M_{i+1} are magnetic moments at temperatures T_i and T_{i+1}, in the presence of a change in magnetic field ΔH_i. The efficiency of a magnetocaloric material is measured by its relative cooling power (RCP), which can be calculated using the relation,

$$RCP = -\Delta S_M^{max}(T,H) \times T_{FWHM} \tag{1.28}$$

Here, T_{FWHM} is the full width at half maximum of the entropy versus temperature curve. There are several ways to find out the order of the magnetic phase transition. One is the slop in M^2 versus H/M plot, Positive slopes indicate second order phase transitions (SOPT), whereas negative slopes indicate first order phase transitions (FOPT) [243]. Second is, the field dependence of magnetic entropy which is represented as, $\Delta S_M^{max} = H^n$. Here, ΔS_M^{max} is the maximum value of ΔS_M at different temperatures. Here n plays a major role, such as the value of $0 < n < 1$ represents SOFT, $n > 1$ represents FOPT and $n = 2$ stands for PM region [71,244,245].

1.13 Literature Survey

As it is explained in the section 1.1, that the perovskite is a class of materials, presented by the chemical formula ABX_3, where 'A' and 'B' are the cations and X is an anion and 'A' is much larger than 'B' [2]. They can have electronic structures that range from insulating to metallic, and they can even be half metallic with spin-polarized electrical conductivity. They also display ferroic atomic displacements, ionic conductivity, and catalytic properties. Coming to the magnetic part, they have magnetic orderings ranging from AFM to FIM and FM. In addition, they exhibit magnetic frustration with no obvious long-range magnetic order. Perovskites may have many of these characteristics all at once, giving rise to novel combination of properties like multiferroicity [2]. In order to tune these properties, the formula is doubled and exactly half of the B-site cations are substituted with another cation which leads to the formation of DP compound $A_2BB'X_6$ [2]. The deviation of perovskite structure from deal cubic phase mostly depends on B/B' ordering.

Based on this we have reviewed the DP compounds by taking various B/B' combinations, which is explained below.

1.13.1 Co-Mn Based Double Perovskite

The ordered DPs belonging to the *Co-Mn* based family R_2CoMnO_6 (*R* - rare-earth element) are significantly explored to understand their magnetic, dielectric, magneto-dielectric and magneto-electric properties. These are mostly found in monoclinic structure with $P2_1/n$ space group at RT [56,57,60,229,247,248]. In the case of ordered R_2CoMnO_6, it is anticipated that the Co and Mn ions will be in the 2+ and 4+ oxidation states and they will both be in 3+ state for disordered phase. They are of great magnetic interest as they belong to a typical FM group. In the ordered state, the SE interactions across Co^{2+}-O^{2-}-Mn^{4+} networks lead to FM ordering [38,57]. Whereas, sometimes due to ASD and APB, the interaction across Co^{2+}-O-Co^{2+} and Mn^{4+}-O-Mn^{4+} networks and the presence of Co^{3+}/Mn^{3+} ions can lead to minor AFM phase [54-62]. However, according to a few observations, in disordered state, the SE interaction across Co^{3+}-O-Mn^{3+} leads to FM at low temperatures [56,58,59]. This complex magnetic structure in *Co-Mn* based DP makes it more promising as it leads to complex magnetic feature at low temperatures [56,58,59]. This mixed phase adds few intriguing magnetic properties to the material, such as breakdown of spatial inversion symmetry and the resulting spontaneous electric polarization [54,55,67,239,250]. La_2CoMnO_6 (LCMO) is one of the most investigated DP compounds in this family because of its complex magnetic features [56,58-60]. However, stabilization of its structure was a great deal. It is interesting to note that the temperature at which the orthorhombic-to-rhombohedral phase transition occurs in LCMO depends on the rate of cooling during synthesis. LCMO possesses a high degree of orderness at 1060 K and gets disordered for $T \geq 1400$ K [251]. Two FM T_C values of 80 K and 230 K have been observed for LCMO. High temperature FM transition at 230 K is attributed to the Co^{2+}-O^{2-}-Mn^{4+} interactions, whereas, the interaction among disordered Co^{3+} and Mn^{3+} ions were predicted to be the source of the low temperature transition at 80 K [56]. A RT magneto dielectric of about 80 % has been observed for LCMO ceramics [58]. It prompts their application in spintronics and multiferroic devices. Researchers may still create multifunctional materials using this combination because of numerous electronic interactions including the Co^{2+}-O-Mn^{4+} interactions. Few researchers replace La^{3+} ions with Sr^{3+} ions in order to get a wide range of characteristics. For 25% replacement of La with Sr, along with the above two FM transition it exhibits a glassy nature, spin phonon coupling and a magneto-dielectric effect close to 45% [59].

However, in 50 % doped sample, complex magnetic properties such as two FM phases, spin glass like feature and EB effect have been observed [60]. The low temperature transition is the AFM one and is caused by the ASD induced exchange interaction across Mn^{4+}-O^{2-}-Mn^{4+} and Co^{2+}-O^{2-}-Co^{2+} networks.

Similarly, the other compounds such as Tb_2CoMnO_6 show metamagnetic phase which lead to a sign reversal in MCE with a maximum value of maximum magnetic entropy (ΔS_m) of 20.8 J/kg.K below 15 K at H = 7 T [64]. Banerjee et. al. reported a FC MR in Er_2CoMnO_6 with T_{comp} = 4 K, [65]. It has also shown a MR in ZFC curve with two T_{comp} at 20 K and 42 K. MR is ascribed to the large uniaxial anisotropy of Er^{3+} ions. It has a FM T_C ~ 67 K. In addition to this, it shows a tunable EB behavior and it is due to the negative exchange interactions between the RE and TM ions. In Y_2CoMnO_6 the up-down arrangement of Co^{2+} and Mn^{4+} magnetic moment leads to a ferroelectricity at 80 K [67]. Y_2CoMnO_6 is also a FM one with T_C = 75 K with a spin glass type of nature at 55 K [46]. MCE shows a maximum ΔS_m of the value 7.3 J/kg.K with RCP of 220 J/kg. Similarly, Sm_2CoMnO_6 is a multiferroic material with a FM T_C of 135 K. Nd_2CoMnO_6 shows a FM T_C of 168 K and it arises due to Co^{2+}-O-Mn^{4+} interaction. A spin glass type of ordering at 135 K as well as a metamagnetic phase, Griffith phase and spin phonon coupling has been reported [248]. Similar type of properties along with EB effect is found in Pr_2CoMnO_6 [54]. Kim et al. taken all the elements from La to Lu at RE site and found that with rise in ionic radii of A site FM T_C is increasing from 48 K for Lu_2CoMnO_6 to 204 K for La_2CoMnO_6 [63]. The magnetic ground state is found to be a F-type for large ions (Ho/Tm) whereas, for smaller one (Yb/Lu) E-type ordering is found between Co^{2+} and Mn^{4+} ions [57]. A few groups have started studying Ho_2CoMnO_6 DPs from the last couple of years, as it has a lower cationic size of 1.07 (2) Å and a greater magnetic moment (10.6 μ_B) compared to other RE elements [44,57,63,71]. It shows a F-type FM ordering across Co^{2+} and Mn^{4+} ions whereas, Ho also takes part in the FM ordering at higher fields [57]. The FM T_C is obtained around 78 K, with a magnetic entropy of 12 J/kg K at 10 K for 7 T field [44,63]. Recently a MR has been observed in ZFC curve of MT data with T_{comp} ~ 50 K, and is ascribed to the exchange interaction among Ho^{3+} and Co^{2+}/Mn^{4+} ions [71].

1.13.2 Fe-Cr Based Double Perovskite

Fe-Cr based perovskite structure are generally found in disordered orthorhombic state (space group - Pbnm, Pnma, R3c etc). Here, Fe and Cr ion randomly distributed in the octahedral site due to their comparable ionic radii (Fe^{3+} (0.645 Å), Cr^{3+} (0.615 Å)), resulting in to octahedral

distortion. The interaction in Fe^{3+}-O-Fe^{3+}, Cr^{3+}-O-Cr^{3+} and Fe^{3+}-O-Cr^{3+} mainly determines the magnetic and electronic properties of these material [50,206,252,253]. It generally shows a canted AFM structure with a weak FM component. $RCrO_3$ is a popularly used materials among the researchers due to its TMR and EB properties and hence its applications in storage devices, spintronics, magnetic switches etc. [72-80]. A multiferroic material $RFeO_3$ has also been shown few applications like ultrafast photomagnetic recording [85], laser-induced ultrafast spin reorientation (SR) [83,84], and ultrafast photomagnetic recording [85]. $YFeO_3$ is a canted AFM with mild FM due to DM interaction and Cr^{3+} ions in orthochromites show the SIA. After looking at the tremendous properties and applications of $RCrO_3$ and $RFeO_3$, researchers started to prepare $RFe_{0.5}Cr_{0.5}O_3$ to tune their properties. In the year 2005, Azad et al. [207] reported MR in $LaFe_{0.5}Cr_{0.5}O_3$ below 210 K, however its origin is yet unknown. In 2011 Mao et. al. prepares $YFe_{0.5}Cr_{0.5}O_3$ and reported temperature as well as field induced MR [252]. Obtained MR is reconfirmed by the tunable BSM below T_{comp} (248 K). It has an AFM ordering temperature at 274 K, whereas, above and below 260 K, it exhibits both normal and inverse MCE. Then in 2012, Dasari et. al. prepared $YFe_{1-x}Cr_xO_3$ ($0 \leq x \leq 1$), and they also reported MR [204]. The temperature dependence and competition between SIA and DM interaction is ascribed to the observed MR in the above two cases [204,252].

In 2013 Bora et. al. synthesised $LaCr_{1-x}Fe_xO_3$ by standard sol-gel route and observed some interesting properties for the various concentration of the sample [206]. For x = 0.05 to 0.15 they observed MR, for x = 0.20 to 0.40 it shows a FM type behavior, whereas, for x = 0.45 - 0.50 again MR has been observed [206]. The reason for the observed MR in lower concentrated samples is attributed to the competition between PM moment of Fe^{3+} ion under the negative internal field and the weak FM component created by the canted Cr^{3+} ion. At the same time the origin of MR in higher Fe concentrated samples are ascribed to the competition between the SIA and DM interaction. In the same year Nair et. al. [134] synthesized $YFe_{0.5}Cr_{0.5}O_3$ by solid state route and reported a canted AFM at 275 K with a weak FM depicted by a MH loop at 20 K. A dielectric relaxation at ~507 K, and at the same temperature a peak in M-T plot revealed a magneto dielectric behavior. BSM as well as the occurrence of both normal and inverse MCE have been observed in materials with TMR [74,252]. This property makes this material applicable in spintronics and magnetic refrigeration. Fe-Cr based perovskites are extensively studied whereas, Fe-Cr based DP are very less explored few of which are listed here. In R_2FeCrO_6 DP, the magnetic ordering is also

determined by the SE interaction across Fe^{3+}-O^{2-}-Fe^{3+}, Cr^{3+}-O^{2-}-Cr^{3+} and Fe^{3+}-O^{2-}-Cr^{3+} networks as that of perovskite structure [2]. Due to its multiferroic properties, Bi_2FeCrO_6 (BFCO) has been the subject of much investigation [86-89]. Its structural fragility at high temperatures is however a disadvantage [87-89,254]. In 2008 Ju et. al. [86] gave a theoretical aspect for colossal MCE in BFCO.

In 2012 Nechache et. al. reported a progress on stabilization of ordered BFCO by tuning the mismatch in radii of substrate and BFCO [88]. It leads to a novel multiferroic properties at RT [88]. Similarly, Sha et. al. deposited BFCO on Pt/Ti/SiO/Si substrate by PLD, and reported a FM behavior at RT [87]. A type-I multiferroic known as Pr_2FeCrO_6 is a rare member of this family which has an exceptional structural stability up to 1500 K [253,255]. It could be a strong contender for spintronics applications because of its high Curie temperature (FM T_C~562 K) and multiferroicity as reported by S. Ravi [253]. Recent research on Pr_2FeCrO_6 nanoparticles by Gaikwad et. al. revealed that they exhibit a structural stability at 923 K with increased magnetic characteristics [135]. Pr_2FeCrO_6 has also been shown to exhibit complex magnetic behaviour and a maximum value of $-\Delta S_m = 2.06$ J kg^{-1} K^{-1} at 14 K for H = 9 T [90]. Recently a magneto-dielectric behaviour has been seen in Y_2FeCrO_6 [91]. It has been discovered that an artificial superlattice of $LaFeO_3$ and $LaCrO_3$ exhibits FM behaviour. However, La_2CrFeO_6 is yet disordered and magnetically it is AFM with a weak FM component [207,256].

1.14 Motivation

In view of the above literature survey, we learned that the family of DP materials is of tremendous interest in physics and materials science because of the vast variety of multifunctional characteristics integrating magnetic, electric, and thermal properties. Despite their enormous practical and scientific significance, it is still difficult to achieve a well-controlled behavior in magnetoelectric and multiferroic properties at RT. Most of the magnetic properties such as EB and MR which are the key factor for spintronic, storage application, and switching elements are found at low temperature. It generates a thermal barrier that prevents these systems from being used in RT applications. We've also discovered amazing features for Co/Mn-based DPs and Fe-Cr-based perovskite structures. Despite the fact that, Ho possess a high magnetic moment compared to Co and Mn, and the multiferroic property of YFCO. It is worth noting that, there are just a few reports on Ho_2CoMnO_6, and Y_2FeCrO_6 DPs. As a result, there is no comprehensive research on the

magnetic properties at various temperatures and magnetic fields of these compounds. So, for the thesis work, we have chosen two parent compounds, Ho_2CoMnO_6, and Y_2FeCrO_6 DPs. It was anticipated that by reducing the size of a system, it would be possible to preserve the original characteristics of the system while also giving a few new magnetic properties. To the best of our knowledge, research on nanostructured Ho_2CoMnO_6 and Y_2FeCrO_6 DPs is still lacking and of large interest. Therefore, in this work we have focused on the preparation of nanostructured Ho_2CoMnO_6 and Y_2FeCrO_6 DPs and studied there structural and magnetic properties. In the current thesis work, we have focused on magnetization reversal (MR), exchange bias (EB) behavior and/or tunable EB behavior, as well as raising the ordering temperature by appropriate doping. So that, these materials might be used for spintronics, memory elements, and switching elements across a wide temperature range.

For the present thesis work, we have prepared the following nanostructured double perovskite compounds.

6) Nanocrystalline $(Ho_{1-x}Sm_x)_2CoMnO_6$ for x = 0.0 to 0.5
7) Nanorods of Ho_2CoMnO_6
8) Nanocrystalline $Ho_2CoMn_{1-x}Ni_xO_6$ for x = 0 - 0.4
9) Nanocrystalline $Ho_2CoMn_{1-x}Cr_xO_6$ for x = 0 - 0.5
10) Nanoparticles of Y_2FeCrO_6

In the first series we have doped Sm in Ho_2CoMnO_6 compound at Ho site, up to 50% replacement of Ho. As per literature survey Sm_2CoMnO_6 is a multiferroic system with a FM T_C larger than Ho_2CoMnO_6, and ionic radii of Sm is larger than Ho. The goal is to induce some anisotropy in the system, which lead to complex magnetic interactions and look for EB behavior. It is also expected to get a higher FM T_C with Sm substitution. Second one is the nanorod of Ho_2CoMnO_6 DP, here the aim is to report and analyses a detailed comparative study of the structural and complex magnetic properties with that of the bulk and nanocrystalline Ho_2CoMnO_6. Due to the transfer of the structure from bulk to nanorod, the possibility of surface spin canting is there, and is might unlock complex magnetic properties. Also, the structural distortion leads to a variation in bond angle of TM ions thereby tuning the ordering temperature. Third and fourth series are the TM ion (Ni, Cr) doped series at the Mn site. As Ni^{4+} ion has smaller magnetic moment compared to Mn^{4+}, so to tune the FM interaction Ni is doped. At the same time Cr^{3+} is the element

which has the same electronic configuration as that of Mn^{4+} ion. Also, the literature survey says that, the replacement of Mn by Cr give rise to multiple oxidation states for Mn. So, it is expected to get a complex magnetic property due to the magnetic interaction between Mn and other TM ions. Further, it might lead to EB behavior and MR in the system as obtained in systems with Cr doping. As $YFe_{0.5}Cr_{0.5}O_3$ is AFM in nature and Fe/Cr are randomly distributed at the same crystallographic site. So, it is aimed to go for nanoparticles of Y_2FeCrO_6, with the possibility of surface spin canting. In such a case, one would expect the ASD and associated weak FM components which gives rise to a higher magnetic moment as compared to bulk counterpart. Smaller the particle size larger the structural distortion and this also helps in tuning the bond angle of TM ions and thus exchange interactions. So, in order to tune the T_C and improve the functional properties, we have synthesized nanoparticles of Y_2FeCrO_6 and studied its structural and magnetic properties.

Chapter 2

Synthesis and Characterization Technique

The sample preparation techniques and sophisticated tools used for sample characterization and measurements are covered in this chapter. For the preparation of samples, we have used two methods: auto combustion and hydrothermal method. For the study of structural and magnetic properties, we have used various instruments which are described in detail in this chapter.

2.1 Synthesis Methods

Auto Combustion

By combining various elements at the atomic level to create nano-sized, homogenous, and highly reactive powders, auto combustion is a quick and affordable method for creating particulate products. It has been widely utilized to create a range of metal - oxides and alloy nanoparticles. Here, the primary forms of the starting chemicals employed were nitrate or acetate. In our case, to prepare polycrystalline samples of $(Ho_{1-x}Sm_x)_2CoMnO_6$ (x = 0.0-0.5) we have taken the initial compounds as, cobalt nitrate hexahydrate ($Co(NO_3)_2.6H_2O$, 99.0% purity) and manganese acetate tetrahydrate ($C_4H_6MnO_4.4H_2O$, 99.0% purity). However, for holmium and samarium we have used oxides and glycine ($C_2H_5NO_2$, 99.0% purity) was used as a fuel for combustion. To prepare the sample, diluted nitric acid (HNO_3) was added to the stoichiometric ratio of holmium oxide (Ho_2O_3, 99.9% purity) and samarium oxide (Sm_2O_3, 99.9% purity) to produce their nitrates. The prepared nitrates were added to the solution containing uniform mixture of $Co(NO_3)_2.6H_2O$ and $C_4H_6MnO_4.4H_2O$, which were dissolved in distilled water. Glycine was added to the solution in 1:2 molar ratio with metal ions. The resulting solution was progressively heated at 70 ^{0}C and transformed into gel. After the gel was formed, it was allowed to burn by raising the temperature, resulting in black fluffy powder. The powder was grinded further for uniform mixture then was pre-sintered at 650 ^{0}C for 6 hours. The final sintering took 6 hours at 850 ^{0}C. Similarly, for polycrystalline $Ho_2CoMn_{1-x}Ni_xO_6$ (x = 0.0 - 0.4) and $Ho_2CoMn_{1-x}Cr_xO_6$ (x = 0.0 - 0.5) we have followed the same procedure. Where we have taken nickel nitrate hexahydrate ($Ni(NO_3)_2.6H_2O$, 99.99% purity) for Ni substitution and chromium nitrate nonahydrate ($Cr(NO_3)_3.9H_2O$, 99.99%

purity) for Cr substitution. However, for the synthesis of Y_2FeCrO_6 nanoparticles, we used 99.9% pure yttrium nitrate nonahydrate ($Y(NO_3)_2.9H_2O$), iron nitrate nonahydrate ($Fe\ (NO_3)_2.9H_2O$) and chromium nitrate nonahydrate ($Cr\ (NO_3)_2.9H_2O$) and followed the steps outlined above. But in this case, the final sintering was at 650^0 C for 6 hours.

Hydrothermal

One of the frequently utilized synthesis techniques for the creation of nanoparticles, nanorods, nanotubes, nanosheets, etc. is the hydrothermal method. The reactions take place at high pressure and temperature inside a hydrothermal autoclave. For the synthesis of Ho_2CoMnO_6 nanorods, holmium oxide (Ho_2O_3), cobalt nitrate hexahydrate ($Co(NO_3)_2.6H_2O$) and manganese acetate tetrahydrate ($C_4H_6MnO_4.4H_2O$) with 99.9% purity were used as initial precursors. As a precipitating agent and a capping agent, aqueous ammonia (NH_4OH) and cetyltrimethyl ammonium bromide (CTAB) were utilized. As previously mentioned, Ho_2O_3 was first transformed into nitrates, followed by the dissolution of $Co(NO_3)_2.6H_2O$ and $C_4H_6MnO_4.4H_2O$ in distilled water. CTAB was then added in each beaker in 1:4 molar ratio with the respective metal ions. A single beaker containing the three combined solutions was stirred for two hours at 80^0 C. To bring the PH value near to 11, drop by drop, aqueous ammonia was added. The precipitate was then separated using a centrifuge. The precipitate was re-dispersed in methanol and stored in a hydrothermal that was heated to 120^0 C for 24 hours in a hot air oven. After naturally cooling to RT, the precipitate was rinsed multiple times with distilled water and it was centrifuged to separate the precipitate. The precipitate was collected in a petri dish and dried at 80^0 C. Final sintering was done for 6 hours at 1000^0 C.

2.2 High Temperature Furnace

The pre-sintering and final sintering of the as prepared samples were carried out using a high temperature furnace. This is manufactured by Nabertherm with Model number HTCT 03/15, and has a maximum working temperature of 1500 ^{0}C. Figure 2.1 shows the diagram of the high temperature furnace. It has a double wall insulating chamber, outermost layer is made up of stainless steel. A PID programmable temperature controller (model number C450) was used to regulate the temperature. As a temperature sensor, a S type thermocouple (Platinum Rhodium-10%/Platinum) was employed and Silicon-Carbide (Si-C) rods were employed as heating element. To turn on the power supply to the Si-C rod, a solid-state relay was employed as a switching

device. The furnace's working voltage ranges from 380 V to 400 V, and its maximum current capacity is 20 A.

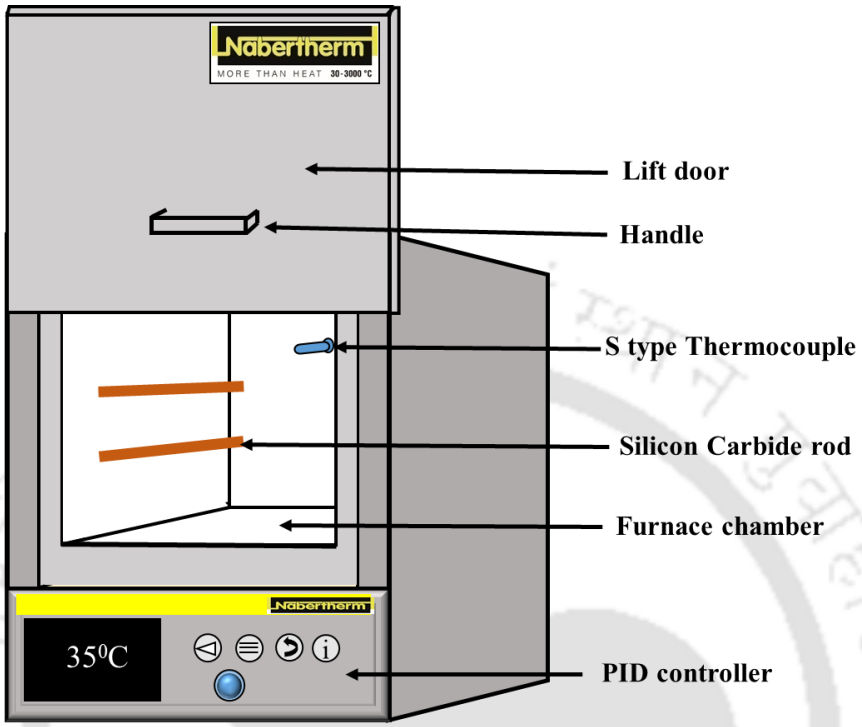

Fig. 2.1: Schematic diagram of high temperature furnace.

2.3 X-ray Diffraction

A wide range of materials, from single crystal and epitaxial thin films to polycrystalline powders and even randomly oriented amorphous materials, are studied using the x-ray diffraction (XRD) method. This method reveals details regarding the phase purity of the sample. In an XRD experiment, the mounted sample is illuminated with a beam of x-rays. The x-ray tube and detector move in a synchronized motion. The diffracted x-rays from the sample is recorded and plotted, where peaks are observed related to the crystal structure of the sample. The instrumental setup is shown in Figure .2.2 (a). Most of the materials are made up of many small crystals, each of these crystals is composed of a regular arrangement of atoms and unit cell. X-rays are high energy light with a wavelength (λ), which is generally comparable to the interlayer spacing of atomic arrangement. When the atomic planes are exposed to an x-ray beam, x-rays are scattered by the regularly spaced atoms. Interference of the emitted signals occurs at very specific angles, leading to peak for specific glancing angle popularly known as Bragg angle. The pictorial representation

of diffraction is shown in Figure 2.2 (b). The angle between the incident and the scattered beam is called 2θ. The relationship between the Bragg angle (θ), spacing between the atoms (d) and wavelength (λ) can be determined by applying the Bragg's law. It is named after William Henry and William Lawrence Bragg the father son team, who won the Novel prize in 1915 for their work of analyzing crystal structure with XRD. Bragg's law can be express as [257],

$$2dsin\theta = n\lambda \tag{2.1}$$

Here, n is the order of diffraction. For all of our samples we have used 9 kW powder XRD system which is Rigaku made diffractometer (model- smart lab) with Cu K_α radiation ($\lambda = 1.5406$ Å) in order to get the RT XRD patterns.

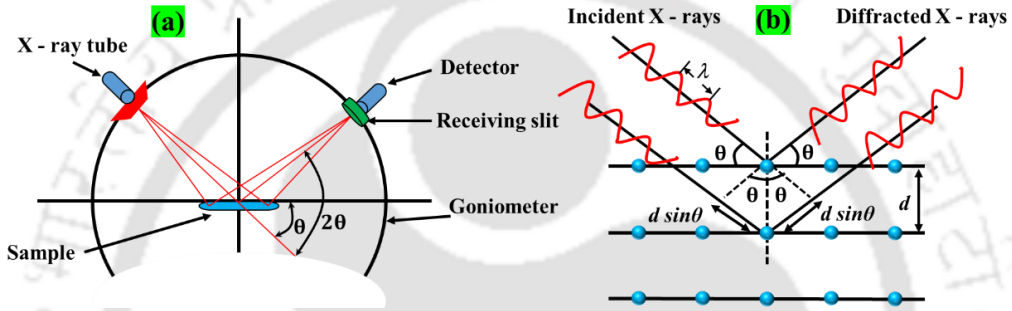

Fig. 2.2: (a) Instrumental arrangement of XRD and (b) schematic diagram of Bragg's Law.

2.4 Raman Spectroscopy

Raman spectroscopy is a method for understanding the crystal structure. C. V. Raman discovered Raman scattering in 1928. It is a type of vibrational spectroscopy that is often used to investigate structural features including crystalline phases, defects, strain, etc. When a sample is exposed to monochromatic light in visible region, major portion of the light gets elastically scattered. However, a minute part of the light gets inelastically scattered by the sample in all directions. One can observes the scattering at right angle to the incident beam. The incident light has a particular frequency (ν_i). If the scattered light has a same frequency (ν_s) as that of incident light, then scattering is called as Rayleigh scattering. However, it has been observed that about 1% of the total ν_s occurs at frequencies different from the ν_i, this is called as Raman scattering. When an incident monochromatic light interacts with an electron in the sample, the electron absorbs energy from the incident photon and rises to a higher state of energy. The Raman spectra comprise three distinct portions: Rayleigh scattering, Stokes scattering, and anti-Stokes scattering. When both the incident and scattered light frequencies are same Rayleigh scattering occurs. If the

frequency of scattered photon is less than the frequency of incident photon ($\nu_i > \nu_s$), Stokes lines are observed. Similarly, when frequency of emitted photon is greater than incident photon ($\nu_i < \nu_s$), anti-Stoke lines are observed. We can observe the presence of Raman shift, denoted as $\Delta\nu = \nu_i - \nu_s$. If $\Delta\nu$ is positive it is known as red-shift or stokes shift. At the same time if $\Delta\nu$ is negative, it is known as blue-shift or anti-stokes shift. The Raman spectra is different for different material. By studying this, one can identify the rotational levels and thus a particular molecule. It helps in performing qualitative analysis. Similarly, the intensity value of a particular Raman lines helps to determine the concentration of a molecule in a sample. In this manner quantitative analysis can be done. Thus, Raman spectroscopy can be used to perform both quantitative and qualitative analysis on a sample [258].

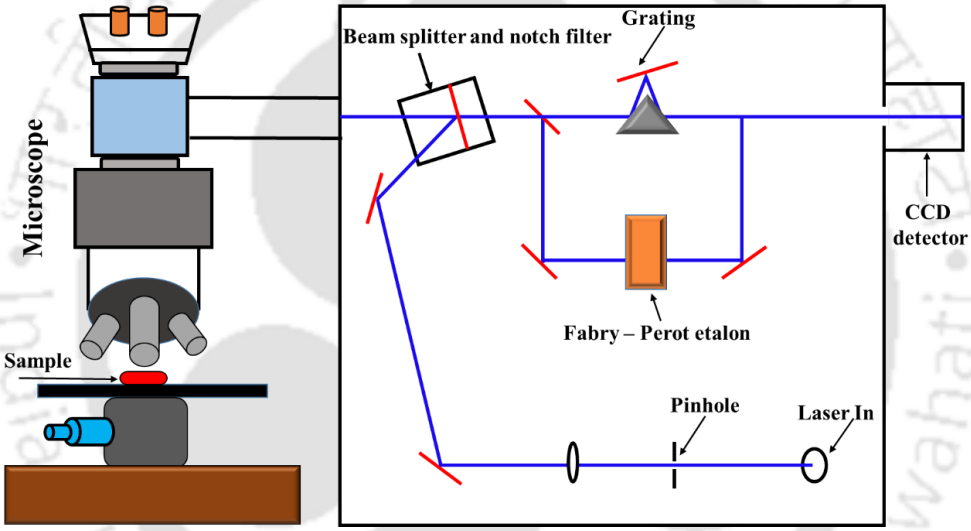

Fig. 2.3: Instrumental arrangement of Raman Spectrometer.

For our work, we have used a Horiba Jobin Yvon make micro-Raman spectrometer (model-LabRam HR 800,) equipped with the Argon laser (λ = 488 nm), objective lens (50X long distance, numerical aperture 0.5, working distance 10.6 mm) and grating (1800 grating/mm) to record Raman spectra at RT. Here, the system is a dispersive type, the instrumental part is shown in Figure 2.3. To see Raman effect, we need only four main components, a laser, an optical filter, a spectrometer and a charge couple device (CCD) detector. From the laser we can shoot the sample with as many as photon we need and all these photons have the same energy or wavelength. Next is the optical filter, it only allows Raman scattered light to pass through and reflect Rayleigh scattered light. Now, only the Raman scattered photons are left but to interpret them, we still need

to know their exact wavelengths. The third component is the spectrometer, just like a prism it guides the photons to different directions according to their wavelength. The grating and etalon enabled the scattered light to pass through, which improved the resolution of the weak inelastic scattered wavelength coming from the sample. Finally, the Raman scattered photons fall on distinct positions on the CCD detector and thus, a Raman scattered light can be captured. However, in Raman spectroscopy, the data obtained is in the form of intensity versus wavenumber, where wavenumber is in the range of 100 to 1400 cm^{-1}.

2.5 Field Emission Scanning Electron Microscope (FESEM)

Field emission scanning electron microscopy (FE-SEM) is a sophisticated technique, most widely used for capturing the microscopic picture of materials through scanning the surface of a materials by focused electron beam passed through the different electromagnetic lenses and apartures in high vacuum conditions. For the image formation, the focused electron beam scans over the surface area of a given specimen and generate rectangular image. FE-SEM champer is normally maintained in a high vacuum. For better results, our sample should be sufficiently dry and coated with conductive layer to prevent the charging of the samples. If it is a nonconducting sample, it should be safe to record it with a protective coating such as gold. The instrumental setup is shown in Figure 2.4. The electron gun is a zirconium oxide coated with tungsten (ZrO_2/W) emitter. The positively charged, anode is to guide the produced electrons from the electron gun. The function of first and second condenser is to give a proper shape to the electron beam. After passing through the scanning coil, also known as the obstacle lens, the beam falls on the sample.

The total system should be in high vacuum and after acheving the vacuum we can apply the high electric voltage. Depending on the applications, different magnitude of electric voltage is applied for example, 5kV is applied for imaging and 20kV is appled for recording elemental composition. The secondary electron (SE) detector, detects SE emitted from the sample and its amplified signal is connected to computer. The scanning coils scan the surface of the samples, controlled by the scan generator and connected to the CPU. The resulting image is visualized on the computer monitor, depicting the interaction between the electron beam and the specimen (see Figure 2.5). The back scattered electrons are detected by a detector mounted just before the sample.

When high energy incident electron pass the sample, and transmit without any interaction with the specimen, that is called transmitted electrons. When the high energy incident electron beam strikes the atoms, some of the electrons from the inner shell (mostly K-Shell) of atom may

get ejected and they are called the SE. The recording of SE as SEM image reveals surface morphology of the material. After this process the vacant space created by the SE is filled up by the electron from the upper shell. This process leads to the release of x-ray and through this x-ray we can analyze the composition of the samples. Other one is BSE, it is nothing but the incident electron beam that is reflected from the atom. The BSE bears some characteristics of the nucleus by this we can get the information about the nucleus of atom as it is related with the specimen's atomic number Z ($\sim 0.05Z^{1/2}$). In adition to this other electrons like auger electrons, cathodoluminoscence, characteristic and continuum X-rays also generated. For our work we have used ZEISS make FESEM with model - Sigma 300.

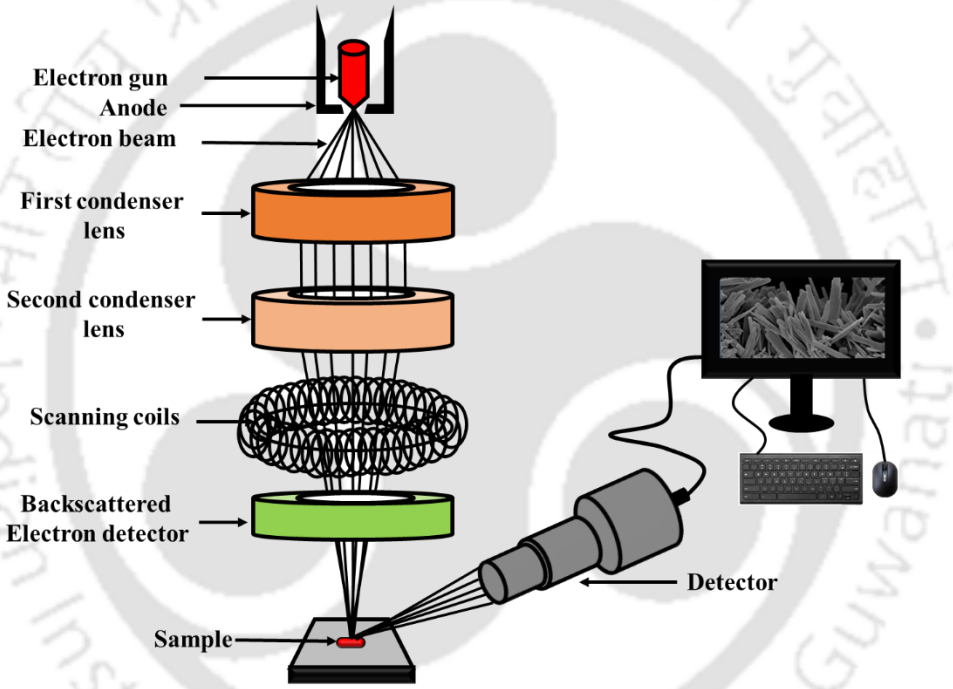

Fig. 2.4: The instrumental setup for FESEM.

Energy Dispersive X-ray Spectroscope (EDS) is a tool inside a microscope and it gives the information of elemental composition of any material. The characterisation approach is based on the fact that each element has a distinct atomic structure and emits a distinct x-ray. As mentioned above that after the formation of SE, x-ray is produced and this x-ray can be used for the analysis of comoposition of any specimen. As the x-ray is nothing but the energy difference of the two energy levels (upper and lower energy). Thus, one may determine the elements by measuring the energy emitted by x-rays. As a result, the output is a spectrum with peaks corresponding to the

energy levels. Information about the elements and their relative concentration are also estimated from this spectra. The EDS spectra of the samples of this thesis were recorded utilizing a Zeiss manufactured FESEM (model-Gemini) equipped with an EDS facility.

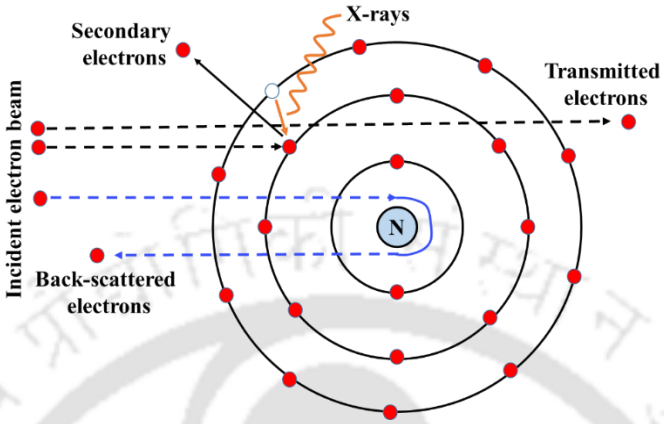

Fig.2.5: The interaction between electron beam and specimen.

2.6 Transmission Electron Microscope (TEM)

Transmission electron microscopy is a method in which an image is formed by passing an electron beam through a material. The specimen is usually an ultrathin slice less than 100 nm thick on a grid suspension. The interaction of the electrons with the sample is similar as that of FESEM. However, here the transmitted electron is used to get the image instead of SE. The picture is then enlarged and focused on an imaging device, such as a fluorescent screen linked to a sensor. The Figure 2.6. shows the construction of TEM. The basic parts of TEM are (i) An electron gun, (ii) The condenser system, (iii) The image producing system and (iv) The image recording system. Similar to FESEM here also electron gun produces electron beam. It is a cathode in the form of heated tungsten filament. It is accelerated with the help of anode and pass through its aperture. Then the condenser system focusses the electron beam on to the sample. Then the image producing system consist of objective lenses and intermediate lenses. These lenses focus the beam passing through the specimen, to form a real and highly magnified image. The magnification is done by the projector lenses. The last part is the image recording system, it converts the electron image into a format that can be seen by human eye. It consists of fluorescence screen for viewing the image. For our measurements we have used a JEOL make TEM, model number 2100 F.

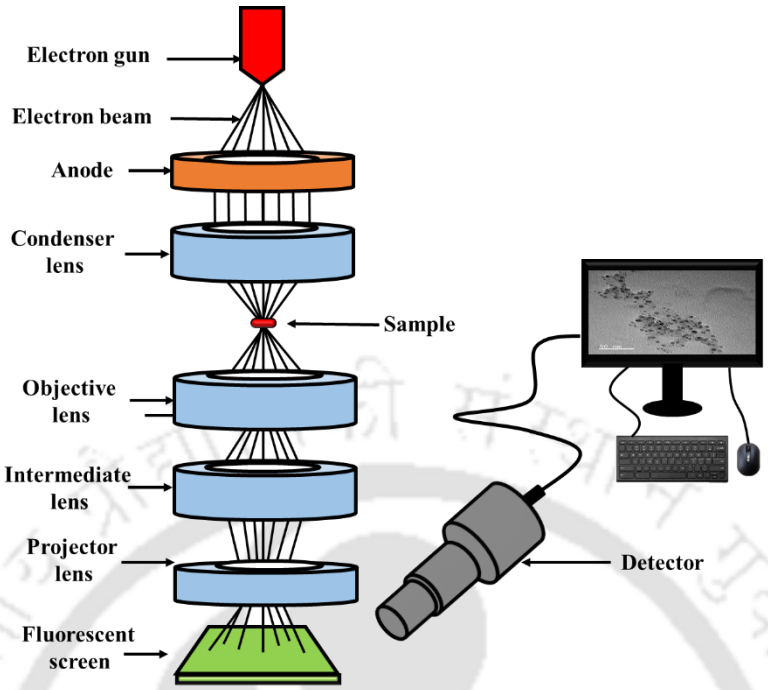

Fig.2.6: The instrumental setup for TEM.

2.7 X-ray Photoelectron Spectroscopy (XPS)

X-ray photoelectron spectroscopy (XPS) is a surface sensitive technique which typically analyses sample to a depth of 5-10 nm. It is very useful in processes that only occur at the top few atom layers of materials such as heterogeneous catalysis, adsorption, corrosion and adhesion. The basic principle of XPS is the photoelectric effect (PEE), which was discovered by Albert Einstein in 1905. PEE says that, when electromagnetic (EM) radiation (light) hits a material, electron from the surface are emitted out. So, the basic equation for the ejection of electron from the surface by EM radiation becomes;

$$h\nu = BE + KE + \phi \qquad (2.2)$$

Here, $h\nu$ is the photon energy, BE and KE are the binding energy and kinetic energy of electron and ϕ is a constant known as work function. As we know the sum of binding energy and work function is the minimum energy required to remove an electron from the surface. That means, some of the energy of the EM radiation is used to remove the electron, and remaining energy is used to accelerate electrons away from the surface which is KE of electron. Analyzer of XPS instrument measures the KE of electron and if we know energy of incident EM radiation we can easily find the BE of the emitted electron. The instrumental set up of XPS is shown in Figure 2.7.

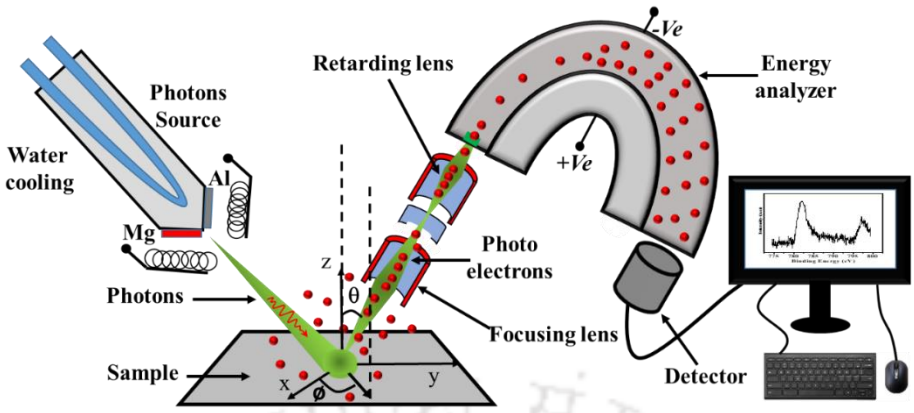

Fig. 2.7: Schematic diagram for instrumental setup of XPS.

The first part of the instrumentation is the source of photon. It is made up of a metal tube and the end of the tube is having two surfaces one is coated with Mg and other is coated with Al and very close to these coatings two filaments are arranged. When current in these filaments are supplied they gets heated and starts emitting electrons. These electrons collide with the surface coated with Mg/Al which is made up of cathode. By applying very high voltage about 20 kV on metal tube they produce x-ray. Cooling water is used to cool the cathode. The sample is illuminated by the incident x-ray, which causes the electron to escape from the surface with a variety of energies and directions. The electrostatic lenses then collect the emitted electrons which are focused to the entrance slit of the analyzer. Here, the analyzer is hemispherical, which is made up of two hollow hemispherical electrodes. Outer sphere is negatively charged and inner sphere is positively charged. Electrons are typically ejected in a straight line, but when they enter analyzer, they are attracted to the positive electrode and repelled by the negative electrode. If a constant voltage difference is applied across two hemispherical electrodes, the electron with a high KE will be bent less and will collide with the outer wall. Similarly, if the ejected electron has a low KE, it will be bent more and will strike the inner wall of the analyzer. Only specific electrons with fixed KE will follow the path precisely and be permitted to exit through the slit. Electrons coming out from the slit are counted by the detector and the KE of the electron are communicated to the computer, it converts the KE to BE and plots a graph of BE versus electron counts. Each element produces a set of characteristic XPS peaks. These peaks correspond to the electronic configuration

of the atoms, such as $1s^2$, $2s^2$, $2p^6$, $3s^2$ etc. For our measurement we have used XPS with model number PHI 5000 Versa Probe III.

2.8 Physical Properties Measurement System (PPMS)

For the magnetic properties of our samples, we have used Quantum Design make, the DynaCool physical properties measurement system (PPMS) equipped with vibrating sample magnetometer (VSM). The physical characteristics of materials in bulk, thin film, and powder form can all be measured using the DynaCool PPMS system. A quick, accurate, and fully automated DC magnetometer is the VSM option. By oscillating the sample in a pickup coil and synchronously detecting the induced voltage, this measurement is carried out. The system can resolve magnetic moment of 10^{-6} emu at a data rate of 1 Hz by utilizing a compact gradiometer pickup coil configuration, a relatively large oscillation amplitude and a frequency of 40 Hz. The VSM offered by quantum design has the same basic components. However, instead of an electromagnet the field is generated by a superconducting solenoid. Quantum Designs' linear transport motor offers sample translation and vibrations, and the pickup coils are housed in the VSM coil section. The pickup coils arrangements with the protective cover removed are shown in Figure 2.8.

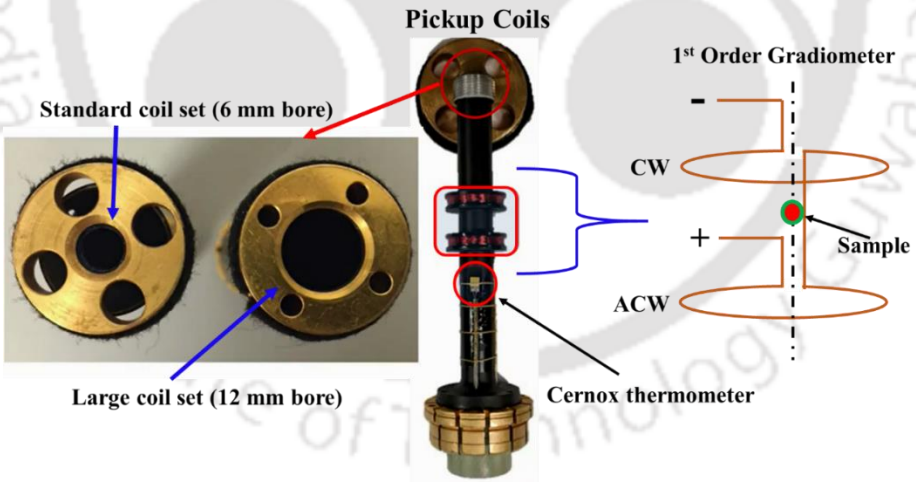

Fig. 2.8: Picture of the pickup coils along with two different coil sets.

The pickup coils are arranged in a first ordered gradiometer configuration with clockwise and anticlockwise windings separated by about 1 cm. The vibrations occur much faster and at a smaller amplitude of 2 mm with a typical frequency of 40 Hz. The first order gradiometer can be seen here along with the Cernox thermometer. VSM has two type of Pick-up coils with different internal bore sizes. One is standard coil set having 6 mm bore with a sensitivity of about 6×10^{-7}

emu. The large coil set has 12mm bores size, with a sensitivity of 1.5×10^{-6} emu. The physics behind the VSM is governed by the Faradays law of induction, represented as;

$$V_{coil} = -\frac{d\Phi}{dt} = -\left(\frac{d\Phi}{dz}\right)\left(\frac{dz}{dt}\right) \tag{2.3}$$

Which is expressed as;

$$V_{coil} = CmA\omega\, sin(\omega t) \tag{2.4}$$

Here, V_{coil} is the induced voltage in the coil, Φ is the magnetic flux through the coils z is the vertical position of the sample. This voltage in turns proportional to the amplitude of the oscillation (A), frequency (ω) and magnetic moment (m) of the sample. A calibration constant C can be used to calibrate the response. Calculation of magnetic moment is based on the in-phase component of the induced voltage with respect to sinusoidal vibration. Figure. 2.9 shows a block diagram of the various steps that are involved in VSM mode.

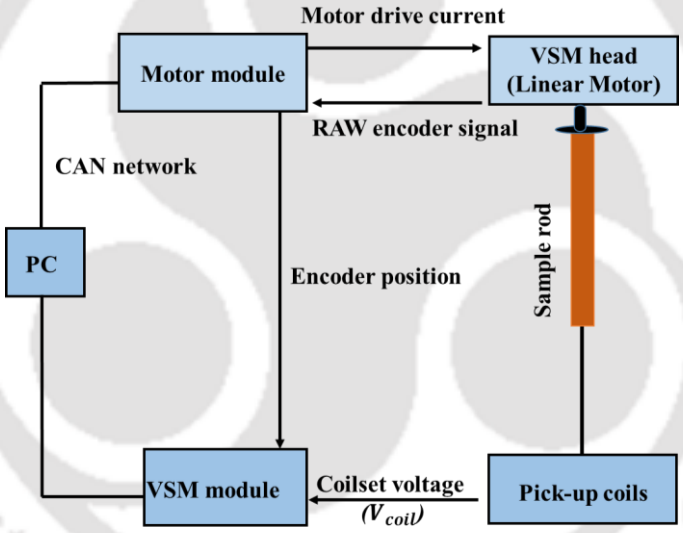

Fig. 2.9: Block diagram of various steps that are involved in VSM mode.

The sample rod is inserted into the chamber with the sample mounted at one end. By calibrating the sample, the sample is positioned at the center of the gradiometer pickup coils. The output voltage of the pickup coil is connected to the preamplifier and the VSM module which contained a Lock-in amplifier providing phase sensitive detections. PPMS operates with extreme precision in the temperature range of 1.8 K to 400 K.

Chapter 3

$(Ho_{1-x}Sm_x)_2CoMnO_6$ series and Ho_2CoMnO_6 Nanorods

3.1 Nanocrystalline samples of double perovskite $(Ho_{1-x}Sm_x)_2CoMnO_6$ (x = 0 - 0.5)

Ho_2CoMnO_6 DPs forms generally in monoclinic structure with $P2_1/n$ space group [57]. It is a FM compound with $T_C \sim 78\ K$ and it is attributed to the SE interactions across Co^{2+}-O^{2-}-Mn^{4+} networks. Sometimes, the presence of AFM phase is also observed due to the interactions across Co^{2+}-O^{2-}-Co^{2+} and Mn^{4+}-O^{2-}-Mn^{4+} networks which is originated by the ASD. Also, the presence of Co^{3+}/Mn^{3+} ions can lead to a minor AFM phase [57]. It has a F-type FM magnetic structure with a magnetic saturation value of ~ 15.5 μ_B/f.u. and a coercivity of ~ 4.5 kOe at low temperature [71]. In addition, a magnetic entropy value of 12 J/kg K at 10 K for 7 T field has been observed [44,63]. A MR has been observed in ZFC curve with T_{comp} ~ 50 K, and the presence of spin glass type of behavior has also been observed [71]. In view of the above intriguing results on Ho_2CoMnO_6 and to understand the role of Ho in the magnetic and EB properties, we have prepared the Sm doped $(Ho_{1-x}Sm_x)_2CoMnO_6$ (HSCMO) for x = 0.0 to 0.5 series. The Sm is chosen because of the known interesting multiferroic properties in Sm_2CoMnO_6 [70] as well as the larger FM T_C compared to Ho_2CoMnO_6. Such substitution is also expected to give further insight in to magnetic interaction between RE and TM ions in this series. We have prepared this series using auto combustion method as described in chapter 2 (Section 2.1) and studied their structural and magnetic properties.

3.1.1 Structural properties

Room temperature XRD patterns of the HSCMO samples are shown in Figure.3.1, where all the observed peaks are indexed based on monoclinic structure with space group $P2_1/n$. The XRD data of samples were analyzed using Rietveld refinement method. Rietveld analysis reveals that all the samples are in single phase form with monoclinic structure (space group: $P2_1/n$). The Rietveld refined data along with experimental data are shown in Figure.3.2 (a-f) for x = 0.0-0.5 respectively. The magnified view of (112) reflection (Figure.3.2 (g-l)) reveals the prominent shift

of the peak towards lower Bragg angle (2θ) with Sm substitution. This clearly indicates the increase in lattice parameters with Sm substitution. These features are the indication of a decrease in crystallite size. The merging of (200) and (021) peaks are observed for $x \leq 0.2$, however they split which are quite clearly visible for $x \geq 0.3$ as shown in Figure.3.3. It indicates the persistence of monoclinic symmetry in samples for higher Sm concentration [50].

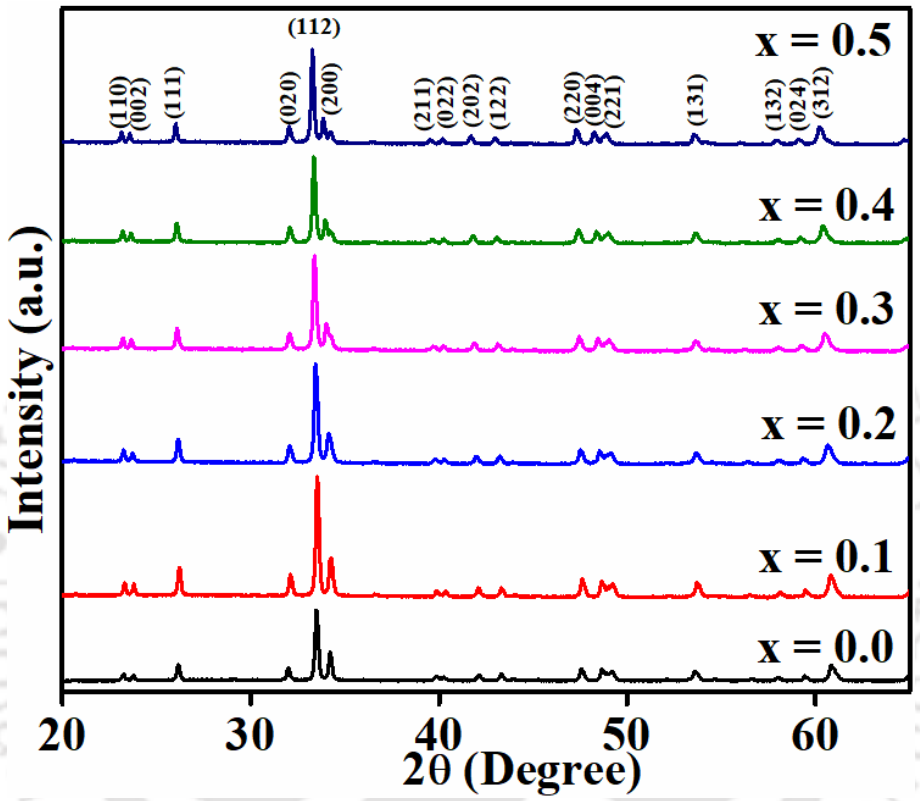

Fig.3.1. Room temperature XRD patterns of HSCMO series.

The lattice parameters a and c along with the unit cell volume are found to increase with Sm concentration, however no appreciable variation in lattice constant b is observed for $x > 0.1$ samples. This type of small variation in lattice parameter b is also earlier reported [50]. The unit cell expansion with Sm substitution is due to the partial replacement of Ho^{3+} ions having ionic radii of 1.015 Å with Sm^{3+} (1.079 Å) ions. The crystallographic angle $\alpha = \gamma = 90°$ and the β values for various samples are given in Table-3.1. The lattice parameters of the parent compound are comparable to those reported by Mazumdar et.al. [71]. After refinement we have observed a tilt in CoO_6 and MnO_6 octahedra in the unit cell of HSCMO samples. Hence, the overall tilting in unit

cell is measured by looking at the angle between CoO_6 and MnO_6 octahedra along c-axis. The calculated bond angles between TM ions with O_1, O_2 and O_3, are shown in Figure. 3.3 (a-d).

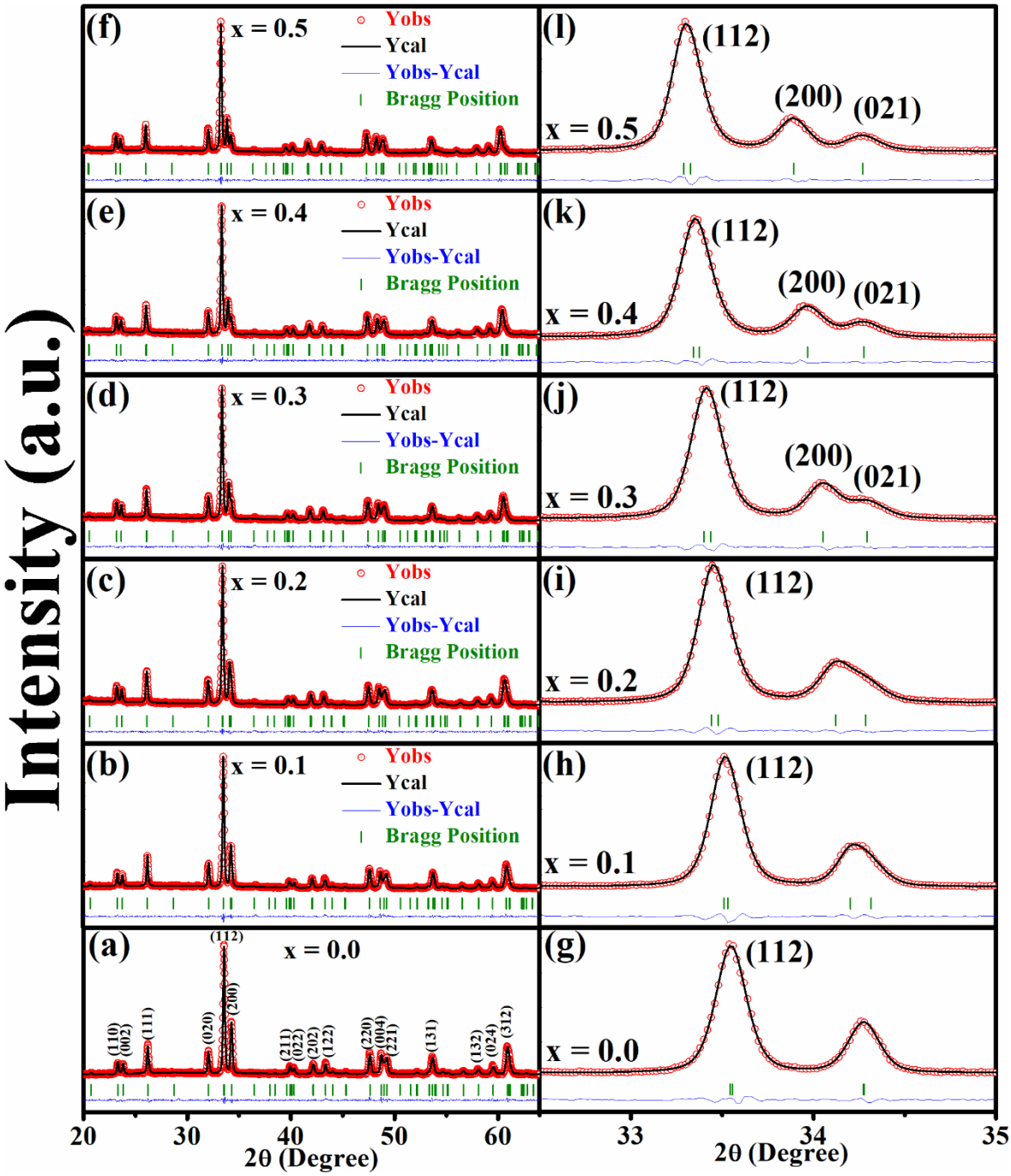

Fig.3.2. (a-f) Rietveld refinement for x = 0.0 - x = 0.5 and (g-l) zoomed view of (112) peak.

We found the angle made by TM ions with O_1 is decreasing, however with O_2 and O_3 increasing with Sm concentration. The average bond angle is also found to increase with Sm

concentration. For a perfect DP, the 180^0 bond angle between the TM ions situated at octahedral sublattices gives rise to a strong FM SE interaction in Co^{2+}-O-Mn^{4+} networks, as predicted by Goodenough-Kanamori rules [38,39]. Here the deviation from 180^0 must affect the SE interactions [2]. However, the rise in bond angle with Sm concentration might lead to strengthening of the SE interaction and increase in the FM T_C which will be discussed later.

Table - 3.1. Structural parameters of HSCMO series.

Sample	x = 0.0	x = 0.1	x = 0.2	x = 0.3	x = 0.4	x = 0.5
a (Å)	5. 228	5. 239	5. 251	5. 261	5. 274	5. 286
b(Å)	5. 581	5. 573	5. 572	5. 572	5. 572	5. 572
c(Å)	7. 469	7. 479	7. 494	7. 505	7. 521	7. 534
V($Å^3$)	217.9	218.3	219.4	220.0	221.1	222.0
β (°)	89.93	90.03	90.06	90.07	90.08	90.05
R_f	7.70	4.08	2.29	2.95	2.76	2.59
R_{Bragg}	4.46	2.93	1.96	2.14	2.22	2.01
χ^2(%)	1.55	1.37	1.16	1.20	1.23	1.25
Average crystallite size(nm)	35	34	31	31	31	30
Micro-strain (10^{-3})	2.21	2.17	2.21	2.0	2.18	1.61

The average crystallite size and the micro-strain parameter were calculated from the XRD peaks using the Williamson-Hall (WH) method [259] as given by the equation;

$$B\cos\theta = \frac{k\lambda}{D} + 4\varepsilon \sin\theta \qquad (3.1)$$

Here, B is defined as the full width at half maximum (FWHM) of XRD peaks, k is the Debye-Scherer constant (k = 0.94), λ = 1.5406 Å (wavelength of the x-ray source), D is crystallites size, ε is the micro-strain parameter and θ is the XRD peak position. The WH Plot (Bcosθ versus 4sinθ) is shown in Figure.3.4 (a-f). They are well fitted with the linear equation which are represented by red solid lines. The values of average crystallite sizes, as well as micro-strain parameters are evaluated from the intercept and slope of the straight line respectively.

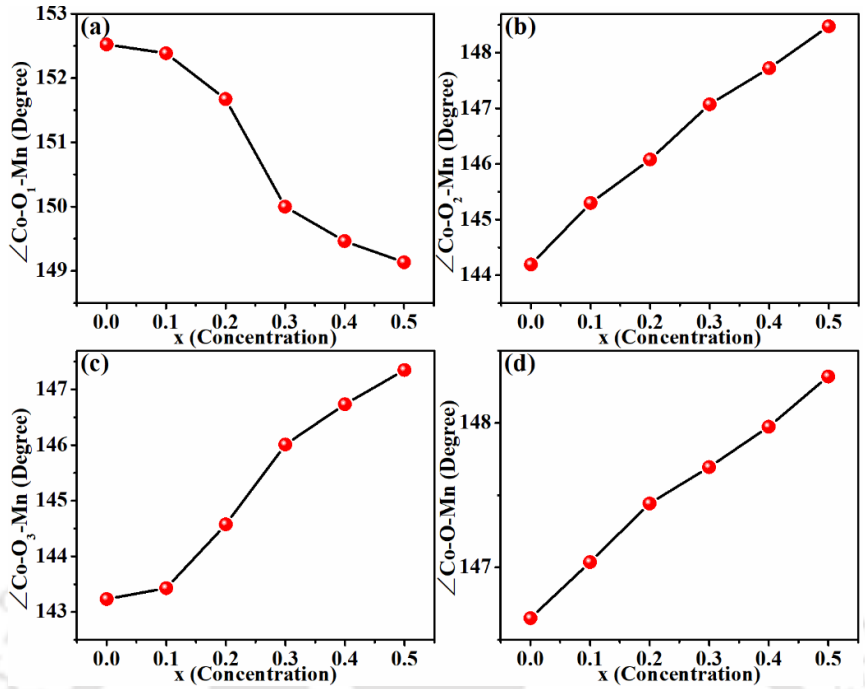

Fig.3.3. (a-d) Bond angle of TM ions with O_1,O_2,O_3 and average bond angles of HSCMO series

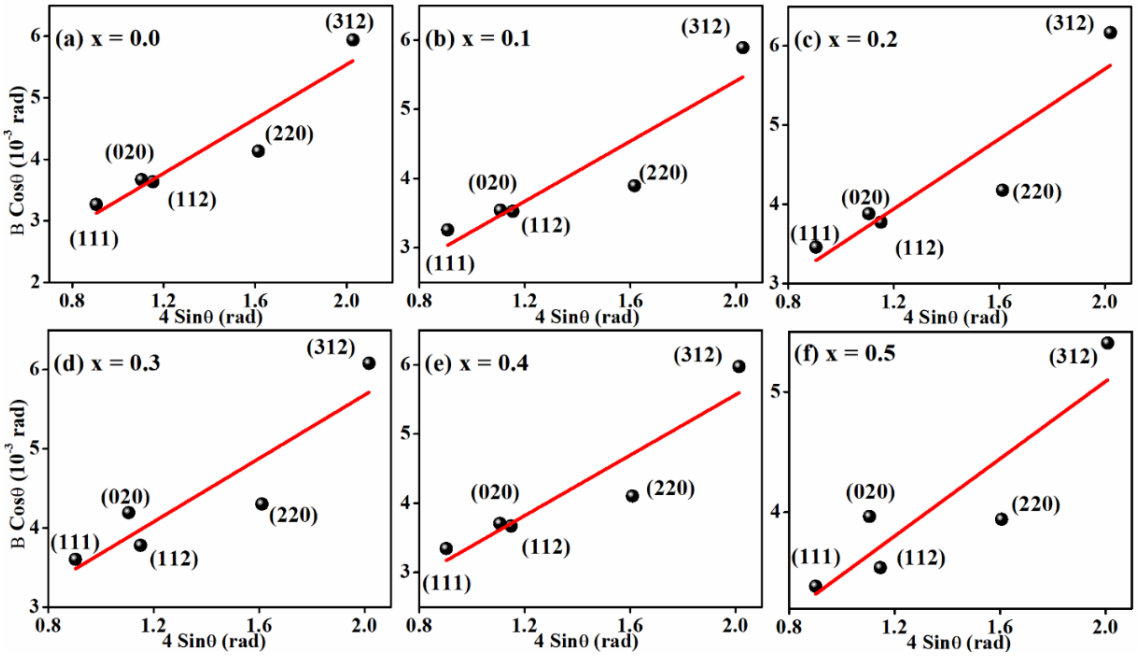

Fig.3.4. (a - f) Williamson-Hall plots of HSCMO samples for x = 0.0 to 0.5.

The estimated values of average crystallite size of samples show no appreciable variation with Sm doping as listed in Table-3.1. All the samples are found to be in nanocrystalline form. Similarly, the observed micro-strain parameters are also do not reflect any appreciable variation as no appreciable change in surface to volume ratio is found with increase in Sm concentration.

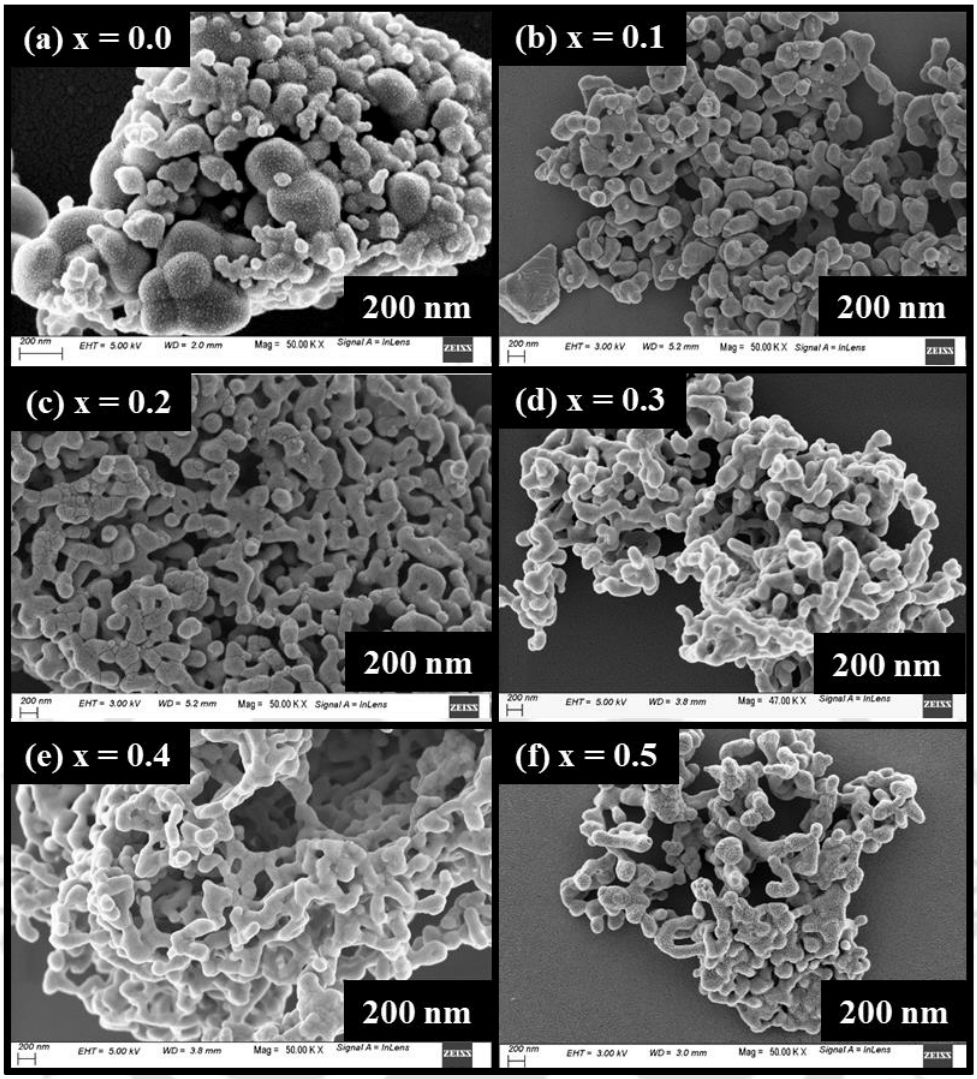

Fig.3.5. (a - f) FESEM images of HSCMO samples for x = 0.0 to 0.5.

The FESEM images of HSCMO samples are shown in Figure.3.5 (a-f). The particles are highly agglomerated and interconnected to each other leaving considerable porosity in the system. Such agglomeration makes it difficult to estimate the average particle size. Hence, the calculated crystallite size is provided in Table - 3.1. The elemental composition was evaluated from EDS analysis and the spectra are shown in Figure.3.6 (a, b). It confirms the presence of Ho, Sm, Co, Mn and O with desired composition. The uniform distribution of these elements is confirmed by elemental mapping as shown in Figure.3.6 (c, d).

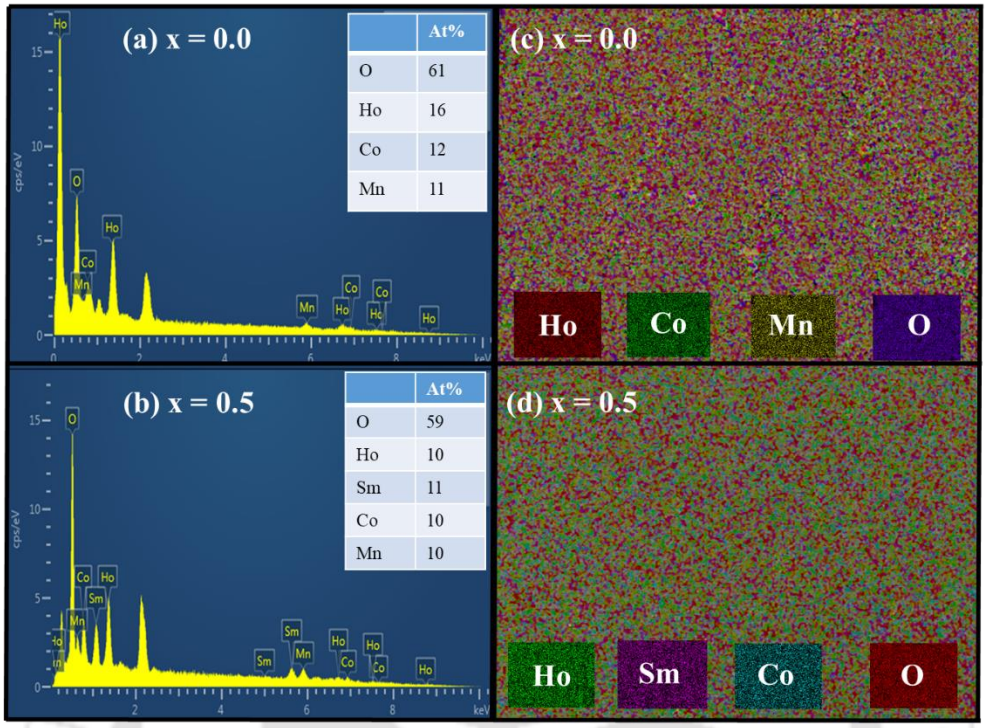

Fig.3.6. EDS spectra of (a) x = 0.0 and (b) x = 0.5 samples and their respected elemental mapping (c, d).

RT XPS data along with the Gaussian fit for x = 0.4 and 0.5 are shown in Figure.3.7 (a - h). The oxidation states of Co/Mn were measured by deconvoluting $2P_{3/2}$ and $2P_{1/2}$ peaks. Whereas, for Ho and Sm were obtained by the deconvolution of 4D and 3D peaks. For x = 0.4, the 4D core-level spectrum of Ho consists of peaks at 159.72 eV and 161.47 eV. The 3D core-level spectrum of Sm consist of peaks at 1081.75 eV and 1082.68 eV. The obtained positions of peak say that Ho is in the state of 3+ and Sm is in the state of 2+/3+ [260,261]. However, the Sm^{2+} is much small in amount as compared to Sm^{3+} so it can be neglected. Similarly, the 2P core-level spectrum, of Co consists of four peaks at 780.13 eV, 783.74 eV, 795.86 eV and 802.86 eV and Mn spectrum has the peaks at 641.49 eV, 642.42 eV, 653.59 eV, and 664.38 eV. The peak positions of both Co and Mn reveal that, Co is in the oxidation state of 2+/3+ and Mn is present in 3+/4+ states respectively [261-266]. For x = 0.5, the peak positions for Ho is at 159.57 eV and 161.18 eV; for Sm it is at 1081.72 eV and 1083.55 eV; for Co it is at 780.03 eV, 783.83 eV, 795.74 eV and 801.49 eV and for Mn it is at 641.69 eV, 643.70 eV, 653.10 eV and 654.39. All these positions represent the presence of above stated oxidation states for individual elements [261-266].

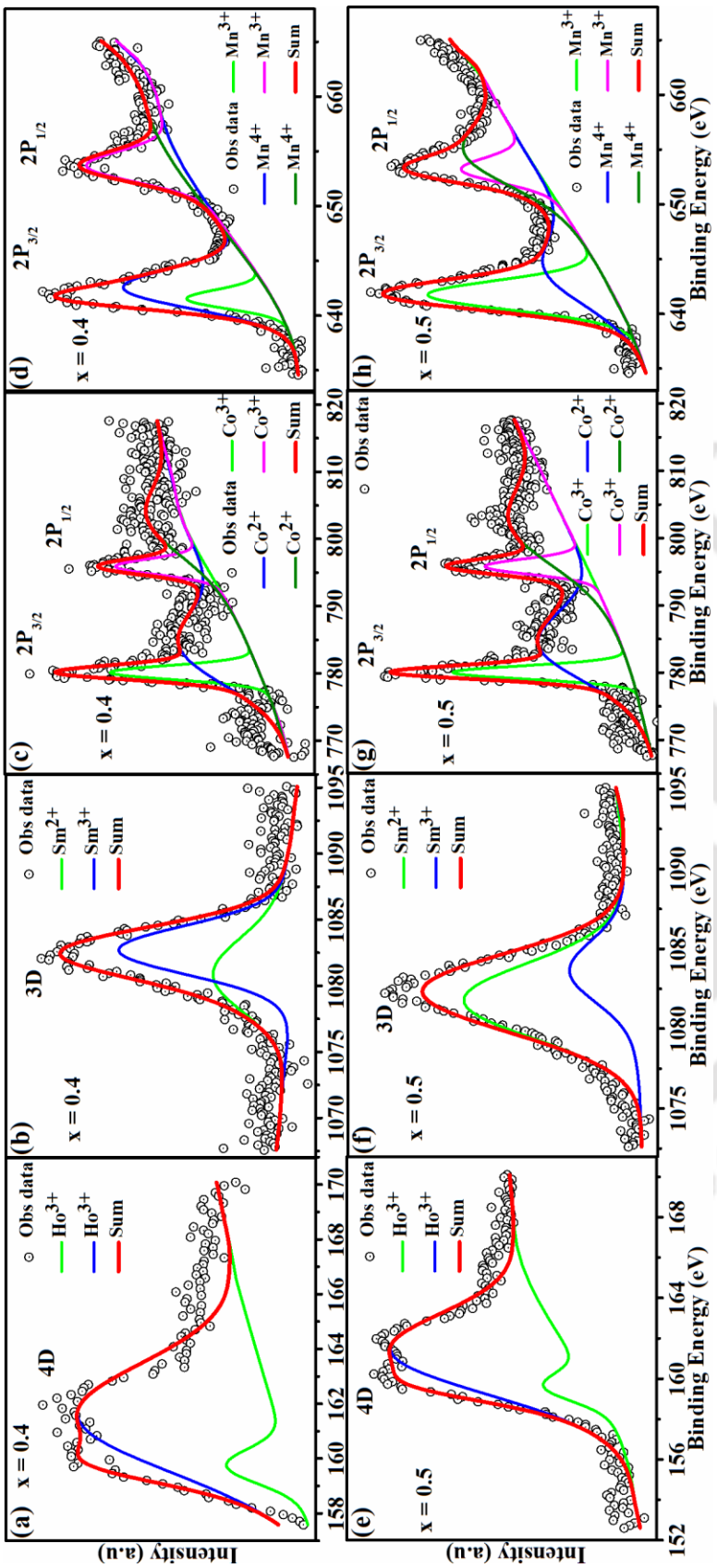

Fig.3.7 X-ray photoelectron spectroscopy for (a-d) x = 0.4 and (e-h) x = 0.5 for Ho, Sm, Co and Mn elements.

3.1.2 Magnetic properties

The measured temperature variations of magnetization (MT) under ZFC and FC condition for an applied field of H = 100 Oe are shown in Figure.3.8 (a-f). The ZFC MT plot of x = 0.0 sample shows a sharp rise in magnetization for T ≤ 85 K followed by a peak like structure at T_{peak} = 75 K. However, for T < 50 K, a secondary rise in magnetization is observed with decrease in temperature. Similar type of peak like structure followed by secondary rise in magnetization is reported by Blasco et.al. [57] and Jia et.al. [44] in Ho_2CoMnO_6. The FC magnetization shows a sharp rise in magnetization at T < 85 K followed by tendency towards saturation. A large irreversibility of the order of 1.24×10^3 % is observed for x = 0.0 sample at 5 K. The irreversibility is quite prominent especially for T < T_{peak}, indicating competing magnetic interaction or spin geometric frustrations such as spin glass or cluster glass at lower temperatures. The FC MT plot indicates a typical FM transition. The FM transition temperature (T_C) is determined by plotting first derivative of the ZFC magnetization with respect to temperature (dM/dT) versus temperature and the T_C is found to be 83 K for x = 0.0. Similar MT plots are observed in Sm doped samples however the FM T_C is found to increase with Sm concentration as shown in Table-3.2. The T_C is found to increase from 83 K for x = 0.0 to 115 K for x = 0.5. It can be attributed to the increased bond angle resulting from Sm substitution and the corresponding strengthening of SE interaction. For a clear view, ZFC plots are shown in the inset of Figure.3.8 (a-f).

Table - 3.2. Data obtained from MT measurements and modified Curie-Weiss law fitting.

Sample	T_C (K)	$\frac{\Delta M}{M_{ZFC}} \times 100$ (5K) (10^3%)	θ_{TM} (K)	θ_{RE} (K)	μ_{eff}^{Exp}(TM) μ_B/f.u.	μ_{eff}^{Exp}(RE) μ_B/f.u.	μ_{eff}^{Th}(RE) μ_B/f.u.
x = 0.0	83	1.24	82	-9	4.8	14.7	14.9
x = 0.1	87	1.14	86	-24	5.2	15.8	14.2
x = 0.2	95	1.22	93	-15	5.2	15.4	13.4
x = 0.3	100	1.18	98	-13	5.3	14.2	12.5
x = 0.4	108	1.33	107	-12	5.2	13.4	11.6
x = 0.5	115	1.38	114	-8	5.2	12.5	10.6

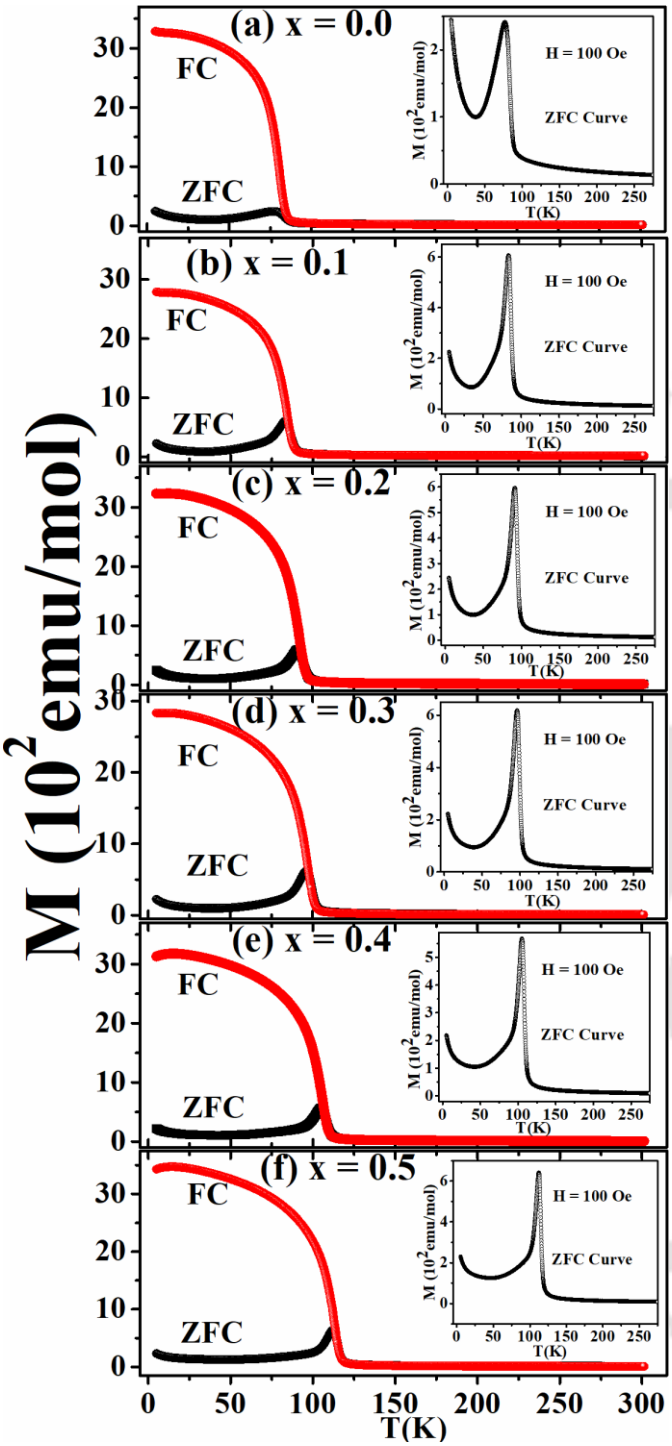

Fig.3.8. ZFC and FC, M versus T plots at an applied field of H = 100 Oe for (a) x = 0.0, (b) x = 0.10, (c) x = 0.2, (d) x = 0.3, (e) x = 0.4, and (f) x = 0.5, Inset shows ZFC M - T plots in expanded scale for clear view of ZFC curves for the respective samples.

In order to understand the nature of magnetic interaction, we have analyzed the PM susceptibility data. Typical plot of inverse susceptibility as a function of temperature for x = 0.0, 0.1, 0.3 and 0.5 samples are shown in Figure.3.9 (a-d) and they considerably deviate from linearity and as a result they could not be fitted to Curie-Wiess law (CWL). So, we have fitted the data by

modified CWL as explained in section 1.5.3 (Eqn. 1.7) which is mostly used for DP systems [143]. They are reproduced here for convenience

$$\chi = \frac{C_{TM}}{T-\theta_{TM}} + \frac{C_{RE}}{T-\theta_{RE}} \quad (3.2)$$

Here TM and RE ions are treated independently i.e., by considering no interaction between TM and RE ions [143]. However, at low temperatures, such interaction cannot be ruled out. The fitted data are shown as solid line in Figure.3.9 (a-d) which closely follow the experimental data down to FM T_C. The estimated values of θ_{TM} and θ_{RE} for x = 0.0 sample are found to be 82 K and -9 K respectively. The θ_{TM} value is quite close to the measured FM T_C (83 K). The fitted θ_{RE} value is quite small and negative, it indicates the AFM interaction among RE ions at low temperature. We have also repeated the fitting by fixing the θ_{TM} as experimental T_C value as per the procedure reported in Ref. [143], however, no appreciable variation in the fitted parameters is seen. Similar fitting was carried out for other Sm substituted samples and in all cases θ_{TM} is found to be quite close to the respective FM T_C. θ_{RE} is found to be negative value and its magnitude mostly decreases with Sm concentration. The effective PM moment (μ_{eff}) is calculated by using the formula, $\mu_{eff}^{Cal} = \sqrt{3k_B C/N_A}$, where k_B is Boltzmann constant, C is the Curie constant (C_{TM} / C_{RE}) and N_A is the Avogadro number. Theoretical effective magnetic moments of RE ions per formula unit can be calculated using the relation;

$$\mu_{RE}^{Th} = \sqrt{2 \times ((1-x)\mu_{Ho}^2 + x\mu_{Sm}^2)} \quad (3.3)$$

Similarly, the effective moment of TM ions can be calculated by using the relation;

$$\mu_{TM}^{Th} = \sqrt{\mu_{Co}^2 + \mu_{Mn}^2} \quad (3.4)$$

Here μ_{Ho}, μ_{Sm}, μ_{Co}, μ_{Mn} are the ground state effective magnetic moments of Ho^{3+}, Sm^{3+}, Co^{2+}, and Mn^{4+} ions respectively, x is the doping concentration of Sm. The effective ground state PM moments used for calculations are 10.60 μ_B for Ho^{3+}, 0.85 μ_B for Sm^{3+} and 3.87 μ_B for both Co^{2+} and Mn^{4+} ions. The μ_{TM}^{Th} value is found to be 5.47 μ_B/f.u. The experimental values of μ_{eff}^{Exp} (TM) and μ_{eff}^{Exp} (RE) are tabulated in Table-3.2. The μ_{eff}^{Exp} (TM) values are mostly comparable to the theoretical values except for x = 0.0 sample. The smaller experimental values for this sample could be due to the presence of some fraction of $Co^{3+/}Mn^{3+}$ ions, with Co^{3+} ($t_{2g}^6 e_g^0$) ions in low spin state as reported in various Co/Mn based DPs [8,13,14,18,20,23]. The calculated value of μ_{eff}^{Exp} (RE) is

decreasing with the Sm substitution, it confirms the substitution of Sm^{3+} (0.85 μ_B) at Ho^{3+} (10.60 μ_B) site. Here μ_{eff}^{Exp} (RE) values are appeared to be slightly overestimated compared to theoretical values. The possible reason is the domination of first term associated with TM ions in Eqn. (3.2) and hence the considerable error in parameter related to the second term, i.e., RE ions term.

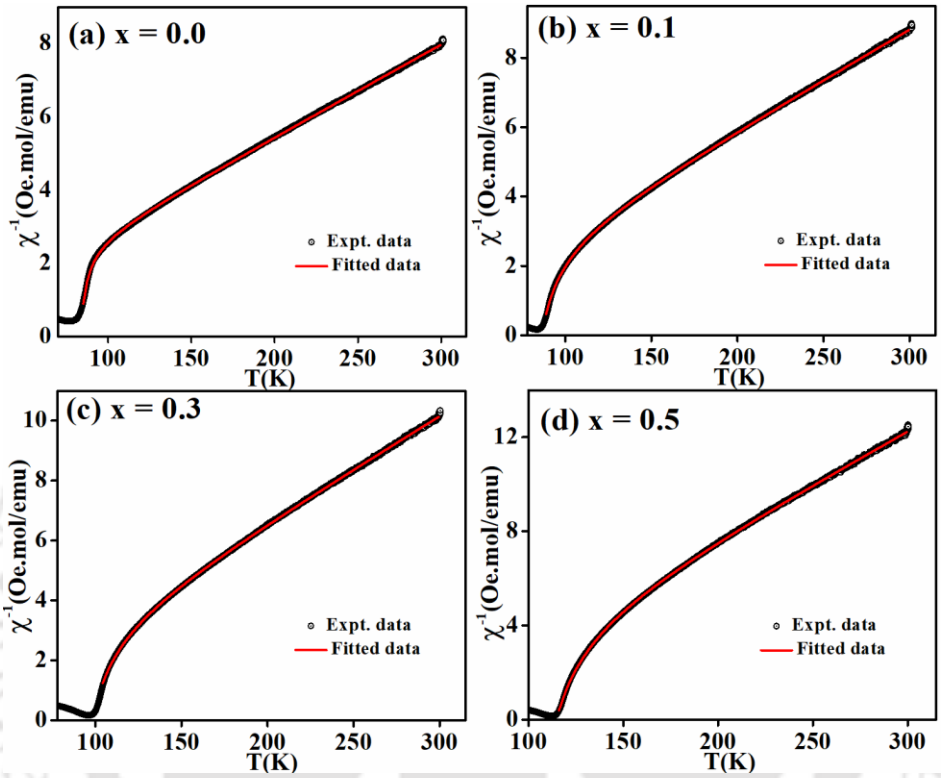

Fig.3.9. Inverse susceptibility, fitted with modified Curie-Weiss law for (a) x = 0.0. (b) x = 0.1, (c) x = 0.3 and (d) x = 0.5 respectively.

We have also taken up the M-T measurements for x = 0.0 and 0.5 samples by varing the applied field from H = 100 Oe to 10 kOe and they are shown in Figure.3.10 (a-d). The ZFC M-T plots of x = 0.0 sample show the peak like structure for T < 85 K followed by secondary rise in magnetization at low temperature. However, with increase in H value the peak is getting broadened and shifting towards low temperature due to the forced magnetic polarization against the anisotropic field. For H = 10 kOe, the peak like structure disappears and only a step like behavior is observed. The secondary rise in magnetization at low temperature is now much prominent due to forced magnetic polarization of RE element due to large applied field. Simillarly in FC MT plots of x = 0.0 sample show low temperature (T<25 K) rise in magnetization for H ≥ 500 Oe. Thus with increase in applied field, the RE moments are forced to align along FM moment. Similar behavior

of peak broadening and secondary rise in magnetization at low temperature is observed in ZFC MT plots of x = 0.5 sample. However, here the peak like structure remains even for H = 10 kOe and it indicates the presence of robust magnetic anisotropy or competing AFM interaction with increase in Sm substitution. The FC MT plots of x = 0.5 sample also show similar trend of x = 0.0 sample with secondary rise in magnetization at low temperature. However, the secondary rise is more prominent for H > 3 kOe.

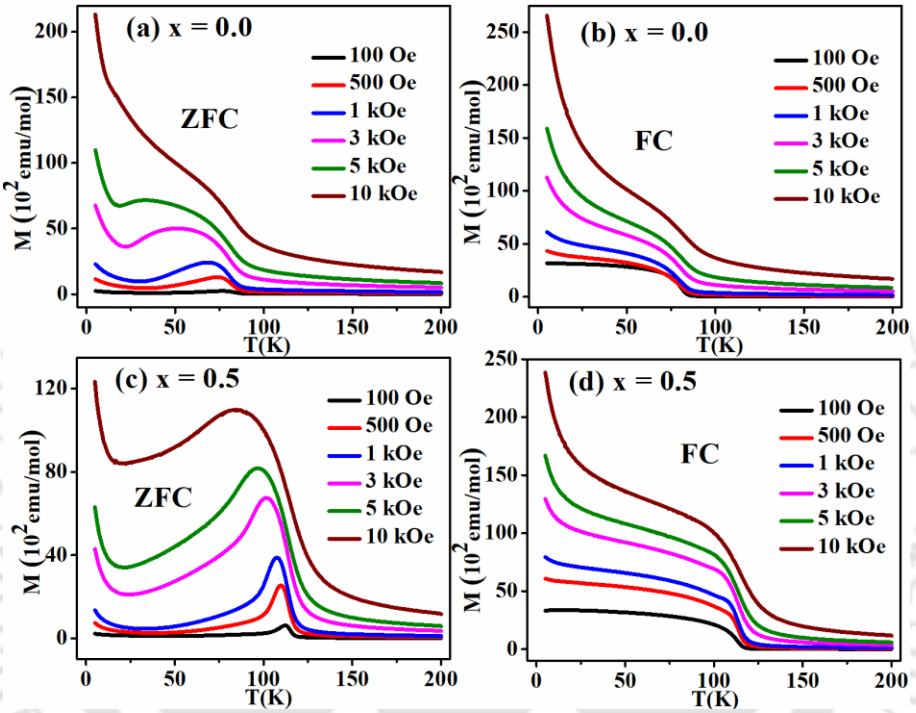

Fig.3.10. (a, b) ZFC and FC, M versus T plots at an applied field of H = 500 to 10 kOe for (a, b) x = 0.0 and (c, d) x = 0.5 respectively.

(i) Study of M-H Loops

The magnetic hysteresis loops recorded at 5 K for magnetic field up to ± 9 T are shown in Figure.3.11 (a). At the outset they all exhibit typical FM behavior with a considerable saturation magnetization and coercive field. Even for H = 9 T, the magnetization is not saturated and considerable linear behavior is observed. This can be attributed to the presence of spin canted AFM or considerable PM moment at low temperature. To determine the saturation magnetization values, the initial magnetization curves were analyzed based on LAS model as given below [267],

$$M = M_S \left(1 - \frac{b}{H^2}\right) + cH \qquad (3.5)$$

Here M_S is the saturation magnetization and c is a constant related to the forced magnetization at high field. The parameter b can be written as follows,

$$b = \frac{8K_1^2}{105\mu_0^2 M_S^2} \quad (3.6)$$

Here K_1 is the effective magneto-crystalline anisotropy constant. The initial magnetization data along with fitted data (solid red line) are shown in Figure.3.11 (b). The obtained M_S and K_1 values are given in Table-3.3.

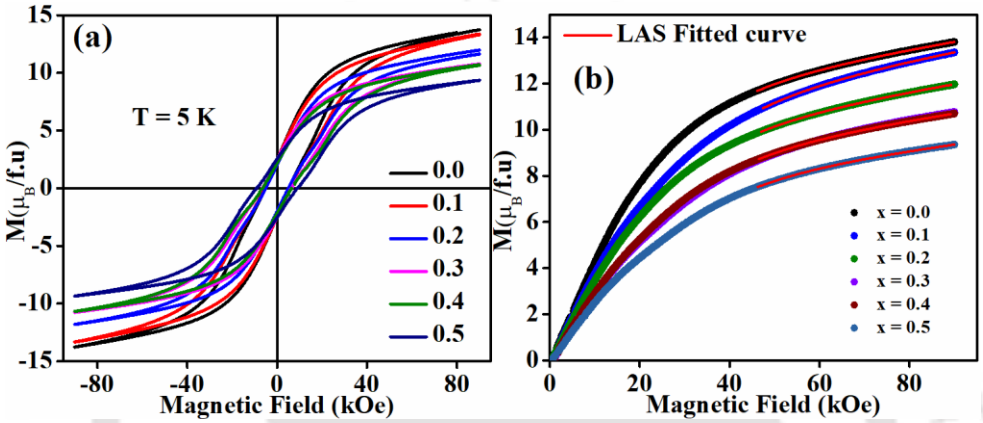

Fig.3.11 (a) M-H loops measured at 5 K under ZFC condition (b) initial M-H loop along with fitted data using LAS model for x = 0.0 - 0.5.

The M_S value for x = 0.0 sample is found to be 11.64 μ_B/f.u. and it decreases to 7.86 μ_B/f.u. for 50 atomic % of Sm substitution. The FM transition in these samples are expected to originate from Co^{2+}-O^{2-}-Mn^{4+} networks. For SE interaction in such networks, one would not expect more than 6 μ_B/f.u. (Co^{2+} = Mn^{4+} = 3 μ_B/ion). So, the observed large value of 11.64 μ_B/f.u. for x = 0.0 sample is expected to originate from the RE ions contribution to the FM moment. The magnetic moment of each Ho^{3+} ion is 10 μ_B and having two Ho^{3+} ions per formula unit, one would expect total magnetization of 26 μ_B/f.u. if all the Ho^{3+} ions take part in FM interaction. Since the obtained M_S value is much less than 26 μ_B/f.u., it is attributed that some components of Ho^{3+} moment contribute towards ferromagnetism. This can be visualized as a weak AFM interaction among Ho^{3+} ions giving rise to canted FM moment aligned along the net magnetization of TM ions. As the doping concentration is increased, M_S value is found to decrease and it is consistent with Ho^{3+} ions having larger magnetic moment being substituted with Sm^{3+} ions (0.71 μ_B/ion). However, unlike M_S values, M_r and H_C values are found to increase with Sm concentration. This can be attributed

to lattice distortion associated with Sm substitution as well as larger concentration of grain boundaries in Sm substituted samples. The K_1 values are found to be in the order of 10^4 erg/cm^3 indicating no strong magnetic crystalline anisotropy in the system.

Table - 3.3. Data obtained from M-H Loops recorded at 5 K along with H_{EB} values.

Sample	x = 0.0	x = 0.1	x = 0.2	x = 0.3	x = 0.4	x = 0.5
H_C (Oe)	5328	5160	5694	6565	6632	9275
M_r (μ_B/f.u.)	2.0 (4)	2.2 (4)	2.4 (3)	2.5 (4)	2.6 (4)	2.7 (3)
M_S (μ_B/f.u.)	11.6 (3)	11.0 (3)	10.0 (3)	9.1 (3)	8.8 (3)	7.9 (3)
K_1 (10^4erg/cm^3)	1.9 (3)	2.0 (3)	1.7 (4)	1.6 (2)	1.4 (3)	1.3 (2)
H_{EB} (Oe)	-30	-62	-81	-127	-162	-237

In order to understand that whether the magnetism in the system originates from single magnetic phase or some competing complex magnetic behavior, we have plotted loop width (ΔH) versus magnetization (M) as shown in the Figure.3.12 (a-d). In a system having single magnetic phase, one would expect a Gaussian curve with a maximum at M = 0 [268]. On the other hand, in the present system a dent is seen at M = 0 followed by two broad peaks on either side. This indicates that more than one magnetic interaction exists in the present system.

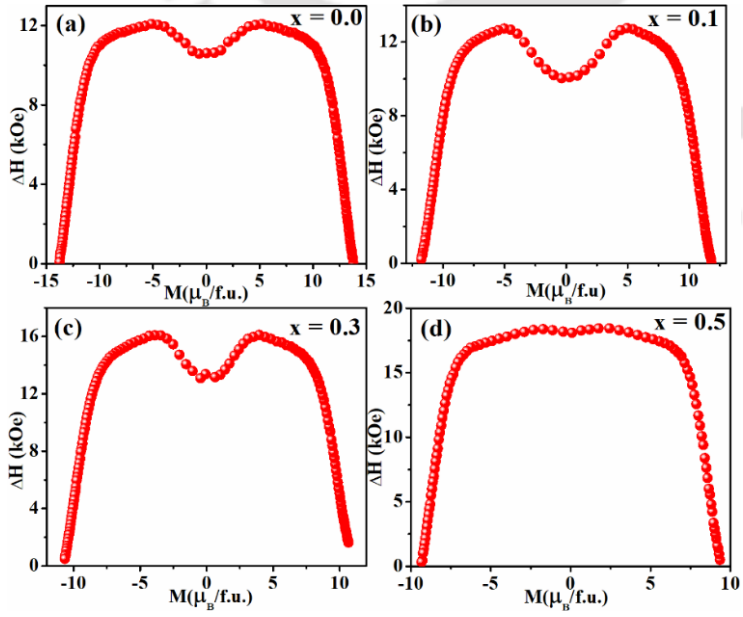

Fig.3.12. Loop width (ΔH) versus M plots for ZFC MH loops measured at 5 K for (a) x = 0.0, (b) x = 0.1, (c) x= 0.3, (d) x= 0.5 sampls respectively.

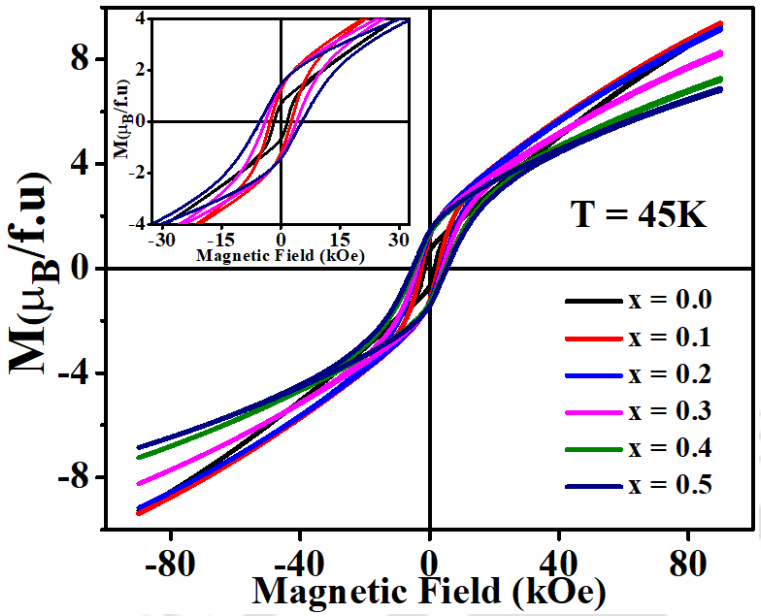

Fig.3.13. M-H loops measured at 45 K under ZFC condition. Inset shows the enlarged view near coercivity.

We have also recorded the magnetic hysteresis loops at 45 K i.e., above the secondary rise in magnetization and they are shown in Figure.3.13. Looking at the figure we can say that all the samples show FM behavior. The magnetization shows a linear behavior above 3 T and the coercive field is increasing with Sm substitution. By using Eqn. (3.5) we have estimated M_S values at 45 K and they are found to be in the range of 3 μ_B/f.u. to 3.7 μ_B/f.u. for various samples. These values are certainly less than 6 μ_B/f.u. indicating no FM contribution from RE ions at 45 K. So, it can be concluded that RE ions contribution to total magnetic moment comes into picture only below the temperature of secondary rise in magnetization. So, this leads to large magnetic moment at T = 5 K. However, the M_S values at 45 K are not close to the expected value of 6 μ_B/f.u. due to magnetic interaction in Co^{2+}-O^{2-}-Mn^{4+} networks. One possibility is due to the chosen temperature is relatively close to FM T_C leading to considerable thermal agitation induced depolarization of magnetization. Inset of Figure.3.13. shows the enlarged view of loop near H_C.

Having gone through the MT plots under ZFC and FC condition and MH loops at 5 K and 45 K for various samples, the following discussions can be made. The sharp rise in ZFC magnetization of x = 0.0 sample at T < 85 K and at higher temperature for Sm doped samples, as well as clear positive Curie temperature (θ_{TM}) suggest that this transition is due to FM interaction. Here the estimated θ_{TM} values are also comparable to the FM T_C. The FM interaction originates from Co^{2+}-O^{2-}-Mn^{4+} networks in this series. Such FM interaction in DPs has been reported earlier [54,60]. In conventional FM transition, one would expect magnetization tending towards saturation for T < T_C, however here a peak like structure is seen in ZFC MT plots. One of the

following reasons can contribute to such peak like structure: (i) AFM interaction between RE and TM ions. (ii) strong magnetic anisotropy leading to FM domains in random direction. (iii) ASD of a few TM ions leading to AFM arrangement across Co^{2+}-O^{2-}-Co^{2+} or Mn^{4+}-O^{2-}-Mn^{4+} at FM interface. (iv) Sometimes the presence of Co^{3+}/Mn^{3+} ion can lead to an AFM interaction between the ions. So, the observed peak like behavior in ZFC is expected mainly due to the presence of minor AFM ordering due to APB and/or ASD. Such APB have been reported in La_2CoMnO_6 system [54,58]. From the XPS data, we have observed the presence of Co^{3+}/Mn^{3+} which could also be a reason of the minor AFM phase in this series and it leads to the peak like behavior in ZFC MT curve. The MT plots carried out at different applied fields indicate the broadening of the peak and shifting towards low temperature. This can be attributed to forced magnetization and the suppression of AFM interaction across ASD due to large applied field. For H = 10 kOe, no peak is seen for x = 0.0 sample but the peak remains for x = 0.5 sample up to H = 10 kOe. The variation in peak structure in the ZFC MT curves with increase in field is due to the strongly temperature dependent coercivity of these samples [269]. When the value of applied field is less than H_C at low temperature (5 K) and by increasing the temperature, the measured magnetization will remain very weak until near T_C. Just below T_C, the temperature dependence of H_C gives rise to sudden rise in M_{ZFC} (T) curves to form a peak like structure.

Another prominent observation in ZFC MT plots is the secondary rise in magnetization for T < 50 K. This can either be due to PM contribution of Ho^{3+} ions at low temperature or due to the partial FM interaction between Ho^{3+} ions and net moment of TM ions. From MCW law fitting, we have interpreted that Ho^{3+} ions them self interact antiferromagnetically at low temperature. However, one cannot rule out the spin-canted AFM interaction of Ho^{3+} ions leading to some FM component along the moment of TM ions. The secondary rise in magnetization is found to be quite dominant with increase in applied field. This can be attributed to polarization of Ho moment along the direction of field. Similar strengthening of secondary rise in magnetization is observed in Sm substituted samples. The large M_S value beyond the expected values from TM ions alone at 5 K, can be attributed to the additional FM component from the RE sublattices. The smaller M_S values in Sm substituted samples are mainly due to smaller Sm^{3+} moment compared to Ho^{3+} ions. Such FM component from RE ions in the present series at 5 K can be further supported from the observation of low M_S value that is less than 6 μ_B/f.u. in DPs without magnetic RE ions [54, 58,

68]. Our measurements at 45 K also show that M_S value is less than 6 μ_B/f.u. and it indicates that RE ions order only at low temperature.

(ii) Study of Exchange Bias Behavior

In view of the presence of multiple magnetic sublattices and their complicated magnetic interaction along with disorder induced APBs, it is worth exploring of EB behavior in the present series. Typical MH loop under FC condition for x = 0.3 sample is shown in Figure.3.14 (a), along with the plot in expanded scale close to M = 0 (Figure.3.14 (b)). We can see a clear shift of MH loops towards negative field axis indicating EB behavior. Similar plot is shown in Figure.3.14 (c) for x = 0.5 sample. However, to rule out any stray field induced artefacts on EB field (H_{EB}) we have recorded negative (0→-9→+9→-9 T) MH loop along with the positive (0→+9→-9→+9 T) MH loop for x = 0.5 sample as shown in Figure.3.14 (c, d) and are found to shift in opposite direction indicating intrinsic EB behavior. The H_{EB} was determined and are given in Table-3.3, they found to increase with Sm concentration. This can be attributed to the exchange anisotropy between the FM moment of TM ions and the spin canted AFM ordered Ho^{3+}/Sm^{3+} ions. As the Sm concentration is increased, the lattice distortion gives rise to further spin canting and enhanced exchange anisotropy.

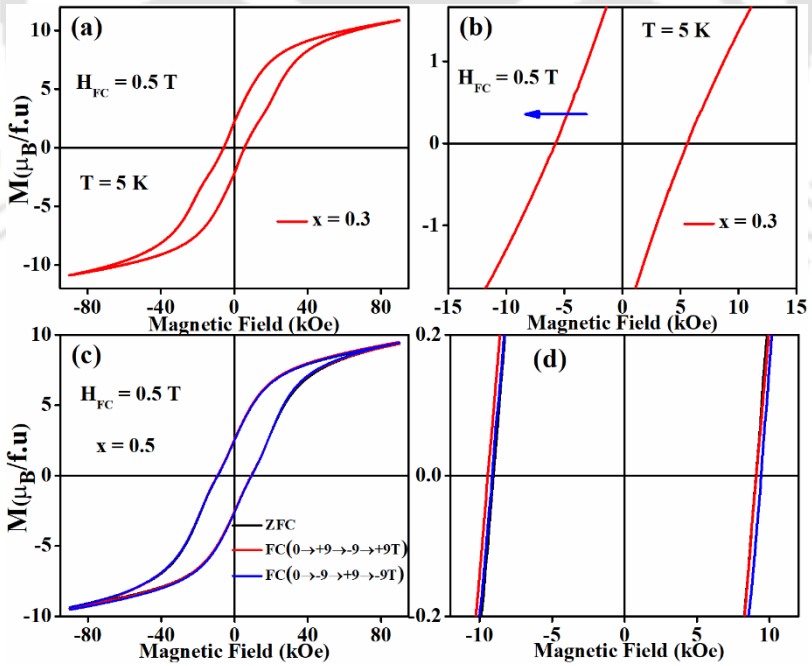

Fig.3.14. (a) M-H loops under FC condition for x = 0.3 and (b) its enlarged view in the vicinity of coercivity (H_C), (c) ZFC, positive and negative FC MH loops for x = 0.5 sample and (d) their enlarged view in the vicinity of coercivity.

Here x = 0.5 sample shows relatively large H_{EB} value at 5 K. For this sample we have recorded several MH loops under FC condition in the temperature range of 5 K to 95 K. These are shown in Figure.3.15 (a) along with the plots in expanded scale (Figure.3.15 (b)). We can see that all of them show EB behavior. The H_{EB} values determined from these loops are plotted as a function of temperature as shown in Figure.3.16 (a). It is found to fall exponentially with increase in temperature. It is fitted to an exponential function of the form [270],

$$H_{EB}\,(T) = H_{EB}\,(0)\,exp^{\left(-T/T_1\right)} \qquad (3.7)$$

Here, H_{EB} (0) is the EB value at T = 0 K and T_1 is a constant. The fitted data are shown as solid line in Figure.3.16 (a). The fitted values of H_{EB} (0) and T_1 are found to be -394 ± 10 Oe and 9.8 ± 0.4 K respectively. We can see a sharp fall in H_{EB} especially for T ≥ 20 K. This can be understood that the exchange interaction between RE and TM ions in the perovskite structure based materials are generally strong for T < 20 K [240]. Thus, for T > 20 K the weakening of anisotropic exchange interaction gives rise to decrease in the value of H_{EB}. We have also plotted the variation of H_C with temperature, which is shown in Figure.3.16 (b). It is found that it follows the modified Kneller's law [271].

$$H_C\,(T) = H_C\,(0)\,[1 - (T/T_B)^{\gamma}] \qquad (3.8)$$

Here, H_C (0) is the value of coercivity at T = 0 K, T_B is the blocking temperature and γ is a constant. According to Kneller's law in single crystalline materials, the value of γ = 0.5. However, we are dealing with polycrystalline samples, So, a deviation from original Kneller's law is expected. From the fitted data, the value of H_C (0), T_B and γ are found to be 8068 ± 302 Oe, 106 ± 3 K and 1.29 ± 0.1 respectively.

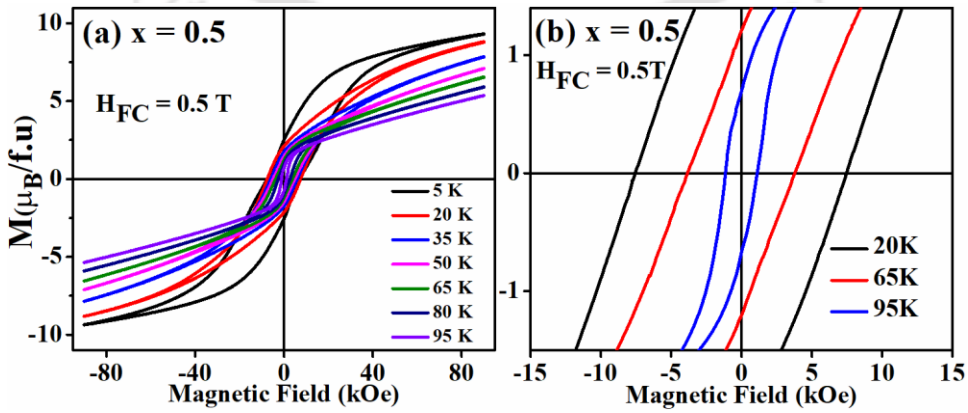

Fig.3.15. (a) M-H loops measured at different temperature under FC condition with H_{FC} = 0.5T and (b) enlarged view of the loops near coercive field at T = 20, 65 and 95 K for x = 0.5 sample.

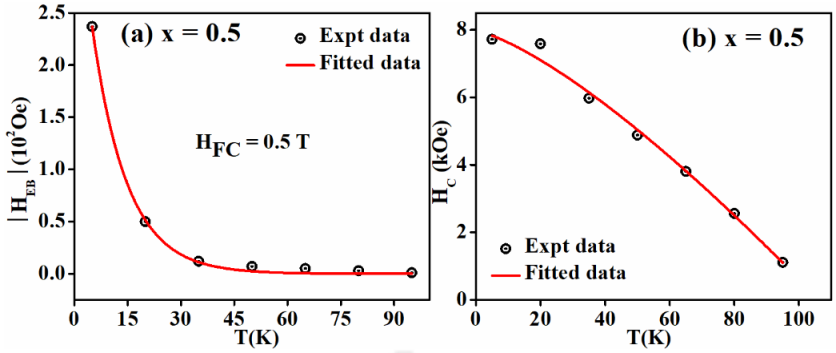

Fig. 3.16. Temperature variation of (a) exchange bias field (H_{EB}) and (b) coercivity for x = 0.5 sample.

EB behavior depends on both cooling field (H_{FC}) and maximum measuring field (H_{max}). To study the variation of EB on H_{FC} at 5 K, we have recorded MH loops for x = 0.5 sample after cooling the samples at H_{FC} = 300 Oe to 5 T, as shown in Figure.3.17 (a). It is observed that the EB value is keep on increasing with H_{FC}, however the increment after 1 T is quite large (inset of Figure.3.17 (a)). Based on previous reports [57], the Ho interacts with Co/Mn at higher magnetic field. As a result, the anisotropic exchange interaction between the FM and AFM components exhibits a sharp increase after reaching 1 T (H_{FC}), it leads to a larger H_{EB}. To see the variation of EB on H_{max}, each loop of the sample was FC at H_{FC} = 0.5 T then the measurement was done up to various measuring fields such as H_{max} = ± 6 to ± 9 T respectively. We have observed a clear exponential decay of EB values with increase in measuring field (Figure.3.17 (b)), and it is well fitted with an exponential function indicated by red solid lines (inset of Figure.3.17 (b)). This may be due to the reduction of exchange anisotropy at higher measuring field. That is, the dominance nature of Zeeman energy overcomes the exchange anisotropy leads to a drop in H_{EB} value.

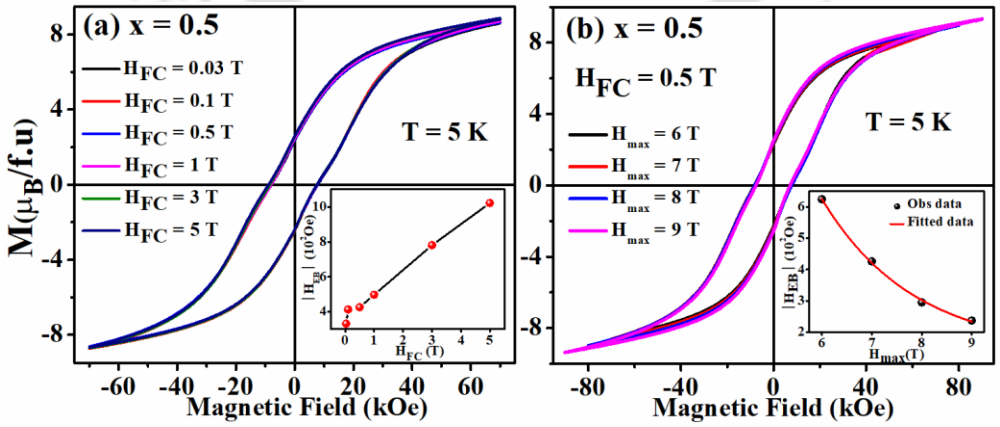

Fig.3.17. FC M-H loops taken at (a) different applied cooling field (H_{FC}), inset shows H_{EB} versus H_{FC} and at (b) different maxmium measuring field (H_{max}), inset shows H_{EB} versus of H_{max}.

3.2 Ho_2CoMnO_6 Flat Nanorod

In the present section, we are going to cover the structural and magnetic properties of Ho_2CoMnO_6 (HCMO) nanorods. As explained earlier, materials with decreased dimensions such as thin films, wires/rods, and nanoparticles, whose properties differ from those of bulk have drawn lot of research interest since they add functionality to multiple applications. Due to the transfer of the structure from bulk to nanorod, the possibility of surface spin canting is there, and it might unlock complex magnetic properties. Also, the structural distortion leads to a variation in bond angle of TM ions thereby tuning the ordering temperature. Several reports have already been published on the fabrication of nanorods with magnetic perovskites. However, to the best of our knowledge, investigations on nanostructured HCMO, like reported in the present work, is still missing and of large interest. So, the current motivation in the present work is to synthesize 1D HCMO nanostructured material with desired functionality for specific and efficient applications. So here we have synthesized single-phase nanorods of DP HCMO by following a hydrothermal route as described in the section 2.1 and carried out a detailed comparative study on structural and complex magnetic behavior with that of the bulk and nanocrystalline samples. Various enhanced properties such as a large increase in FM T_C as well as additional magnetic properties such as AFM and re-entrant spin glass (RSG) ordering have been noticed in this nanorods.

3.2.1 Structural Properties

The powder XRD patterns at RT for HCMO flat nanorod, calcined at different temperature are shown in Figure.3.18 (a). The as synthesized sample shows a clear amorphous nature, after calcination at 650^0 C the (112) and (200) reflections are observed. At 850^0 C annealing all the reflections of the monoclinic phase are found along with two impurity peaks which are indicated by star symbol. On further sintering, the impurity peaks are removed and the pure monoclinic phase was observed at 1000^0 C. However, as calcination temperature rises, the reflection peaks become more sharper and narrower, indicating an increase in crystallinity. Figure.3.18 (b) shows the Rietveld refinement of XRD data along with all the reflection peaks readily indexed. Rietveld analysis reveals that the HCMO flat nanorods are formed in pure monoclinic phase with space group: $P2_1/n$. Extracted unit cell parameters for the HCMO flat nanorods and the earlier reported values for bulk [71] and single crystalline [63] HCMO samples are as follows. For the flat nanorods the lattice parameter a (5.246 Å) and b (5.648 Å) are found to be higher than those of reported bulk

sample (a = 5.239 Å, b = 5.587 Å), as well as the single crystalline HCMO (a = 5.2454(2) Å, b = 5.5988(2) Å) which leads to unit cell expansion (220.9 $Å^3$) as compared to bulk (219.19 $Å^3$) and single crystalline (220.06(1) $Å^3$) samples. However, the value of lattice parameter c is smaller (7.457(0) Å) compared to both bulk (7.486 Å) and single crystalline sample (c = 7.4934(2) Å). The monoclinic angle β is found to be 90.1° for the present sample. Here all the errors are found to be beyond the given significant digits.

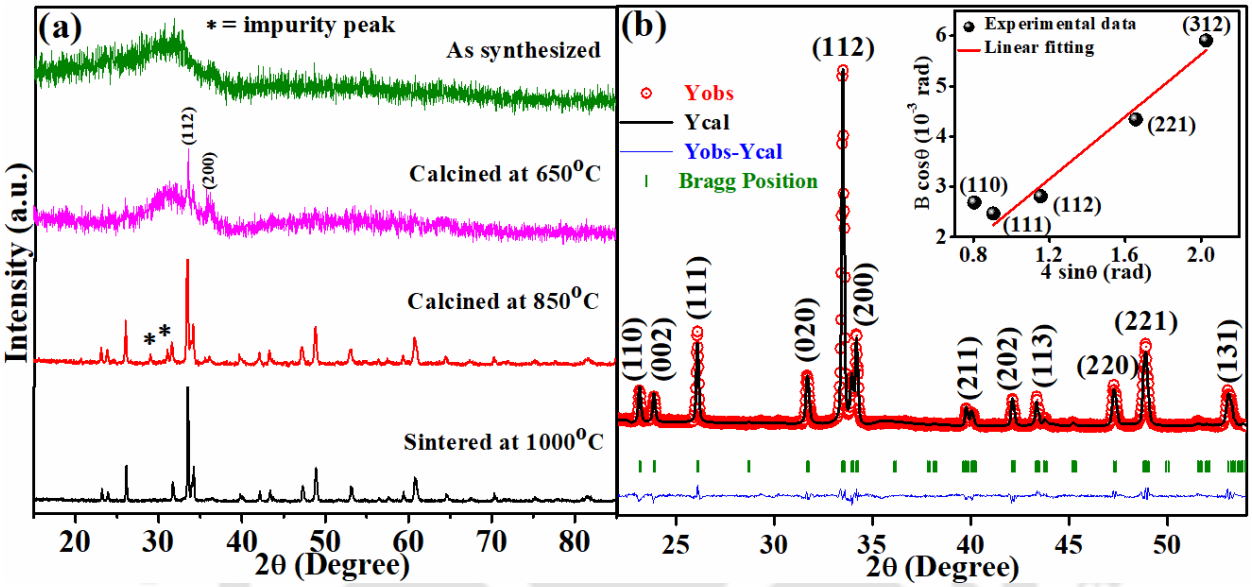

Fig.3.18. (a) Room temperature XRD patterns of HCMO nanorod calcined at different temperature, (b) Rietveld refined data, inset shows Williamson-Hall plot.

The relation of WH plot as given in Eqn. 3.1 is used to calculate the crystallite size, as well as micro-strain parameters [259]. The WH Plot is shown in the inset of Figure.3.18 (b) and it is well fitted with the linear equation which is represented by the red solid line. The value of average crystallite size is found to be 42 (±5) nm. Whereas, the value of micro-strain parameter is found to be 3.1×10^{-3} which is much higher than the bulk [71] as well as from the nanocrystalline sample of HCMO as we reported in section 3.1 (our work). It can be understood as follows; the change of structure from bulk/nanocrystalline to 1D nano form leads to a rise in the surface to volume ratio hence rise in micro-strain parameter. Unit cell model of HCMO flat nanorods is shown in Figure.3.19 (a) where CoO_6 and MnO_6 octahedra are situated alternately at the corner of the unit cell and Ho at the void space between them. These corner shared octahedra are not symmetrically placed rather they are tilted and stretched. The overall tilting in unit cell is measured by looking at

the angle between CoO_6 and MnO_6 octahedra in horizontal and vertical direction (c axis) as shown in Figure.3.19 (b, c). CoO_6 and MnO_6 form an angle of 159.5^0 between them with respect to horizontal axis. Similarly, the tilt with respect to vertical axis gives rise to an angle of 144.3^0. The 180° bond angle between TM ions in a DP generates a strong FM SE interaction [38,39]. As the bond angles between the TM ions with O_1 and O_3 are much higher than the reported bulk HCMO [71], one can expect a higher FM T_C in the present case. By observing the bond angles between octahedra with O_1, O_2 and O_3 (Figure.3.19 (d)), we can say this structural distortion may also cause ASD leading to AFM spin couplings across the ions. This type of feature is also observed in Pr_2FeCrO_6 nanoparticles [135].

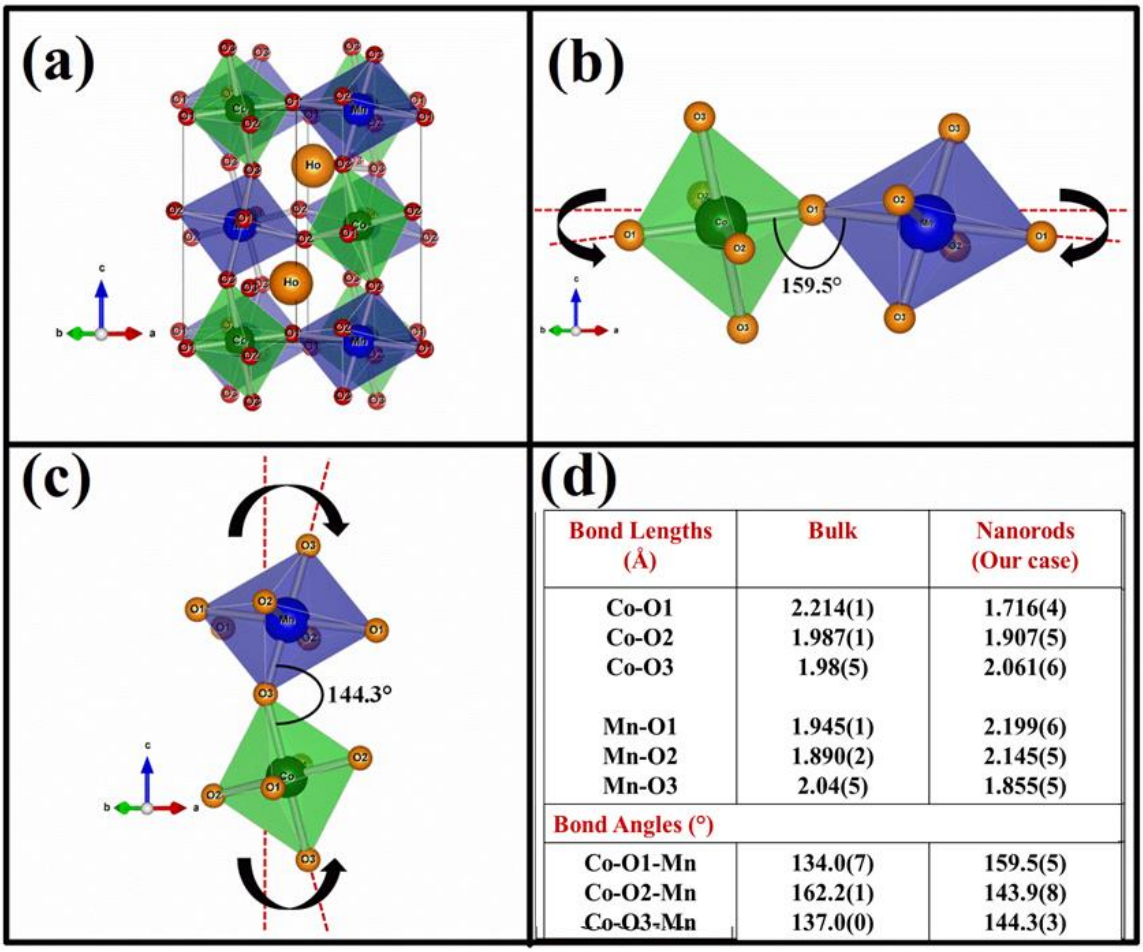

Bond Lengths (Å)	Bulk	Nanorods (Our case)
Co-O1	2.214(1)	1.716(4)
Co-O2	1.987(1)	1.907(5)
Co-O3	1.98(5)	2.061(6)
Mn-O1	1.945(1)	2.199(6)
Mn-O2	1.890(2)	2.145(5)
Mn-O3	2.04(5)	1.855(5)
Bond Angles (°)		
Co-O1-Mn	134.0(7)	159.5(5)
Co-O2-Mn	162.2(1)	143.9(8)
Co-O3-Mn	137.0(0)	144.3(3)

Fig.3.19. (a) Unit cell of HCMO flat nanorods, (b) horizontal representation of CoO_6 and MnO_6 octahedra, (c) Vertical representation of CoO_6 and MnO_6 octahedra along c- axis, (d) Comparison of structural parameters of HCMO flat nanorods with their bulk sample.

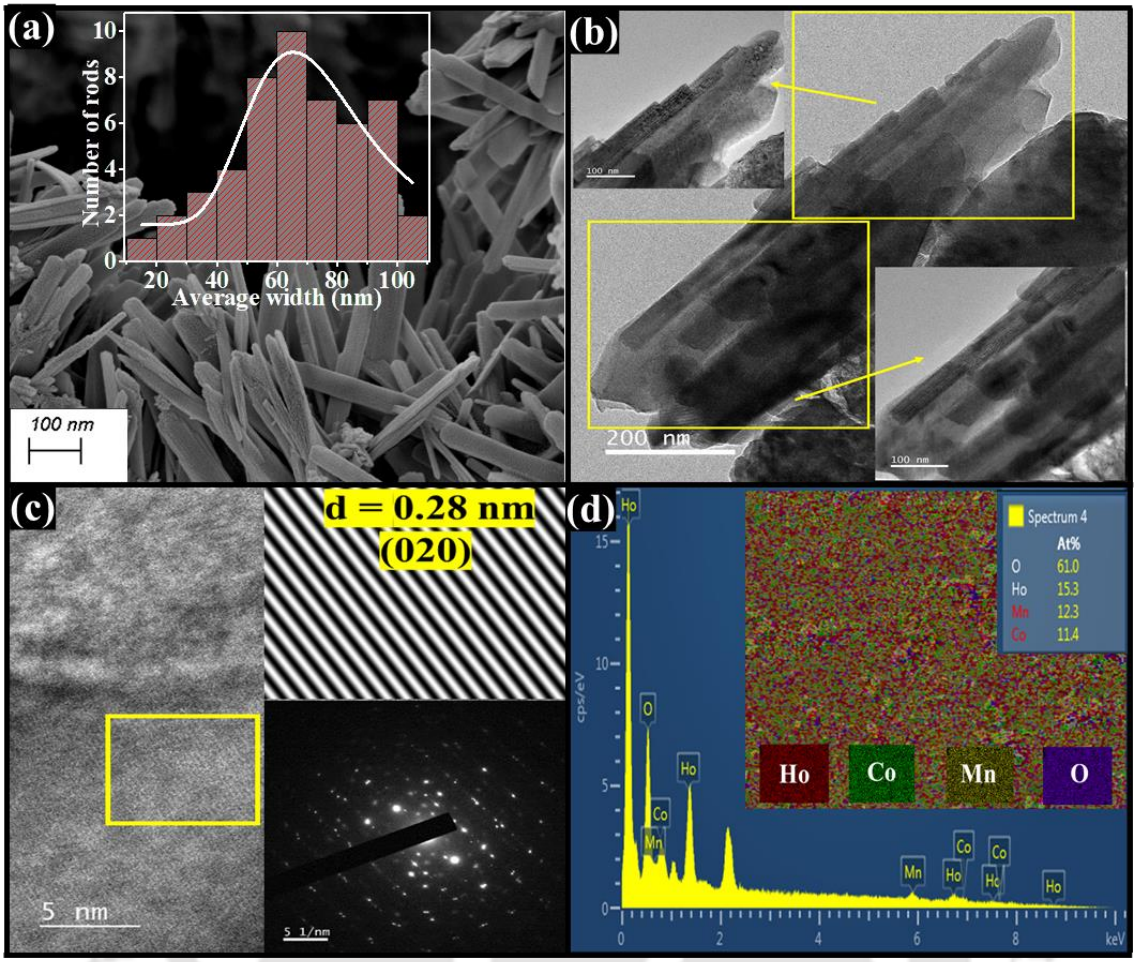

Fig.3.20. (a) FESEM image, inset shows the log-normal fitting to determine average width of HCMO flat nanorods, (b) TEM image, inset shows the enlarged view of the rods at specified region, (c) HR-TEM and SAED pattern of (020) plane and (d) EDS spectra, inset shows elemental mapping for HCMO flat nanorods.

FESEM examination revealed a clear image of HCMO flat nanorods as shown in Figure.3.20 (a). It is named as flat nanorods as it is not looking like a cylindrical rod but as a flat shaped rod. A distribution of 10 to 110 nm of width has been noticed for the rods. The average width is determined to be 71 (±3) nm as displayed in the inset of Figure.3.20 (a). The development of flat nanorods is also seen in the TEM picture (Figure.3.20 (b)), and its width is compatible with the FESEM analysis. The plane (020) is confirmed by the selected area diffraction (SAED) pattern, which agrees with the XRD results (inset of Figure.3.20 (c)). The SAED pattern confirms the single crystalline/unidirectional growth of the particle. EDS is used to determine the composition

of the elements. It verifies the existence of Ho, Co, Mn, and O in the appropriate composition (Figure.3.20 (d)). The elemental mapping (inset of Figure.3.20 (d)), confirms the homogeneous distribution of these elements.

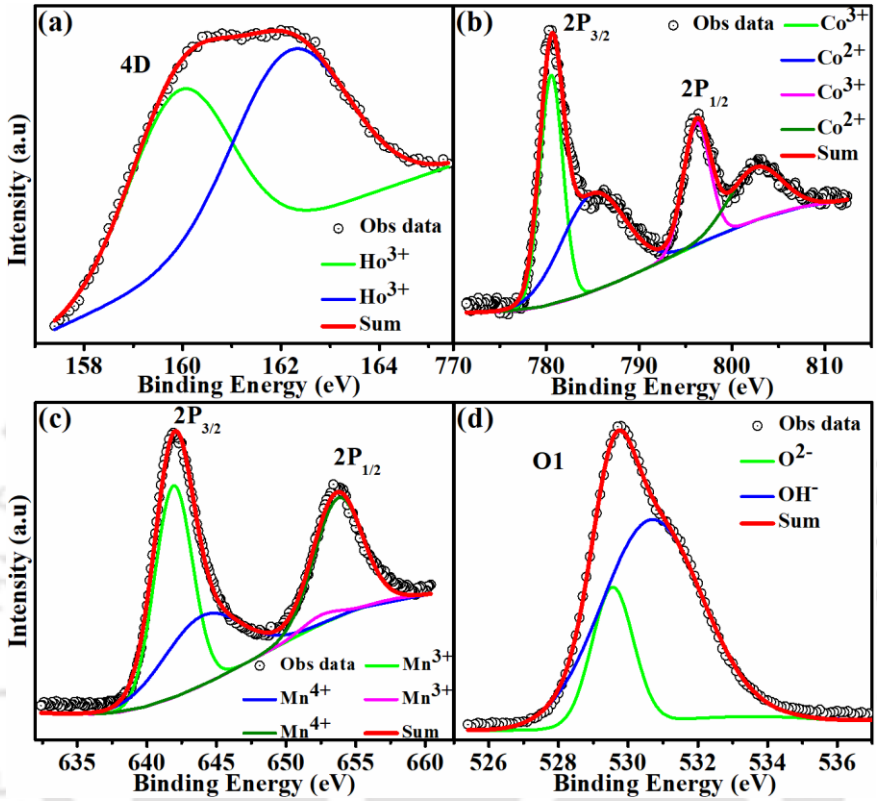

Fig.3.21. XPS data for (a) Ho4D, (b) Co2P, (c) Mn2P levels and (d) O1 respectively.

The room temperature XPS data along with the Gaussian fit of Mn and Co for HCMO flat nanorods are shown in Figure.3.21 (a-d). The oxidation states of Co/Mn were measured by deconvoluting $2P_{3/2}$ and $2P_{1/2}$ peaks of Co and Mn. The oxidation states of Ho are measured by deconvoluting 4D peaks of Ho. Whereas, the O1s peaks of XPS gives the oxidation states of oxygen. The spectrum for Ho consists of peaks at 159.9 eV and 162.18 eV as shown in Figure.3. 21 (a) and it is attributed to the 3+ state of Ho [260]. Figure.3.21 (b) shows the 2P core-level spectrum of Co, it consists of four peaks, peaks at 780.54 eV, and 785.03 eV belong to $2P_{3/2}$ levels. Whereas, peaks at 796.18 eV and 802.48 eV represent $2P_{1/2}$ levels. Similarly, Figure.3. 21 (c) represents the 2P core-level spectrum of Mn, it also has four peaks, the peaks at 641.91 eV and 643.97 eV represent $2P_{3/2}$ levels, and peaks at 652.50 eV, and 653.74 eV represent $2P_{1/2}$ levels. As per the previous studies, the peak positions of both Co and Mn confirms their presence in 2+/3+

and 3+/4+ states respectively [261-266]. The fitting peak of oxygen generally gives two distinct peaks, here also we found two peaks as shown in Figure.3. 21 (d). The peak at 529.5 eV is ascribed to the presence of O^{2-} in a typical metal-oxygen bond. The peak at 530.6 eV is corresponded to the hydroxyl groups OH^- through O-H bonds respectively [260].

3.2.2 Magnetic properties

Temperature variation of magnetization (MT) of HCMO flat nanorods recorded at 100 Oe, in both ZFC and FC condition are shown in Figure.3.22 (a). ZFC plot shows a sharp rise in magnetization at T < 182 K and it keeps on increasing, which indicates the transition of the system from the so-called disordered state (PM) to a magnetically ordered state. Further lowering the temperature, the magnetization value keeps on increasing, but with a peak around 31 K. The FC data show rise in magnetization around 182 K, i.e., a FM T_C. The magnetization increases continuously with decrease in temperature followed by a broad peak at 97 K. In addition, a small kink is observed at 31 K coinciding the peak observed in ZFC curve. A large bifurcation is observed between ZFC and FC magnetizations below 185 K, signifying the existence of thermomagnetic irreversibility. Transition temperatures were determined by plotting first derivative of the magnetization (for both FC and ZFC) with respect to temperature versus temperature as shown in the inset of Figure.3. 22 (a). Three strong anomalies have been observed in the dM/dT plots at 182 K, 97 K and 31 K (inset of Figure.3. 22 (a)). The anomaly at 182 K is nothing but the FM transition temperature (T_C) originating from the SE coupling between half-filled Co^{2+} ($3d^7$:- $t_{2g}^3 \uparrow t_{2g}^2 \downarrow e_g^2 \uparrow$) and empty e_g level of Mn^{4+} ($3d^3$:- $t_{2g}^3 \uparrow e_g^0$) orbitals via O^{2-} ions. This FM T_C is much higher than the bulk HCMO samples [44,57,64,71]. As the SE interactions are affected by the presence of surface spin disorder in nanoparticles and the deviation of bond angles from 180^0 [2]. Here the bond angles between CoO_6 and MnO_6 octahedra through O_1 and O_3 are found to be 159.5^0 and 144.3^0 respectively (shown in the inserted table in Figure.3.19 (d)). These values are much higher than those observed in the HCMO bulk sample [71]. This clearly says that in HCMO flat nanorods, the octahedral angles approaching towards 180^0 and hence the FM SE interaction in Co^{2+}-O-Mn^{4+} networks are getting stronger and it leads to increase in FM T_C in this compound. The peak in dM/dT plot at 95 K is attributed to the Neel temperature (T_N). It may arise from the number of reasons, which may cause strong AFM interactions in the system, (i) AFM coupling between Ho^{3+} and Co^{2+}/Mn^{4+} ions in the FM matrix. (ii) AFM coupling between Co^{2+}-O-Co^{2+} and Mn^{4+}-O-Mn^{4+} networks which arises in the disordered DPs, (iii) the presence of

Co^{3+} and Mn^{3+} ions and the AFM interaction between them. However, the peak at 31 K is ascribed to the re-entrant spin glass transition temperature (T_{sg}). The presence of this spin-glass phenomena is further confirmed and discussed later by the magnetic relaxation phenomena and aging effect. The spin mechanism of the system can be explained as follows, for T > T_C the system is in PM state, for T_N < T ≤ T_C, the interaction between the 3d-3d (Co-Mn) ions is strong and it gives rise to the FM in the system. While, in T_{sg} < T ≤ T_N the AFM ordering starts within Co^{2+}-O^{2-}-Co^{2+} and Mn^{4+}-O^{2-}-Mn^{4+} networks as discussed above. Below this temperature i.e., T ≤ T_{sg} the RE ions get polarized in the field direction, hence below T_{sg} magnetization value is kept on increasing [57,71].

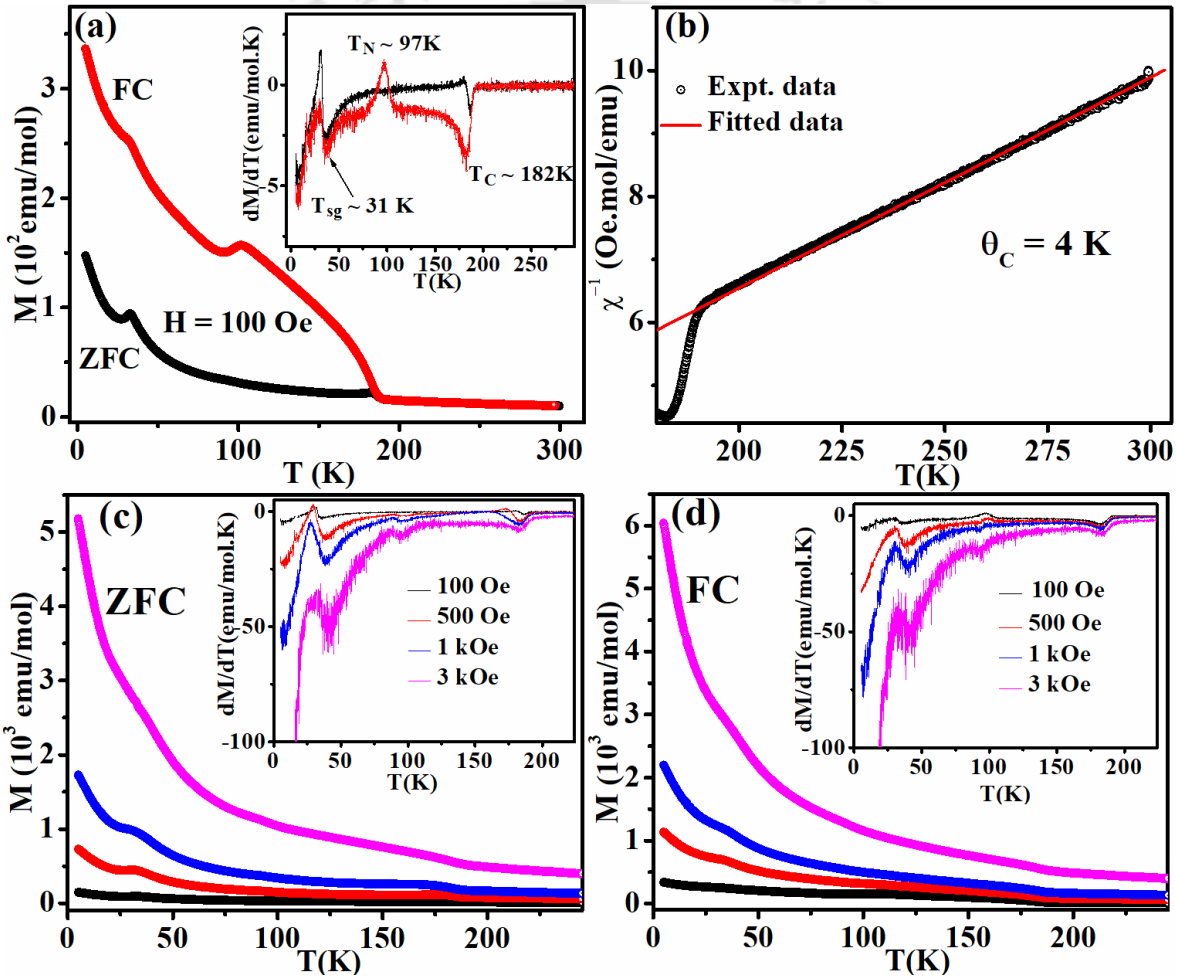

Fig.3.22. (a) M-T plots at an applied field of 100 Oe, inset shows the dM/dT plots, (b) Inverse susceptibility fitted with Curie-Weiss law, (c) at various applied field in ZFC mode and (d) in FC mode, inset shows the dM/dT plots.

To further understand the magnetic properties in detail, we have analyzed the inverse susceptibility as a function of temperature in the PM region (T > T_C) as shown in Figure.3.22 (b).

We have found that far above the T_C, the inverse susceptibility follows the Curie-Weiss (CW) law as explained in section 1.5.3 (Eqn. 1.6). The experimental data are well fitted to Eqn. 1.6 as represented by red solid line in Figure.3.22 (b). Obtained values of C and θ_C are 29.94 emu K mol^{-1} Oe^{-1} and 4 K respectively. The positive value of θ_C confirms the dominant nature of the FM exchange interaction in the system. The experimental effective PM moment (μ_{eff}^{exp}) of the sample is estimated by using the relation $\mu_{eff}^{exp} = \sqrt{3k_B C/N_A}$, where k_B is Boltzmann constant and N_A is the Avogadro number. As earlier reports say that the presence of some fraction of Co^{3+}/Mn^{3+} ions, with Co^{3+} in low spin state leads to a drop in magnetic moment in the Co/Mn based DP [28,59,70,248]. As per our XPS data, the presence of Mn^{3+} and Co^{3+} have been confirmed. Therefore, by considering the exact cationic population observed from XPS data, we have calculated the theoretical effective magnetic moment by using the relation [136],

$$\mu_{eff}^{Th} = \sqrt{[2 \times \mu_{Ho}^2 + 0.82 \times \mu_{Co2+}^2 + 0.18 \times \mu_{Co3+}^2 + 0.73 \times \mu_{Mn4+}^2 + 0.27 \times \mu_{Mn3+}^2]} \qquad (3.9)$$

Here the spin only effective magnetic moments of Ho^{3+}, Co^{2+}/Co^{3+} and Mn^{4+}/Mn^{3+} ions are represented by μ_{Ho}, μ_{Co2+}/μ_{Co3+} and μ_{Mn4+}/μ_{Mn3+} respectively. Here for the calculation, we have used 10.60 μ_B for Ho^{3+}, 3.87 μ_B for both Co^{2+} and Mn^{4+}, 0 μ_B for Co^{3+} and 2.82 μ_B for Mn^{3+} ions (considering both Co^{3+}/Mn^{3+} at low spin state) as the effective PM moments. After substituting all these values in Eqn. 3.9 the μ_{eff}^{Th} value is determined to be 15.81 μ_B/ f.u. However, the μ_{eff}^{exp} value is found as 15.47 μ_B/ f. u., which is quite close to the theoretical value.

To study the influence of higher applied field on MT we have also carried out the MT measurements at different applied field in the range of 100 Oe - 3 kOe in both ZFC and FC mode. The ZFC and FC MT plots are shown in Figure.3.22 (c, d), while inset shows the dM/dT plots of the respective curves. The ZFC curve shows a sharp rise in magnetization value at 189 K followed by two cusp in the intermediate temperature region. One may look at the valley of dM/dT versus T plot, which shows that the position of the valley increases with applied field. A closer view on dM/dT plots illustrate the T_N peak is positive (upward peak from the origin) at low field, while with increasing field it is getting supressed and finally at 1 kOe field it is showing downward peak (valley). This is ascribed to the forced alignment of AFM spins at high magnetic field and the dilution of AFM ordering. The sharp peak at 31 K at 100 Oe applied field is getting broadened with increase in field and is also shifting towards low temperature due to the forced magnetic polarization against the anisotropic field. At 3 kOe, the peak like structures almost disappears from

the MT curve. The rise in magnetization at low temperature (T < T_{sg}) is now much prominent due to forced magnetic polarization of RE element with large applied field. Simillar type of behavior is observed in FC MT plots.

(i) Study of M-H Loops

Below T_C, number of MH loops are measured at different temperatures, in an applied field of ± 9 T which are shown in Figure.3.23 (a). A small hysteresis is observed at 5 K without any saturation of magnetization signifying large AFM contribution or uncompensated spin structures at low temperature. We noticed that MH loops at higher temperatures and in the high field region is in straight line form, however near origin a small loop is observed at all the temperature (inset of Figure.3.23 (a)). At 175 K, the loop is showing a small opening near origin signifying the system is entering towards FM state from a PM state. By subtracting the linear part, the MH loop at 175 K is shown in the inset of Figure.3.23 (b), where a clear FM loop is seen. Which indicates that, as the conflicting interactions are existing in the system, the FM behavior is suppressed, and the FM loop is not readily visible in the as recorded loop at 175 K.

Table - 3.4. Parameters obtained from M-H Loops.

Sample	H_C (kOe)	Mr (μ_B/f.u)	M_S (μ_B/f.u)
Bulk 3 K [Ref. 71]	4.34	3.31	15.28
Nanocrystalline 5 K	5.33	2.0 (4)	11.6 (3)
Nanorod [present work]			
5 K	0.96	0.30	8.53 (1)
25 K	0.29	0.05	5.62 (2)
95 K	0.55	0.03	0.46 (0)
175 K	0.08	0.003	0.05 (0)

The initial loop of the MH curve is fitted with the LAS model to get the M_S value [267]. Table-3.4 shows the M_r, H_C, and M_S values which are extracted from the 5 K MH loop. From the fitting we have obtained the M_S value as 8.53 μ_B/f.u. which is quite smaller than the values obtained in bulk HCMO sample [71]. However, the value is higher than the FM ordered Co/Mn sublattices (6 μ_B/f.u.), which signifies the contribution of the RE ion moment in the FM ordered

domain. The existence of higher oxidation states of ions, as well as the introduction of AFM ordering and frustration in the system, causes the M_S value to drop.

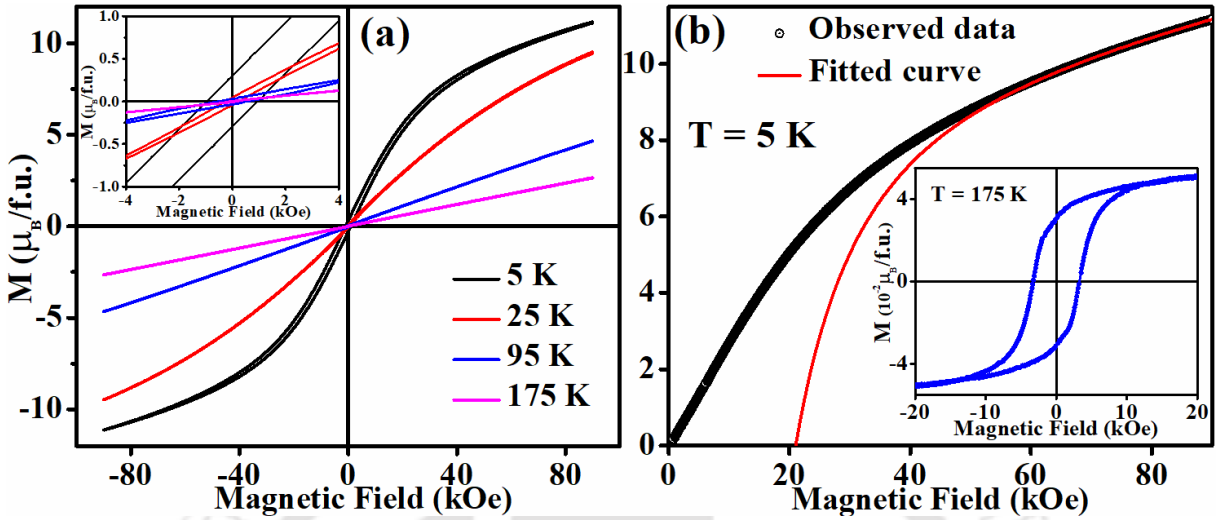

Fig.3.23. (a) MH Loops taken at different temperature, (b) initial MH loop along with the LAS fitting.

3.2.3 Magnetic Relaxation

In order to understand the presence of cluster glass/re-entrant spin glass behavior we have investigated the time (t) evolution of magnetization (M). The measurement was performed in FC mode at different temperatures, such as at 150 K, 70 K and 25 K under the applied field of 100, 300 and 500 Oe. However, only at 25 K a strong relaxation is observed, which is shown in Figure.3.24 (a-c). So, initially the sample was FC from 300 K to 25 K at an applied field of 100 Oe, then the field was switched off and we have waited for t_W = 120 sec. Then the recording of remnant magnetization as a function of time (M_t) was carried out up to t = 6500 sec. Same protocol was followed for H = 200 and 300 Oe. Generally, for non-spin glass system, M-t plot will show a rapid drop in magnetization to nearly a constant value but in our case, we can see that the magnetization is not going to a constant value even after a time of ~2 hours. Which reveals that the system is showing glass like relaxation behavior. The magnitude of decay is relatively high and tends to decrease with increase in applied field value. The M-t can be described by stretched exponential relaxation function, which is well explained in Eqn.1.12 (chapter-1). They are reproduced here for convenience,

$$M(t) = M_0 + M_{sg}\,[\exp(-(t/\tau)^{1-n})] \qquad (3.10)$$

Here, M_0, M_{sg}, τ and n stand for intrinsic FM component, magnetic contribution from spin glass component, relaxation characteristic time, and critical exponent respectively. The magnitude of magnetic relaxation is represented by the value of critical exponent n, so its magnitude plays a major role in the relaxation phenomenon. Generally, n value should lie in between 0 to 1, if n = 0, the system relaxes exponentially, if n =1, the system doesn't show any relaxation behavior. However, for $0 \leq n \leq 1$ value, and a larger τ value is attributed to a slow variation of M-t. The measured data were well fitted by the Eqn. 3.10 which is represented by the red solid lines shown in Figure.3.24 (a-c). The fitted parameters are listed in Table-3.5. From the parameters, it can be seen that the FM contribution (M_0) along with the spin glass contribution is increasing with field. The decrease in value of τ indicates that less time is required to come back to the equilibrium state from the frustrated state. Which further indicates the decreasing frustration/spin glass in the system due to field which may arise due to the reduction in the depth of the trap which is explained in the next part. In this compound, the observed cluster glass/re-entrant spin glass behavior can be assigned to the presence of both FM and AFM interactions among the ions which leads to a frustration at low temperature.

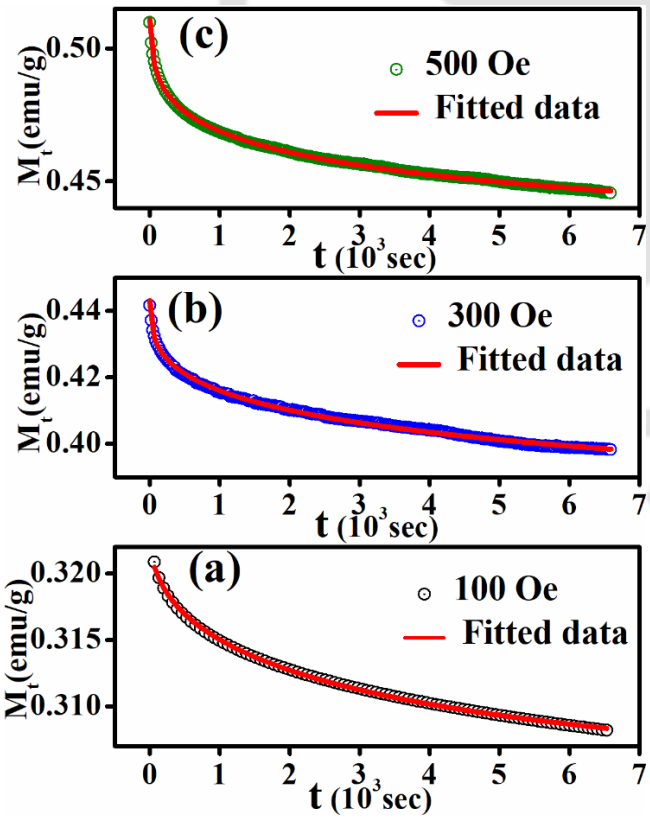

Fig.3.24. Relaxation of thermoremanent magnetization at 25 K measured for (a) 100 Oe, (b) 300 Oe and (c) 500 Oe.

Table - 3.5. Parameters obtained from magnetic relaxation measurements.

Field (Oe)	M_0 (emu/g)	M_{sg} (emu/g)	τ (10^3 sec)	n	E_Z (10^{-16} erg)
100	0.30	0.02	4.07 (0.05)	0.51	0.13
300	0.38	0.06	4.00 (0.05)	0.42	0.12
500	0.41	0.11	3.99 (0.17)	0.29	0.11

3.2.4 Aging effect

The aging behavior of a cluster glass/re-entrant spin glass system is a general characteristic that may be studied using M versus t measurements. Here the sample is FC through T_{sg} to the desired temperature and the magnetic field was switched off and wait for a time t_w. This generates a response function called spin relaxation rate 'S' and it is defined in Eqn.1.13 (chapter-1). It is reproduced here for convenience,

$$S(t) = \frac{d[-M(t,t_w)/H]}{d\ln(t)} \tag{3.11}$$

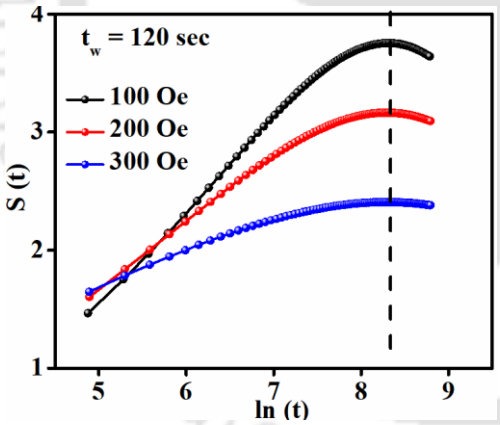

Fig.3.25. Relaxation rate S(t) versus ln(t) for different magnetic fields.

The measurements were performed at 25 K with a waiting time of 120 sec for three different fields 100, 300 and 500 Oe respectively. The S(t) versus ln (t) data are plotted for different magnetic fields as shown in Figure.3.25. From the graph we can see a peak for all fields around t = 3000 sec (ln(t) = 8), indicating the nonequilibrium states such as cluster glass/re-entrant spin glass in the present system. It is clear that the S (t) behavior is strongly influenced by the magnetic field, as the magnitude of the peak is found to decrease with increase in field. Similar results were reported in certain manganese-based perovskites [184,185]. The above feature is explained in

terms of reduction in the depth of the trap by an amount E_Z (Zeeman energy) due to the applied magnetic field, which helps the spins to move from a region of unfavourable state to a region of more favourable state. From the measured t_{eff} and using the relation ln (t_{eff} /t_w) = - E_Z /K_BT [274], E_Z values are determined and are given in Table-3.5.

3.2.5 Magnetocaloric effect

After observing a number of magnetic phases in the present compound, we are encouraged to study the MCE. For which we have recorded a number of isothermal magnetization curves at various temperatures from 3 - 220 K with the required temperature interval (ΔT), over a maximum field of 7 T (Figure.3.26 (a)). It was observed that, at low temperature magnetization sharply increases with the field up to 5 T, then the increment slows down at higher magnetic field. Which indicates the uncompensated spins and/or mixed magnetic interactions at low temperatures. Near T_C, the increment in magnetization at low field is visible however the rate of increment is very much small as compared to the low temperature isotherms. As the temperature crosses T_C, observed isotherms show a linear type behavior throughout the field variation (0-7 T), which is the hint of system getting into the PM region. To find out the order of the magnetic transition we have investigated the isotherms measured at different temperature.

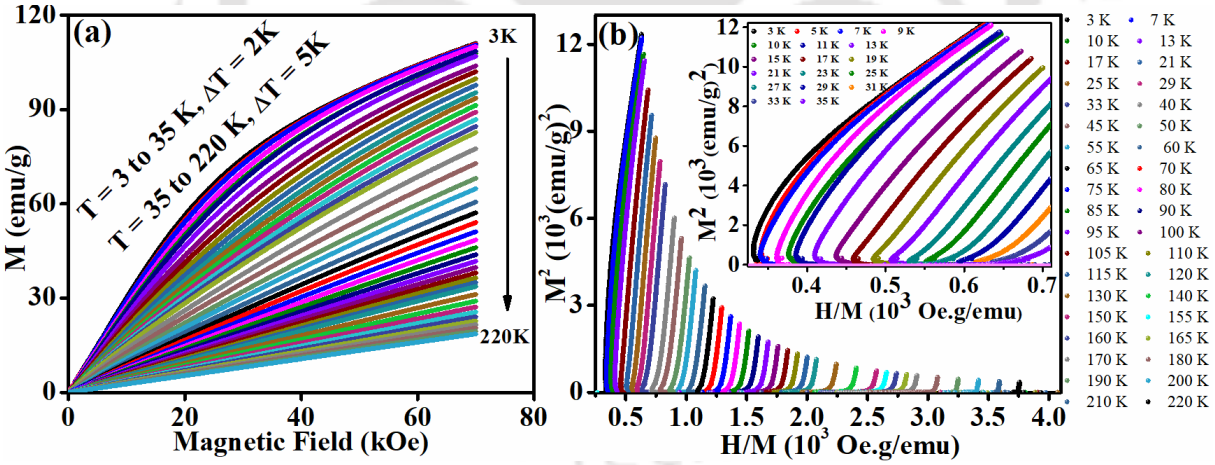

Fig.3.26. (a) Isothermal magnetization curves from 3 - 220 K and (b) M^2 versus H/M plots at various temperature range, inset shows the closer view of low temperature isotherms.

According to Banerjee [273], the order of the phase transition depends on the slop of the M^2 versus H/M plot. If the slope is positive it represents second order phase transition (SOPT) at the same time negative slope represents first order phase transition (FOPT). From the M^2-H/M plot

(Figure.3.26 (b)) we can see the negative slope at low temperature (inset plot), this type of curve is also observed by Pakhia et.al. [244] which indicates FOPT. However, the further confirmation of FOPT will be discussed later in this section.

Further to study, how the magnetic entropy (ΔS) is varying with respect to temperature at different field we have followed the Maxwell thermodynamic relation [242]. This relation is well explained in chapter 1 in section 1.12. Here the variations of -ΔS versus temperature at different applied fields are shown in Figure.3.27. Inset shows the semilogarithmic plot, it is given for a clear visualization of the peaks at lower temperatures. From the figure we can see a number of peaks throughout the temperature range of 3 K to 220 K. Which confirms the presence of multiple magnetic phases in the present HCMO flat nanorods. The value of -ΔS is increasing with rise in applied field. However, at low, field (≤ 5 kOe) negative value of -ΔS has been observed in low temperature region. This type of behavior is known as inverse magnetocaloric effect (IMCE), which is the indication of presence of AFM components at low temperature [50]. It further justifies the obtained AFM transition in this compound. We have observed five distinct peaks in the -ΔS versus T plot. Out of which two peaks are observed at lower temperature, and other three are observed in the vicinity of ordering temperatures which were explained in the MT data such as spin glass, AFM and FM ordering temperatures.

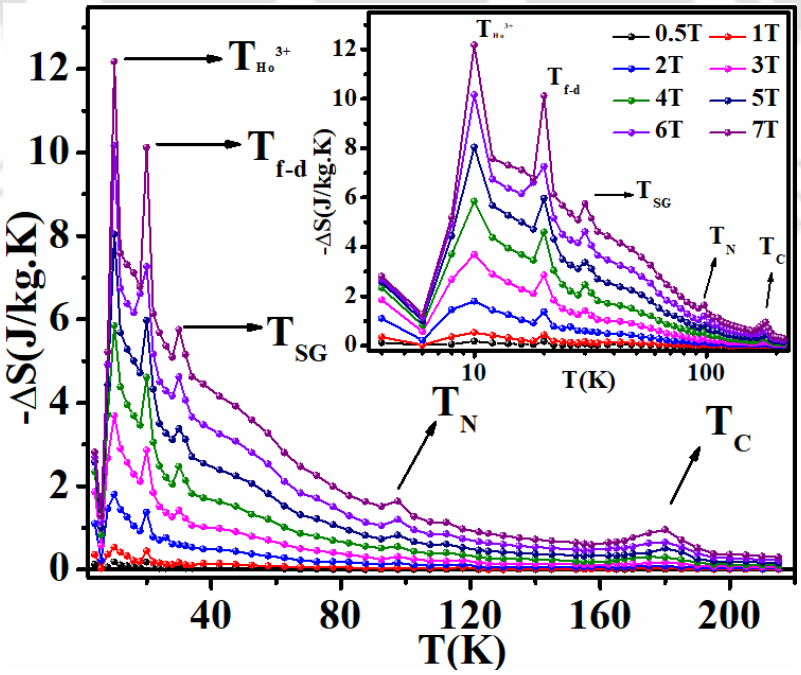

Fig.3.27. Variation of -ΔS with temperature at different field.

The peak at 10 K is denoted by T_{Ho}^{3+}, it is attributed to the active polarization of RE ions due to the exchange interaction across Ho^{3+}-O-Ho^{3+} networks [44,45]. Here the maximum entropy ($-\Delta S^{max}$) is obtained as 12.4 J/kg.K and it is comparable with the earlier report on bulk HCMO sample [44,71]. Further at T = 20 K, another peak is observed and it is denoted as $T_{f\text{-}d}$, similar type of peak is reported by Jia et. al. [44] and Majumdar et. al. [71]. According to them it might be attributed to a large magneto crystalline anisotropy caused by the spin orbit coupling of Co-Mn networks, or it could be linked to the 3d-4f exchange interactions between the FM network of Co/Mn sublattice and Ho^{3+} spins. Here $-\Delta S^{max}$ is found to be 10 J/kg.K. In addition to this, two more peaks are observed at 30 K and 97.5 K, represented as T_{sg} and T_N respectively. The former one is attributed to the re-entrant spin glass and the later one is the AFM transition with $-\Delta S^{max}$ of 5.8 and 1.6 J/kg.K respectively. Another peak at 180 K has been observed with $-\Delta S^{max}$ of 1.0 J/kg.K. This peak is attributed to the FM ordering among Co^{2+} and Mn^{4+} ions that is nothing but the FM T_C. However, the value of entropy at T_C is quite low as compared to the bulk HCMO sample [44,71]. It is due to the incomplete saturation and low value of magnetization in the compound. RCP can be calculated from the following equation, $RCP = |\Delta S|^{max} \times \delta T_{FWHM}$, where δT_{FWHM} is the full width at half maximum of $-\Delta S^{max}$-T plot. The estimated RCP value at an applied field of 7 kOe is found to be 53 J/kg for the HCMO flat nanorod.

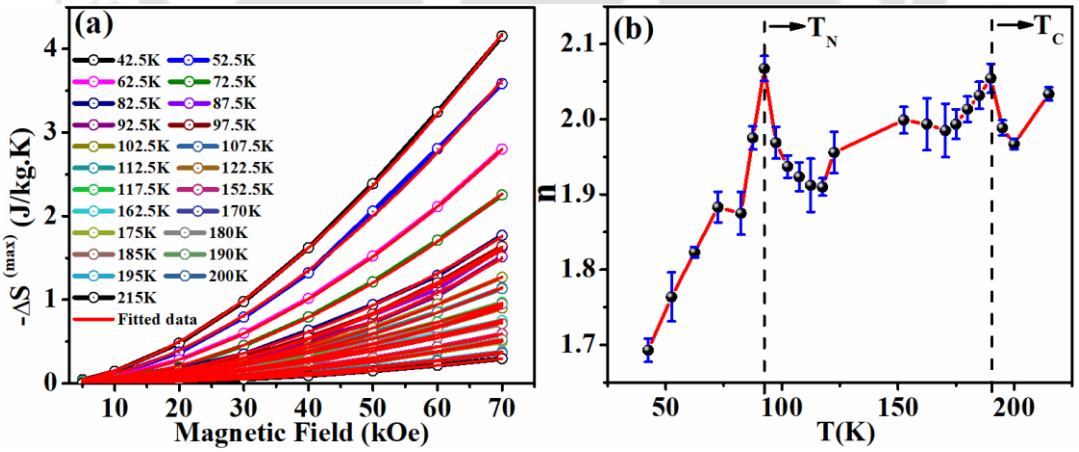

Fig.3.28. (a) -ΔS versus field at different temperature along with the fitted curve to power law equation and (b) variation of n with temperature.

In order to confirm the order of the magnetic phase we have analyzed the field dependence of ΔS as represented by a power law; $\Delta S^{max} \propto H^n$ [44,71,244]. According to the earlier reports, for 0<n<1 it indicates SOPT, and n>1 corresponds to FOPT respectively. However, n = 2 indicates complete PM region. On the other hand, Jia et. al. [44] proved that n>2 corresponds to FOPT. To

investigate the order of the magnetic phase we have used the above power law, by considering n as a free parameter. The fitted curve along with the plot of ΔS^{max} versus H for different temperature are shown in Figure. 3.28 (a). Afterwards, the obtained values of n are plotted as a function of T (Figure.3.28 (b)). We have observed that the value of n is < 2 below T_C, then it increases to a value > 2 near T_C. Further increase in temperature, its value gradually reaches to n = 2. This is a distinct feature of FOPT [245]. The similar feature is observed in the vicinity of T_N, which indicates, may be T_N is also a FOPT. So, we could say that the magnetic phase transitions in HCMO flat nanorods comes under FOPT. Furthermore, we have also fitted the ΔS^{max} versus H plots at various temperatures using the above power law, but this time by fixing the value of n = 2, and we found that the data are well fitted for T ≥ 215 K. This clearly confirms that the sample is in PM state above 215 K.

3.3. Conclusion

Single phase nanocrystalline samples of $(Ho_{1-x}Sm_x)_2CoMnO_6$ (x = 0.0 to 0.5) were successfully prepared by auto combustion method. Analysis of XRD patterns show that these samples crystallize in monoclinic structure with $P2_1/n$ space group. The lattice parameters, unit cell volume and bond angle between the TM ions are found to increase with Sm substitution. The MT measurements show complex magnetic properties such as FM transition with peak like structure followed by secondary rise in magnetization. They are explained based on FM interaction in Co^{2+}-O-Mn^{4+} networks clubbed with AFM interaction at APBs. The FM T_C is found to increase from 83 K for x = 0.0 to 115 K for x = 0.5. It is attributed to the strengthening of SE interaction among Co^{2+}-O-Mn^{4+} networks, due to the increase in bond angle between CoO_6/MnO_6 octahedra with Sm substitution. The secondary rise in magnetization is attributed to FM interaction of some of RE ions with net magnetic moment of TM ions. Such interaction is supported by the observed large M_S value of the order of 11.64 μ_B/f.u. at 5 K. These materials also show the EB behavior with a maximum H_{EB} of 237 Oe at 5 K. Temperature variations of H_{EB} and H_C were analyzed based on exponential law and modified Kneller's law.

Similarly, single-phase Ho_2CoMnO_6 flat nanorods were successfully synthesized through a hydrothermal process. RT XRD analysis state that the sample crystallizes in monoclinic structure with $P2_1/n$ space group. The lattice parameters, unit cell expansion as well as tilting angles are much higher than that reported for bulk sample. FESEM and TEM study confirms the formation of HCMO flat nanorods with an average diameter of 71 (±3) nm. MT study show the FM transition

at 182 K followed by AFM and re-entrant spin glass transitions at 97 and 31 K respectively. The higher FM transition as compared to bulk is attributed to the strengthening of FM interaction in Co^{2+}-O-Mn^{4+} networks due to the increase in bond angle between CoO_6/MnO_6 octahedra. The AFM transition is expected due to the presence of AFM coupling between the ASD ions. The presence of FM and AFM interactions and the ASD leaves the system in a random frustrated spin configuration which leads to re-entrant spin glass behavior. However, some visible contribution related to the polarization/ordering of Holmium at low temperature has been observed. Isothermal magnetization measurements at 5 K show that the system has uncompensated spin structure. The presence of higher oxidation states of ions, introduction of AFM and frustration in the system leads to a lower value of M_S. The maximum value of magnetic entropy is observed as 12.4 J/kg.K.

Chapter 4

$Ho_2CoMn_{1-x}M_xO_6$ (M = Ni and Cr) Series

4. $Ho_2CoMn_{1-x}M_xO_6$ (M = Ni and Cr) Series

MR in RE oxides such as manganite ($RMnO_3$) have sparked a lot of interest, driven by both fundamental physics and potential applications [74]. Some TM ions substitution at Mn site has been reported to show MR such as in $ErMn_{1-x}M_xO_3$ (M = Ni,Co) [274,275], $BiFe_{0.5}Mn_{0.5}O_3$ [205], $Bi_{0.3}Ca_{0.7}Mn_{0.75}Cr_{0.25}O_3$ [68], $ErCo_{0.5}Mn_{0.5}O_3$ [200]. More interestingly, in a single compound such as $LaCr_{0.85}Mn_{0.15}O_3$ [203] and $NdCr_{1-x}Mn_xO_3$ (x = 0.0 - 0.30) [276] sign reversal of both MR and EB field has been observed. However, to the best of our knowledge there is no report available, where Mn is replaced by any other TM ion in Ho_2CoMnO_6 to study the MR and EB behavior. Therefore, it was thought that by doping Ni and Cr in place of Mn, it would be possible not only to sustain the FM properties of the system Ho_2CoMnO_6, but also induce few novel magnetic properties. So, in this chapter we are going to study the structural, MR as well as EB behavior by doping Ni and Cr at Mn site.

4.1 Nanocrystalline samples of DP $Ho_2CoMn_{1-x}Ni_xO_6$ (x = 0 - 0.4)

We have synthesized nanocrystalline $Ho_2CoMn_{1-x}Ni_xO_6$ (x = 0-0.4) (HCMNO) DP by following auto combustion method as described in section 2.1 (Chapter 2). This work analyses in detail the crystalline structure of the sample and their complex magnetic properties. Additional FM phase, magnetic compensation with MR, BSM and sign reversal in EB field with the Ni substitution, are some of the characteristic features present in these samples.

4.1.1 Structural properties

The powder XRD patterns of HCMNO series were collected at RT are shown in Figure.4.1, where all the observed peaks are indexed based on monoclinic structure with space group $P2_1/n$. The obtained RT XRD data of x = 0.0 to 0.5 were refined by using the Rietveld refinement technique as shown in Figure.4.2 (a-e) by red solid line. From the Rietveld analysis we found that all the patterns are well fitted to the monoclinic structure with space group $P2_1/n$. The enlarged view of intense peaks such as (112), (020) and (200) are shown in Figure.4.2 (f-j). The shifting of

the peaks with Ni concentration towards higher 2θ (Bragg angle) value along with increase in broadening indicates the decrease in lattice parameters and particle/crystallite size as described below.

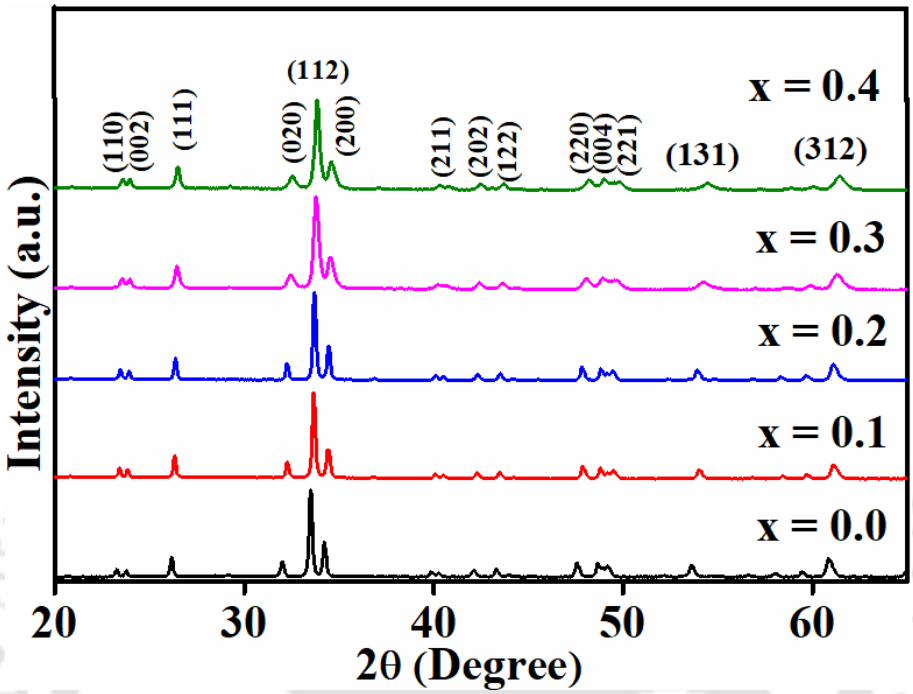

Fig.4.1. Room temperature XRD patterns of HCMNO series.

The obtained structural parameters from the Rietveld refinement are listed in Table-4.1. Here, with increase in Ni concentration a drop in the value of lattice parameters along with the unit cell volume has been observed. It is attributed to the partial replacement of larger Mn^{4+} ions (0.53 Å) with the Ni^{4+} ions having smaller ionic radii (0.48 Å). The value of monoclinic angle $\beta \neq 90°$, whereas the crystallographic angle α and γ are found to be 90° which is consistent with the monoclinic structure. The reliability factors such as R_f, R_{Bragg}, goodness of fit (χ^2) are found to be small value, indicating a good fitting of the XRD patterns.

The tilt in CoO_6 and MnO_6 octahedra in the Unit cell of HCMNO series were calculated along c-axis with O_1, O_2 and O_3, and are shown in Figure. 4.3 (a-d). Bond angle across TM ions with O_1, O_2 and O_3 are found to be increasing with Ni concentration and so does the average bond angle (Figure. 4.3 (d)). This result indicates strengthening of SE interaction and increase the FM T_C with Ni concentration which will be discussed in the magnetic section.

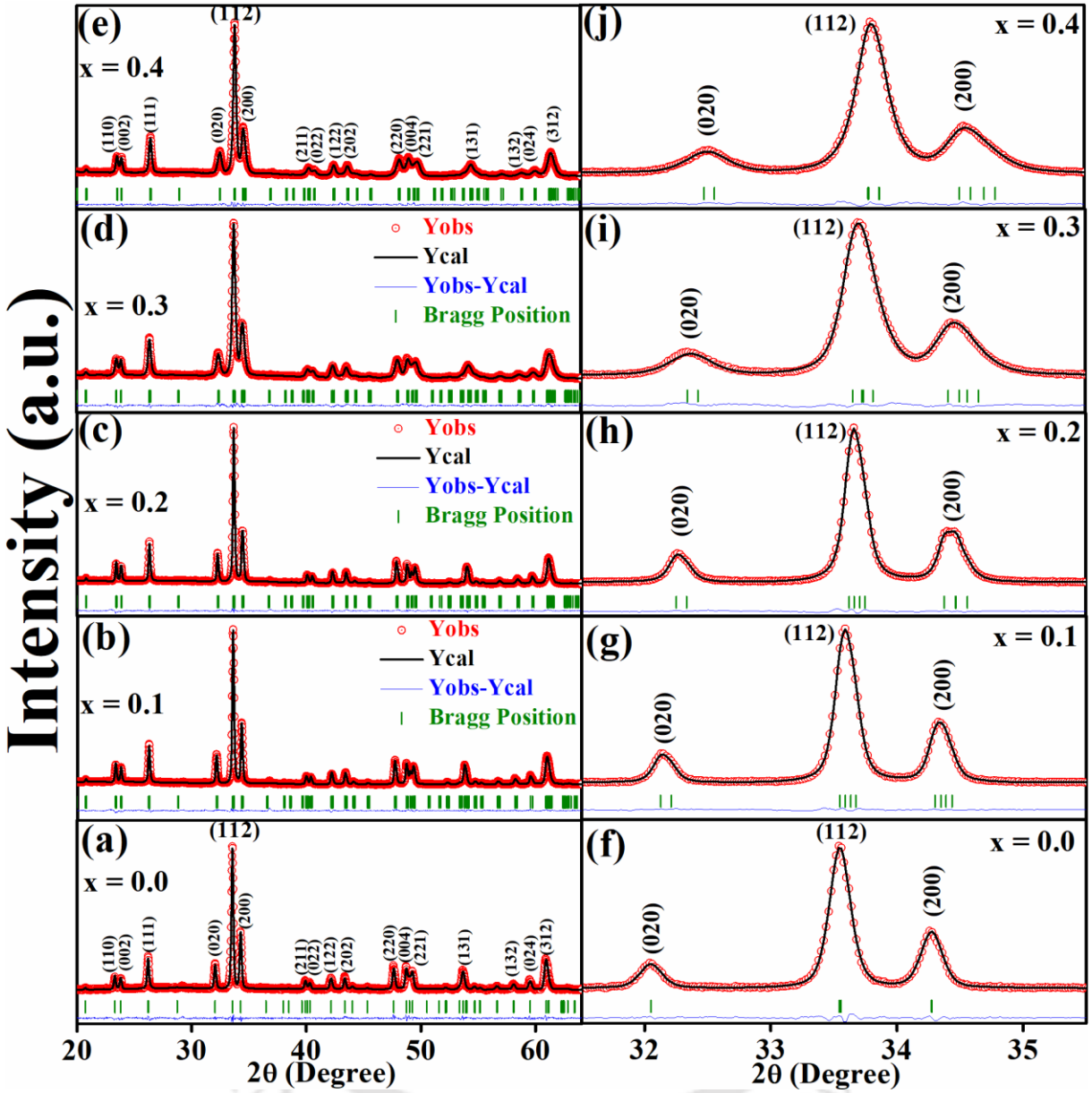

Fig.4.2. (a-e) Rietveld refinement of RT XRD patterns of HCMNO series, and (f-j) enlarged view of (020), (112), and (200) peaks for x = 0.0 to 0.4 respectively.

The WH plot method [259] is used to calculate the average crystallite size and the micro-strain parameter as explained in Eqn. 3.1. The WH Plot for x = 0.1 to 0.4 are shown in Figure.4.4 (a-d). Here, x = 0.0 is excluded as it is presented in chapter-3 in Figure.3.4. From the graph one can see that, they are well fitted with the linear equation as represented by red solid lines. The estimated average crystallite size of the samples is found to be 35 nm up to x = 0.2 then decreases to 19 nm for x = 0.4 sample as given in Table-4.1. With increase in Ni concentration, an overall

decrease in crystallite size has been observed. However, all the samples are found to be in nanocrystalline form. Similar to crystallite size, the observed micro-strain parameters are also do not reflects any huge variation up to x = 0.2 sample then suddenly it increases to 9.5 for x = 0.3 and finally goes to 10.1 for x = 0.4. It indicates, higher surface to volume ratio as the average crystallite size is decreasing with Ni concentration.

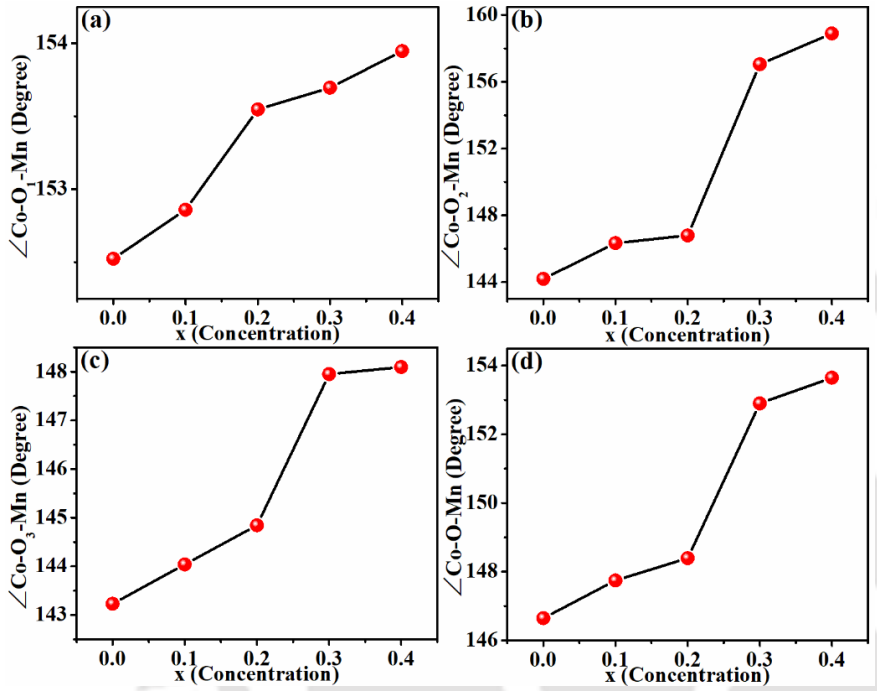

Fig.4.3. (a-d) Bond angle of TM ions with O1,O2,O3 and average bond angles of HCMNO series.

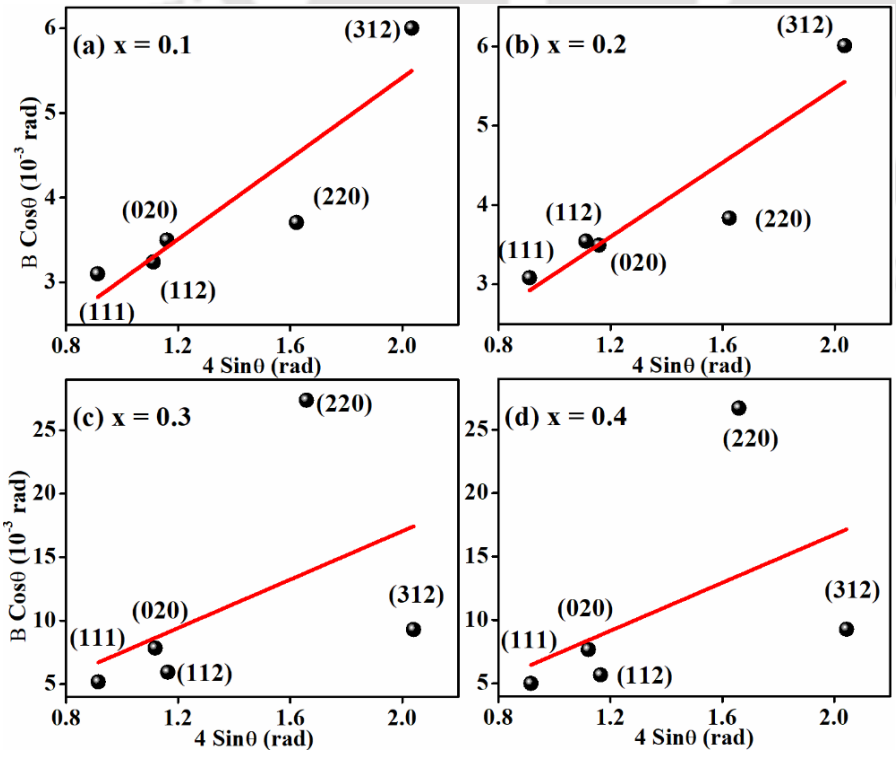

Fig.4.4. (a - f) Williamson-Hall plots of HCMNO series for x = 0.1 to 0.4 respectively.

The FESEM microstructural images reveal a highly agglomerated particles as shown in Figure.4.5 (a-d) for x = 0.1 to 0.4 samples. The calculated crystallite size is tabulated in Table - 4.1. The particles in all of the samples are linked weakly such that, porosity is quite significant. EDS analysis was used to determine the elemental composition for x = 0.0, 0.1, 0.3 to 0.4 samples, and the resulting spectrum is given in Figure.4.6 (a-d). It validates the existence of the appropriate composition of Ho, Co, Mn, Ni and O in the present series.

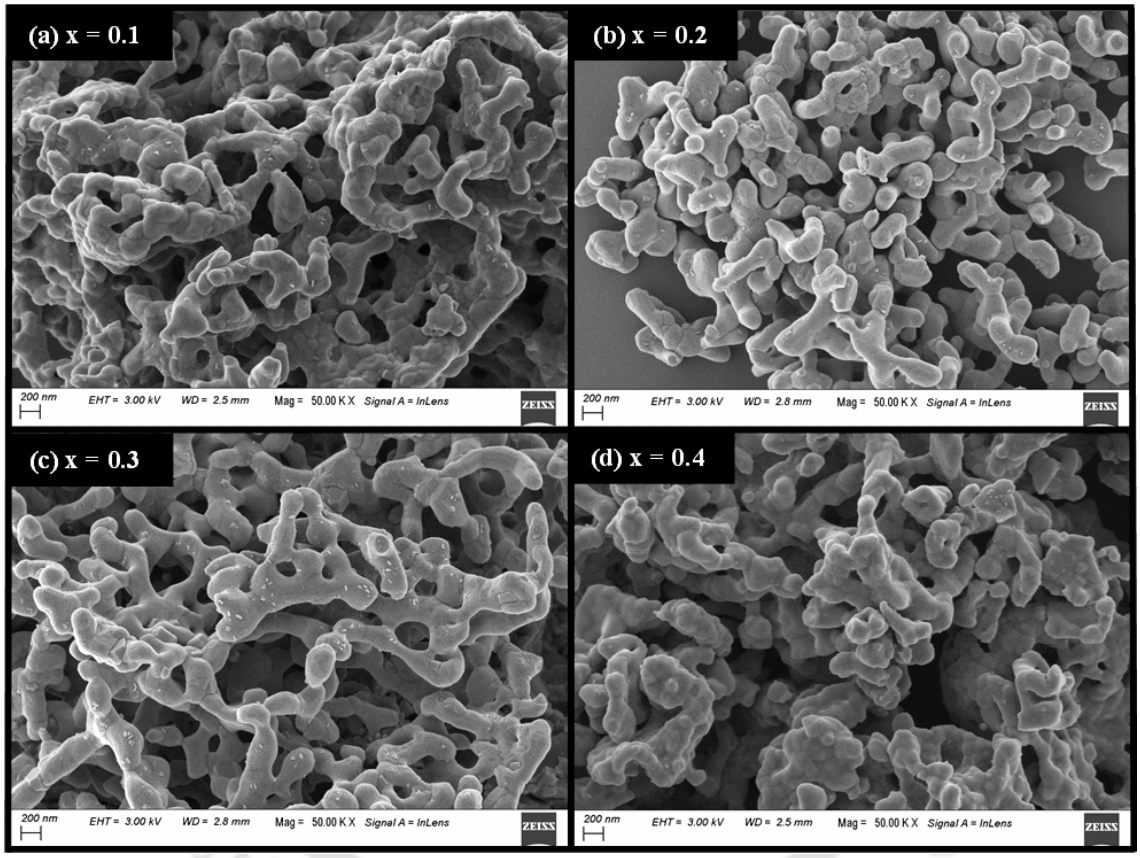

Fig.4.5. (a-d) FESEM images of HCMNO series for x = 0.1 to 0.4.

The RT Raman spectra in the range of 100 - 1400 cm^{-1} of wavenumber for HCMNO series are shown in Figure.4.7 (a). Generally, for monoclinic structure, Raman spectra should give two active modes; one is around 600 cm^{-1} another one near 400 - 500 cm^{-1} [60]. From Figure.4 (a) we can see two Raman active modes for all the samples; one band is in the range of 427 - 490 cm^{-1} while the other one is in the range of 609 - 631 cm^{-1}. After fitting the observed data of x = 0.0 sample to Lorentz fit, we found two peaks at 427 and 609 cm^{-1} (Figure.4.7 (b)), which are comparable to the previous reports for Co/Mn based DPs having monoclinic structure [60].

However, after fitting the data of all other samples, we found that with Ni substitution both the peaks are shifting towards higher wavenumber (Blue shift) representing decrease in lattice parameters with Ni substitution. The peaks are assigned as A_g and B_g mode, where A_g (427 - 490 cm^{-1}) mode represents the antisymmetric stretching and bending/rotational motions of $(Co/Mn)O_6$ octahedra and B_g (609 - 631cm^{-1}) mode represents the symmetric mode, attributed to stretching vibration of $(Co/Mn)O_6$ octahedra [60].

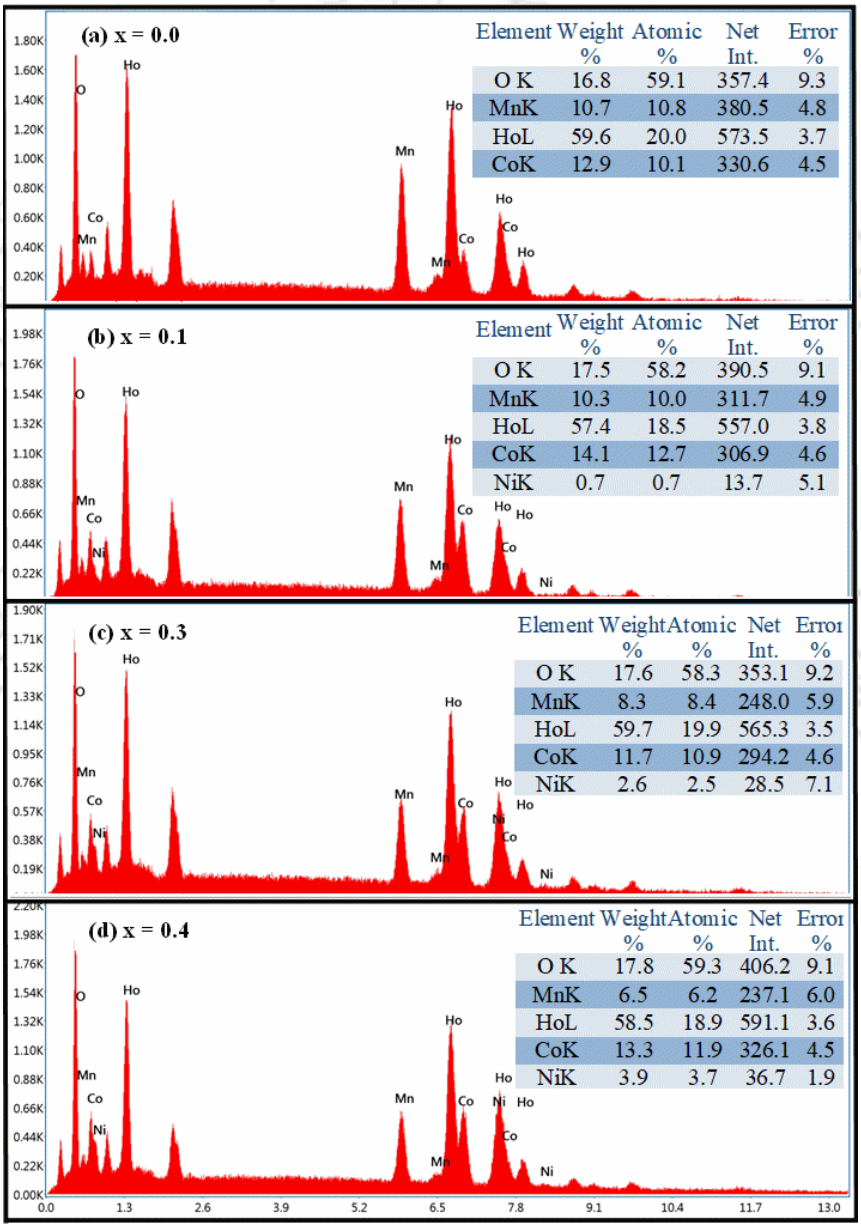

Fig.4.6. EDS spectra of materials with (a) x = 0.0, (b) x = 0.1, (c) x = 0.3 and (d) x = 0.4.

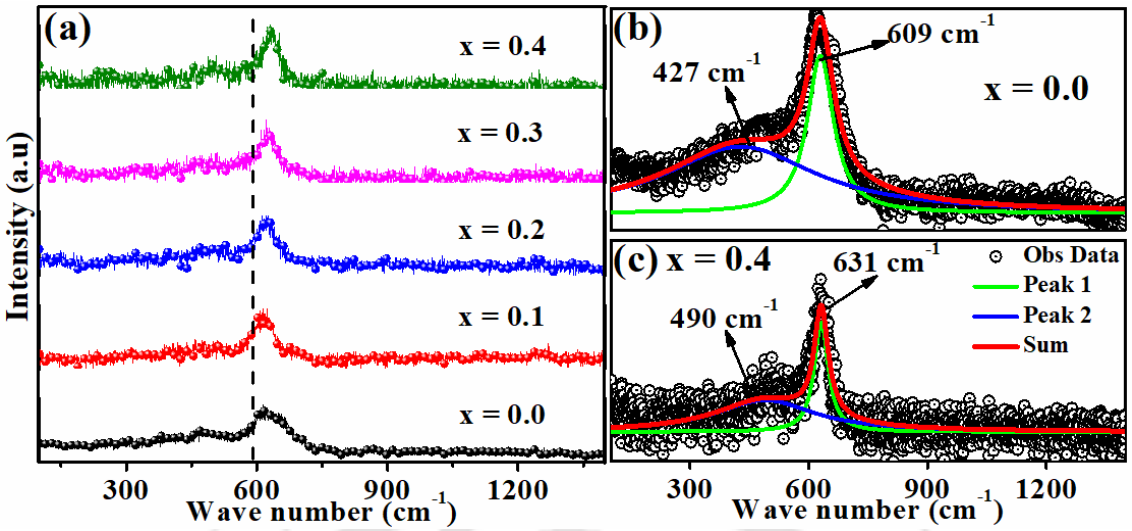

Fig.4.7. (a) Room temperature Raman spectroscopy for x = 0.0 - 0.4, and (b, c) Lorentz fit for x = 0.0 and 0.4 samples.

Table - 4.1. Data obtained from structural studies of HCMNO compound.

Sample	x = 0.0	x = 0.1	x = 0.2	x = 0.3	x = 0.4
a (Å)	5. 228	5.224	5.213	5.207	5.193
b (Å)	5. 581	5.567	5.546	5.531	5.507
c (Å)	7. 469	7.472	7.462	7.454	7.438
V(Å^3)	217.9	217.3	215.8	214.7	212.8
β (°)	89.93	89.91	89.91	89.83	89.99
R_f	7.70	3.58	2.11	1.56	1.50
R_{Bragg}	4.46	2.53	1.83	1.73	1.68
χ^2(%)	1.55	2.29	2.10	2.05	1.88
Average crystallite size(nm)	35	35	35	20	19
Micro-strain (10^{-3})	2.21	2.3	2.3	9.5	10.1

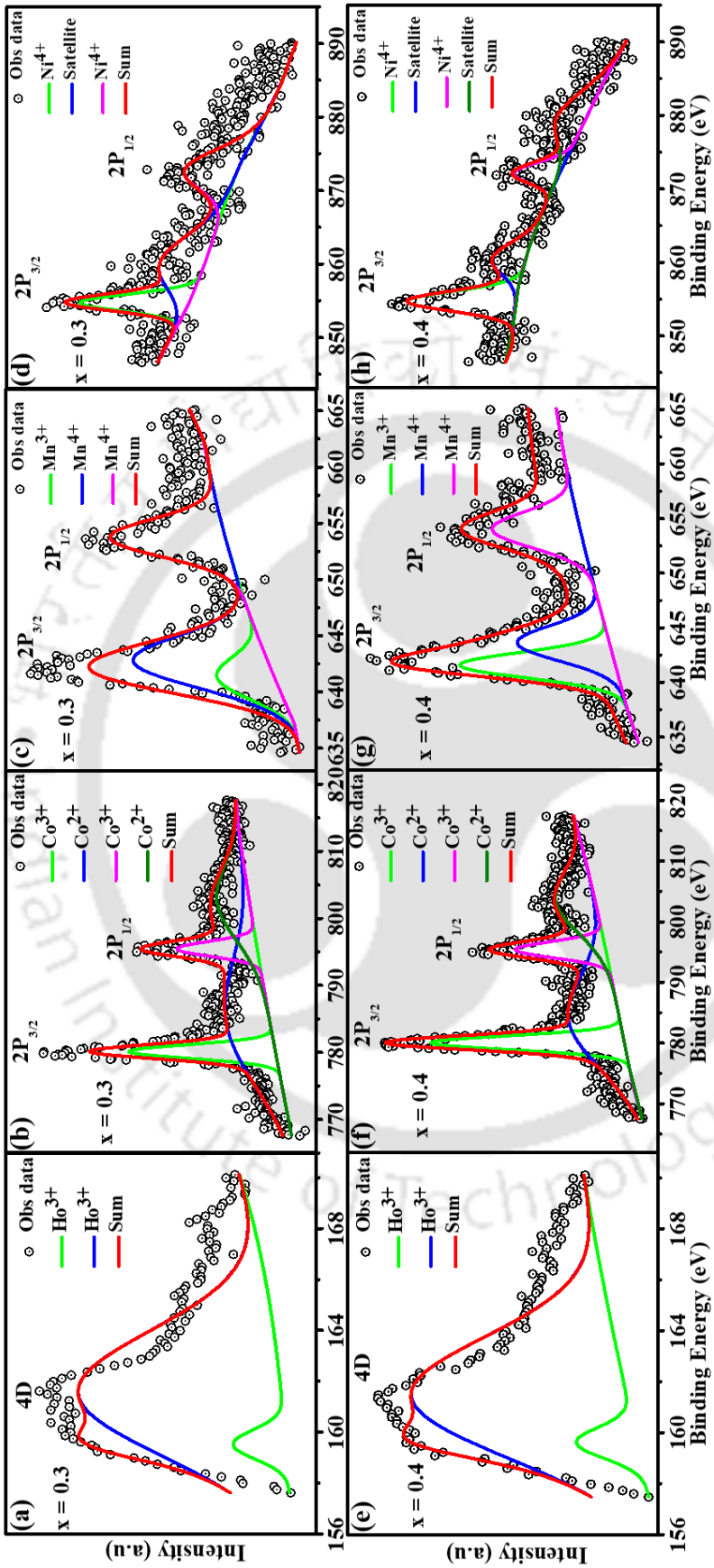

Fig.4.8. X-ray photoelectron spectroscopy for (a-d) x = 0.3 and (e-h) x = 0.4 for Ho, Co, Mn and Ni elements respectively.

In order to identify the oxidation states of each elements we have carried out the RT XPS measurements for x = 0.3 and 0.4 and fitted the data with Gaussian model are shown in Figure.4.8 (a-h). The oxidation states of Co, Mn and Ni were studied by using their $2P_{3/2}$ and $2P_{1/2}$ peaks. However, the oxidation states of Ho are analyzed using deconvoluted 4D peaks. From the graph we have observed, for x = 0.3, Ho consists of peaks at 159.51 eV and 161.51 eV indicating the presence of 3+ state [260,261]. The 2P core-level spectrum, of Co consists of four peaks at 780.13 eV, 784.26 eV, 795.43 eV and 802.26 eV. However, Mn shows three peaks at 641.21 eV, 642.65 eV and 653.68 eV. The peak positions of both Co and Mn reveal that, Co is in the oxidation state of 2+/3+ and Mn is present in 3+/4+ states respectively [261-266]. Figure.4.8 (d) shows the XPS of Ni $2P_{3/2}$ and $2P_{1/2}$ and it consists of peaks at 856.77 eV, 860.22 eV and 872.86 eV. Out of these three peaks the peak at 860.22 eV can be assigned to satellite peak and the rest two are assigned to 4+ state [277]. Similarly, for x = 0.4, the peaks are observed for Ho at 159.59 eV and 161.35 eV, for Co at 780.03 eV, 783.52 eV, 795.36 eV and 803.13 eV, for Mn at 641.57 eV, 643.57 eV and 653.96 eV and for Ni at 856.72 eV, 860.52 eV, 872.18 eV and 879.85 eV. All these positions represent the presence of above stated oxidation states for individual elements. This illustrates the presence of mixed valence states of Mn and Co, whereas, Ho and Ni are present in 3+ and 4+ states respectively.

4.1.2 Magnetic properties

Figure.4.9 (a-d) shows the MT plots at an applied field of 100 Oe, under both ZFC and FC conditions. The ZFC curve for x = 0.0 sample exhibits a rapid rise in magnetization below 85 K, followed by a peak-like structure, and then a secondary rise in magnetization below 50 K, which is well explained in chapter - 3. Similarly, the FC curve and a large irreversibility at 5 K are also well explained in chapter - 3 for x = 0.0 sample. The ZFC plots of all Ni substituted samples show two peaks followed by secondary rise in magnetization for T<50 K. Whereas the FC magnetization curves of all Ni doped samples show a sharp rise in magnetization below 90 K followed by a steep fall in magnetization value at T < 50 K. Interestingly, this downfall in magnetization value leads to MR in the higher Ni concentration samples such as $x \geq 0.3$ as shown in Figure.4.9 (c, d). The compensation temperature (T_{comp}) increases from 4.4 K for x = 0.3 to 10 K for x = 0.4. Here the transition temperatures (T_{C1}/T_{C2}) are estimated by taking first derivative of magnetization (ZFC) with respect to temperature (dM/dT) and it is plotted as a function of temperature as shown in the lower inset of Figure.4.9 (a-d). Interestingly for x = 0.0 sample, we have observed one FM

transition at 83 K which is represented as T_{C1}. However, for all Ni substituted samples we found two FM transitions designated as T_{C1} and T_{C2}. The former transition (T_{C1}) is found to decrease from 83 K for x = 0.0 to 76 K for x = 0.4 sample, whereas the later transition (T_{C2}) is found to increase from 84 K for x = 0.1 to 88 K for x = 0.4 sample as shown in the lower inset of Figure.4.9 (a-d). The upper inset of Figure.4.9 (a-d) shows the enlarged view of ZFC curves of the respective samples in the vicinity of the transitions.

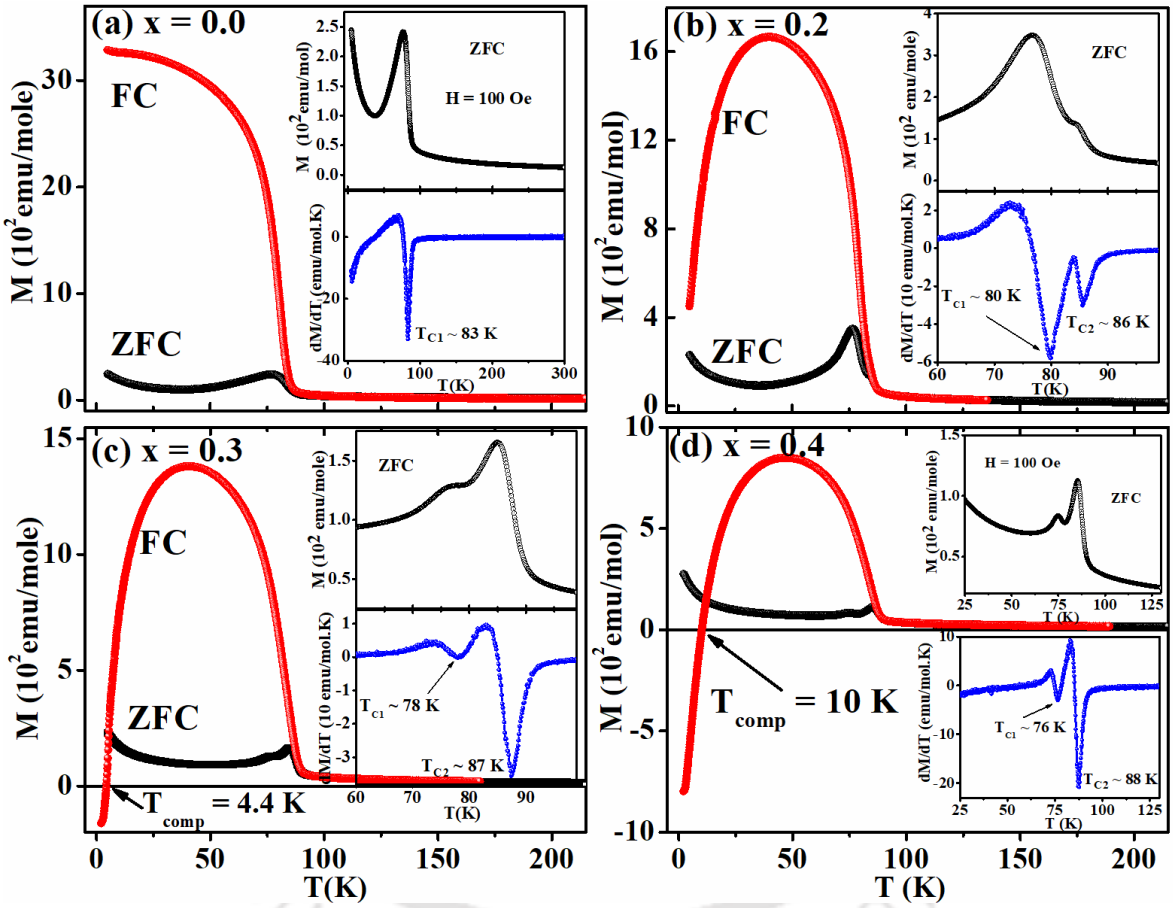

Fig.4.9. M versus T plots in both ZFC and FC conditions at an applied field of H = 100 Oe for (a) x = 0.0, (b) x = 0.2 (c), x = 0.3 and (d) x = 0.4. Insets show ZFC M - T plots in expanded scale (Upper) and dM /dT versus T plots (lower) respectively.

The transition T_{C1} arises due to the FM SE interaction in Co^{2+}-O-Mn^{4+} networks. The additional FM transition which is observed after Ni doping i.e., T_{C2} is attributed to the SE interaction across Co^{2+}-O-Ni^{4+} networks governed by the Goodenough Kanamori rule [38,39]. The variations in the values of T_{C1} and T_{C2} are tabulated in Table-4.2. The peak which is associated with the T_{C2} is getting prominent (upper inset of Figure.4.9 (a-d)) keeping the T_{C1} peak suppressed

with Ni concentration. This typical behavior represents the strengthening of the SE interaction of Co^{2+}-O-Ni^{4+} networks at the same time weakening of the SE interaction of Co^{2+}-O- Mn^{4+} networks. So, it leads to the increase in T_{C2} value with Ni concentration along with a drop in T_{C1} value.

Table. 4.2. Magnetization versus temperature analyzed data.

Sample	T_{C1} (K)	T_{C2} (K)	θ_{RE} (K)	μ_{eff}^{Exp} (TM) μ_B/f.u	μ_{eff}^{Exp} (RE) μ_B/f.u	μ_{TM}^{Th} μ_B/f.u
x = 0.0	83	--	-9	4.8	14.70	5.47
x = 0.1	82	84	-3	5.30	15.60	5.33
x = 0.2	80	86	-4	4.72	15.30	5.19
x = 0.3	78	87	-17	4.99	15.17	5.04
x = 0.4	76	88	-13	4.33	15.26	4.89

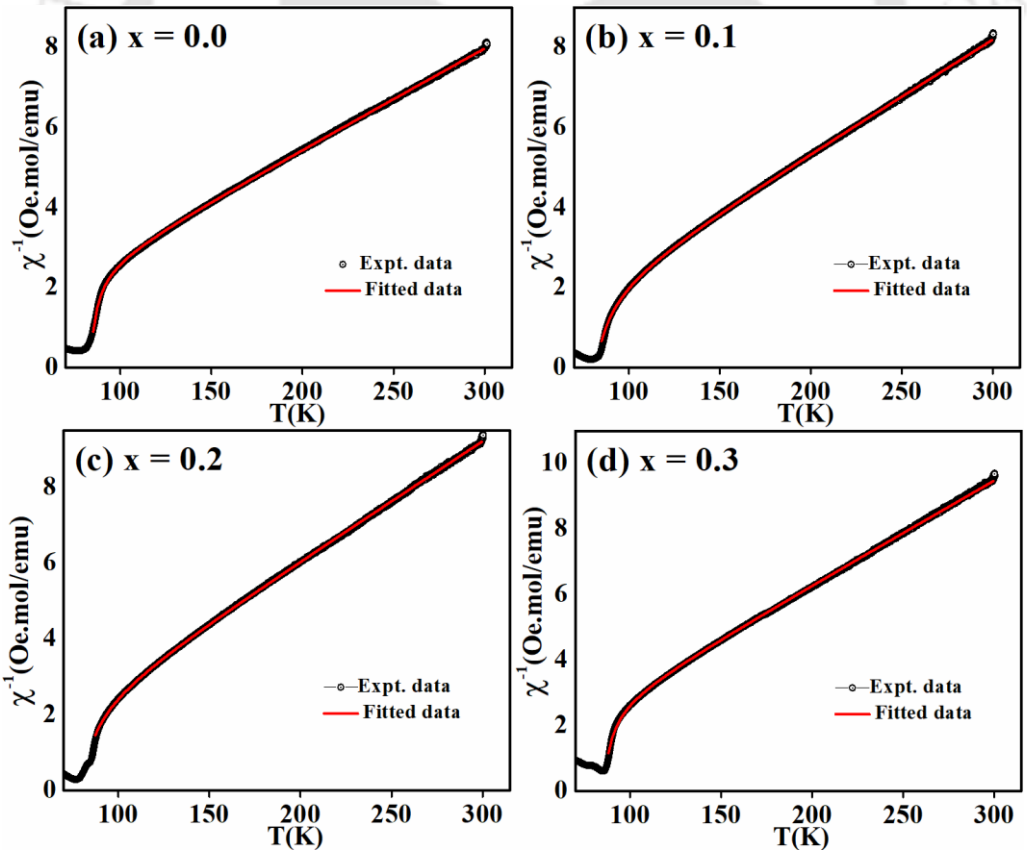

Fig.4.10. χ^{-1} versus T plots, with a modified Curie-Weiss law fitting for (a) x = 0.0, (b) x = 0.1, (c) x = 0.2 and (d) x = 0.3 respectively.

The inverse susceptibility versus temperature (χ^{-1} -T) has been studied in the PM region. Here we have used a modified CWL as explained in Eqn. 1.7, to fit and analyze the observed data. The result of fitted data are shown in Figure.4.10 (a-d) for x = 0.0-0.4. The θ_{TM} value is quite close to the measured FM T_C. So, we have fixed the θ_{TM} as observed T_C value for all the samples and proceeded for the fitting, which was also done by Chakraborty et. al. [143]. However, the small negative value indicates low temperature AFM interaction between the RE ions [71]. The formula used to estimate the experimental effective PM moment (μ_{eff}^{Exp}) is, $\mu_{eff}^{Exp} = \sqrt{3k_B C/N_A}$, where k_B, N_A and C represent Boltzmann constant, Avogadro number and Curie constant (C_{TM}/C_{RE}) respectively. While the theoretical effective moments of RE (μ_{RE}^{Th}) and TM (μ_{TM}^{Th}) ions are calculated by using the formula, $\mu_{RE}^{Th} = \sqrt{2 \times \mu_{Ho}^2}$ and $\mu_{TM}^{Th} = \sqrt{\mu_{Co}^2 + ((1-x)\mu_{Mn}^2 + x\mu_{Ni}^2)}$. Here the ground state effective magnetic moments of the respective ions are presented by μ (with the suffix of respective chemical symbol). The value of μ_{RE}^{Th} is found to be 14.99 μ_B/ f.u., while the μ_{TM}^{Th} values for the respective samples and μ_{eff}^{Exp} (TM and RE) values are tabulated in Table- 4.2. The values of μ_{eff}^{Exp} for TM are comparable to the theoretical values of all Ni doped samples. Whereas the smaller value of μ_{eff}^{Exp} for x = 0.0 sample is attributed to the presence of Co^{3+}/Mn^{3+} ions, with Co^{3+} ions in low spin state [28,59,250,248].

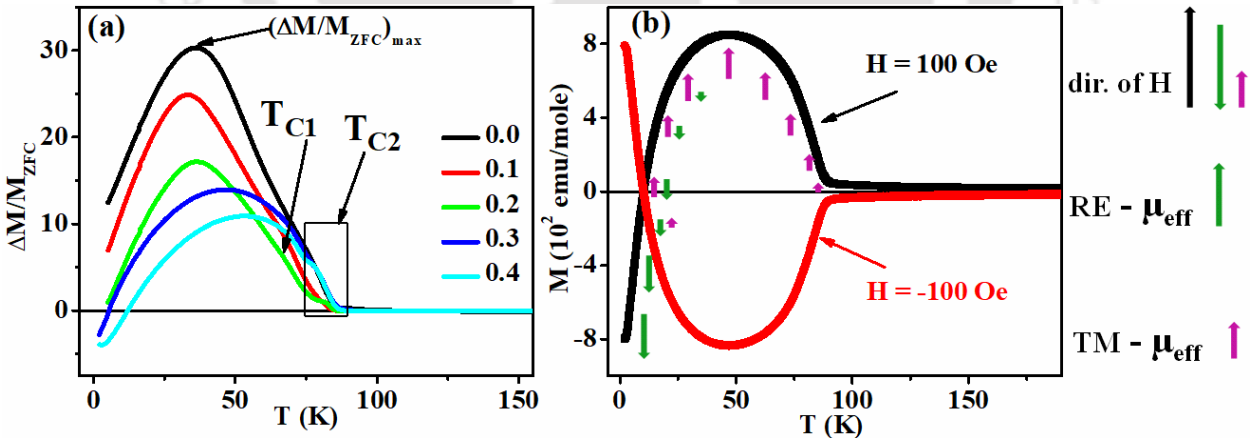

Fig.4.11. (a) $\Delta M/M_{ZFC}$ versus temperature for all the samples and (b) M versus T plots in FC condition at an applied field of H = ± 100 Oe for x = 0.4.

The magnitude of irreversible magnetization, $\Delta M/M_{ZFC} = (M_{FC} - M_{ZFC})/M_{ZFC}$ is found to decrease as doping concentration increases. One of the possible explanations is the presence of

two FM super exchange interactions and an increase in the strength of the SE interaction in Co^{2+}-O-Ni^{4+} networks. Figure.4.11 (a) depicts a typical plot of $\Delta M/M_{ZFC}$ versus T for all samples, with a clear peak in the vicinity of FM transition temperature T_{C2}. At T_{C1}, we also discovered a broad hump like structure, as shown in the Figure.4.11 (a). All samples with x = 0.0 to 0.4 displayed a similar property. However, after Ni doping, the $(\Delta M/M_{ZFC})_{max}$ shifts towards higher temperatures with increasing Ni concentration, which could be due to an increase in the T_{C2} value.

(i) Study of Magnetization Reversal

As a MR has been observed for higher Ni concentration samples (x = 0.3 and x = 0.4), to make sure that it is not due to any stray field or any instrumental artifacts, we have recorded the FC magnetization curve for x = 0.4 sample for H_{FC} = ±100 Oe as shown in Figure.4.11 (b). A mirror image is observed for the applied field in opposite directions, it confirms that the observed MR phenomena is the intrinsic property of the sample. Earlier a MR has been reported in Co/Mn based DPs in ZFC curve by several authors [71,248,287]. However, a similar kind of MR in the FC curve is observed by Banerjee et.al. in Er_2CoMnO_6 [65] and Aswathi et. al. in Sm_2CrMnO_6 [278]. This MR in FC curve is well explained by Banerjee et.al. considering the negative exchange interaction between the RE and TM sublattices located at two different crystalographic sites in the unit cell [65]. The obtained MR in the present case can be attributed to the negative exchange interaction between RE and TM ions spins. So, basically the Ho moment is antiparrell to the overall ferromagnetically ordered Co/Mn moment. Here, the 3d orbital configuration of the TM ions are Co^{2+} ($3d^7$:- $t_{2g}^3 \uparrow t_{2g}^2 \downarrow e_g^2 \uparrow$), Mn^{+4} ($3d^3$:- $t_{2g}^3 \uparrow e_g^0$) and Ni^{+4} ($3d^6$:- $t_{2g}^6 \uparrow\downarrow e_g^0$), where Co and Mn are at high spin state and Ni is at low spin state. The effective ground state PM moments of the ions are 10.60 μ_B for Ho^{3+}, 3.87 μ_B for both Co^{2+} and Mn^{4+} and 0 μ_B for Ni^{4+}. So, when we are doping Ni at Mn site, the overall FM moment is further decreasing leading to the domination of Ho sublattice moment. However, one cannot rule out the movement of few Ni^{2+} ions towards the Co^{2+} site in the octahedral environment, which can also lead to a drop in the overall moment of TM sublattices. It is already known that the moment of RE orders at low temperature (generally below 30 K). So, on field cooling the sample through T_C, the moments of TM ions (M_{TM}) align along the field direction keeping moment of RE (M_{Ho}) sublattices in PM state (Figure.4.11 (b)). On further lowering the temperature and due to the presence of negative or antiparallel exchange interaction between Ho^{3+} ion and $Co^{2+}/Mn^{4+}/Ni^{4+}$ ions, the Ho^{3+} sublattice orients opposite to the applied field direction. As a result, the value of M_{Ho} becomes equivalent to the combined moment of TM

sublattices (M_{TM}). The mutual cancelation of the magnetic moment takes place due to the antiparallel alignment of M_{Ho} with M_{TM}. The temperature at which the net magnetization is zero is known as compensation temperature (T_{comp}). On further decreasing the temperature, magnetization turns out to be negative due to the dominant nature of the M_{Ho} over the M_{TM} for x = 0.3 and x = 0.4 samples.

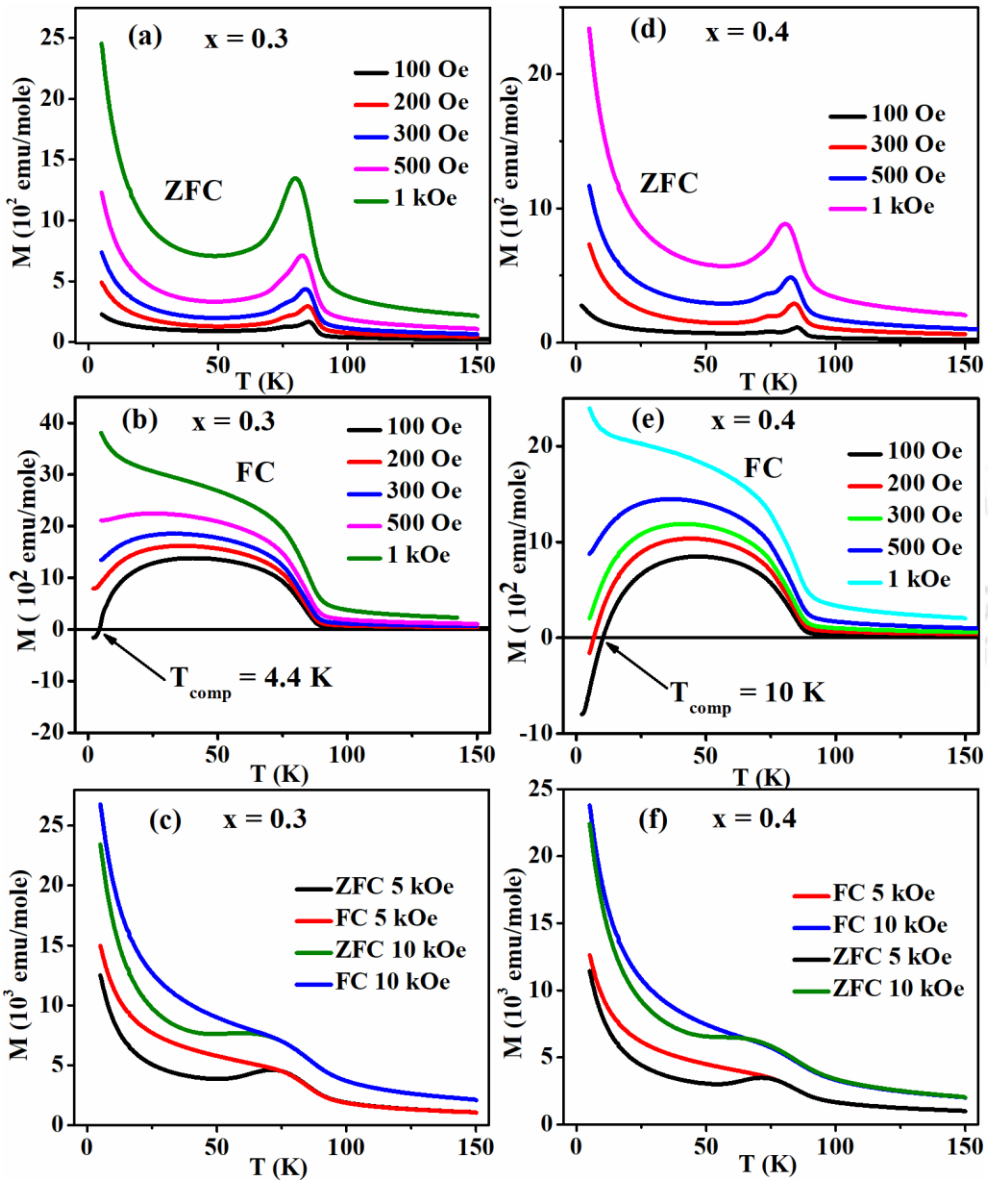

Fig.4.12. Field variation of M-T plots in both (a,d) ZFC and (b,e) FC conditions, and (c,f) M-T plots at H ≥ 5 kOe for x = 0.3 and 0.4 samples respectively.

In order to understand and investigate the field variation of magnetization, we have carried out the MT measurements under both ZFC and FC conditions for H = 100 Oe to 10 kOe for x =

0.3 and x = 0.4 samples as shown in Figure.4.12 (a - f). The M-T plots in ZFC condition for x = 0.3 are shown in Figure.4.12 (a), where one can see the broadening of the peak at T_{C1} and T_{C2}, along with the secondary rise in magnetization when the field increases. Similar type of behavior in ZFC mode is noticed for x = 0.4 sample (Figure.4.12 (d)). This type of variation in the peak structure of ZFC M-T curves with increase in field is also reported by Ivanov et.al. [269] and it is attributed to the temperature dependent coercivity (H_C) of the samples. When the magnitude of applied field is smaller than H_C at low temperature such as at 5 K and by raising the temperature, the observed magnetization will stay extremely weak till approaching T_C. The temperature dependence of H_C just below T_C causes a abrupt rise in ZFC curve to produce a peak like shape. At a field higher than the H_C, the peaks get dissappeared and left with a step like structure. The MT graphs carried out at various applied fields illustrate the widening of the peak and moving towards low temperature. It can be ascribed to forced magnetization and the suppression of AFM interaction across ASD owing to excessive applied field. The magnetization below 50 K is getting much prominent with rise in field and it is due to forced magnetic polarization of RE ions. The FC MT plots for x = 0.3 and 0.4 as shown in Figure.4.12 (b,e) are completely different from the ZFC curve as discussed above. Here we found a remarkable change in the low temperature magnetization data with rise in field value. At low fields, magnetization at low temperature drops to negative values, while with increasing field, T_{comp} shifts towards low temperature. Then for a particular field i.e., H ≥ 200 Oe for x = 0.3 (Figure.4.12 (b)) and at H ≥ 300 Oe for x = 0.4 (Figure.4.12 (e)) sample, MR disappears and magnetization is positive in all temperature range. As discussed above, the MR value at low temperature is associated with the opposite orientation of the Ho sublattice moment with respect to the applied field. On further increasing the field, the Ho moment will tend to get aligned along the field as well as along the FM moments of TM ions against the anisotropic field. It leads to a resultant positive magnetization for higher applied fields. With increasing applied field, the secondary rise in magnetization below 30 K is observed to be fairly dominant. This is due to the polarization of the Ho moment along the highly polarized FM field. For, further rise in field value (H ≥ 1 kOe) the peak broadening has been observed. Meanwhile, in the ZFC plots (Figure.4.12 (c,f)), T_{C1} is getting merged with T_{C2} at higher fields i.e., for H ≥ 5 kOe. However, FC curves for H ≥ 5 kOe show a step like behavior without a clear peak. It is owing to the large applied field's forced magnetization and the suppression of AFM interaction across ASD.

After looking at the FC MT plots for different cooling fields, and the suppresion of MR beyond certain field, we are encouraged to study the magnetic field induced MR phenomenon at a given temperature below T_{comp}. That is the switching of magnetization value between positive and negative values and vice versa with the change in magnitude of applied magnetic field without changing its direction. Here we have carried out this measurement for x = 0.3 at 2 K and 0.4 sample at 5 K as shown in Figure.4.13 (a) and Figure.4.14 (a). In order to achieve the switching behavior, the sample is first FC to a temperature below T_{comp} (it is 2 K for x = 0.3 and 5 K for x = 0.4) at an applied field of 100 Oe and the magnetization was recorded for 100 sec, and it is found to be negative as shown in Figure.4.13 (a) and Figure.4.14 (a). As the MR vanishes for H >100 Oe (for x = 0.3) and 300 Oe (for x = 0.4), so the field was increased to 120 and 350 Oe for the respective samples to switch the magnetization to a positive value and the magnetization was again recorded for 100 sec. The process was repeated for several times by varing the field from + 100 to +120 and back to +100 Oe (for x = 0.3) and + 100 to +350 and back to +100 Oe (for x = 0.4) and the bipolar switching of magnetization is consistent. This result indicates reproducible field induced bipolar switching of the magnetization.

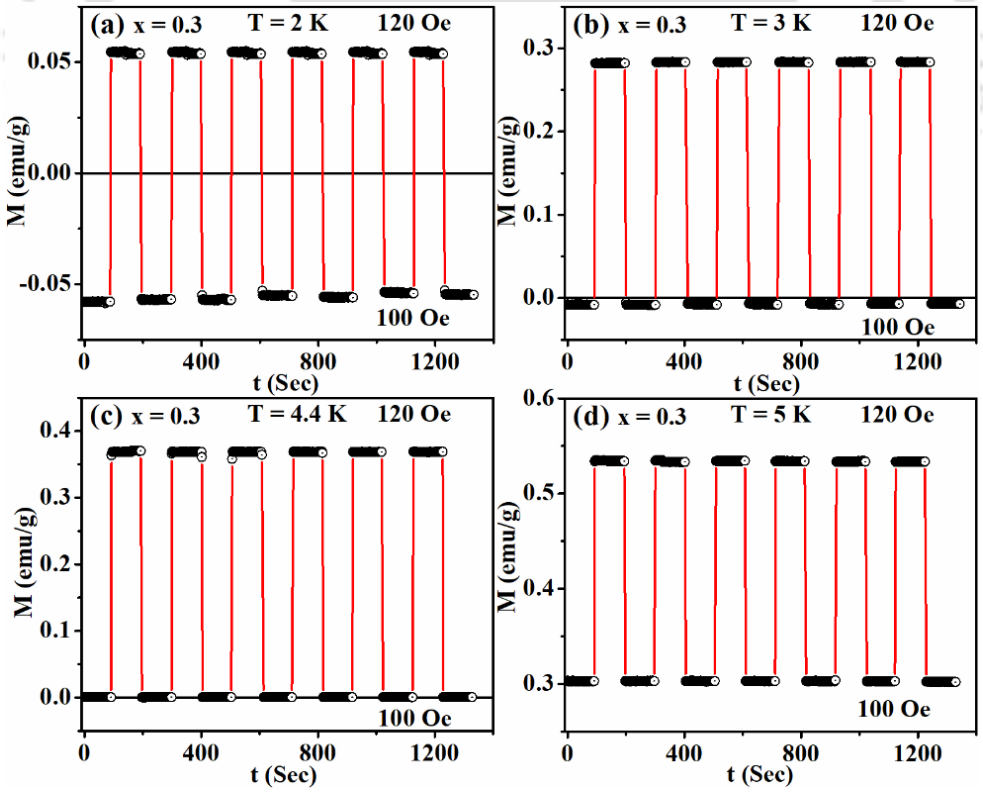

Fig.4.13. Bipolar switching of magnetization for x = 0.3 sample in between 100 to 120 Oe, at (a) 2 K, (b) 3 K, (c) 4.4 K and (d) 5 K.

In order to further study the magnetic switching behavior below, above and at T_{comp}, we have carried out the M-t measurements for x = 0.3 and 0.4 at various temperatures and the data are shown in Figure.4.13 (b-d) and Figure.4.14 (b-d)). For both x = 0.3 and x = 0.4, we have observed a typical switching behavior below the T_{comp}. However, at T_{comp} the magnetization is almost zero at 100 Oe and positive for 120 Oe (x = 0.3) and 350 Oe (x = 0.4), which is consistent with the MT data. Then above T_{comp} the magnetization is completely positive for both low and high field. It justifies the presence of magnetization switching behavior in the present series for x = 0.3 and 0.4 samples respectively.

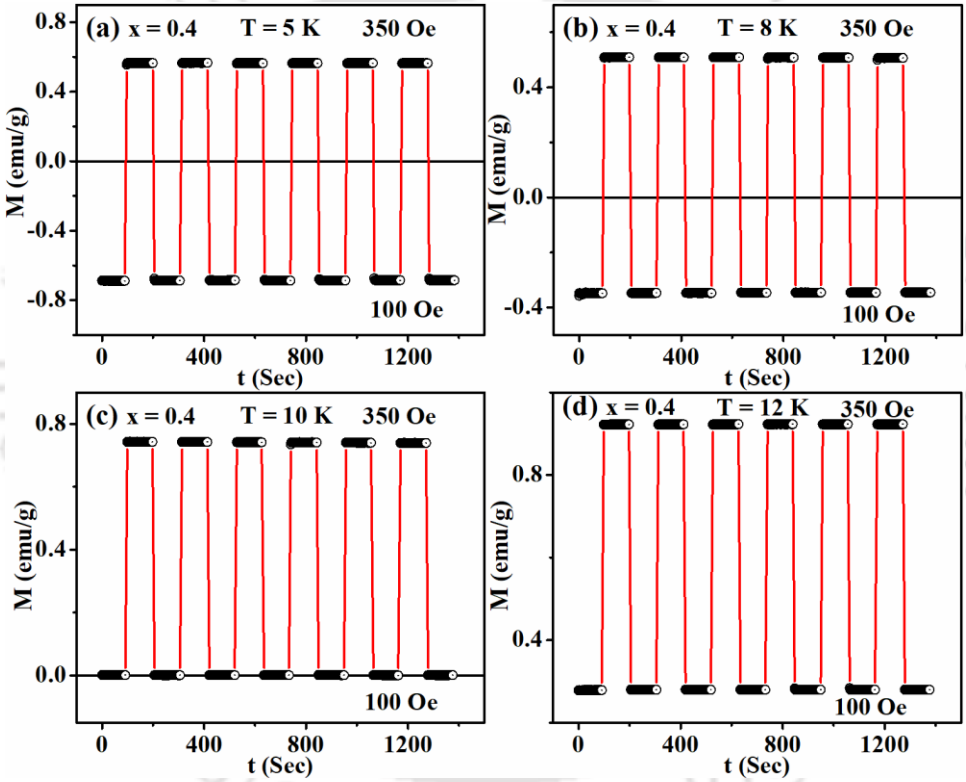

Fig.4.14. Bipolar switching of magnetization for x = 0.4 sample in between 100 to 120 Oe, at (a) 5 K, (b) 8 K, (c) 10 K and (d) 12 K.

(ii) Study of M-H Loops

We have recorded the magnetic hysteresis (MH) loops of all the samples at 5 K at an applied field up to ± 9 T as shown in Figure.4.15 (a). They all exhibit a typical FM behavior however even at 9 T field, the loops are not getting saturated and it is attributed to the uncompensated spin structure at low temperature. In order to estimate M_S value, we have analyzed

the initial curves based on LAS model [267] as expressed in Eqn. 3.5, The observed initial magnetization data fitted to Eqn.3.5 are shown in Figure.4.15 (b). The obtained values are tabulated in the Table-4.3, here the H_C, M_S, Mr and K_1 values are decreasing with Ni substitution. In these samples, the two FM transitions are attributed to arise from interactions in Co^{2+}-O^{2-}-Mn^{4+} and Co^{2+}-O^{2-}-Ni^{4+} networks. For such case, the maximum moment of TM sublattices should not be more than 6 μ_B/f.u. for x = 0.0 sample (Co^{2+} = Mn^{4+} = 3 μ_B/ion and Ni^{4+} = 0 μ_B/ion). However, by looking at the values of M_S, which are higher than the FM ordered Co/Mn/Ni sublattices, the partial contribution of RE moment to the overall FM moment is confirmed. The drop in M_S value with Ni substitution can be understood by the replacement of Mn^{4+} ions having larger magnetic moment ions with Ni^{4+} ions.

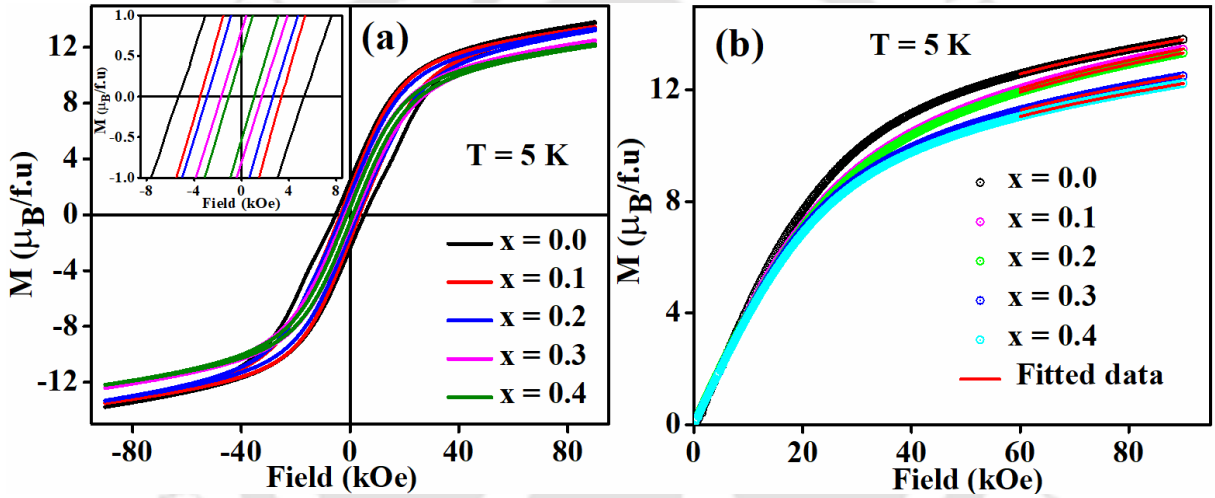

Fig.4.15. (a) MH loops recorded at 5K, inset shows the expanded view of loops near coercive field and (b) initial MH loop along with fitted data to Eqn. (3.5) for HCMNO series.

Table. 4.3. Estimated data from the hysteresis loops (ZFC and FC).

Sample	x = 0.0	x = 0.1	x = 0.2	x = 0.3	x = 0.4
H_C (Oe)	5328	3477	2910	1737	1110
M_r (μ_B/f.u)	2.00	1.80	1.45	0.80	0.53
M_S (μ_B/f.u)	11.60	11.26	11.08	10.40	10.27
K_1 (10^4erg/cm^3)	1.90	1.79	1.78	1.35	1.32
H_{EB} (Oe)	-114	30	131	225	230

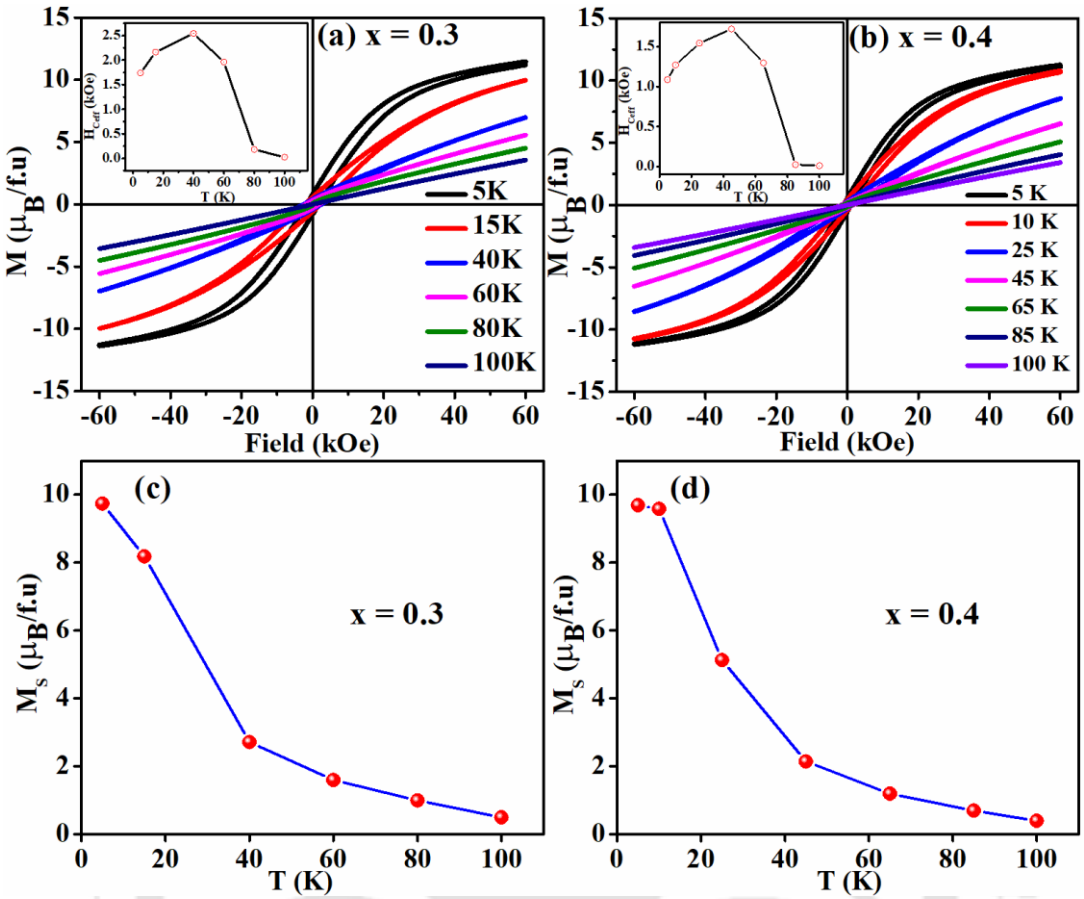

Fig.4.16. (a,b) M-H loops measured in the temperature range of 5 - 100 K and (c,d) saturation magnetization versus temperature for x = 0.3 and 0.4 samples.

Again, to see the temperature dependence of magnetization for x = 0.3 and x = 0.4 samples we have recorded several MH loops in the temperature range of 5 to 100 K, as shown in Figure.4.16 (a,b). We found that the M_S value is decreasing with increase in temperature, however, H_C value is initially increasing with a maximum value at 40 K for x = 0.3 and at 45K for x = 0.4 then again decreasing with further rise in temperature as shown in inset of Figure.4.16 (a,b). This behavior suggests a maximum anisotropy/uncompensated spins at 40 K and/or 45 K among the sublattices. By looking at the shape of H_C versus T plot one can say that it reflects the FC MT plot. As we have explained earlier that the shape of the peak in ZFC curve is due to the temperature dependent coercivity of the samples. By observing Figure.4.16 (a,b) we can also say that the FC MT may also represent the temperature dependent coercivity of these samples.The variation of Ms value with temperature for x = 0.3 and x = 0.4 are shown in Figure.4.16 (c,d). The M_S value varies from 9.74 to 0.49 μ_B/f.u. for x = 0.3 for a temperature span of 5 to 100 K, while it varies from 9.69 to 0.39

μ_B/f.u. for x = 0.4 sample. In these samples, the maximum moment of TM sublattices should not be more than 5.1 μ_B/f.u. for x= 0.3 and 4.2 μ_B/f.u. for x = 0.4 sample. However, the obtained higher value of M_S is only up to a temperature of 25 K and it signifies that the contribution of RE ions is appreciable only up to 25 K. smaller moment < 6 μ_B/f.u. for T > 30 K can be attributed to the presence of Co^{3+} and Mn^{3+} ions and their AFM interaction.

(iii) Study of Exchange Bias Behavior

As the negative exchange interaction between RE and TM sublattices in HCMO gives rise to MR. So, in order to understand the EB behavior in HCMNO series we have recorded MH loops at 5 K under a FC condition with a cooling field of H_{FC} = 0.5 T and by varying the measuring field up to ± 6 T as shown in Figure.4.17 (a-d). Here we have observed a clear shift of MH loops indicating EB behavior.

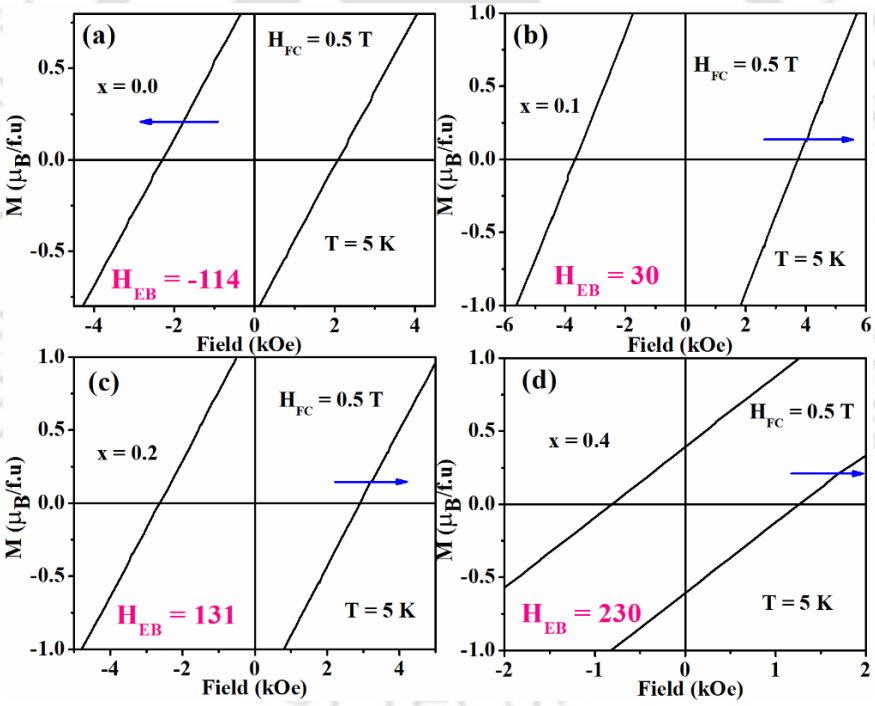

Fig.4.17. Enlarged view of FC M-H loops at 5 K for (a) x = 0.0, (b) 0.1, (c) 0.2 and (d) 0.4 respectively.

However, to rule out the stray field effect/instrumental artefacts, we have carried out the MH loop for both H_{FC} = ± 0.5 T for x = 0.4 sample at T = 5 K as shown in Figure.4.18 (a, b). From the figure we can see a clear shift of the loop in the opposite direction as the cooling field is reversed. The enlarged view of MH loops in the vicinity of coercivity is shown in Figure.4.17 (a-d) and it clearly shows EB behavior in HCMNO series. Unlike the parent compound, Ni substituted

samples show loop shifting along positive field direction and this shifting is increasing with Ni concentration. The maximum value of H_{EB} = 230 Oe is obtained for x = 0.4 sample at 5 K.

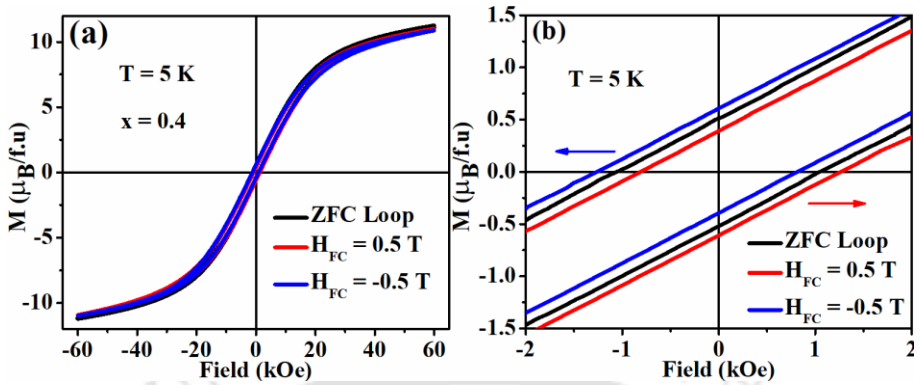

Fig.4.18. (a) M-H loops of x = 0.3 sample under ZFC and FC (H_{FC} = ± 0.5 T) and (b) its enlarged view in the vicinity of coercivity (H_C).

The obtained values of H_{EB} are tabulated in Table-4.3. Here the EB is attributed to the competition between spin canted magnetic moment of RE ions and FM moment of TM ions. For x = 0.0, the loop was shifting towards negative field direction. However, after Ni substitution the loop was shifting towards positive field direction. Here we have tried to explain this phenomenon by using the schematic diagram of spin configuration for x = 0.0 and Ni substituted samples as presented in the Figure.4.19.

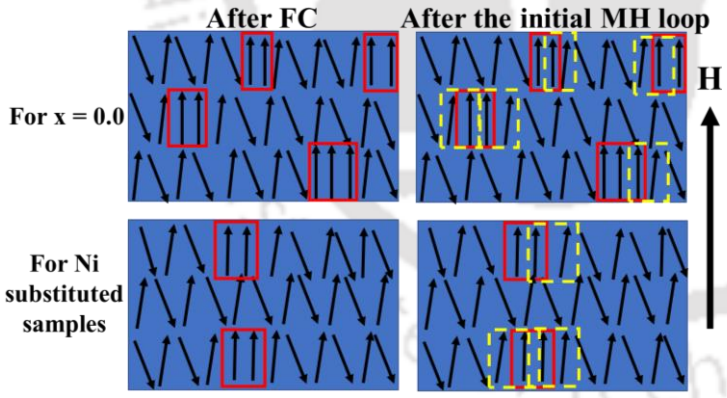

Fig.4.19. Schematic diagram of spin configurations before and after field cooled the sample for parent and Ni substituted samples.

Below the FM T_C, few FM clusters are present along with the canted spin components even at H = 0 Oe (after FC). During the FC process the FM spins are strongly coupled with canted spins and form two integrated anti-parallel spin systems. The field ramping then creates more such clusters during the first loop of FC MH, increasing the number of FM and/or canted spin interfaces. Hence, during the descending field, the FM spins impose a microscopic torque on the canted spins, while they were trying to keep the spins aligned along the measuring field direction. As a result,

larger negative field is required to align the canted spins along the field direction. The loop is shifted towards the negative field direction throughout this operation, resulting in a negative exchange bias in the x = 0.0 sample. In the meanwhile, when we consider the Ni substituted samples, here the FM moment is decreased due to the replacement of Mn^{4+} with Ni^{4+}. As the FM components are small here, so, during the descending branch of MH loop the FM spins easily flip its spin along the direction of field without imposing torque on the canted components. However, during the ascending branch of MH loop, it required more amount of positive field to further align the FM and canted spins along the direction of applied field. So, it results into shifting of the loop towards right side. The increment of H_{EB} value with Ni concentration is attributed to the strengthening of canted magnetic components of RE ions.

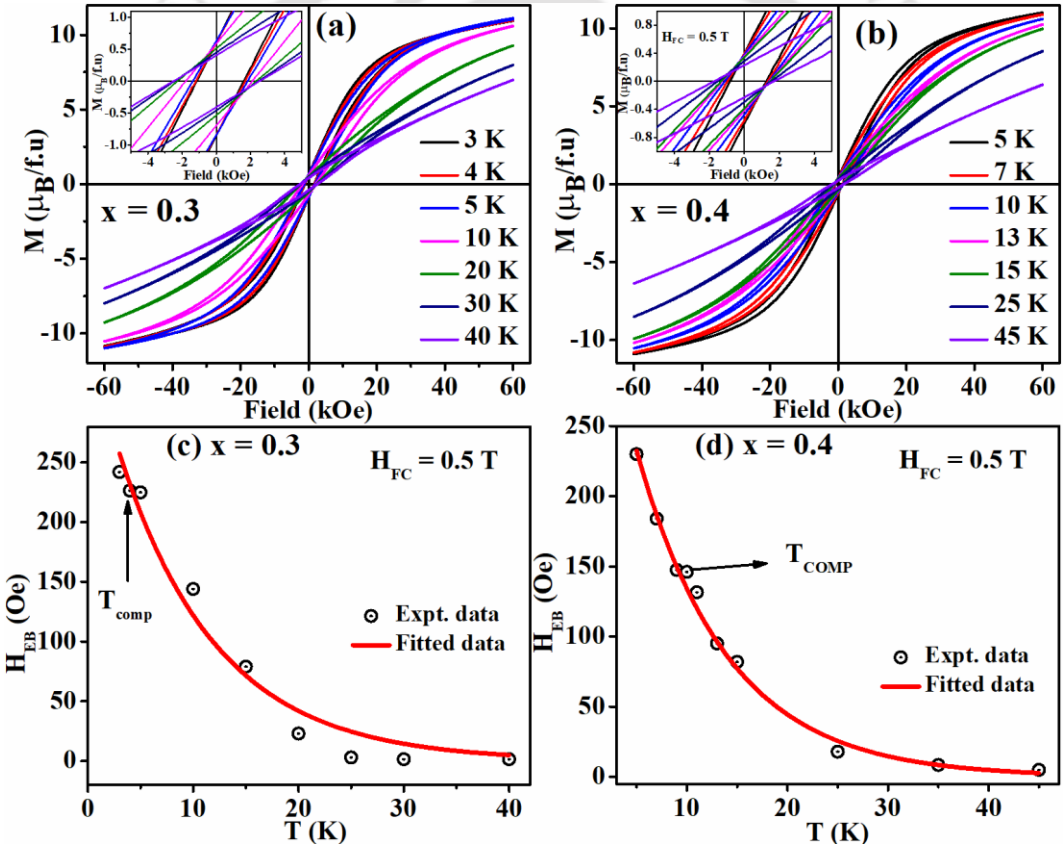

Fig.4.20. (a, b) Temperature variation of FC M-H loops with H_{FC} = 0.5 T for x = 0.3 and 0.4 samples with inset showing the enlarged view of the loops near coercive field, and (c, d) H_{EB} versus temperature along with the fitted data to Eqn. 3.7.

Many systems showing MR are reported to exhibit sign reversal in EB near T_{comp} [65,203,240]. So, it encouraged us to carry out the temperature variation of EB for x = 0.3 and x = 0.4 samples. Here we have measured the FC MH loops in the temperature range of 3 to 40 K for

x = 0.3 and 5 to 45 K for x = 0.4 which are shown in Figure.4.20 (a, b). Insets of Figure.4.20 (a, b) show enlarged view of the curves near coercivity. The values of H_{EB} are plotted with respect to temperature as shown in Figure.4.20 (c, d). Here, we have not observed any sign reversal in EB in the vicinity of T_{comp} as the H_{EB} value decreases with temperature. As the EB in this compound is caused by the competition between RE and TM sublattice moment. The decrement in the value of H_{EB} with temperature can be explained as follows: As the RE contribution is minimal above a certain temperature (20 K), the FM component of TM ions do not encounter any competing anisotropic magnetic moment. Thus, at T > 20 K, the exchange interaction weakens, resulting in a decrease in H_{EB}. However, the obtained H_{EB} versus T follows the exponential function as explained in Eqn. (3.7) and are shown as solid lines in Figure.4.20 (c,d). The H_{EB} (0) values are found to be 355 ± 25 Oe and 403 ± 11 Oe for x = 0.3 and 0.4 respectively and the T_1 values are close to 9 K.

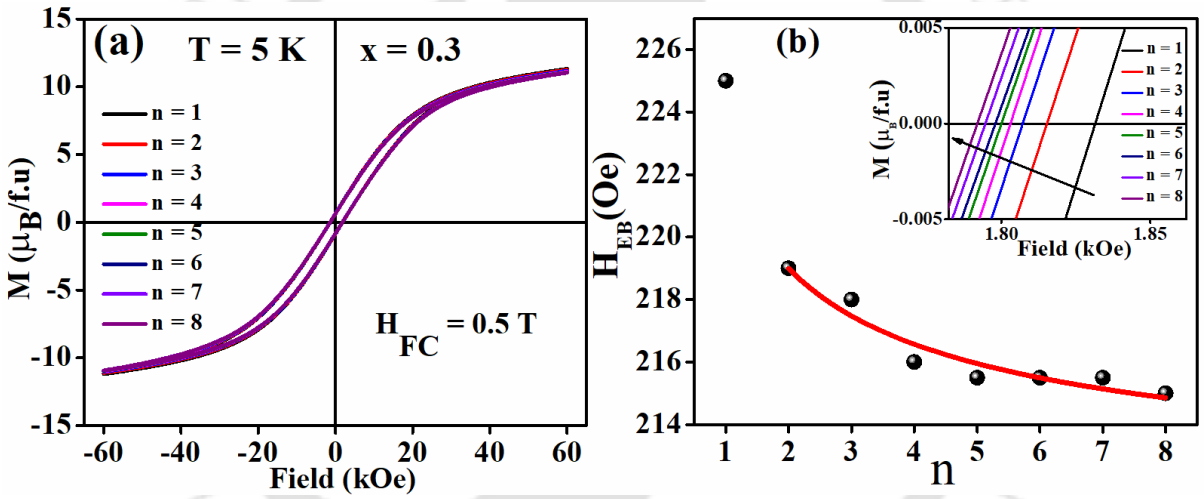

Fig.4.21. (a) Consecutive 8 M-H loops recorded at T = 5 K for x = 0.3 and (b) H_{EB} versus n along with fitted data to Eq. (4.1), inset shows the loops in expanded scale.

The training effect, is one of the conclusive tests for EB, where H_{EB} decreases with the number of successively measured loops [212]. In order to investigate this, we have measured 8 consecutive FC MH loops at 5 K with H_{FC} = 0.5 T for x = 0.3 (Figure.4.21 (a)). The loop shifting is shown in the inset of Figure.4.21 (b), however, the loop number (n) dependency of H_{EB} is shown in Figure.4.21 (b). It is found that the H_{EB} versus n (for n > 1) follows a power-law [209],

$$H_{EB}(n) - H_{EB}(\infty) \propto 1/\sqrt{n} \qquad (4.1)$$

Here $H_{EB}(\infty)$ is the EB field for n→∞. The fitted data to Eqn. 4.1 is represented by solid red line in Figure.4.21 (b). The obtained experimental value of $H_{EB}(\infty)$ is found to be 210 ± 0.7 Oe.

4.2. Nanocrystalline samples of DP $Ho_2CoMn_{1-x}Cr_xO_6$ (x = 0.0 - 0.5)

From the literature review it has been found that, the replacement of Mn by Cr will give rise to multiple oxidation states for Mn. So, to explore additional magnetic properties, we have used auto combustion method to prepare nanocrystalline $Ho_2CoMn_{1-x}Cr_xO_6$ (x = 0-0.5) DP as describe in section 2.1 (Chapter - 2). Here, we explored the effect of the above substitution on the structural and magnetic properties of Ho_2CoMnO_6 compound. After Cr substitution, an additional AFM phase, a MR with T_{comp} = 7 K, BSM below T_{comp} and sign change in EB field are some of the characteristic features of the present discussion.

4.2.1 Structural properties

XRD patterns of the HCMCO series taken at RT are shown in Figure.4.22. We are able to index the XRD peaks to a single phase monoclinic structure with space group $P2_1/n$. The obtained RT XRD data of x = 0.0 to 0.5 are refined by using the Rietveld refinement technique as shown in Figure.4.23 (a-f) by red solid line. One can see the observed data are well fitted to the monoclinic structure with space group $P2_1/n$ and accordingly the diffraction peaks are well indexed. The enlarged view of most intense peak of (112) and (020), (021) reflection in the range of Bragg angle 32.5 to 35 degrees are shown in Figure.4.23 (g-l). The most intense peak of (112) reflection is found to shift towards higher 2θ with an increase in Cr concentration. In addition, the peak shows a small broadening with the increase in Cr concentration. These features are the indication of a decrease in particle/crystallite size and lattice parameters. Here, it has to be noted that the broadening of x = 0.4 sample is maximum as compared to others. The merging of (200) and (021) peaks are observed for $x \leq 0.4$, however they split and are quite clearly visible for x = 0.5 sample as shown in Figure.4.23 (l). It indicates the persistence of monoclinic symmetry in samples for higher Cr concentration [50]. The angle β in the crystal structure is consistent with the monoclinic structure, keeping α and γ at 90°. Obtained chi-square (χ^2) values along with reliability factors for the HCMCO compound from the Rietveld refinement are listed in the Table-4.4 and are found to be quite small indicating a good fitting. All the structural parameters for the HCMCO series are listed in Table. 4.4. The decrease in lattice parameters along with the volume is consistent with the uniform shifting of the peaks towards higher Bragg angles. Here we have assumed that some of the Mn^{3+} ions (0.645 Å) present in the sample are replaced by the Cr^{3+} ions (0.61 Å) rather than the abundant Mn^{4+} ions (0.53 Å) present in the material. As the concentration of Mn^{3+} ions in the

parent compound is quite small, so there is no variation in the lattice parameter as well as volume in the 10 % Cr substituted sample. Then a visible variation can be seen for x ≥ 0.2 sample.

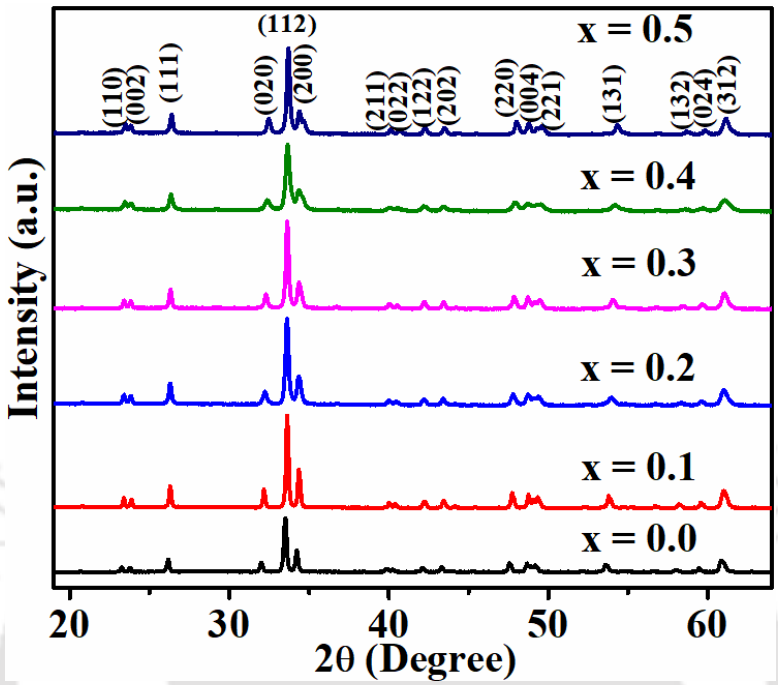

Fig.4.22. Room temperature XRD patterns for HCMCO series.

Figure. 4.24 (a-d) depicts the bond angle made by CoO_6 and MnO_6 octahedra with O_1, O_2 and O_3 along c-axis. A smooth decrease in bond angle by TM ions with O_1 has been observed up to x = 0.4 sample. However, a sharp fall has been observed for x = 0.5 sample (Figure. 4.24 (a)). Similarly, the angle with O_2 is found to be increase up to x = 0.4 but for x = 0.5 sample a decrease in the value is observed (Figure. 4.24 (b)). Furthermore, the bond angle of TM ions with O_3 are found to be unchanged up to x = 0.2, whereas for x ≥ 0.3 a rise in the bond angle value has been observed (Figure. 4.24 (c)). Whereas, the average value of bond angle of the TM ions shows a monotonous rise up to x = 0.4 and a drop in the value for x = 0.5 (Figure. 4.24 (d)).

The average crystallite size and the micro-strain parameters are calculated using the WH method [259] as shown in Figure.4.25 (a-f) and is listed in the Table. 4.4. They are well fitted to the linear equation which are represented by red solid lines. We have observed an overall decrease in the crystallite size from 35 to 29 nm for x = 0.0 to 0.5 as tabulated in Table-4.4. Which shows that, all the samples are found to be in nanocrystalline form. This decrease in crystallite size with Cr doping may lead to spin canting, which further leads to complex magnetic interactions among the spins and decrease in overall magnetic moment etc. However, we found some anomaly in the

size for x = 0.2 and 0.4. A minimum value of the crystallite size was obtained for x = 0.4 sample, which is consistent with the maximum broadening of the (112) reflection as compared to other samples. It could be due to the presence of multiple oxidation states of the ions with varying ionic radii. Similar to crystallite size, the observed micro-strain parameters are also showing the same variation. It shows a maximum value of 3.07 for x = 0.4 indicating higher surface to volume ratio for this sample.

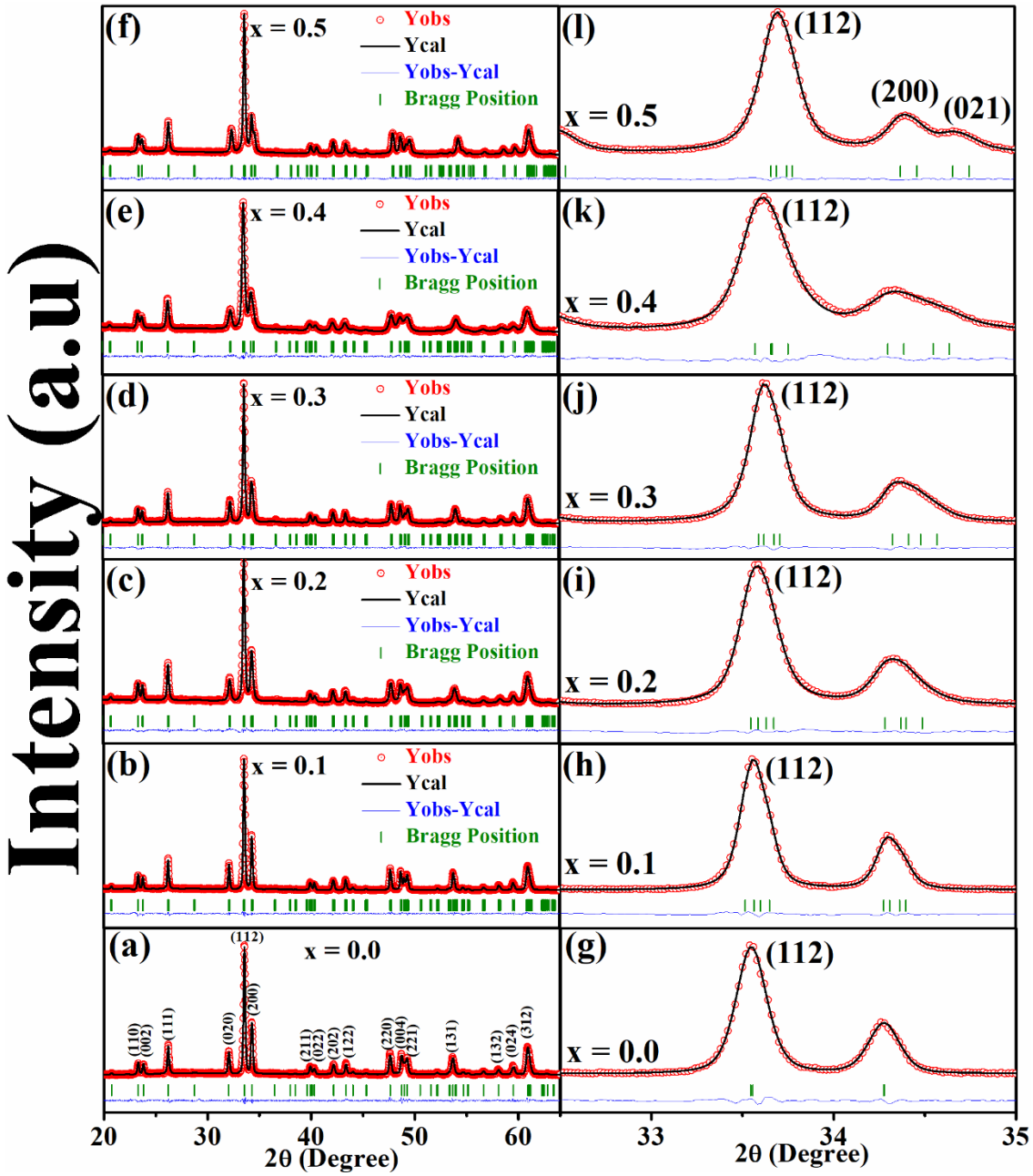

Fig.4.23. (a-f) Rietveld refinement of RT XRD patterns of HCMCO series, and (g-l) enlarged view of (112), (200), and (021) peaks for x = 0.0 to 0.5 respectively.

Table. 4.4. Extracted Refined structural parameters and reliability factors for the HCMCO compound.

Sample	x = 0.0	x = 0.1	x = 0.2	x = 0.3	x = 0.4	x = 0.5
a (Å)	5. 228	5. 228	5. 226	5. 220	5. 223	5. 213
b(Å)	5. 581	5. 574	5. 557	5. 543	5. 531	5. 513
c(Å)	7. 469	7. 477	7. 476	7. 473	7. 471	7. 467
V(Å3)	217.9	217.9	217.1	216.2	215.8	214.6
β (°)	89.93	89.88	90.09	90.07	90.21	90.06
R_{Bragg}	4.42	3.05	2.16	3.06	2.02	1.80
R_f	7.64	3.95	2.31	3.54	2.19	2.07
χ^2 (%)	1.55	1.66	1.45	1.52	1.51	1.29
Average crystallite size(nm)	35	39	28	30	17	26
Average particle size(nm)	120	179	161	94	61	78
Micro-strain (10^{-3})	2.21	2.41	2.38	2.4	3.07	1.98

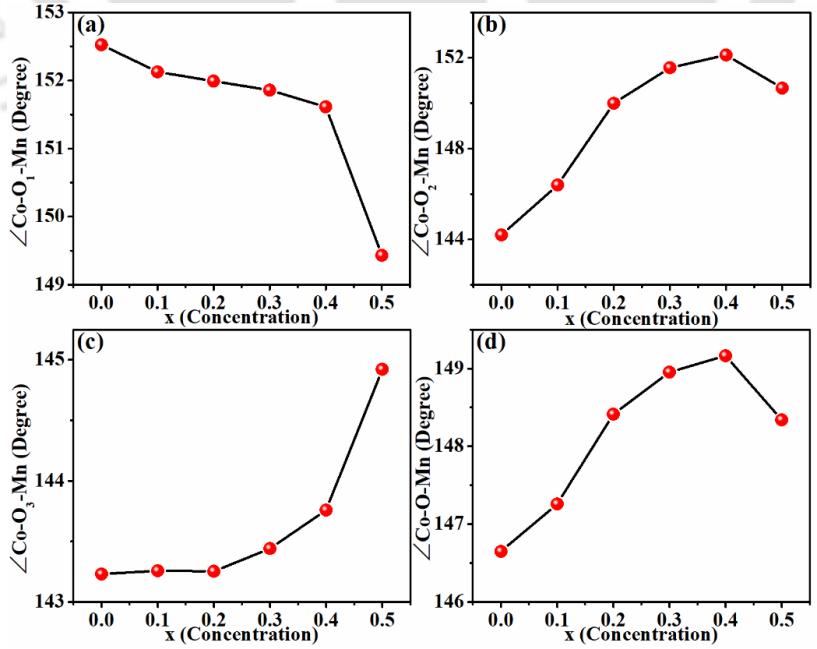

Fig.4.24. (a-d) Bond angle of TM ions with O_1,O_2,O_3 and average bond angles of HCMCO series.

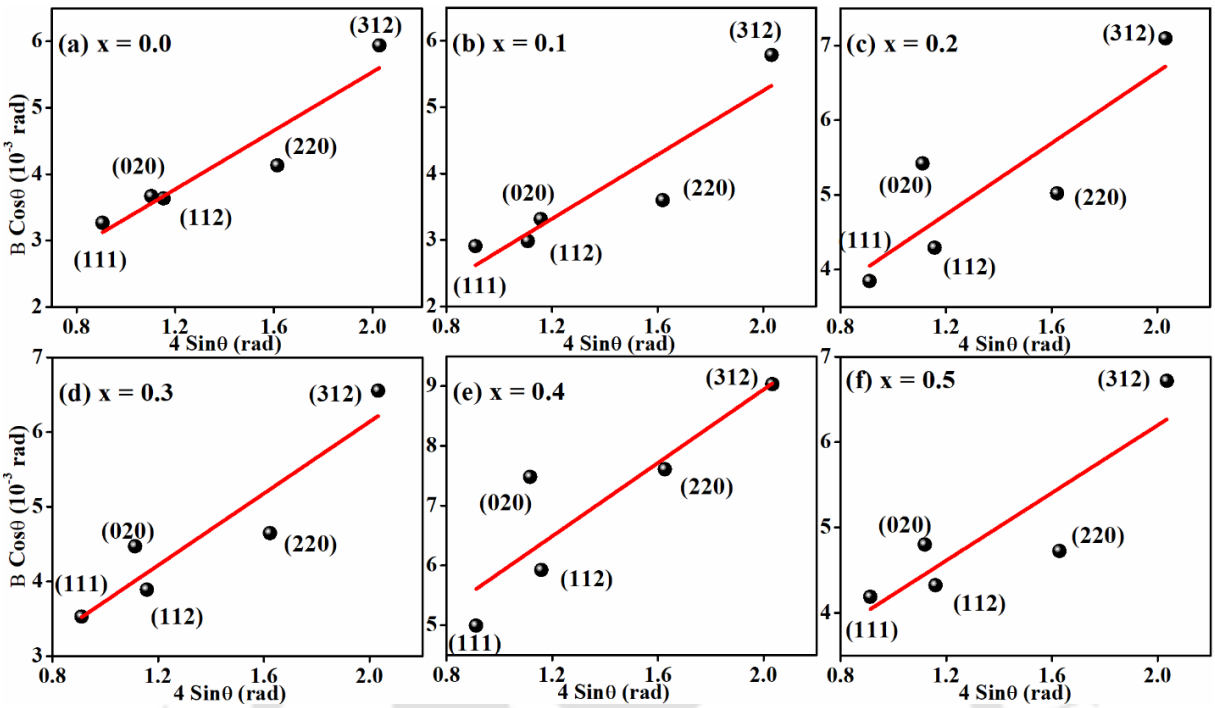

Fig.4.25. (a - f) Williamson-Hall plots of HCMNO series for x = 0.1 to 0.4 respectively.

For FESEM images we have followed a drop cast method to prepare the samples, in order to get an image of well separated particles from one another. The FESEM images for x = 0.0, 0.3, 0.4 and 0.5 with a 200 nm of scale size are shown in Figure.4.26 (a-d). It reveals a quite agglomerated particles with an overall decrease in particle size from x = 0.0 to 0.5. However, the smallest particle size is obtained for x = 0.4 sample as shown in Figure.4.26 (c) which is further consistent with the crystallite size, as explained in the previous paragraph. The average particle and crystallite size are listed in Table. 4.4. The elemental composition was determined using EDS analysis for x = 0.2, 0.3, 0.4 and 0.5 samples, and the resulting spectrum is shown in Figure.4.27 (a-d). It confirms the presence of Ho, Co, Mn, Cr, and O in desired elemental composition in the current series.

The oxidation states of Co/Mn/Cr were measured using deconvoluted $2P_{3/2}$ peaks of Co, Mn, and Cr, using XPS spectrum as shown in Figure.4.28 (a-f) for x = 0.0 and 0.4 samples. According to the results, Co is present in the compound in the 2+/3+ oxidation state, while Mn and Cr are found in the 3+/4+ oxidation state. The observed peak locations agree with previous observations [262-266]. Mostly in DPs a little amount of the formation of Co^{3+} and Mn^{3+} ions have

been reported [248], which can also be seen in our case. However, as previously stated, the replacement of Mn^{3+} by Cr^{3+} leads to a decrease in lattice parameters. By looking at the ratio of

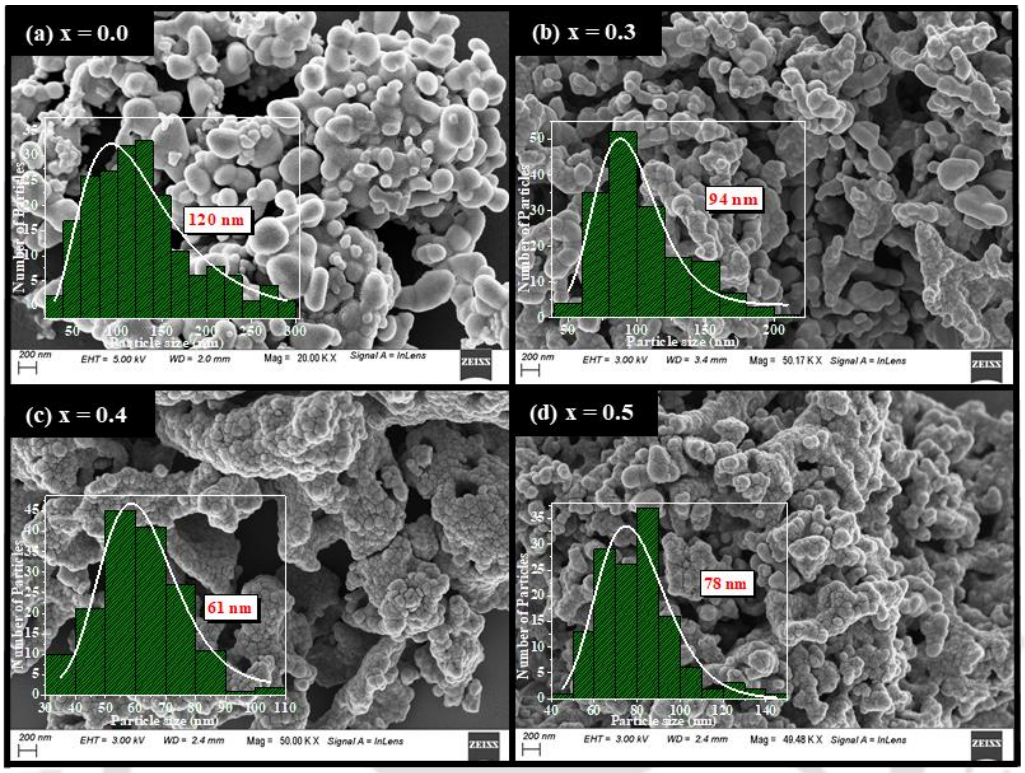

Fig.4.26. FESEM images of HCMCO series for (a) x = 0.0, (b) 0.3, (c) 0.4, and (d) 0.5.

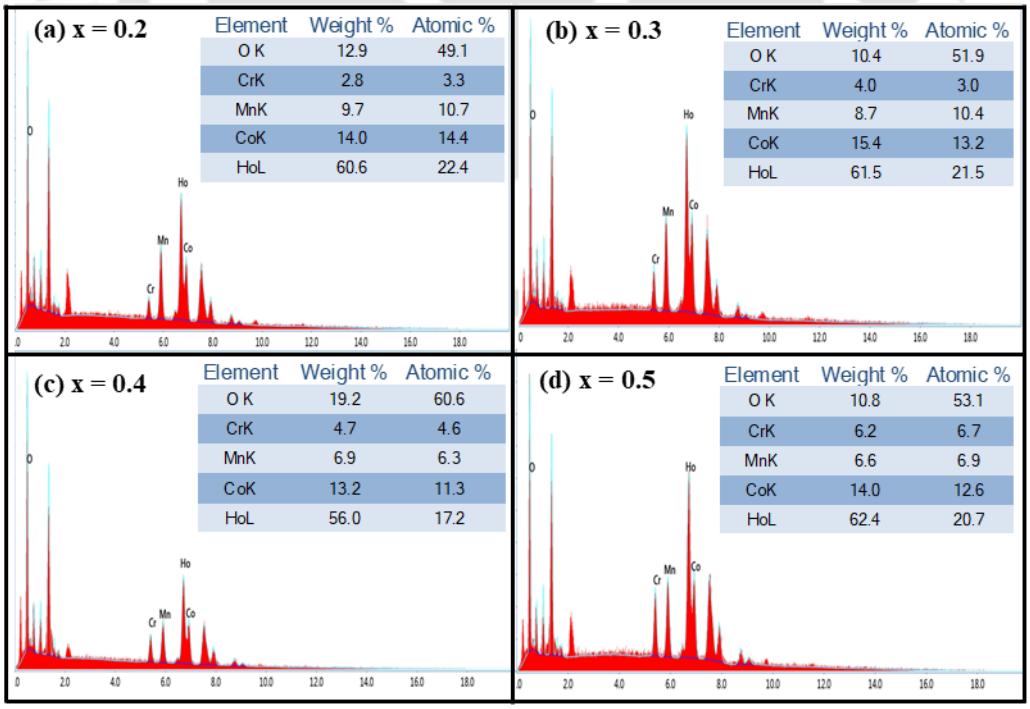

Fig.4.27. EDS spectra for (a) x = 0.2, (b) x = 0.3, (c) x = 0.4 and (d) x = 0.5.

Mn^{3+}/Mn^{4+} and Cr^{3+}/Cr^{4+} in the XPS data this statement is best understood. Table. 4.5 shows that the ratio between the concentration of Mn^{3+} and the combined concentration of Mn^{4+} and Cr^{3+} is around 1:1 for x = 0.2 and 0.4 sample and such arrangement would lead to charge ordering (CO). A small amount of Cr^{4+} ions is also detected in the current system. However, because its amount is very much small as compared to Cr^{3+}, so it might be neglected.

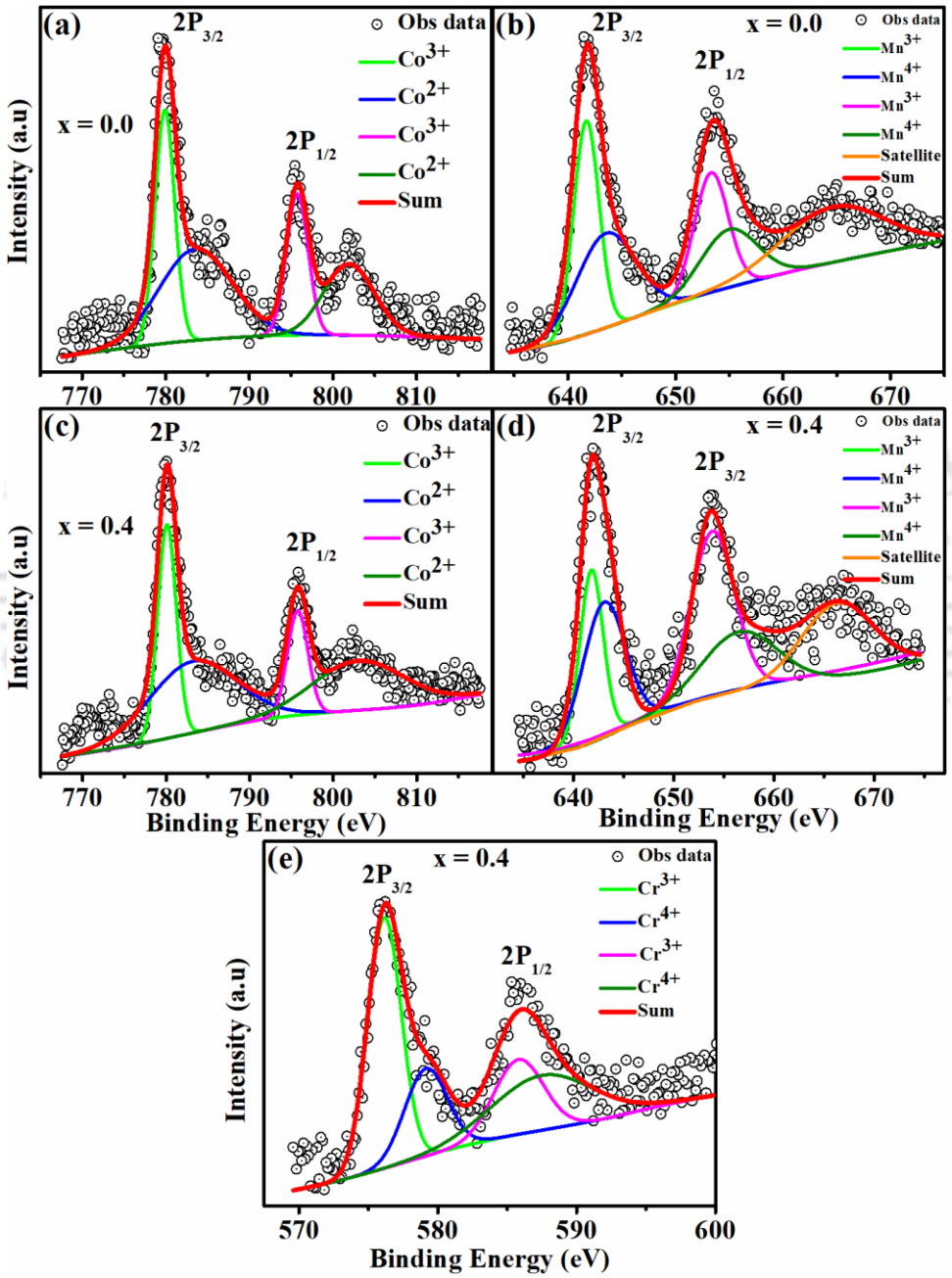

Fig.4.28. X-ray photoelectron spectroscopy for (a,b) x = 0.0 and (c-e) x = 0.4 for Co, Mn, and Cr elements.

Table. 4.5. Extracted elements and their proportions in the respective ionic state from XPS data.

Sample	Percentage of oxidation states of elements						Composition of each concentration
	Mn^{3+}	Mn^{4+}	Cr^{3+}	Cr^{4+}	Co^{2+}	Co^{3+}	
x = 0.0	25.89	74.10	--	--	67.38	32.61	$Co^{3+}_{0.33}Co^{2+}_{0.67}Mn^{3+}_{0.26}Mn^{4+}_{0.74}$
x = 0.2	49.37	30.56	10.64	9.36	62.73	37.27	$Co^{3+}_{0.37}Co^{2+}_{0.63}Mn^{3+}_{0.49}(Mn^{4+}_{0.31}Cr^{3+}_{0.11})Cr^{4+}_{0.09}$
x = 0.3	10.65	59.35	25.57	4.42	62.35	37.64	$Co^{3+}_{0.38}Co^{2+}_{0.62}Mn^{3+}_{0.11}(Mn^{4+}_{0.59}Cr^{3+}_{0.26})Cr^{4+}_{0.04}$
x = 0.4	38.78	21.21	22.79	17.2	63.41	36.58	$Co^{3+}_{0.37}Co^{2+}_{0.63}Mn^{3+}_{0.39}(Mn^{4+}_{0.21}Cr^{3+}_{0.23})Cr^{4+}_{0.17}$
x = 0.5	12.36	37.64	35.15	14.85	70.62	29.38	$Co^{3+}_{0.29}Co^{2+}_{0.71}Mn^{3+}_{0.12}(Mn^{4+}_{0.38}Cr^{3+}_{0.35})Cr^{4+}_{0.15}$

4.2.2. Magnetic properties

(i) Magnetization versus Temperature (MT) Study

Figure.4.29 (a-f) depicts the MT measurements of HCMCO series in ZFC and FC mode in an external field of 100 Oe. The nature of ZFC (M_{ZFC}) and FC curve for x = 0.0, already been explained previously. The MT plots for Cr doped samples are shown in Figure.4.29 (b-f). A similar type of behavior (as that of the parent compound) for M_{ZFC} curve has been observed up to x = 0.2 samples. However, the M_{ZFC} curve of other Cr substituted samples such as for $x \geq 0.3$ show two peaks followed by a secondary rise in magnetization for T < 50 K. Unlike the FC curve of the parent compound here for x = 0.1 and 0.2, it shows a sharp increase in magnetization value below 90 K, followed by a sharp decrease in magnetization value for T < 50 K as shown in Figure.4.29 (b,c). Whereas, for $x \geq 0.3$ it shows two peaks similar to the ZFC curve below 90 K as shown in Figure.4.29 (d - f). This decrease in M_{FC} value, causes MR in the x = 0.5 sample at lower field and it will be detailed later. In addition, for the intermediate compositions such as x = 0.2 and 0.4 (Figure.4.29 (c) and (e)), they exhibit another peak in both ZFC and FC curves at a temperature of 120 K. This is attributed to the charge ordering temperature (T_{CO}). The transition temperatures are determined by calculating M_{ZFC}'s first derivative with respect to temperature (dM/dT) and plotting it with temperature (lower inset of Figure.4.29 (a-f)). Single magnetic transition (T_{C1}) is observed for $x \leq 0.2$. Whereas, for $x \geq 0.3$ we have observed two transitions namely T_{C1} and T_{C2}.

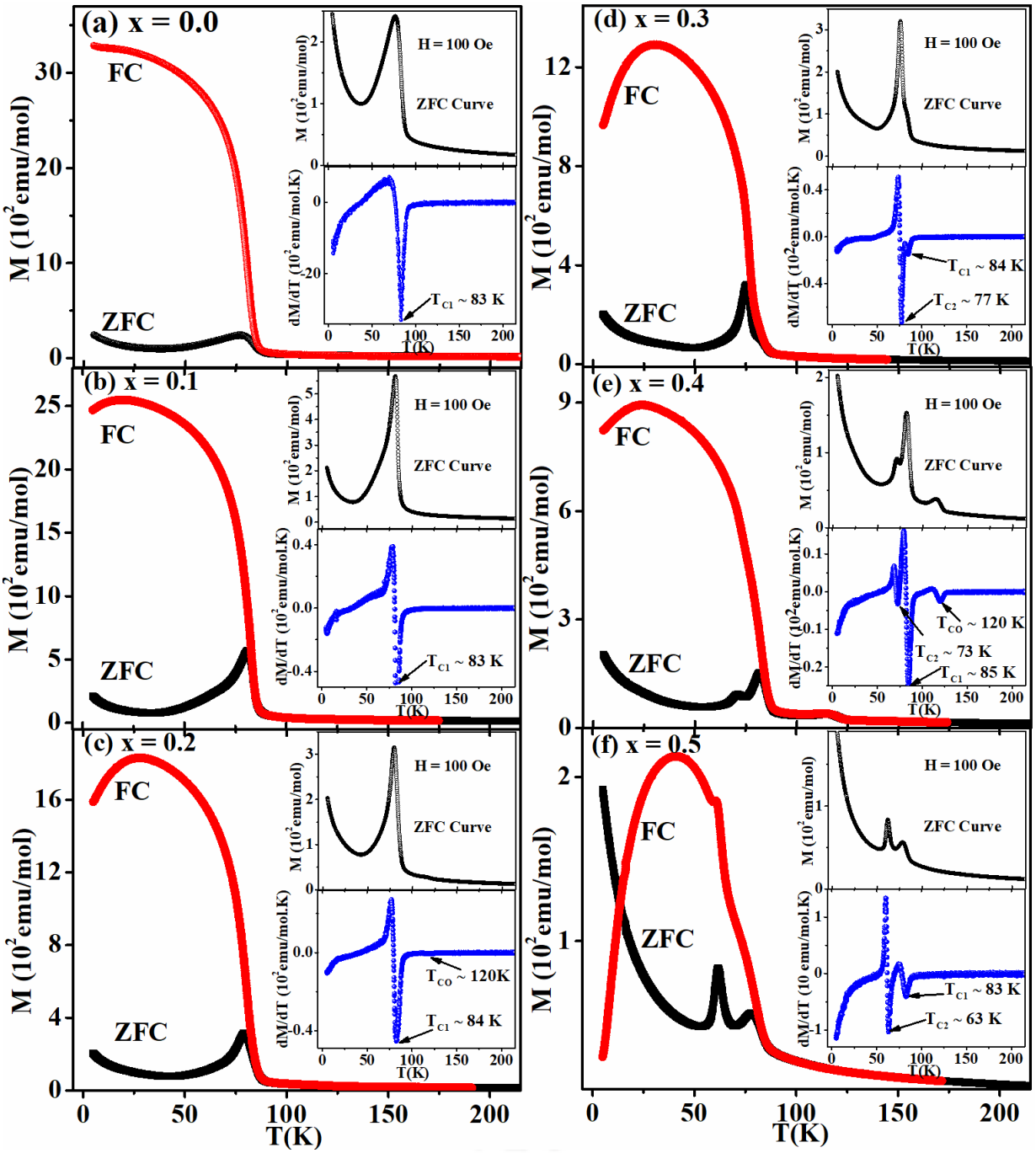

Fig.4.29. (a-f) M - T plots in both ZFC and FC conditions at H = 100 Oe applied field, the lower and upper inset show dM /dT versus T plots, and ZFC M - T plots in expanded scale for x = 0.0 to x = 0.5 respectively.

As illustrated in Figure.4.29 (a-f), the former transition (T_{C1}) is found to be in the range of 83 - 85 K. The later transition temperature (T_{C2}) decreases from 77 K for x = 0.3 to 63 K for x = 0.5 sample. The non-monotonous variation of the bond angle with respect to Cr concentration

could be a reason for this variation in the T_C. However, for the intermediate compounds (x = 0.2 and 0.4), we found another third transition at high temperature i.e., at 120 K. This transition is attributed to the charge ordering temperature (T_{CO}). From the XPS data we have also found a 1:1 ratio of Mn^{3+} and Mn^{4+}/Cr^{3+} ions for x = 0.2 and 0.4 samples which is one of the proofs for charge ordering. Further signature in the field dependent MT plots is discussed later. The upper insets provide an expanded view of the individual ZFC curves near the transitions.

The d - shell electronic configuration for the TM ions Co^{2+} and Mn^{4+}/Cr^{3+} are, Co^{2+}:- $t_{2g}^5e_g^2$ and Mn^{4+}/Cr^{3+}:- $t_{2g}^3e_g^0$ respectively. According to Goodenough - Kanamori rule, Co^{2+} has a FM interaction with Mn^{4+}/Cr^{3+} and an AFM interaction with Mn^{3+}:- $t_{2g}^3e_g^1$, whereas Cr^{3+} has an AFM interaction with Mn^{4+} and a FM interaction with Mn^{3+} [38,39]. So, here the transition T_{C1} is attributed to the SE interaction in Co^{2+}-O^{2-}-Mn^{4+} networks which result in a FM ordering. T_{C1} is almost unchanged for Cr doped samples. The second transition T_{C2} could be due to two possible reasons. One is FM interaction across Mn^{3+}-O^{2-}-Cr^{3+} networks via DE interaction, because it is similar to Mn^{3+}-O^{2-}-Mn^{4+} networks in terms of electronic configuration. Second is, an AFM interaction caused by SE interaction between Cr^{3+}-O^{2-}-Cr^{3+} and/or Cr^{3+}-O^{2-}-Mn^{4+} ions. However, one cannot rule out that at higher Cr concentration Mn^{3+} concentration would be small as compared to that of Mn^{4+} and Cr^{3+}, as most of the Mn^{3+} ions are replaced by Cr^{3+}. This deficiency in Mn^{3+} ion with Cr concentration is also visible from XPS data as tabulated in Table. 4.5. So, the AFM interaction becomes stronger in Cr^{3+}-O^{2-}-Cr^{3+} and/or Cr^{3+}-O^{2-}-Mn^{4+} networks as compared to the DE driven FM interaction in Mn^{3+}-O^{2-}-Cr^{3+} and Mn^{3+}-O^{2-}-Mn^{4+} networks. Hence, we have considered the transition T_{C2} is the result of AFM ordering arising from the SE interaction in Cr^{3+}-O^{2-}-Cr^{3+} and/or Cr^{3+}-O^{2-}-Mn^{4+} networks. The AFM interaction is dominating at $T \leq T_{C2}$, which can also be visible from the MT plot of x = 0.5. Where the transition at T_{C2} is much sharper as compared to lower Cr concentration samples. This type of FM/AFM ordered phase in a single compound is also noticed earlier in Co/Mn based DP [248] and Cr doped samples [279]. The magnetic irreversibility ($\Delta M/M_{ZFC} = (M_{FC} - M_{ZFC})/M_{ZFC}$) is highly visible for all the samples, particularly below the ZFC peak temperature. Which is an indication of frustrated spin structure such as spin glass. At 5 K, an irreversibility of 12.4 is seen for x = 0.0. However, the magnitude decreases to 3 for x = 0.4 and eventually to -0.9 for x = 0.5 as $M_{FC} < M_{ZFC}$ at 5 K for x = 0.5 sample.

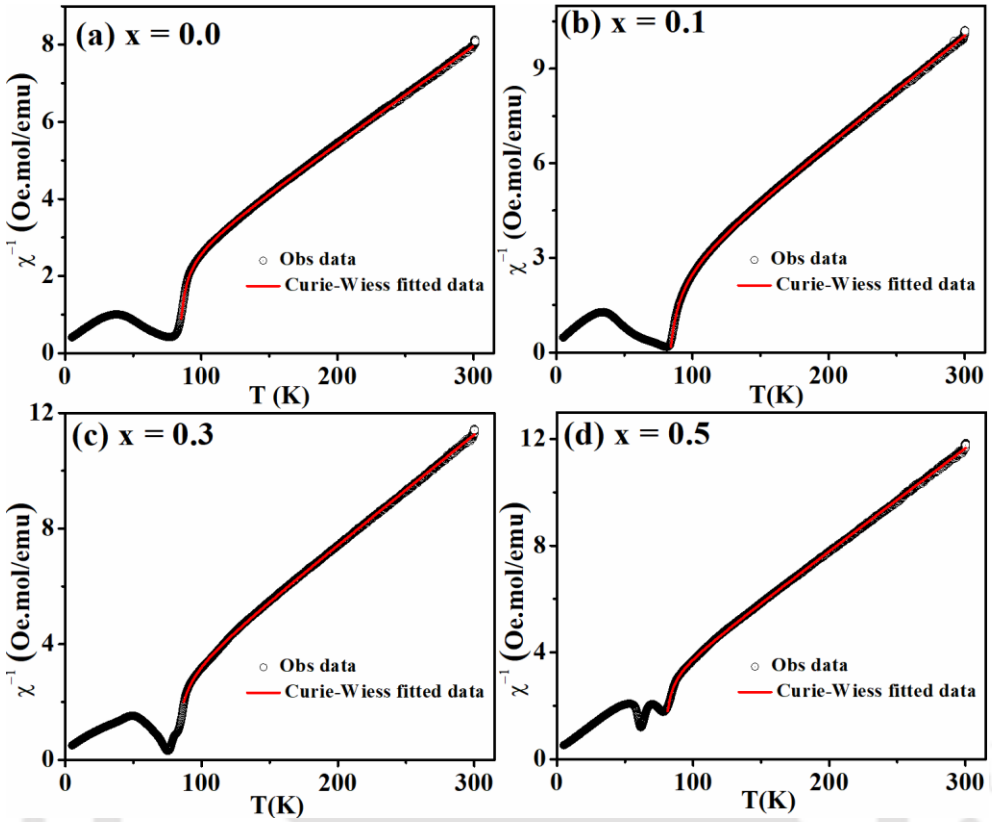

Fig.4.30. Fitted data of inverse susceptibility (χ^{-1}) versus T plots, with a MCWL for (a) x = 0.0, (b) x = 0.1, (c) x = 0.3, and (d) x = 0.5 respectively.

Table. 4.6. Data extracted from the M-T study.

Sample	T_{C1} (K)	T_{C2} (K)	T_{CO} (K)	θ_{RE} (K)	μ_{eff}^{Exp} (TM) μ_B/f.u	μ_{eff}^{Exp} (RE) μ_B/f.u
x = 0.0	83	--	--	-9	4.8	14.70
x = 0.1	83	--	--	-7	4.59	14.65
x = 0.2	84	--	120	-8	3.66	14.35
x = 0.3	84	77	--	-4	3.28	14.17
x = 0.4	85	73	120	-5	4.40	14.01
x = 0.5	83	63	--	-6	2.18	14.27

We have fitted the PM inverse susceptibility data with the MCWL as explained in Eqn. 1.7. Figure.4.30 (a-d) shows the fitted data for x = 0.0, 0.1, 0.3 and 0.5 samples by red solid lines.

One can see, this closely follows the experimental results all the way down to FM T_C. The estimated values of θ_{TM} for all the samples are found to be close to FM T_C. So, we have fixed the value and not tabulated here. However, the value of θ_{RE} for all the samples are found to be quite small and negative as tabulated in Table-4.6. With Cr doping, θ_{RE} value is not varying vigorously, it suggests that the growth of Cr concentration has no significant influence on the Ho site. According to previous report, the presence of some fraction of Co^{3+}/Mn^{3+} ions with Co^{3+} in low spin state causes a decrease in magnetic moment in the Co/Mn based DP [248]. The presence of Mn^{3+}, Co^{3+} along with Cr^{4+} in HCMCO has been confirmed by our XPS data. As a result, using the exact cationic population, we have calculated the theoretical effective magnetic moment for RE (μ_{RE}^{Th}) and TM (μ_{TM}^{Th}) ions, using the formula [136],

$$\mu_{RE}^{Th} = \sqrt{2 \times \mu_{Ho}^2} \quad (4.3)$$

$$\mu_{TM}^{Th} = \sqrt{[Y_1 \times \mu_{Co2+}^2 + Y_2 \times \mu_{Co3+}^2 + Y_3 \times \mu_{Mn4+}^2 + Y_4 \times \mu_{Mn3+}^2 + Y_5 \times \mu_{Cr3+}^2 + Y_6 \times \mu_{Cr4+}^2]} \quad (4.4)$$

Here, the ground state effective magnetic moments of the respective ions are represented by μ (with the suffix of respective chemical symbol). The coefficients, Y_1 to Y_6 represent the ionic population of that particular ion. From this study, we have found that, the theoretical effective PM moment of RE ion (μ_{eff}^{Th}(RE) = 14.99 μ_B/f.u) is comparable to the experimental values tabulated in Table. 4.6. The value of experimental effective PM moment μ_{TM}^{Exp} is decreasing more rapidly with Cr concentration, it confirms the substitution of Cr^{3+} (3.87 μ_B) at the Mn site and replacing the Mn^{3+} (4.89 μ_B) ions. However, there is a small discrepancy in the μ_{TM}^{Th} and μ_{eff}^{Exp} (TM) values. The theoretical value (μ_{TM}^{Th}) is quite large than the calculated effective moments. It may be attributed to the presence of some fraction of Mn^{3+} ions in low spin states. However, one can notice a sudden increase in μ_{eff}^{Exp} (TM) values for x = 0.4 sample. It could be understood by looking at the 1:1 ratio of Mn^{3+} and Mn^{4+}/Cr^{3+} ions from XPS data as tabulated in Table. 4.5.

Furthermore, various MT data were collected at different applied fields in both ZFC and FC mode for x = 0.3, 0.4 and 0.5 as shown in Figure.4.31 (a-f). Figure.4.31 (a) shows ZFC curves in an applied field varying from 100 to 3 k Oe for x = 0.3 sample. The presence of long-range FM phase Co^{2+}-O^{2-}-Cr^{3+} and/or Co^{2+}-O^{2-}-Mn^{4+} in HCMCO is confirmed by a field independent magnetic transition at T_{C1}. However, the field dependent T_{C2} is merged with T_{C1} with a rise in the

field (Figure.4.31 (a)). T_{C2} can be clearly visible in the ZFC curve at lower applied fields (up to 500 Oe). The merging behavior of T_{C2} in x = 0.3, can be explained in two ways, (i) The FM interactions between the ions is trying to dominate the AFM interaction in Cr^{3+}-O^{2-}-Cr^{3+} and/or Cr^{3+}-O^{2-}-Mn^{4+} networks at higher applied field,

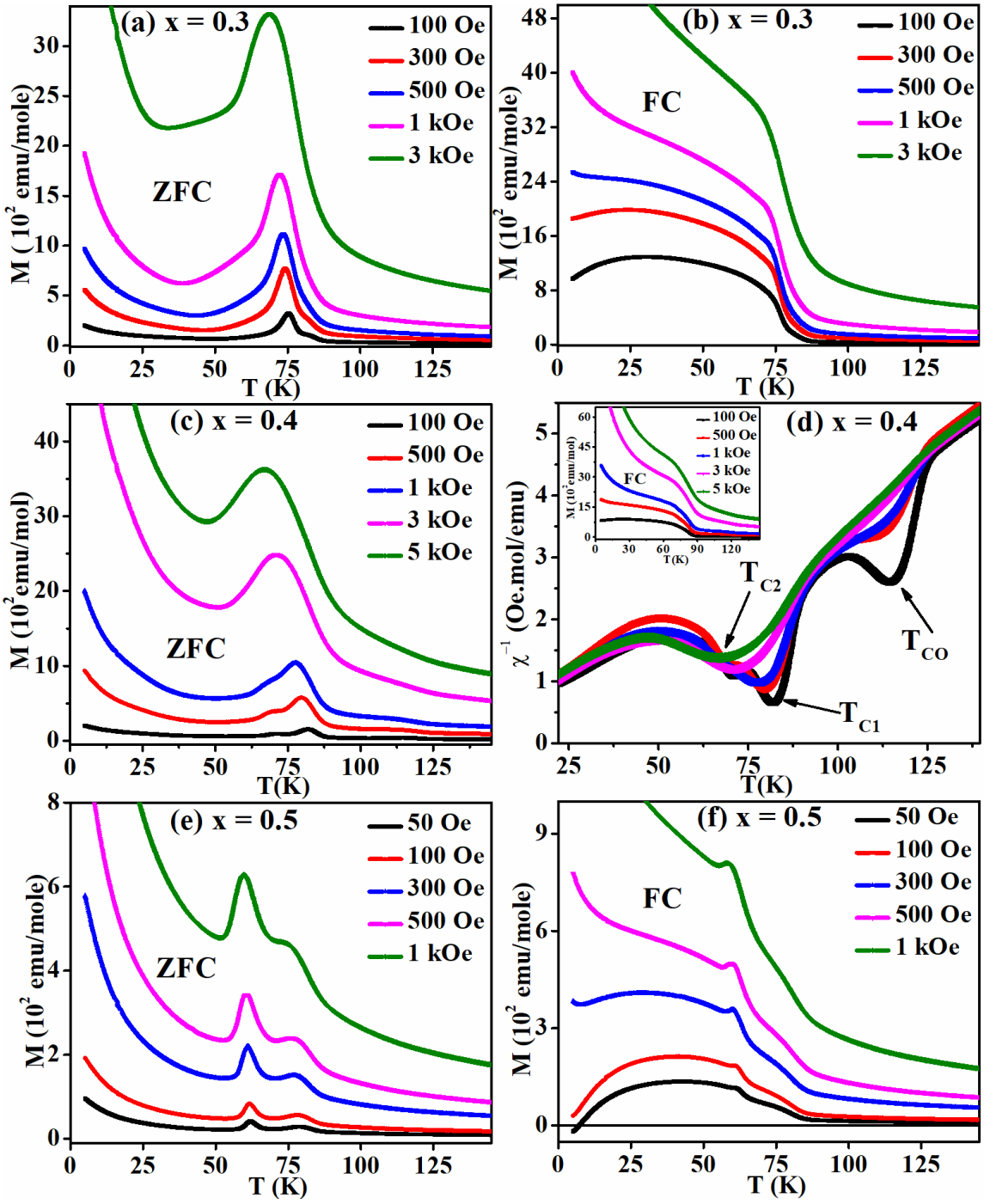

Fig.4.31. MT plot in both ZFC and FC modes at various applied fields (a, b) for x = 0.3, (c) ZFC curve, (d) χ^{-1} - T plots, inset shows FC curve for x = 0.4 sample and (e,f) for x = 0.5 sample.

(ii) the AFM phase is somewhat weaker here than the long range FM T_{C1}, hence, with rise in field, the AFM domains get forced aligned along the direction of field and merged the T_{C2} with T_{C1}. This type of behavior is also observed by Ranjana et.al. in Nd_2CoMnO_6 compound [248]. Below 50 K the magnetization value is sharply rising with field, which is attributed to the polarization of the RE ions moment with magnetic field. The FC curve of x = 0.3 is presented in Figure.4.31 (b) and it shows a similar type of behavior as that of ZFC curve, however, the rise in magnetization is much higher than the ZFC curve. As T_{C2} is quite weak as compared to long range FM transition at T_{C1}, so, it is not clearly observed in the FC curve. Figure.4.31 (c) shows ZFC curves in an applied field varying from 100 Oe to 5 kOe for x = 0.4 sample, it shows that T_{CO} is field dependent and with a rise in applied field value it is getting suppressed and finally no trace of CO is seen at 5 kOe field. Here also the presence of long range FM transition T_{C1} is confirmed by observing its field independent nature. The transition at T_{C2} can be clearly visible in the ZFC curve at lower applied fields (up to 1 kOe). However, similar to x = 0.3, the field dependent T_{C2} is merged with T_{C1} with a rise in the field as shown in Figure.4.31 (c). The merging behavior of T_{C2} in x = 0.4, can also be explained as that of x = 0.3 sample. Similar to x = 0.3, a sharp rise in the magnetization value has been observed below 50 K, and ascribed to the polarization of the RE ions with magnetic field. To visualize the suppression of T_{CO} properly, we have plotted the inverse susceptibility versus T plot (ZFC) at different applied fields, as shown in Figure.4.31 (d). The FC curve of x = 0.4 is presented in the inset of Figure.4.31 (d) and it shows a similar type of behavior as that of FC curve of x = 0.3 sample.

Similarly, the field variation of ZFC and FC curves of magnetization for x = 0.5 sample are shown in Figure.4.31 (e) and (f) respectively. Unlike x = 0.3 and 0.4, here one can clearly see the two transitions T_{C1} and T_{C2} in both ZFC and FC curves. Starting with ZFC curve, T_{C1} is independent of the field as described in the above paragraph. However, T_{C2} is field dependent, unlike the behavior of x = 0.3 and 0.4 here, T_{C2} is getting more prominent with rise in field. So, as explained earlier, the deficiency of Mn^{3+} ions in the higher Cr concentration samples leads to strengthening the SE driven AFM interactions in the system. A similar type of feature has also been observed by Capogna et.al. in Cr doped systems [279]. Here, T_{C2} transition is quite sharper indicating dominating AFM ordering. Whereas, the sharp rise in magnetization value below 50 K is still noticed as that of x = 0.3 and 0.4 sample. The variations that are observed for T_{C1} and T_{C2} in ZFC for x = 0.5 sample, is also consistent with the FC curve. However, at lower fields, there

was a downfall in the FC magnetization value below 50 K. It results in MR for 5O Oe of applied field with a T_{comp} of 7 K. On the other hand, MR disappears as the applied magnetic field increases. A sharp upturn is observed below 25 K, indicating the polarization of RE ions. From the MT data, we can make a statement that Cr doping dilutes the long range order of ferromagnetism. A conclusion can be made from the MT plots carried out at different applied fields. The merging of T_{C1} and T_{C2} for x = 0.3 and 0.4 along with broadening of the peak can be attributed to forced magnetization and the suppression of AFM interaction due to large applied field. The variation in peak structure in the ZFC MT curves with increasing field might be caused by the substantially temperature dependent coercivity of these samples [269]. When the applied field value is less than H_C at low temperature, the measured magnetization will stay extremely weak until approaching T_C. The temperature dependence of H_C causes a sharp spike in ZFC curves just below T_C, resulting in a peak-like shape. The variation of H_C value with temperature will be discussed later. The transition at 120 K is confirmed by the suppression of T_{CO} at higher applied field, which is a basic characteristic of charge ordering.

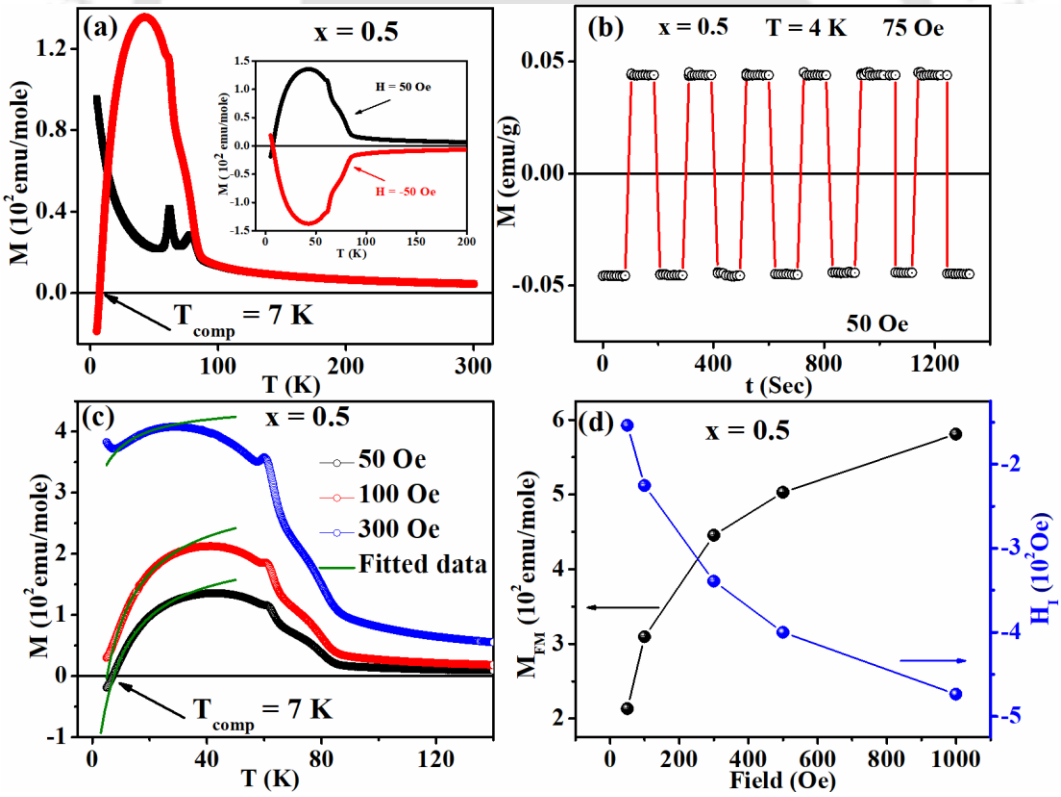

Fig.4.32. (a) MT plot in both ZFC and FC condition, inset shows FC curve at H = ± 50 Oe, (b) Bipolar switching of magnetization at 4 K, (c) FC MT data fitted to Eqn. 1.14 and (d) M_{FM} and H_I versus applied fields for x = 0.5.

The downfall in FC magnetization at T < 50 K at 100 Oe is very prominent with a decrease in magnetic moment which leads to MR at 50 Oe field in x = 0.5 as shown in Figure.4.32 (a). The T_{comp} is observed at 7 K. Capogna et.al. observed a similar pattern of behavior in Cr doped systems [279]. They attributed it to the canted AFM (CAFM) state arising due to the random distribution of Cr^{3+} ions with randomly oriented spin. To examine the instrumental artefact, we have carried out the M_{FC} versus T measurement at an applied field of ± 50 Oe as shown in the inset of Figure.4.32 (a). Obtained mirror image of the MT curves in the opposite applied field confirms that MR is a sample intrinsic property. Figure.4.32 (b) depicts the BSM at 4 K. To achieve BSM, we FC the sample down to 4 K by crossing the T_{comp}, with a 50 Oe applied field. We measured the magnetization value for 100 sec after it reached 4 K and found that it was negative. The magnetization then switched to a positive value when we increased the field to 75 Oe and recorded it for 100 sec. This method was repeated several times, i.e., shifting the field from 50 Oe to 75 Oe and back to 50 Oe, and consistency in BSM is found. This confirms field-induced BSM can be reproduced without changing the direction of the applied magnetic field.

From the field variation of MT plots, we have confirmed that the higher Cr doped compounds exhibit two magnetic ordering; one is FM and the other one is AFM. The MR in such systems is caused by the competition between the PM moment and the FM/AFM component located at different crystallographic sites. Under the influence of an effective molecular field arising from the ordered AFM component, the moments of the PM ion partially align opposite to the applied field. So, the observed MR in x = 0.5 can be explained by considering the competition between the weak FM components of Co^{2+}/Mn^{4+} (M_{FM}) and the PM behavior of Ho^{3+} ions under the influence of negative internal field (H_I) caused by AFM ordered ions. We found that the measured M_{FC} is well fitted to Eqn. 1.14. The fitted data at various fields for x = 0.5 sample are shown as green solid lines in Figure.4.32 (c). The obtained data of M_{FM} and H_I are plotted in Figure.4.32 (d). As can be seen that M_{FM} as well as the magnitude of H_I is increasing with rise in field. Increase in H_I is ascribed to the increase in the size of AFM domains with respect to applied magnetic field. θ values are found to vary from -7 to -9 K for 50 Oe to 1 kOe.

(ii) Hysteresis Loops

MH loops were recorded at 5 K for an applied field up to ± 9 T as shown in Figure.4.33 (a). The magnetization is not saturated even at 9 T, and thus supports the canted/uncompensated spin structure. We used LAS model to analyze the initial curves in order to estimate the M_S value

[267]. We have fitted the high field region data to the LAS model which is shown by green solid lines in Figure.4.33 (b). The obtained parameters such as H_C, M_S, M_r, and K_1 are listed in Table - 4.7. All the parameters are found to decrease with Cr substitution. The drop in the values of M_S is ascribed to the replacement of Mn^{3+} ions having higher magnetic moment (4 μ_B/ion) with the Cr^{3+} ions having lower magnetic moment (3 μ_B/ion). We can see the M_S value is much higher than the expected one (6 μ_B/f.u.) which confirms the RE contribution to the overall FM moment.

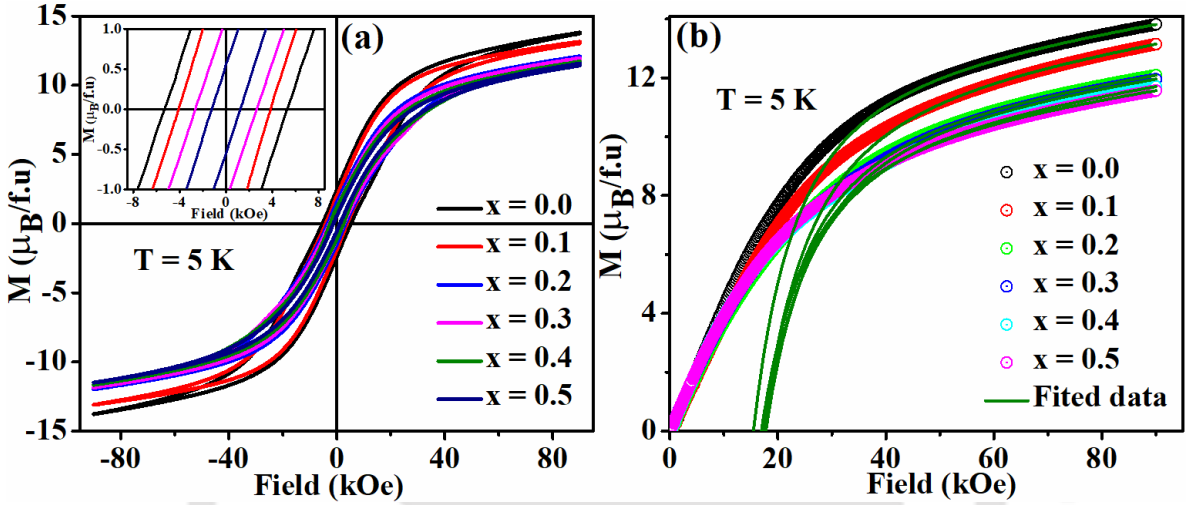

Fig.4.33. (a) Magnetic Hysteresis loops recorded at 5K, with an expanded view of loops near the coercive field (inset) and (b) initial M-H loops fitted with the LAS model for HCMCO series.

Table. 4.7. Magnetic data were estimated from the hysteresis loops (ZFC and FC).

Sample	x = 0.0	x = 0.1	x = 0.2	x = 0.3	x = 0.4	x = 0.5
H_C (Oe)	5328	4086	3329	2723	2580	1289
M_r (μ_B/f.u)	2.00	1.97	1.52	1.13	1.13	0.55
M_S (μ_B/f.u)	11.60	11.13	10.3	10.28	9.86	9.79
K_1 (10^4erg/cm^3)	1.90	1.86	1.52	1.60	1.41	1.31
H_{EB} (Oe)	-114	-110	-26	47	69	208

A number of temperature dependence MH loops were recorded for x = 0.4 and 0.5 samples from 5 K to 140 K as shown in Figure.4.34 (a,b). A drop in the M_S value has been observed with rise in temperature up to 120 K for x = 0.4 and up to 90 K for x = 0.5, then attained a value close to zero by further rising the temperature (inset of Figure.4.34 (a, b)). Observed H_C values with

respect to temperature are plotted with the FC MT plots as shown in Figure.4.34 (c,d). The form of the H_C versus T plot is similar to that of the FC MT plots. A sharp fall in the value of H_C has been observed at T_{C2}. Then a hump like feature is found in the vicinity of transition T_{C1} and T_{CO} respectively. Which may be attributed to the temperature dependent H_C of the sample. Similar type of nature is also explained in section 4.1, where Ni was substituted at the Mn site of Ho_2CoMnO_6 compound. For both x = 0.4 and 0.5 samples, obtained M_S values at any particular temperature below 25 K, are higher than the expected value from the TM sublattice. For x = 0.5 sample, the M_S value is ranging from 8.9 μ_B/f.u. to 8.1 μ_B/f.u. for the temperature 5 K to 10 K, this value is certainly higher than 6 μ_B/f.u. Then it falls to 4.3 μ_B/f.u. at 25 K. However, T > 25 K it starts to drop drastically, indicating a lack of FM contribution from RE ions for T > 25 K.

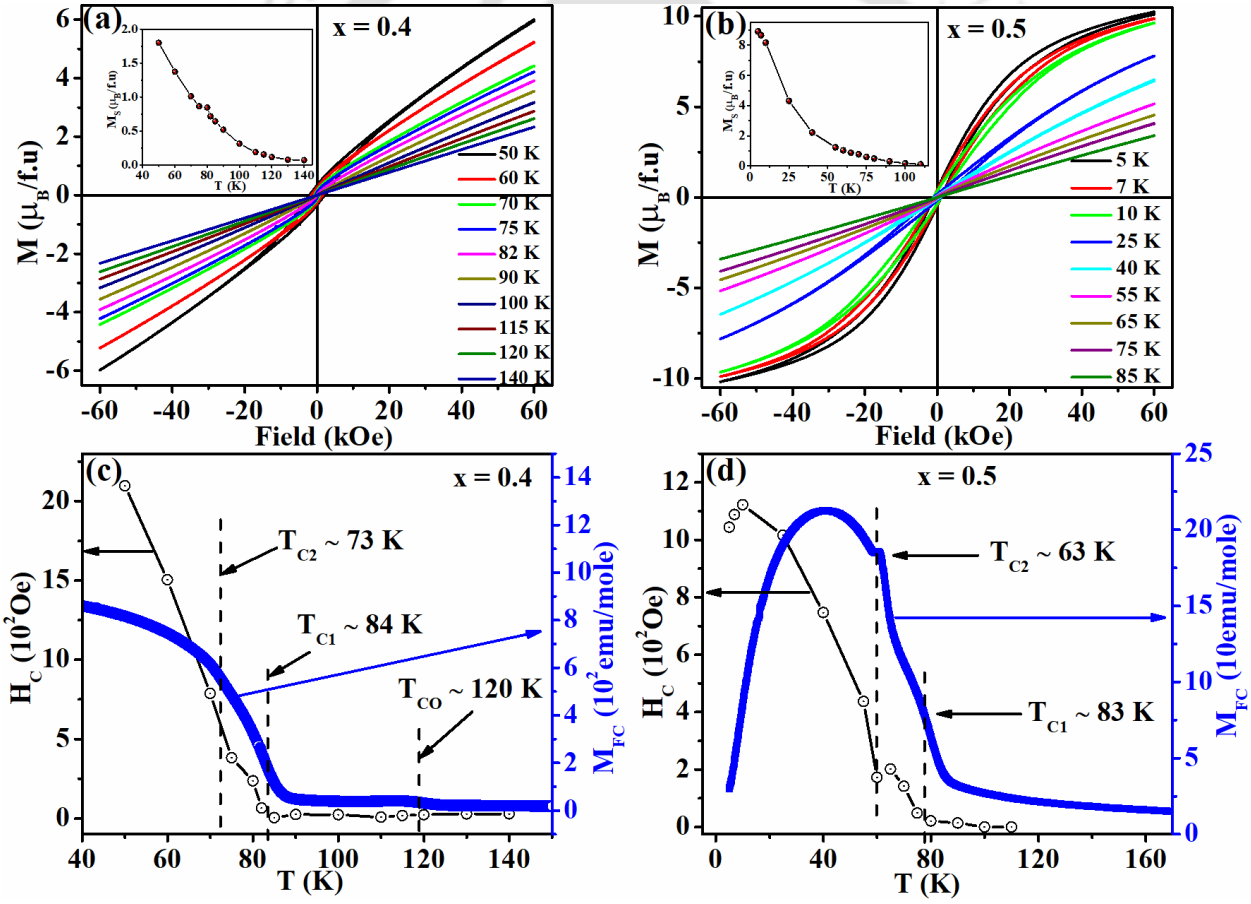

Fig.4.34. (a, b) Temperature variation of M-H loops for x = 0.4 and 0.5, inset shows the MS versus T plot and (c, d) H_C and M versus T plot (M_{FC}) for x = 0.4 and 0.5 respectively.

(iii) Study of Exchange Bias Behavior

For this study, as shown in Figure.4.35 (a-d), we measured FC MH loops at 5 K with a cooling field of H_{FC} = 0.5 T and a measuring field varying up to ± 6 T. We found a clear shift of MH loops, indicating EB behavior.

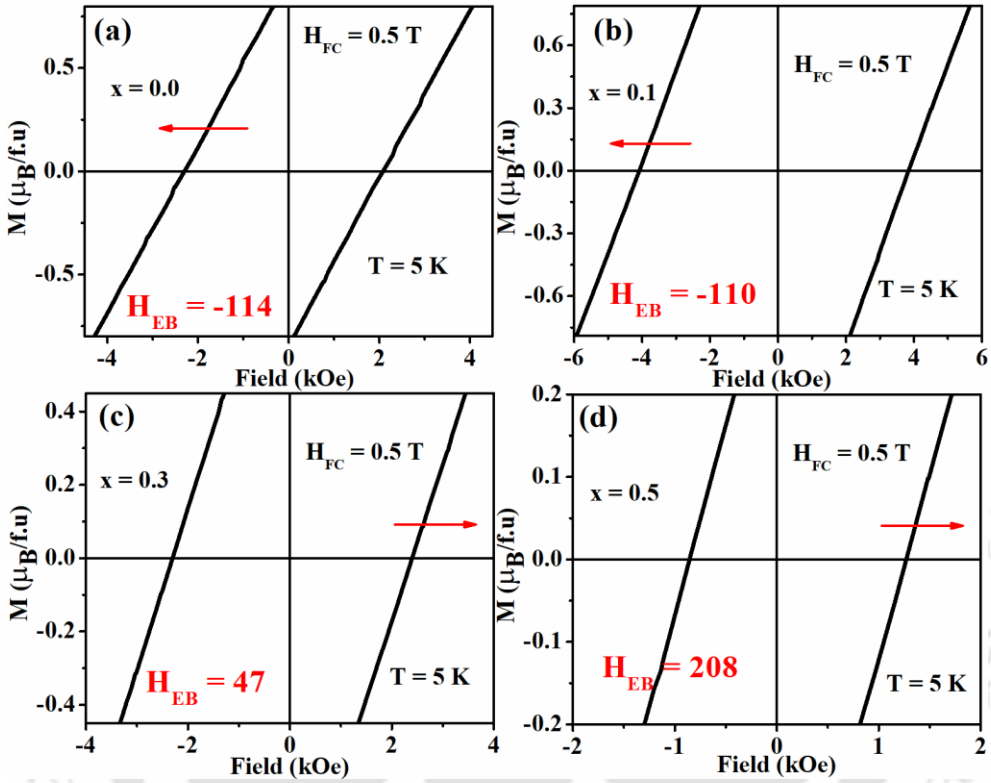

Fig.4.35. Enlarged view the FC M-H loops at 5 K for (a) x = 0.0, (b) 0.1, (c) 0.3, and (d) 0.5.

To ensure the observed shift in FC MH is not attributable to any stray field effect, we have measured the loop for both H_{FC} = ± 0.5 T for x = 0.5 sample at T = 5 K as shown in Figure.4.36 (a, b). As the cooling field is reversed, we can witness a definite shift of the loop in the opposite direction. Figure .4.37 (a-d) depicts an expanded view of hysteresis loops at low field region and it clearly demonstrates EB behavior in the present series. However, here we found an interesting fact that, up to x = 0.2 the loop is shifting towards the negative field axis which leads to a negative EB field value (H_{EB}). Then, for x ≥ 0.3 we found the loop is shifting towards the positive field axis and gives rise to a positive H_{EB}, and this value is increasing with Cr. We found a maximum positive value of H_{EB} = 208 Oe for x = 0.5 sample. The observed H_{EB} values are tabulated in Table - 4.7. Here, the reason for the observed EB for parent and Cr doped sample is considered to be different. For the parent compound it is attributed to the competition between FM moment of TM ions and

the spin canted magnetic moment of RE ions. RE ions are PM at T > 25 K, but below that, they begin to polarize along the direction of the field. Yet, some of spins are not entirely polarized but rather canted. As a result, the competition between canted moment of RE ions and TM ions causes a shift in the MH loop for the x = 0.0 sample towards the negative field direction. Moreover, the role of ASD induced AFM cannot be ruled out. However, the competition between the FM and the AFM components which are arising due to the Cr doping is considered to be the reason for the EB in the Cr doped samples.

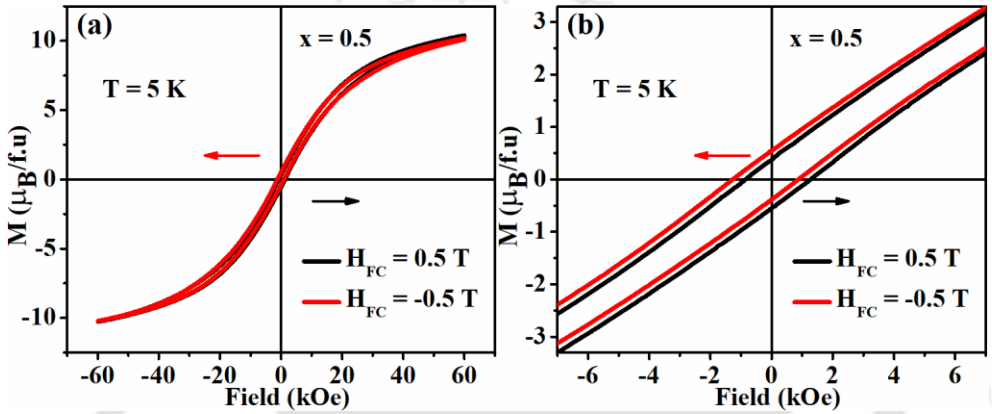

Fig.4.36. (a) FC hysteresis loops for x = 0.5 sample with H_{FC} = ± 0.5 T and (b) its enlarged view in the vicinity of coercivity (H_C).

Shifting of the loop to positive direction in the higher Cr concentrated samples can be explained as follows. Initially in the parent compound, after FC (at H = 0 Oe), a few FM clusters are present below the FM T_C, along with the canted magnetic components of the RE ions. The FM spins are strongly coupled with the canted spins throughout the FC process, resulting in two integrated anti-parallel spin systems. During the first loop of FC MH, field ramping produces additional FM clusters, increasing the number of FM and/or AFM interfaces. As a result, while striving to keep the spins aligned with the field direction, the dominant FM spins impose a tiny torque on the canted spins during the descending field. As a result, to align the canted spins in the field direction, a bigger negative field is necessary. Throughout this procedure, the loop is pushed towards the negative field direction, resulting in a negative EB in the x = 0.0 sample. At the same time, Cr substitution in the HCMO sample introduces an AFM ordering in the form of Cr^{3+}-O^{2-}-Cr^{3+} and /or Cr^{3+}-O^{2-}-Mn^{4+} networks. And this AFM interaction gets more and more prominent with Cr concentration which is also proven by the field dependent MT measurement of x = 0.5 sample. Now, unlike to the parent and lower Cr concentration samples, now at the interface AFM

spin structure is more prominent. Hence, instead of FM spins, now AFM spins giving a torque to the FM spin structure to get aligned along the spin structure. So, it leads to the shift of the loop towards the positive field axis and results in to a positive H_{EB}. The increase in H_{EB} value with Cr is attributed to the strengthening of AFM components in the system as compared to the FM spin structure at the interfaces.

Many MR systems have been found to display sign reversal in EB around T_{comp} [65,203,240]. As a result, it encouraged us to test the temperature variation of EB. As a result, we only measured EB versus T for the x = 0.5 sample (Figure.4.37 (a)). So, for this, we have chosen the temperature range of 5 to 60 K and recorded the FC MH loops. The enlarged view of this temperature variation of FC MH loops, in the vicinity of H_C are shown in the insets of Figure.4.37 (a). The temperature variation of H_{EB} plots are shown in Figure.4.37 (b). One can clearly see that there is no sign reversal in H_{EB} at the T_{comp}. However, it follows the exponential function as explained in Eqn. 3.7. The fitted data to the Eqn. 3.7 is shown as the red solid line in Figure.4.37 (b). The fitted values for H_{EB} (0) and T_1 are found to be 385 ± 37 Oe and 8 ± 1 K respectively.

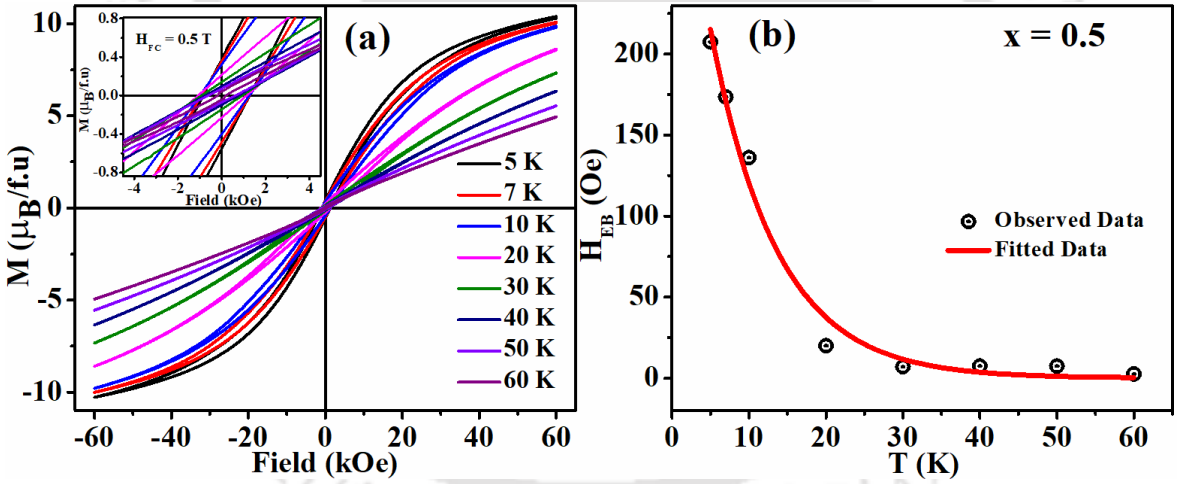

Fig.4.37. (a) FC M-H curves for T = 5 to 60 K with H_{FC} = 0.5 T, inset shows the enlarged view of the loops near the coercive field, and (b) H_{EB} versus T with the data fitted to an exponential function for x = 0.5.

The magnetic phase diagram of our system is shown in Figure. 4.38. From the figure one can see the complex magnetic behaviors such as FM, AFM, RE polarization, and charge ordering. For x = 0.0 to 0.1 mostly a transition from PM to FM has been observed followed by a RE polarization at 25 K. Strong magnetic properties have been observed for x = 0.2 to 0.5 sample. For x = 0.2, PM to a charge ordering phase followed by FM phase has been observed. However, for x

= 0.3 to 0.5, PM, charge ordering (x = 0.2, 0.4), FM, and AFM have been found with decreasing temperature. Unlike, to other Cr concentrations, for x = 0.5, a MR has also been observed below 7 K. Furthermore, at T < 25 K, a rare earth polarization is observed in all the compositions ranging from x = 0.0 to 0.5.

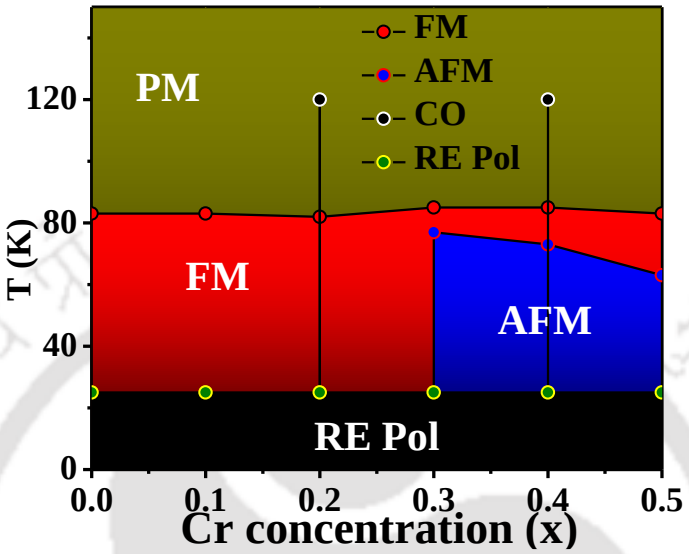

Fig.4.38. Phase diagram of HCMCO series.

4.3. Conclusions

An auto combustion technique was used to prepare nanocrystalline samples of $Ho_2CoMn_{1-x}Ni_xO_6$ (x = 0.0 - 0.4) in single-phase. RT XRD analysis reveals that the samples are formed in monoclinic structure with space group $P2_1/n$. A drop in the lattice parameters as well as unit cell volume are observed with Ni substitution. A shift in the peak of Raman spectra towards higher wavenumber further justifies the drop in the lattice parameters. MT shows two FM transitions for all Ni doped samples. In the present case, the two FM transitions are attributed to the super-exchange interaction in Co^{2+}-O-Mn^{4+} and Co^{2+}-O-Ni^{4+} networks. The transition temperature (T_{C1}), which arises from Co^{2+}-O-Mn^{4+} networks are decreasing from 83 K for x = 0.0 to 76 K for x = 0.4. Whereas the other transition (T_{C2}) which arises from Co^{2+}-O-Ni^{4+} networks is increasing from 84 K to 88 K for for x = 0.1 to x = 0.4. For higher Ni concentrated samples i.e., for x = 0.3 and 0.4 a MR has been observed with a T_{comp} at 4.4 and 10 K respectively and it is due to the negative exchange interaction between the moments of RE ions and TM ions. The magnetization versus field (MH) measurement at 5 K shows a drop in coercivity and saturation magnetization (M_S) with Ni doping. The drop in M_S value is due to the replacement of Mn^{4+} ions having larger magnetic moment with Ni^{4+} ions having negligible moment. However, the observed M_S value of the order

of 11.6 μ_B/f.u. at 5 K is attributed to the FM interaction of RE ions with the net magnetic moment of TM ions. A maximum value of EB field of 230 Oe at 5 K is observed and is attributed to the competition between spin canted magnetic moment of RE ions and FM moment of TM ions.

Similarly, we have investigated the effect of Cr doping on the structural and magnetic properties of HCMO DP. For this we have synthesized single-phase nanocrystalline samples of $Ho_2CoMn_{1-x}Cr_xO_6$ (x = 0.0 - 0.5) through an auto combustion technique. According to Rietveld refinement of XRD data, the samples exhibit a monoclinic structure with space group $P2_1/n$. With Cr substitution, the lattice parameters are found to be reduced. For $x \leq 0.2$ samples, a pure FM phase (T_{C1}) has been observed at 83 K which is confirmed by MT plots. The SE interaction in Co^{2+}-O^{2-}-Mn^{4+} networks is responsible for it. However, with an increase in Cr doping other magnetic state such as AFM (T_{C2}) is observed. The AFM interaction in Cr^{3+}-O^{2-}-Cr^{3+} and/or Cr^{3+}-O^{2-}-Mn^{4+} ions gives rise to T_{C2}. T_{C1} does not show much variation, it stays in the range of 83 K to 85 K. While, T_{C2} drops from 77 K for x = 0.3 to 63 K for x = 0.5 samples. However, for x = 0.2 and 0.4, we discovered another transition at 120 K. This transition is attributed to the charge ordering temperature (T_{CO}). With Cr doping, the downfall in the FC magnetization below 50 K is very prominent with a decrease in magnetic moment. This decrease in moment leads to MR in x = 0.5 sample at lower applied field with a T_{comp} of 7 K. The competition between the PM moment of Ho^{3+}/Mn^{3+} ions under the influence of a negative internal field caused by AFM ordered ions and the FM components of Co^{2+} and Mn^{4+} ions is ascribed to this MR. After Cr substitution, the magnetic hysteresis loops show a reduction in saturation magnetization and coercivity. For samples with x = 0.0 and 0.5, an EB field of - 114 Oe and + 208 Oe is seen. They are explained by the competition between canted magnetic moments of RE ions and FM moments of TM ions, with the former dominating for x = 0.5 sample and the latter one dominating for x = 0.0 sample.

Chapter 5

Nanoparticles of Y_2FeCrO_6 Double Perovskite

Perovskite structures based on Fe-Cr are often found in a disordered orthorhombic form (space group - Pbnm, Pnma, R3c etc). Because of their comparable ionic radii (Fe^{3+} (0.645), Cr^{3+} (0.615), the Fe and Cr ions are randomly distributed in the octahedral site, resulting in octahedral distortion. The magnetic characteristics of these materials are mostly determined by the interaction in Fe^{3+}-O-Fe^{3+}, Cr^{3+}-O-Cr^{3+}, and Fe^{3+}-O-Cr^{3+} networks [50,206,252,253]. It typically exhibits a canted AFM structure with a weak FM component and this is achievable only due of the random distribution of Fe^{3+}/Cr^{3+} ions at the B site and the resulting tilting of the octahedral. $YFe_{0.5}Cr_{0.5}O_3$ shows a temperature as well as field induced MR with T_{comp} ~ 248 K and an AFM ordering temperature at ~ 274 K [252]. However, above and below 260 K, it exhibits both normal and inverse MCE. Along with the MR a magneto dielectric effect has also been observed in this system [134]. Because of this feature, this material is useful in spintronics and magnetic refrigeration. Here, the different temperature dependence of SIA and DM interaction and their competition is ascribed to the observed MR in these types of systems. Fe-Cr based perovskites are extensively studied material whereas, Fe-Cr based DPs are very less explored. For example, recently a magneto-dielectric behavior has been seen in Y_2FeCrO_6 [91]. However, no one reported MR or EB either in bulk or nanostructured Y_2FeCrO_6 DP. With limited work on Y_2FeCrO_6 DP, a complete and systematic investigation of the magnetic property at multiple temperatures and magnetic fields is lacking. As nanoparticles are known to give distinct properties compared to the bulk sample and also helps in tuning the lattice distortion etc. It was thought that by doubling the formula unit from $YFe_{0.5}Cr_{0.5}O_3$ (bulk) to Y_2FeCrO_6 (nanostructured), it would be able to keep the previous features of perovskite structure while additionally inducing a few new magnetic properties into the DP structure. So, to tune the magnetic properties such as T_C, and improve the functional properties, we have synthesized nanoparticles of Y_2FeCrO_6 having a particle size of 67 nm and presents a detailed investigation of structural and magnetic properties. Here we observed the coexistence of MR and sign reversal of both spontaneous and conventional EB field. Unlike the previous reports

on MR on DP, here we suggest a simple mechanism based on the competition between SIA and DM interactions. We have prepared this sample using auto combustion method as described in the section 2.1 (Chapter - 2).

5.1 Structural Properties

The YFCO sample is found to be in single phase form as per the powder XRD pattern recorded at RT. The XRD pattern was analyzed using the Rietveld refinement technique which is shown in Figure.5.1 (a). After fitting our observed XRD data, refinement result confirms the formation of the YFCO compound purely in the orthorhombic phase with the space group Pnma. All the diffraction peaks are well indexed based on the best fit to the orthorhombic structure. No additional impurity peaks have been identified within the resolution limit of the instrument, pointing to the single-phase nature of the compound. The refined lattice parameters and the unit cell volume obtained from the Refinement are as follows: a = 5.5509(1) Å, b = 7.5704(2) Å, c = 5.2635(1) Å and volume, v = 221.191(8) $Å^3$ respectively. These values are comparable with the earlier reports on $YFe_{0.5}Cr_{0.5}O_3$ and Y_2FeCrO_6, where they crystalize in to orthorhombic phase [91,133]. Fe^{3+} and Cr^{3+} ions are distributed in the same crystallographic (4b) site in this space group, ruling out the ordering of Fe and Cr ions [91,133]. The values of reliability factors are found to be R_p = 9.74 %, R_{wp} = 6.95 %, R_{exp} = 6.65 %, R_{Bragg} = 1.0 %, R_f = 1.01 %, and χ^2 = 1.09 respectively, are found to be acceptable in the case of DP compounds.

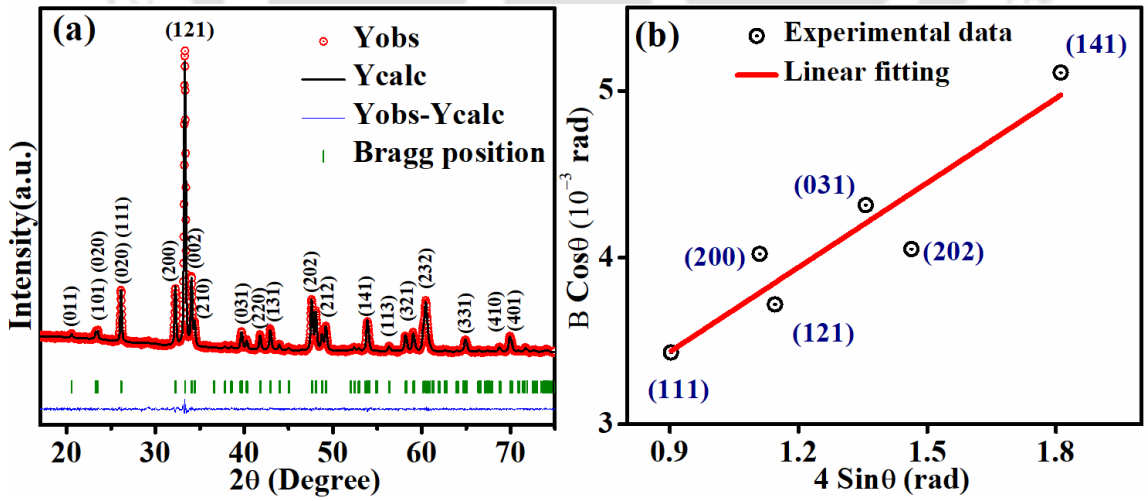

Fig.5.1. (a) Room temperature XRD data along with Rietveld refinement and (b) Williamson-Hall plot of YFCO nanoparticles.

A polycrystalline compound consists of uneven sizes of numerous crystallites. So, the WH plot technique as explained in Eqn. 3.1, was used to calculate the average crystallite size and micro-

strain parameter [259]. A linear fit can be done among the data points of Bcosθ versus 4sin θ as shown in Figure.5.1 (b). The value of average crystallite size is found as 72 nm and the micro-strain parameter is determined to be 1.7×10^{-3}.

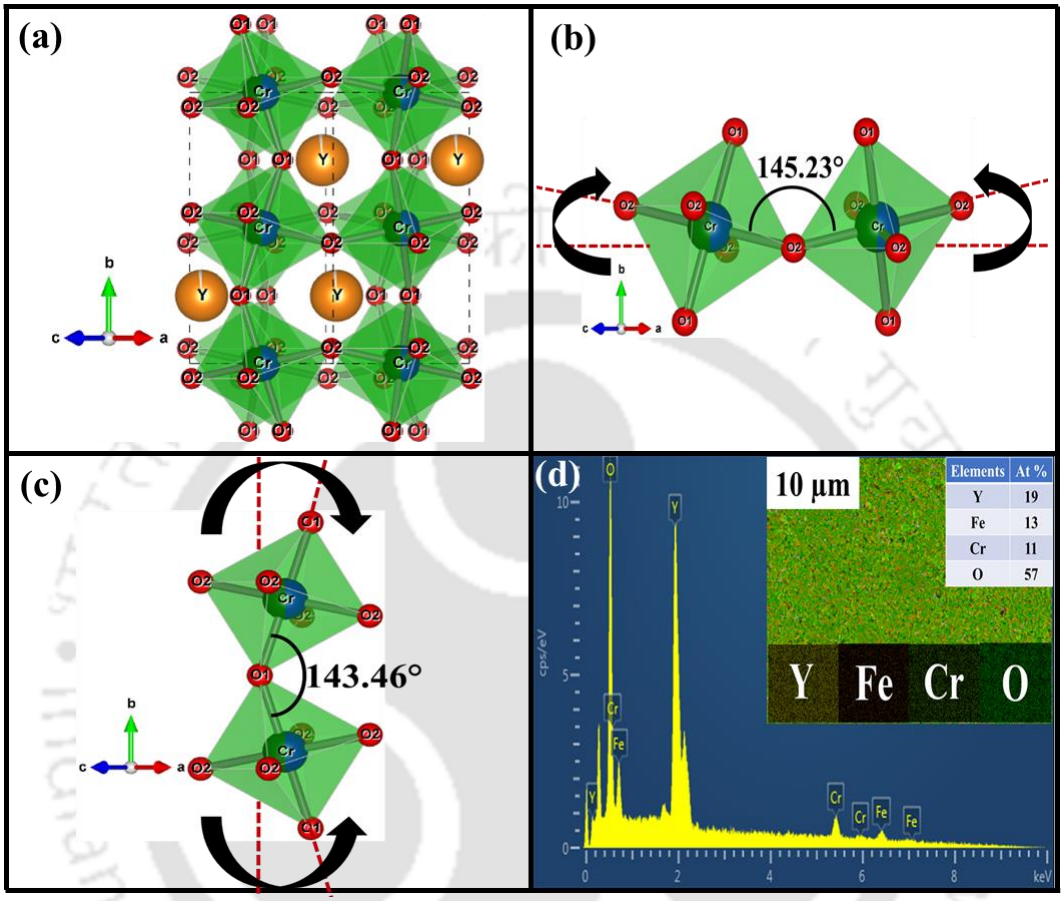

Fig.5.2. (a) Unit cell of YFCO sample, Angle between FeO_6 and CrO_6 octahedra with (b) O_1, (c) with O_3, (d) EDS spectra and elemental mapping (inset) of YFCO sample.

Like typical DP structure of rock salt type arrangement, here, FeO_6 and CrO_6 octahedra are placed alternately at the corner of the unit cell and the RE (Y) is situated in the void space between them as shown in Figure.5.2 (a). However, unlike the typical DPs, here the octahedra are asymmetrically arranged at the corner, which is the most common type of structural distortion in DPs [2]. To examine the distortion, we have calculated the overall tilting in the unit cell by measuring the angle between the two octahedra along O_1, and O_2 ions. The angles of octahedra with respect to O_1 and O_2 are found to be 143.46^0 and 145.23^0 respectively, which are shown in Figure.5.2 (b,c). When the angle between the two octahedra in a perfect DP is 180^0, the SE interactions are expected to be stronger as governed by Goodenough and Kanamori [38,39] rule.

In the present sample, the deviation of the angle from 180^0, indicates a structural distortion which may also cause ASD leading to Fe^{3+}-O^{2-}-Fe^{3+} and Cr^{3+}-O^{2-}-Cr^{3+} AFM spin couplings. Gaikwad et.al. detected this kind of characteristic in Pr_2FeCrO_6 nanoparticles [135]. The elemental stoichiometry is confirmed by the EDS spectra as shown in Figure.5.2. (d). Inset of Figure.5.2 (d) shows the elemental mapping and confirms the homogeneous distribution of all the elements present in the compound.

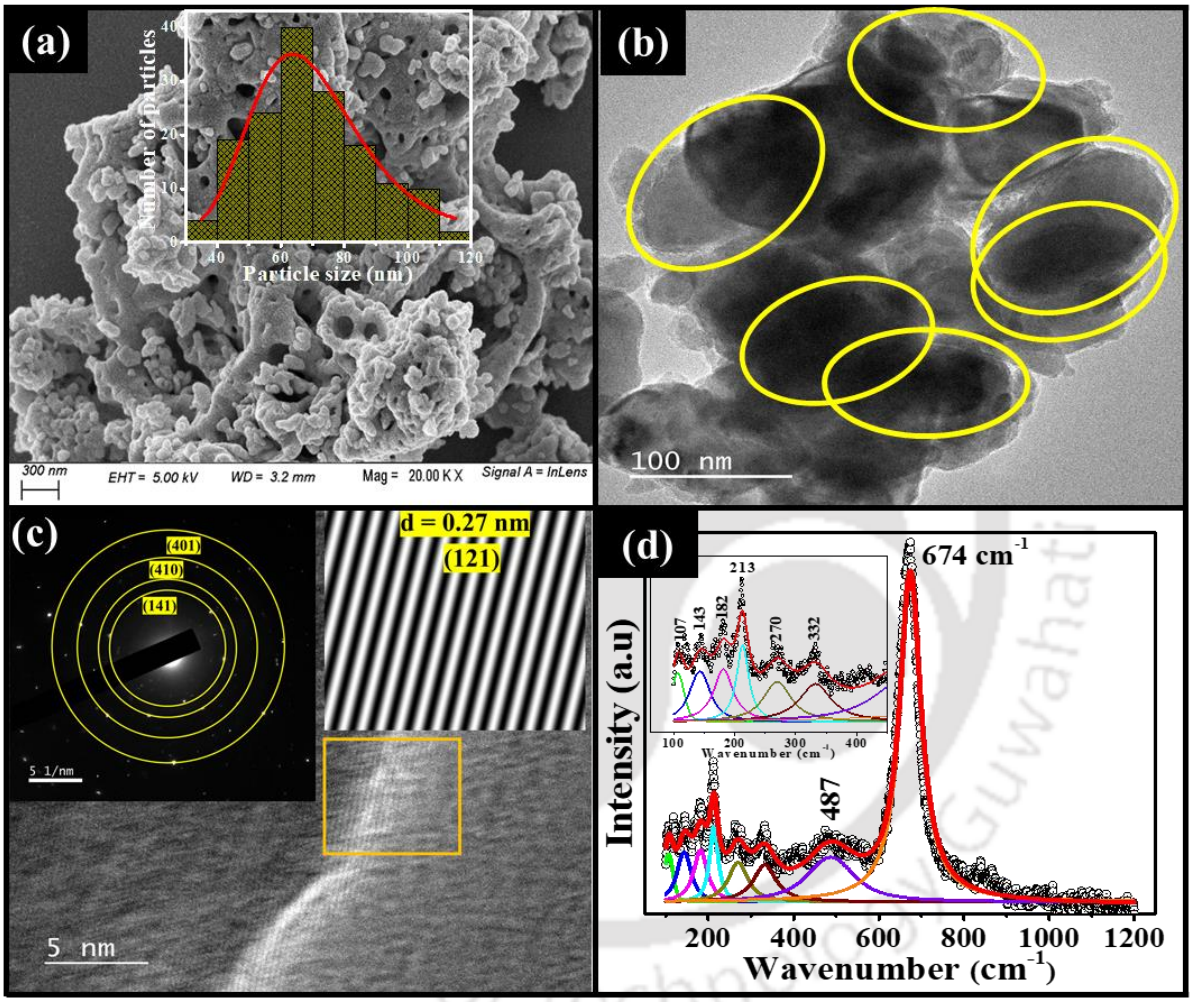

Fig.5.3. (a) FESEM image, along with the log-normal fitting (inset), (b) TEM image, (c) HR-TEM and SAED pattern and (d) Raman spectra for the YFCO sample.

The FESEM microstructural images of *YFCO* samples is shown in Figure.5.3 (a). The average particle size calculation of it is shown in the inset of Figure.5.3 (a). It can be seen from the figure that the particles are oval in shape and are well separated from each other. The calculated average particle size is found to be 67 nm (±2). The development of YFCO nanoparticles is further confirmed by the TEM image which can be seen in Figure.5.3 (b). From the HR-TEM (Figure.5.3

(c)), the (121) plane is confirmed. However, other planes such as (141), (410), (401) are confirmed by the SAED pattern (Figure.5.3 (c)). In order to further study the effect of reduced particle size on the crystal structure and to get a further confirmation on the phase purity, we have recorded RT Raman spectra in the wave number range of 100 to 1400 cm^{-1} and they are shown in Figure.5.3 (d). RE based orthorhombically distorted perovskite structure with *Pnma* space group is known to exhibit 24 Raman active modes namely $7A_g + 5B_{1g} + 7B_{2g} + 5B_{3g}$ [280]. Here, we have observed eight prominent Raman modes at ~107, 143, 182, 213, 270, 332, 487 and 674 cm^{-1}. This is the typical sign for an orthorhombic system, and it is comparable to the previously reported DPs having orthorhombic structure [280], it confirms the orthorhombic phase formation of our compound. The Raman modes observed below 200 cm^{-1} are mainly associated with the vibrations of the RE ions while the Raman modes observed in the mid spectral region are sensitive to the change in the orthorhombic distortion of the lattice. The phonon modes observed in the higher wave number region (487 cm^{-1} and 674 cm^{-1}) are mainly associated with the vibrations of the (Fe/Cr) O_6 octahedra.

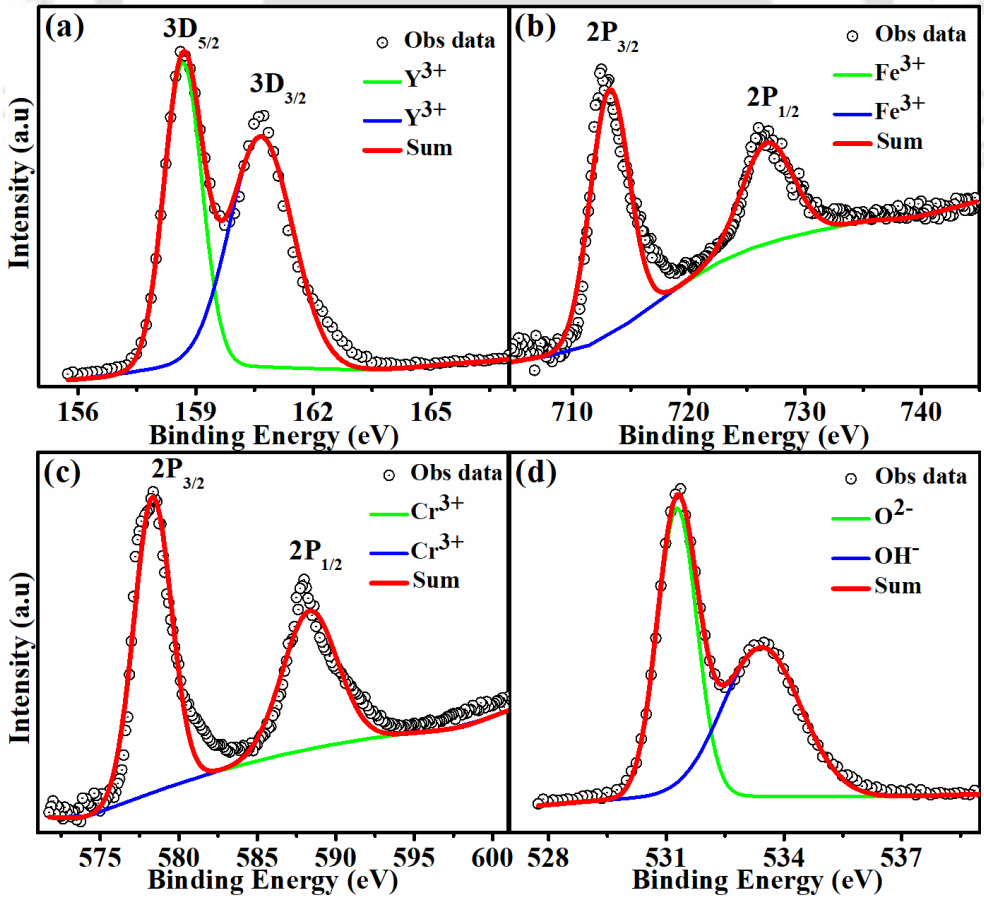

Fig.5.4. XPS data for (a) Y3D, (b) Fe2P, (c) Cr2P levels and (d) O1s respectively.

In order to get an idea about the oxidation states of each element in YFCO sample, we have carried out the RT XPS measurement (Figure. 5.4 (a-d)). The oxidation states of Y are measured by deconvoluting 3D peaks. The oxidation states of Fe/Cr were measured by deconvoluting $2P_{3/2}$ and $2P_{1/2}$ peaks. Whereas, the oxidation states of oxygen are measured using deconvoluted O1s peaks. The 3D core-level spectrum of Y is shown in Figure. 5.4 (a) which consists of peaks at 158.67 eV and 160.66 eV. The observed peak position of Y confirms the 3+ oxidation state of Y [281]. The 2P core-level spectrum of Fe and Cr are shown in Figure. 5.4 (a, b). The peak position of Fe is 713.17 eV and 726.70 eV, whereas, for Cr the peaks are at 578.33 eV, and 588.34 eV respectively. The obtained position of the peaks for Fe and Cr indicates both of them are in 3+ oxidation states [282,283]. Figure.5.4 (d) shows the XPS for O1s peaks of oxygen, it shows two distinct peaks, here also we found two peaks at 531.27 eV and 533.42 eV respectively. The former one is ascribed to the presence of O^{2-} in a typical metal-oxygen bond. However, the later one corresponded to the hydroxyl groups OH^- through O-H bonds respectively [260].

5.2 Magnetic properties

MT measurements were performed for YFCO nanoparticle under both ZFC and field FC conditions by applying various magnetic fields ranging from 100 Oe to 5 kOe within a temperature range of 5 to 300 K as shown in Figure.5.5 (a-f). From the graph, it can be seen that, the AFM ordering temperature (T_N) is present above the measured range of temperature i.e. above 300 K. For $T < T_N$, a peak like structure is observed in all FC MT plots i.e., for different applied fields near 300 K (T_{peak}). The weak ferromagnetic (WFM) component arising out of a canted spin structure of AFM ordered Fe^{3+}/Cr^{3+} ions are likely to play a role in the above magnetization peak [90]. For H = 100 Oe and $T < T_{peak}$, both ZFC and FC curves show a continuous decrease in magnetization towards negative value and cross the temperature axis with compensation temperature $T_{comp} \sim 192$ K. Furthermore, below T_{comp}, magnetization keeps on decreasing towards negative value and attained a negative maximum of -10.7 emu/mole in the ZFC mode and -12 emu/mol in the FC mode with a small bifurcation below 150 K. Raising the field to 500 Oe, a similar trend is observed but with a decrease in T_{comp} value to 172 K. In addition to this, a small hump like structure is noticed in both ZFC and FC curves at T~30 K, which is ascribed to the spin reorientation transition (T_{SR}). Earlier such spin reorientation is reported in orthochromites as well as in orthoferrites such as $RFeO_3$, $RCrO_3$ and $RCr_{1-x}M_xO_3$ (M = Fe, Mn) [206,208]. Here, the magnetic ground state is generally spin canted AFM (CAFM) across Fe^{3+}/Cr^{3+} ions [90,206,208].

As a result, the WFM component is observed given by the magnetic structure of Γ_4 ($G_x A_y F_z$). Further cooling aids the reorientation of magnetic spins of Fe^{3+}/Cr^{3+} sublattices to the magnetic structure of Γ_2 ($F_x C_y G_z$) [76,90,208]. Further raising the field towards 5 kOe, we have found the following changes in MT plots:- (i) An upward shift in the entire MT curve i.e., towards positive M axis. (ii) shifting of T_{comp} towards low temperature i.e., from 192 K for 100 Oe to 66 K for 3 kOe. (iii) suppression of peak at T_{SR} and its disappearance for 5 kOe; where only an upward trend is observed at low temperature. (iv) Increase in bifurcation between M_{ZFC} and M_{FC} below 200 K. Even though $M_{FC}>M_{ZFC}$ below T_N, the M_{FC} value is found to decrease continuously with temperature by crossing the M_{ZFC} at 210 K. It can be understood in this way:- one can expect a higher FC magnetization value in a typical FM material. However, in this system main interaction is AFM, when the system is in FC mode, the domains are aligned with ease, leading to smaller magnetization. The obtained T_{comp} of 155 K at 1 kOe is comparable to the reported T_{comp} value for $LaFe_{0.5}Cr_{0.5}O_3$ compound at 1 kOe [207,284]. The upward shift in magnetization can be attributed to field induced enhancement in the WFM component and such shifting gives rise to a reduction in T_{comp} value. The sharp rise in magnetization at low temperatures is mainly due to the suppression of spin reorientation and the forced alignment of part of AFM moment along the field direction. We can observe that the shape of the ZFC curve mimics the FC data in the low applied field, implying that they may have a similar microscopic origin.

Below 210 K, the MT curves for all applied fields exhibit negative irreversible magnetization ($(M_{FC} - M_{ZFC})/M_{ZFC}$) i.e., $M_{FC}<M_{ZFC}$ as shown in Figure.5.6 (a). This type of negative irreversible magnetization is also reported by several authors in Fe/Cr based perovskites structure [206,207,208,285]. The absolute value of fractional irreversible magnetization, $|\Delta M/M_{ZFC}| = |(M_{FC} - M_{ZFC})/M_{ZFC}|$ is found to decrease with an increase in an applied field. This could be due to the quick alignment of a considerable number of domains for a large applied field even in ZFC condition. This makes the difference smaller with respect to the FC case. In a large applied field even in ZFC condition considerable fraction of AFM domains get aligned, leaving a small fraction of domains left out for further improvement under the FC case. So automatically irreversible magnetization decreases with an increase in field. Thermal hysteresis is a phenomenon in which a system is affected not just by temperature but also by its previous thermal history. It is used to compare the behavior of the magnetic system by heating as well as cooling through the same temperature range.

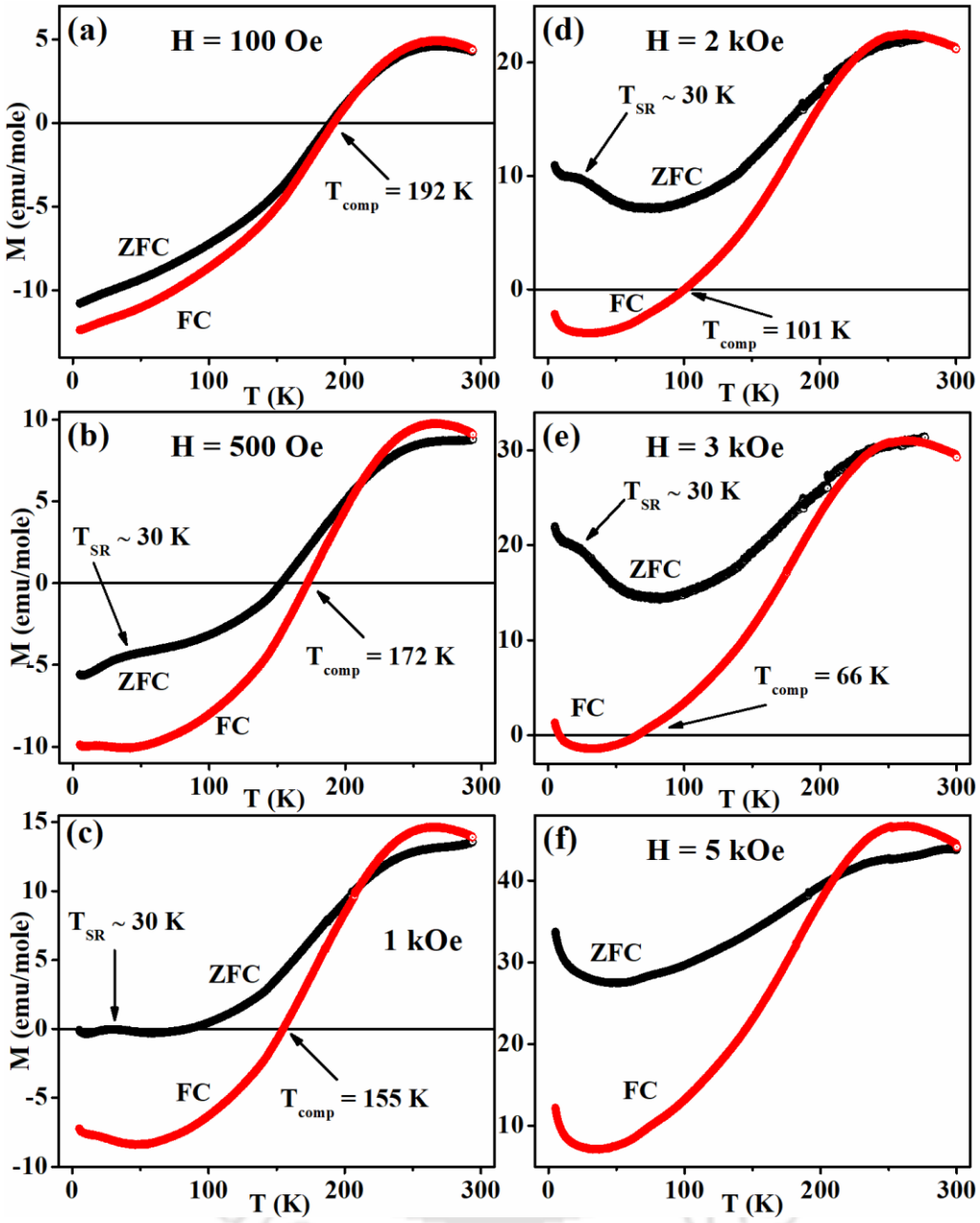

Fig.5.5. Thermomagnetic plots under ZFC and FC conditions for (a) H = 100 Oe, (b) H = 500 Oe, (c) H = 1 kOe, (d) H = 2 kOe, (e) H = 3 kOe and (f) H = 5 kOe.

From Figure.5.6 (b), shows a clear irreversibility between FC MT plot during the cooling (FCC) and warming (FCW) process. Madiligama et. al also observed a similar kind of behavior in the alloys and attributed it to the magnetic phase transformation from a FM to a low magnetization phase upon cooling and from a low magnetization phase to a FM phase upon heating [286]. Thermal hysteresis also represents the first order magnetic phase transition in the system [72,73].

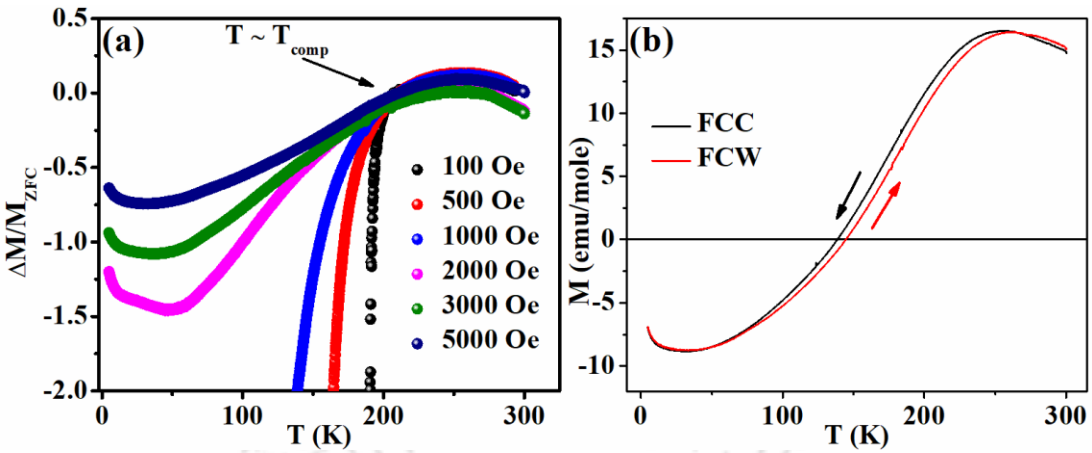

Fig.5.6. (a) Fractional irreversible magnetization versus temperature plots for various applied fields and (b) FC MT plots during cooling and warming processes.

From the field variation of MT plots, we found that T_N should present above 300 K. So, in order to find out the transition temperature, we have carried out the MT measurement at an applied field of 1 kOe in the temperature range of 300 K to 900 K in the ZFC mode as shown in Figure.5.7 (a). From the MT plot we have observed a monotonous increase in magnetization value with decrease in temperature, and a peak like structure around 300 K. This is consistent with part of the peak observed in the vicinity of 300 K in the low temperature MT plot. The transition temperature, T_N = 327 K is found as the AFM transition. Figure.5.7 (b) shows the inverse susceptibility versus temperature plot. Here one can see the linear behavior at high temperature (> 500 K) then it started showing a downfall trend. Around T = 320 K, a sharp fall is observed which is the T_N. We have used the Curie Weiss law as defined in the Eqn. 1.6. The values of C and θ_C are determined as 6.94 emu.K.mol^{-1}.Oe^{-1} and -154 ± 0.34 K respectively. The negative value of θ_C validates the dominating AFM exchange interaction of the system. The relation $\mu_{eff}^{exp} = \sqrt{3k_B C/N_A}$, and $\mu_{eff}^{th} = \sqrt{[2 \times \mu_Y^2 + \mu_{Fe3+}^2 + \mu_{Cr3+}^2]}$ [136] are used to calculate the experimental and theoretical effective moment of the sample. Here k_B and N_A are Boltzmann constant and Avogadro number, μ_Y, μ_{Fe3+}, μ_{Cr3+} are basically the spin only effective magnetic moments of yttrium, iron, and chromium ions respectively. From the relations, μ_{eff}^{th} and μ_{eff}^{exp} values are found to be 7.07 μ_B/f.u. and 7.45 μ_B/f.u. respectively. The observed difference between theoretical and calculated values could be due to some orbital moment contribution.

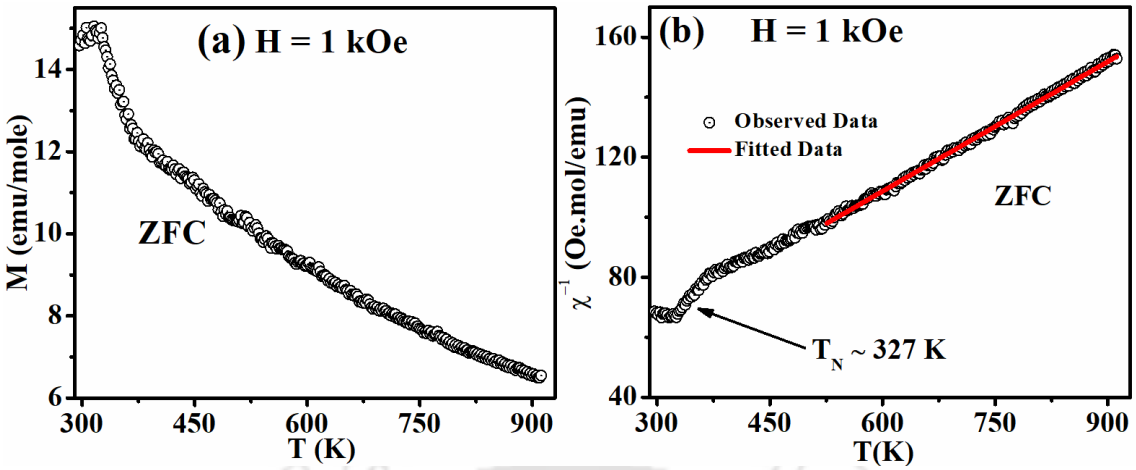

Fig.5.7. (a) Zero field cooled M-T plot at 1 kOe from 300 to 900 K, (b) Inverse susceptibility versus T data along with the linear Curie wiess fit.

(i) Study of Magnetization Reversal

It should be noted that the trapped field in the superconducting magnet can have an effect on the ZFC data. Therefore, before each measurement, we removed the trapped field by bringing the field to zero from a high field in oscillation mode. However, we have seen multiple reports on DPs, where the observation of MR in ZFC mode is very common and is attributed to the APB developed due to the ASD in B/B' crystallographic sites of the system [57,65,287]. Hence, a low magnetic field is insufficient in the ZFC mode to overcome the APBs and orient the frozen spins of clusters and domains along with the applied field direction. As a result, as the temperature is decreased, the antiparallel or canted spins get stabilized, and the net magnetization tends to be negative [50]. Whereas a few authors have attributed the MR to intrinsic property [248].

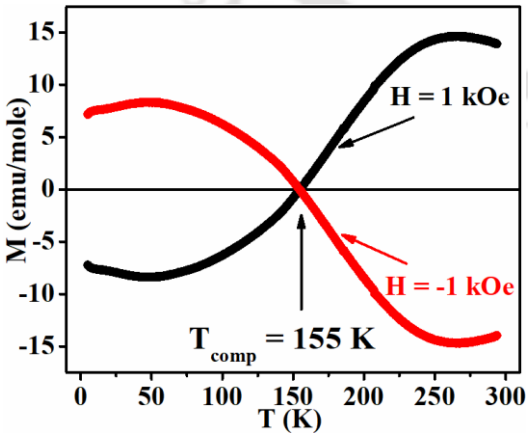

Fig.5.8. M - T plots under FC condition at an applied field of H = ± 1 kOe.

Furthermore, in order to make sure that the obtained MR in FC mode is not due to any instrumental artifacts, we have carried out the FC MT measurement for H_{FC} = ±1 kOe as shown in

Figure.5.8. From the figure in can be seen that, they are mirror image to one another of opposite applied field and hence it confirms that the MR is the intrinsic property of the compound. The trend of FC MT plots in this system is similar to that reported in $YFe_{0.5}Cr_{0.5}O_3$ [204,252,288], $CeCr_{1-x}Fe_xO_3$ [289], $LaCr_{0.5}Fe_{0.5}O_3$ [207] and $BiFe_{0.5}Mn_{0.5}O_3$ [205,140,267]. In the perovskite compounds such as $YFe_{0.5}Cr_{0.5}O_3$ [204] and $LaFe_{0.5}Cr_{0.5}O_3$ [206,207], authors have explained that the competition between SIA and DM interactions is the reason for MR. The $La(Cr,Fe)O_3$ and YVO_3 exhibit distorted perovskite structure due to the tilting of CrO_6/FeO_6 and VO_6 octahedra and it gives rise to the canted spin structure [73]. Because of the titling of CrO_6/FeO_6 and VO_6 octahedra, the intermediate oxygen ion is not at the inversion center of two Cr/Fe/V ions, resulting in an antisymmetric interaction known as the DM interaction. Furthermore, the tilting of $CrO_6/FeO_6/VO_6$ and the corresponding staggered Cr-O/Fe-O/V-O bonds cause the SIA axis to be staggered.

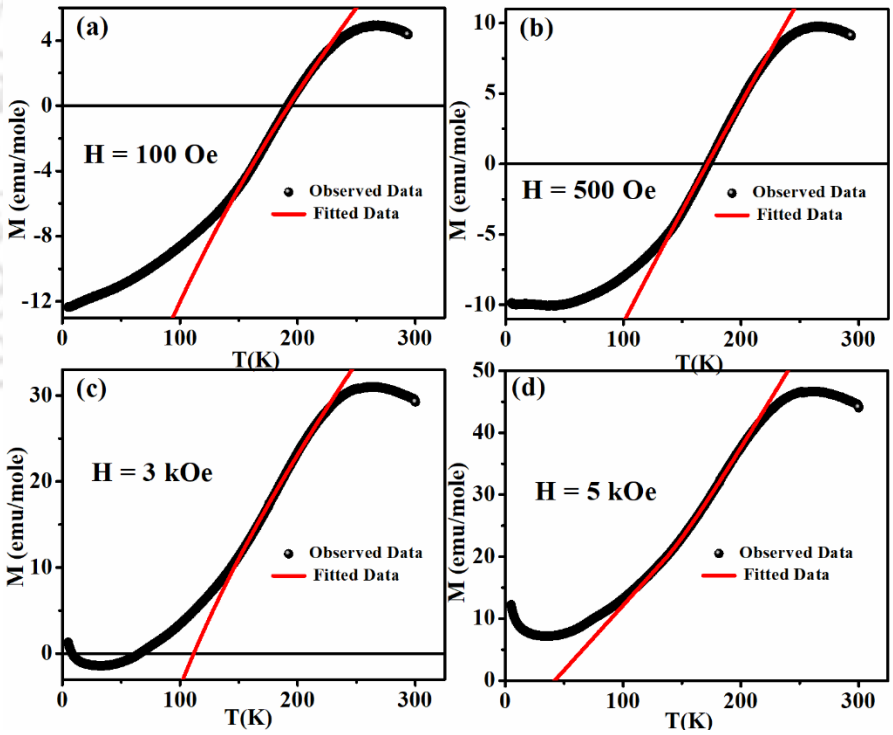

Fig.5.9. (a) The fitted curve of FC M-T data to equation (1.22) at various field for (a) 100 Oe, (b) 500 Oe, (c) 3 kOe, (d) 5 kOe respectively.

In the present case, we have observed tilting of FeO_6/CrO_6 octahedra as previously shown in Figure.5.2 (a) and as per the previous reports on Fe/Cr base perovskites structure it leads to a canted spin structure [73,206]. Here the AFM interaction is expected from Cr^{3+}-O^{2-}-Cr^{3+}, and Fe^{3+}-O^{2-}-Fe^{3+} networks. Since, oxygen ions mediating the SE interaction between two nearest neighbor

ions (Fe/Cr). Since, these two ions are not at the inversion center due to structural distortion. Hence, this leads to DM interaction [140]. In addition to that, the tilting of $(Fe/Cr)O_6$ octahedra results into the staggered Fe/Cr-O bonds and it further leads to staggering of SIA axis [141]. Based on SIA, DM, and AFM interactions the energy of the system can be written as an equation as described in Eqn. 1.16. However, the net magnetic moment of the CAFM system will be represented by Eqn. 1.22.

We have used the Eqn. 1.22 to fit the observed MT data and obtained the fitted parameters. The fitted data at various applied fields are shown in Figure.5.9 (a-d) as the red solid lines. However, the low temperature data are deviating from the fitting, one of the possible reasons is the presence of T_{SR} and also the anisotropy/FIM interaction between Fe^{3+}/Cr^{3+} ions at low temperature. From the fitted parameters, we have calculated the values of γ_D and ξγ and found that γ_D value decreases and ξγ value increases with increase in magnetic field. The values of ξγ and γ_D are found to be in the range of 1.4×10^{-8} to 406×10^{-8} and 5.7 to 0.002 for 100 Oe to 5 kOe respectively. The typical value of ξγ at 100 Oe is found to be 1.4×10^{-8}, and it is very much equivalent in order and magnitude as reported by Ren et.al. for YVO_3 single crystal [73]. However, the γ_D value is much higher than that of reported by both Ren et.al. for YVO_3 single crystal [73] and Tribedi et.al. for $LaFe_{0.5}Cr_{0.5}O_3$ [206]. By observing the ξγ and γ_D values, one can say that the contribution of SIA is getting enhanced and the DM interaction becomes weakened with rise in field. By using the mean field model, the AFM coupling constant (J) can be calculated by the relation, $J = \frac{3k_B T_N}{S(S+1)}$, and the value is found to be 48 K (4.13 meV). As ξ = A/J, we found a large value of anisotropy constant such as 206 K (18 meV) at 100 Oe, which is quite comparable to that of YVO_3 single crystal [73]. Similarly, the estimated value of D is found to be in the range of 546 to 0.2 K for 100 Oe to 5 kOe. Which is quite large from the reported values by Ren et. al. for YVO_3 single crystal and Dasari et al. [73,204] for $YFe_{1-x}Cr_xO_3$ compounds.

The presence of MR in this compond encouraged us to go for the demonstration of BSM, which is shown in Figure.5.10. In order to perform the BSM, we have FC the sample down to 50 K by crossing the T_{comp}, with an applied field of 1 kOe. Once it reaches to 50 K, we have recorded the magnetization value for 100 sec and observed that it gives a negative value. Then by increasing the field up to 3550 Oe and again recorded the magnetization for 100 sec, we found the magnetization switching over to the positive value. This procedure was performed multiple times,

changing the field from 1 kOe to 3550 Oe and back to 1 kOe, a consistency in the BSM is observed. This result indicates reproducible field induced BSM.

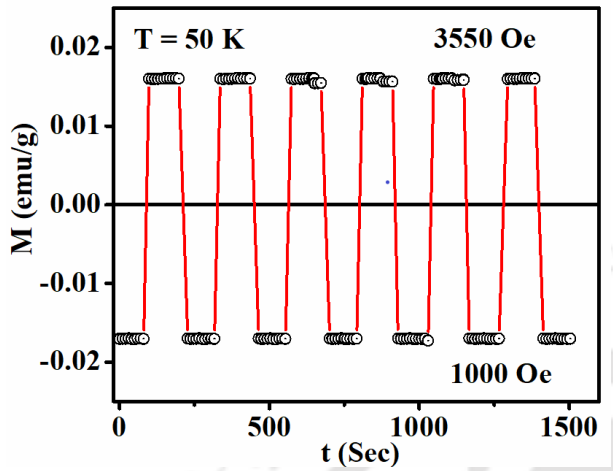

Fig.5.10. Bipolar switching of magnetization at 50 K between the field of 1 kOe and 3550 Oe.

(ii) Study of Spontaneous Exchange Bias Behavior

The MH loops recorded at 5 K for magnetic field up to ± 9 T are shown in Figure.5.11 (a). From the graph we found a predominant linear behavior with a small hysteresis. Which is an indication of uncompensated spins or a predominant AFM exchange interaction, which does not allow the spins to align along the direction of the applied field. In addition to that the shape of the loop is not a normal MH type, one can see that the loop in the vicinity of the origin (M = 0) has some minor elliptical hysteresis loop. So, we have calculated and plotted the loop width versus magnetization (ΔH-M) as shown in the inset of Figure.5.11 (a). Unlike the typical MH loop (where the loop width should be maximum at M = 0), we got two maximum values of loop width on either side of M = 0. This type of trend in the ΔH-M is attributed to the presence of multiple magnetic phases in the compound [268]. Figure.5.11 (b) shows the expanded MH loop at 300 K, where we can see a clear loop in the low field region, which indicates the presence of some WFM moment due to the canted moments of Fe^{3+}/Cr^{3+} ions. We have used the LAS model [267], explained in Equation 3.2 to determine the magnetization saturation (M_S) as shown in Figure.5.11 (c) and the M_S value is found to be 0.02 ± 0.001 μ_B/f.u. Other parameters such as effective coercivity (H_{ceff}), magneto crystalline anisotropy constant (k) and the anisotropy field (H_a) are found to be 2243 Oe, 2.38×10^4 erg/cm^3 and 24.5 kOe respectively. To minimize any minor loop effect, the anisotropy field (Ha) should be modest in comparison to the optimal maximum applied magnetic field. In our case the H_a is found to be 24.5 kOe which is quite smaller than that of $LaSrCoFeO_6$ [43] and much higher than those of Sr_2FeCoO_6 [42] and Y_2CoMnO_6 [61]. Here, the obtained value of M_S is quite

small, which indicates the dominant nature of AFM ordering. However, the non-zero M_S value indicates the presence of WFM moment. The WFM is mainly attributed to the spin canted AFM interaction in Fe^{3+}/Cr^{3+}-O^{2-}-Fe^{3+}/Cr^{3+} networks due to the lattice distortion in FeO_6/CrO_6 octahedra. The shape of the initial MH curve at 5 K is quite irregular, so, we have taken the initial isotherm MH loops at different temperatures and presented the dM/dH versus H plots which are shown in Figure.5.11 (d). A clear peak around 25 kOe field followed by a sharp rise in dM/dH for H < 10 kOe is an indication to the presence of multiple magnetic/metamagnetic phase [71,143].

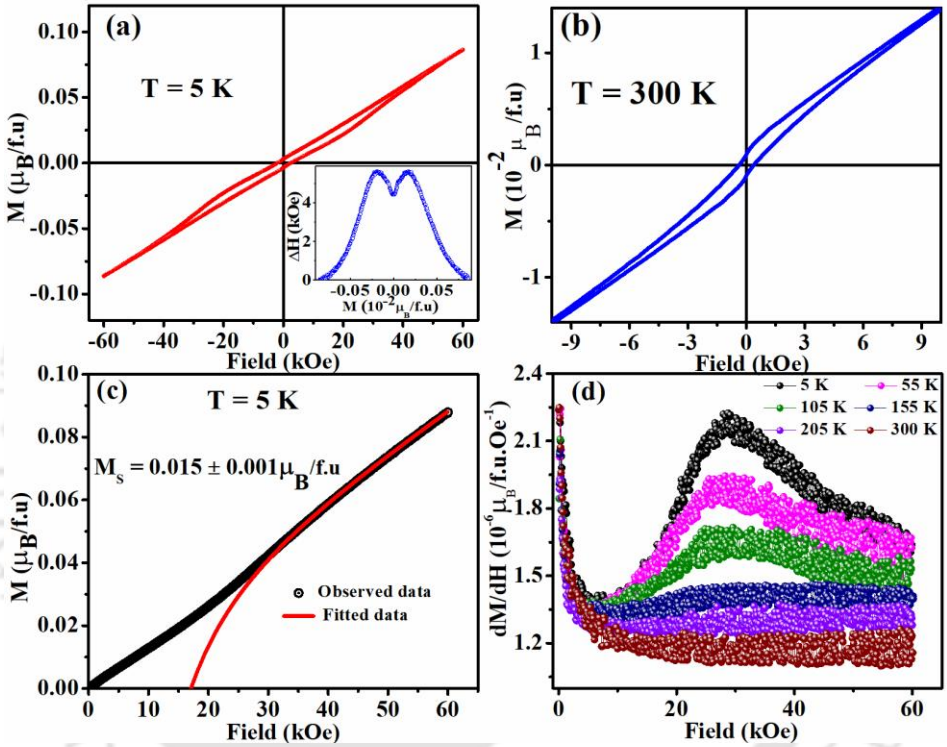

Fig.5.11. Magnetization versus field plots, (a) at 5 K, inset shows loop width versus magnetization, (b) at 300 K, (c) initial curve along with the LAS fitting and (d) dM/dH versus field at various temperature.

We have noticed a shift in the ZFC MH loop along the magnetic field axis, which was not reported earlier in this sample. However, there are several reports on spontaneous EB (SEB) field such as in $Co_{0.8}Cu_{0.2}Cr_2O_4$ ceramics, DPs $La_{1.5}Ca_{0.5}CoIrO_6$, $Sm_{1.5}Ca_{0.5}CoMnO_6$ etc., nanocomposites of $(La,Sr)MnO_3/PbZr_{0.8}Ti_{0.2}O_3/(La,Sr)MnO_3$) and $BiFeO_3$−$Bi_2Fe_4O_9$ and Ni-Mn-In based heusler alloys [224-229]. Rigitano et. al. reported the SEB in Co/Mn based DP and attributed it to the uncompensated AFM coupling between the sublattices [229]; Maity et. al. [226]

and Giri et. al [230] explained it in terms of core- shell model with competition between FM and AFM components. Wang et. al justified this process by considering the interface between different magnetic phases during the initial magnetization process [224]. Murthy et. al attributed it to the large unidirectional anisotropy at the interface of isothermally field induced FM phase and CAFM background [46]. The coupling interaction between the two sublattices is reported to give rise to SEB, as per Wang et. al in 2015 [227].

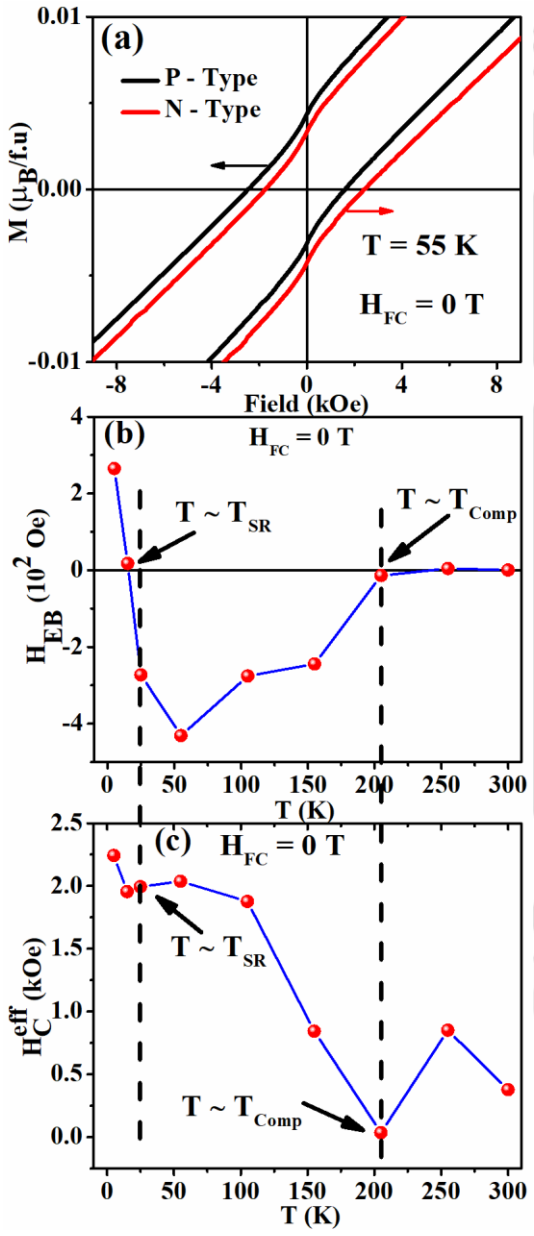

Fig.5.12. (a) the ZFC MH loops at 55 K followed by two different protocols namely P-type and N-type, (b) H_{EB} versus T plot under ZFC condition and (c) effective coercivity versus T plot.

As we have mentioned in the introduction, the loop shift in the ZFC MH plot is generally considered as the stray field effect. Therefore, we have carried out MH loop at 55 K using two

protocols namely P-type and N-type. Here, P-type refers to the measurement protocol of 0 → +6T → -6T → +6T, and the N-Type refers to 0 → -6T → +6T → -6T protocol. The P-type and N-type loops are shown in Figure.5.12 (a). They are clearly showing the loop shift on either side of the field axis for the two different protocols. It justifies the intrinsic SEB in the YFCO nanoparticles. Furthermore, from the initial MH curve (5 K), one can see that the starting value of the magnetization is zero, i.e., unmagnetized, which clearly rules out any stray field effect. To further analyse this SEB phenomena we have taken several ZFC MH loops at various temperatures from 5 K to 300 K, with a maximum applied field of ± 6T. We have estimated the EB field value (H_{EB}) as well as the effective coercive value (H_{Ceff}) and presented the graph with respect to temperature (Figure.5.12 (b, c). The maximum absolute values of H_{EB} and H_{Ceff} are found to be 431 Oe at 55 K and 2243 Oe at 5 K. It is clearly seen from the figure that the sign of the H_{EB} is changing from positive to negative in the vicinity of T_{SR} and then decreases with rise in temperature and it is almost vanishing from T_{comp} to 300 K. The value of H_{Ceff} also shows some anomaly near T_{SR} as well as T_{comp}. It shows two peaks on either side of T_{comp}, and two minimum values at T_{SR} as well as at T_{comp}.

(iii) Study of Conventional Exchange Bias Behavior (CEB)

After observing a large SEB field, we have encouraged to study the CEB. For this, we have carried out several FC MH loops at various temperatures ranging from 5 K to 300 K, after cooling the sample under a field of H_{FC} = 0.5 T, as shown in Figure.5.13 (a-f). A clear shift of MH loops along the field axis is noticed; for a clear view, they are presented in expanded form. However, to clarify the stray field effect, we have taken the MH loops for both H_{FC} = ± 0.5 T at 5 K as shown in Figure.5.14 (a). The symmetric shifting of loops for + 0.5 T and - 0.5 T fields towards positive and negative field axes confirms that the EB behavior is intrinsic. From Figure.5.13 (a-f) one can see an irregular shifting of the loop with respect to temperature. So, after calculating the H_{EB} value, its variation with respect to temperature is shown in Figure.5.14 (b). The maximum value of H_{EB} is found to be 2.1 kOe at 5 K, which is 10 times higher than the SEB value at 5 K. Further increasing the temperature, it shows a monotonous drop in its value, then at T_{comp} it is almost zero and above T_{comp}, it drops to a negative value. Further rise in temperature, a valley like feature is observed followed by H_{EB} going towards zero at a higher temperature, i.e., in the vicinity of T_N. Effective coercivity (H_C^{eff}) versus temperature is shown in Figure.5.14 (c). It shows two peaks on either side of T_{comp} with a minimum value at T_{comp}. This behavior, that is the sign reversal of CEB and the

observed two peaks in the H_C^{eff} are comparable to the reports on perovskite based $LaCr_{1-x}Mn_xO_3$ [140], spinel compound of $Co(Cr_{0.95}Fe_{0.05})_2O_4$ [285] and some intermetallic alloys [234,235].

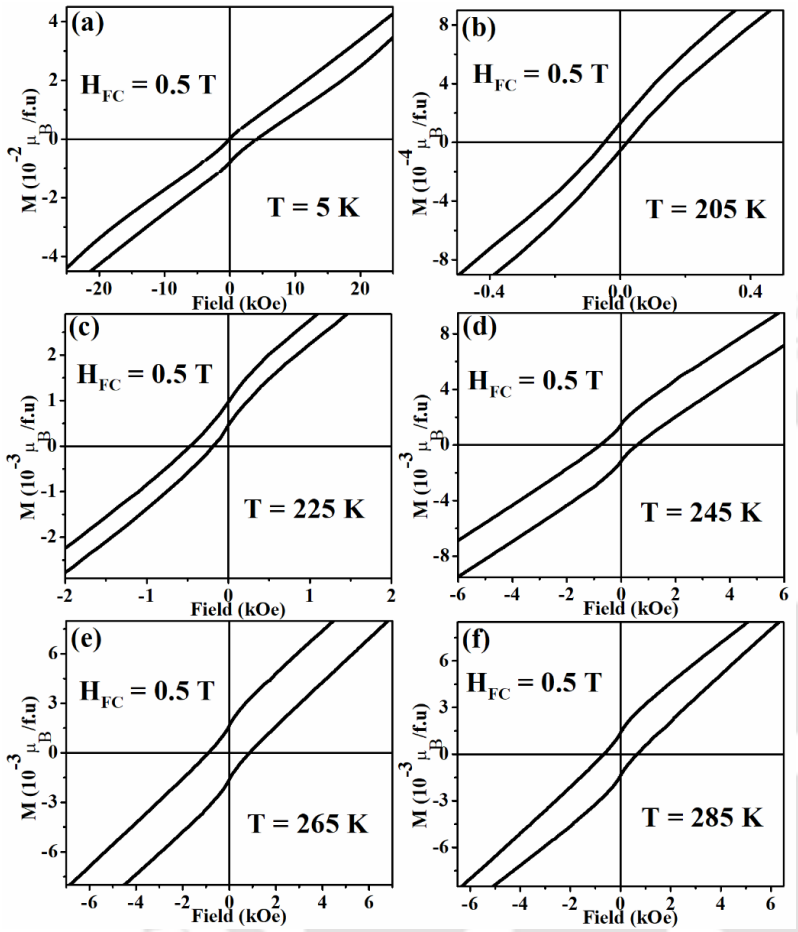

Fig.5.13. (a-f) The enlarged view near coercivity for FC M-H loops measured at various temperature from 5 to 300 K.

After looking at all the magnetization measurements, a discussion can be made that, in YFCO nanoparticles. The observed magnetization value is found to be very small and it is attributed to the AFM interaction between Fe^{3+}-O^{2-}-Fe^{3+} and Cr^{3+}-O^{2-}-Cr^{3+} networks. In this compound, the competition between DM interaction and SIA is considered as the reason for MR. This is further confirmed experimentally, by fitting the observed MT data to Eqn.1.22 and extracting the respective values. Here, the obtained SIA and DM constants are much higher than those of earlier reports on perovskite $LaFe_{0.5}Cr_{0.5}O_3$ [203], $YFe_{0.5}Cr_{0.5}O_3$ [204] and YVO_3 [73].

The MR and EB behavior are explained as follows. Just below T_N, if the SIA is significant, the two sublattice spins prefer to reside near to a local easy axis, resulting in a net magnetic moment along the applied field direction. This net moment will initially increase when the temperature falls due to the growth of SE interaction and hence sublattice magnetization. However, when the

sublattice magnetization grows, so does the antisymmetric coupling (DM interaction), which causes the spins to cant. As a result, as temperature decreases, the net moment reaches a maximum value and subsequently decreases. Further lowering of temperature strengthens DM interaction. At T = T_{comp}, the strength of both SIA and DM interactions are equivalent and leads to a zero

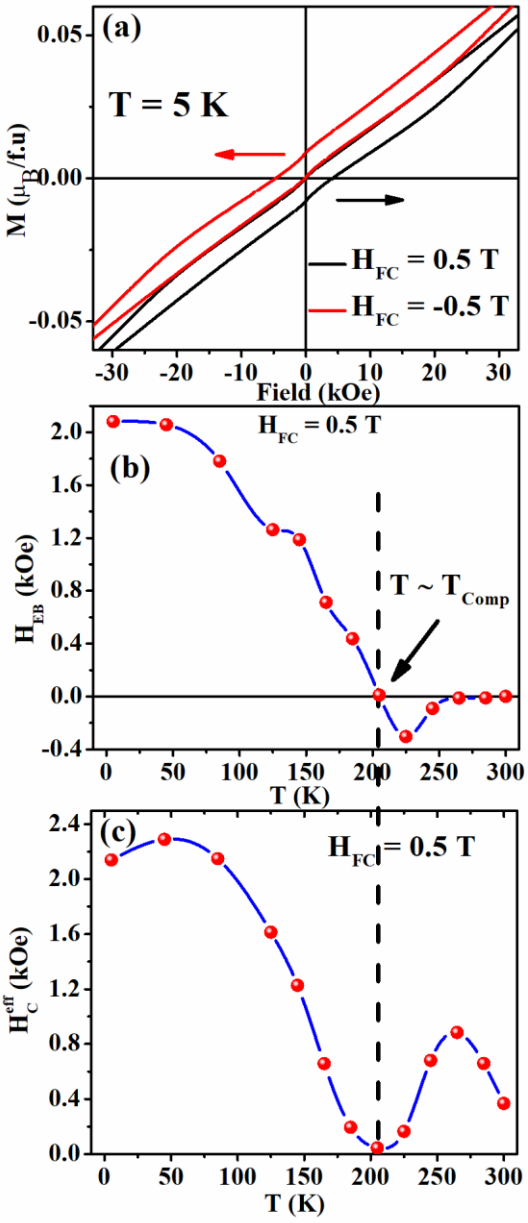

Fig.5.14. (a) Enlarged view of FC MH loop taken at H_{FC} = ± 0.5 T (b) H_{EB} versus T plot and (c) effective coercivity versus T.

magnetization. As temperature falls below T_{comp}, the DM interaction takes over and thus contributes to the magnetic moment, opposite to the applied field. Hence, below T_{comp} MR is observed. A strong external magnetic field can overcome the barrier to sublattice spin rotation, resulting in a reversal of sublattice spin orientation. Which can be seen from the MT plots carried

out at H = 5 kOe. Now coming to the sign reversal of both SEB and CEB. As explained above, below T_{comp} a strong positive field is required to align the spins along the field directions as the DM interaction is stronger. Hence below T_{comp} the FC MH is shifting towards the positive field axis. However, with increasing the temperature both the DM interaction and SIA are getting weakened as they are approaching towards the T_N which leads to a drop in H_{EB} value. At T_{comp} both SIA and DM interaction has equivalent strength, so H_{EB} is zero at T_{comp}. Whereas, above T_{comp}, a small negative H_{EB} is observed, which is possibly due to the flipping of spins by DM interaction. Further raising the temperature, the thermal energy dominates over the competition of magnetic interactions and thus the CEB value is decreasing towards zero. In SEB, the same phenomenon plays a role but the thermal energy overcomes the competition between SIA and DM at a lower temperature as compared to CEB. That's why the sign in SEB is changing near T_{SR} instead of T_{comp}.

5.3 Conclusions

In summary, single phase nanoparticle of Y_2FeCrO_6 DP were prepared by auto combustion method. Structural studies confirm that the sample is crystallized in the orthorhombic phase with the Pnma space group. FESEM and TEM study confirms the formation of nanoparticles with an average size of 67 nm. Presence of all the elements with desirable atomic percentage is confirmed by EDS analysis. Presence of Fe and Cr in the oxidation states of 3+ has also been confirmed by XPS analysis. According to the MT measurements, the system has an AFM transition with a T_N of 327 K. This AFM transition is attributed to arise from the SE interaction in Cr^{3+}-O-Cr^{3+}, and Fe^{3+}-O-Fe^{3+} networks. A MR with a compensation temperature (T_{comp}) of 192 K at 100 Oe and a spin reorientation with T_{SR}~30 K are observed. At 55 K, spontaneous exchange bias (SEB) field exhibit a maximum negative value of -431 Oe. However, after field cooling the sample at 0.5 T, the maximum value of the conventional exchange bias field (CEB) is found as 2.1 kOe, at 5 K. The SEB is confirmed by taking the MH loop in two different protocols (P-Type and N-Type). However, the CEB is confirmed by recording the MH loops, after cooling the samples in positive and negative applied fields. Both spontaneous and conventional EB field show sign reversal across T_{SR} and T_{comp} respectively. In addition to this, the MH loop investigation confirms the existence of a multi-magnetic phase. As well as a typical bipolar switching of magnetization has been demonstrated at 50 K. The above behaviors in the YFCO sample are quantitatively examined using a model that considers the competition between single ion anisotropy and DM interaction.

Chapter 6

Conclusions

This chapter deals with the summary of conclusions obtained from the experimental study of structural and magnetic properties of Sm doped Ho_2CoMnO_6 nanocrystalline, nanorods of Ho_2CoMnO_6, Ni and Cr substituted Ho_2CoMnO_6 nanocrystalline at Mn site and nanoparticles of Y_2FeCrO_6 DP compounds.

$(Ho_{1-x}Sm_x)_2CoMnO_6$ (x = 0.0 to 0.5) DP have been successfully prepared by auto combustion method. There are new results obtained on the influence of Sm substitution on the structural and magnetic properties of Ho_2CoMnO_6 nanocrystalline, particularly those related to the increase of FM T_C and EB field. So, in summary, study of RT XRD patterns reveals that these samples crystallize in monoclinic structure with $P2_1/n$ space group. The lattice parameters along with the unit cell volume are found to increase with Sm substitution. It is ascribed to the partial replacement of Ho^{3+} ions having smaller ionic radii of 1.015 Å with Sm^{3+} ions having larger ionic radii (1.079 Å). FESEM and EDS measurements confirm the nanocrystalline formation and the presence of respective elements respectively in the present series in the required atomic percentage. XPS study reveals the oxidation states of all the elements in the desired states. However, a little amount of Co^{3+} and Mn^{3+} are also observed. The MT measurements shows complex magnetic properties such as FM transition with peak like structure followed by secondary rise in magnetization. They are explained based on FM interaction in Co^{2+}-O-Mn^{4+} networks clubbed with AFM interaction at APBs and/or presence of Co^{3+}/Mn^{3+} ions in the compound. The FM transition is found to increase from 83 K for x = 0.0 to 115 K for x = 0.5. The secondary rise in magnetization is attributed to the polarization of RE ions moment along the field direction at low temperatures. The observed large M_S value of the order of 11.64 μ_B/f.u. at 5 K is ascribed to the FM interaction of some of RE ions with net magnetic moment of TM ions. These materials also show the EB behavior which is increasing with Sm concentration, with a maximum H_{EB} of 237 Oe at 5 K for x = 0.5 sample. This is attributed to the exchange anisotropy between the FM moment of TM ions and the spin canted AFM ordered Ho^{3+}/Sm^{3+} ions. As the Sm concentration is increased, the lattice distortion gives rise to further spin canting and enhanced exchange

anisotropy. Temperature variations of H_{EB} and H_C were analyzed based on exponential law and modified Kneller's law.

In order to investigate and tune the structural and magnetic properties specially the FM ordering temperature, we have prepared the single-phase flat nanorods of Ho_2CoMnO_6 by using a hydrothermal process. Here, we analyzed in detail the crystalline structure of the sample and its complex magnetic properties. The sample presents a nano structure, with some peculiar differences from the bulk counterpart. This translates to peculiar magnetic properties characterized by the occurrence of different magnetic orders at different temperatures, from high temperature dominant FM interactions to AFM ones at intermediate temperature values, and re-entrant spin-glass phenomena at low temperature. In addition, this complex panorama of magnetic features is confirmed by the analysis of MCE. In summary, room temperature XRD analysis state that the sample crystallizes in monoclinic structure with $P2_1/n$ space group as that of nanocrystalline Ho_2CoMnO_6. However, the lattice parameters, unit cell expansion as well as tilting angles are much higher than that reported for bulk sample of Ho_2CoMnO_6. FESEM and TEM study confirms the formation of HCMO flat nanorods with an average width of 71 (±3) nm. XPS analysis reveals a little contribution of Co^{3+} and Mn^{3+} along with the desired Co^{2+} and Mn^{4+} ions in the system. MT study at low fields show the FM transition at 182 K followed by AFM and re-entrant spin glass transitions at 97 and 31 K respectively. The higher FM transition as compared to bulk (83 K) is attributed to the strengthening of FM interaction in Co^{2+}-O-Mn^{4+} networks due to the increase in bond angle between CoO_6 and MnO_6 octahedra. The AFM transition is expected due to the presence of AFM coupling between the ASD ions. In addition, we have also observed a frustrated spin structure at low temperature for this system. The presence of two types of competing magnetic interactions such as FM and AFM leaves the system in a random frustrated spin configuration which leads to re-entrant spin glass behavior in HCMO flat nanorod at ~ 31 K. It is further confirmed by the measurements such as magnetic relaxation at ~ 25 K for different applied fields and aging behavior of the system. MH measurements at 5 K show that the system has uncompensated spin structure at low temperature with a small value of saturation magnetization (Ms). It is concluded that, the presence of multiple interactions in the compound leads to a lower value of M_S. From the study of MCE, we found that the HCMO flat nanorods exhibit FOPT with a maximum value of magnetic entropy as 12.4 J/kg.K.

After getting excited properties such as increase in FM T_C and H_{EB} in Sm substituted HCMO sample. We have prepared nanocrystalline $Ho_2CoMn_{1-x}Ni_xO_6$ (x = 0-0.4) series and investigated the structural, magnetic properties, MR and EB behavior. The magnetization data clearly demonstrate that Ni doping induces an additional FM phase, resulting in the magnetic compensation in the samples and a MR below T_{comp}, which is well confirmed by the BSM. In addition, the H_{EB} changes sign from negative to positive with Ni concentration. In summary, an auto combustion technique was used to prepare nanocrystalline samples of $Ho_2CoMn_{1-x}Ni_xO_6$ (x = 0.0 - 0.4) DP. XRD analysis reveals that the samples are formed in monoclinic structure with space group $P2_1/n$. A drop in the lattice parameters as well as unit cell volume are observed with Ni substitution. It is due to the partial replacement of larger Mn^{4+} ions (0.53 Å) with the Ni^{4+} ions (0.48 Å). The formation of nanocrystallines and the existence of the corresponding elements in the required atomic percentages are confirmed by FESEM and EDS measurements respectively. The oxidation states of all elements in the desired states are revealed by XPS analysis. However, traces of Co^{3+} and Mn^{3+} have been detected. The Raman shifting towards higher wavenumbers also supports the reduction in structural parameters. Unlike the parent compound, for all Ni doped materials, MT measurement reveals two FM phases. The two FM transitions are attributed to the SE interaction in Co^{2+}-O-Mn^{4+} and Co^{2+}-O-Ni^{4+} networks. The transition temperature, which arises from former networks are decreasing from 83 K for x = 0.0 to 76 K for x = 0.4. Whereas the other transition which arises from the later networks is increasing from 84 K to 88 K for for x = 0.1 to x = 0.4. For higher Ni concentrated samples i.e., for x = 0.3 and 0.4 a MR has been observed with compensation temperature at 4.4 K and 10 K respectively. It is due to the negative exchange interaction between the moments of RE ions and TM ions. With Ni doping, the MH measurements at 5 K reveals a decrease in coercivity (H_C) and saturation magnetization (M_S). The decrease in M_S value is caused by the substitution of Mn^{4+} ions with larger magnetic moments with Ni^{4+} ions having negligible magnetic moments. However, the observed higher M_S value is attributed to the FM interaction of RE ions with the net magnetic moment of TM ions. According to EB analysis, the H_{EB} has a negative value of -114 Oe when x = 0.0. By replacing Ni, we could see that the loop was moving in the direction of the positive field, and at x = 0.4, the highest positive H_{EB} value of 230 Oe was discovered. The reason behind the EB is the competition between spin canted magnetic moment of RE ions and FM moment of TM ions.

Similar to the above work, we have investigated the effect of Cr doping on the structural and magnetic properties of HCMO DP. For this work, we have prepared nanocrystalline samples of $Ho_2CoMn_{1-x}Cr_xO_6$ (x = 0.0 - 0.5). According to the RT-XRD pattern, the samples exhibit a monoclinic structure with space group $P2_1/n$. The lattice parameters are found to be reduced with Cr concentration and it is ascribed to the replacement of Mn^{3+} ions (0.645 Å) by the Cr^{3+} ions (0.61 Å). MT measurement reveals that, for $x \leq 0.2$ samples, a pure FM phase has been observed at 83 K. It is attributed to the SE interaction in Co^{2+}-O^{2-}-Mn^{4+} networks. Whereas, the AFM interaction in Cr^{3+}-O^{2-}-Cr^{3+} and/or Cr^{3+}-O^{2-}-Mn^{4+} ions give rise to another AFM phase for higher Cr doped samples. The former transition does not show much variation, it stays in the range of 83 K to 85 K. While, the later one drops from 77 K for x = 0.3 to 63 K for x = 0.5 samples. However, another transition at 120 K has been found for x = 0.2 and 0.4 samples. This transition is attributed to the charge ordering temperature (T_{CO}). For x = 0.5 a MR has been seen with a compensation temperature of 7 K. The competition between the PM moment of Ho^{3+} ions under the influence of a negative internal field caused by AFM ordered ions and the FM components of Co^{2+} and Mn^{4+} ions is ascribed to this MR. After Cr substitution, the magnetic hysteresis loops show a reduction in saturation magnetization and coercivity. It is due to the replacement of Mn^{3+} ions having higher magnetic moment (4 μ_B/ion) with the Cr^{3+} ions having lower magnetic moment (3 μ_B/ion). For samples with x = 0.0 and 0.5, an H_{EB} of - 114 Oe and 208 Oe is seen. They are explained by the competition between canted magnetic moments of RE ions and FM moments of TM ions, with the former dominating for sample with x = 0.5 sample and the latter one dominating for sample with x = 0.0.

A detailed investigation has been done on the magnetic properties of Y_2FeCrO_6 nanoparticles having a particle size of 67 nm. It explains the existence of MR and also details the extensive investigation of EB behavior (both spontaneous and conventional EB effects) in the vicinity of SIA and the DM interaction. In summary, we have prepared the nanoparticle of Y_2FeCrO_6 DP by using auto combustion method. XRD pattern confirm that the sample is crystallized in the orthorhombic phase with the Pnma space group. The Raman spectra further confirms the formation of sample in orthorhombic phase with Pnma space group. The lattice parameters and the unit cell volume are found to be as follows: a = 5.5509(1) Å, b = 7.5704(2) Å, c = 5.2635(1) Å and volume, V = 221.191(8) $Å^3$ respectively. FESEM and TEM confirms the formation of Y_2FeCrO_6 nanoparticles with an average particle size of 67 nm. Presence of all the

elements with desirable atomic percentage is confirmed by EDS analysis. However, the presence of Fe and Cr in the oxidation states of 3+ has also been confirmed by XPS analysis. The MT measurements, reveal that the system has an AFM transition with T_N ~ 327 K. This AFM transition is attributed to arise from the SE interaction in Cr^{3+}-O-Cr^{3+}, and Fe^{3+}-O-Fe^{3+} networks. A MR with a compensation temperature of 192 K has been observed at 100 Oe. A spin reorientation at low temperature of T_{SR}~30 K is also been seen. A spontaneous EB (SEB) exhibit a maximum negative value of -431 Oe at 55 K. However, after field cooling the sample at 0.5 T, the maximum value of the conventional EB (CEB) field is found as 2.1 kOe, at 5 K. The SEB is confirmed by taking the MH loop in two different protocols such as P-Type and N-Type. However, the CEB is confirmed by recording the MH loops, after cooling the samples in positive and negative applied fields. SEB field show a sign reversal across T_{SR}. However, CEB field shows a sign reversal across T_{comp} respectively. A multi-magnetic phase has also been noticed from the MH loop. A typical BSM has been demonstrated at 50 K. The above behaviors in the Y_2FeCrO_6 sample are ascribed to the competition between SIA and DM interaction.

Future Scope

1. Doping has been done in the Ho and Mn site of Ho_2CoMnO_6, one can dope at Co site in order to tune structural and magnetic properties.
2. Magnetocaloric studies can be done in $(Ho_{1-x}Sm_x)_2CoMnO_6$ for x = 0.0 to 0.5.
3. Thin film preparation of these materials and study their negative magnetization, exchange bias and bipolar switching of magnetization.
4. Study of magneto-caloric effect for Y_2FeCrO_6 nanoparticles.
5. Detailed study of magnetization, dielectric response and magneto-electric effect in the vicinity of T_{comp} and T_C for the above mentioned samples

References

[1] T. Mc. Donnell, S. Korsmeyer. Nature. 354, (1991) 56-58.

[2] S. Vasala and M. Karppinen, Progress in Solid State Chemistry. 43, (2015) 1-36.

[3] G. H. Jonker and J. H. Van Santen, Physica. 16, (1950) 337- 49.

[4] C. Zener, Phys. Rev. 81, (1951) 440.

[5] J. Longo and R. Ward, J. Am. Chem. Soc. 83, (1961) 2816-8.

[6] C. N. R. Rao and B. Raveau, New York, Wiley-VCH, (1995).

[7] R. V. Helmolt, J. Wecker, B. Holzapfel, L.Schultz, and K.Samwer, Phys. Rev. Lett. 71, (1993) 2331.

[8] A. J. Millis, P. B. Littlewood, and B. I. Shraiman, Phys. Rev. Lett. 74, (1995) 5144.

[9] B. Samantaray, S. Ravi, A. Das and S. K. Srivastava, J. Appl. Phys. 110, (2011) 093906.

[10] Y. Tokura, Rep. Prog. Phys. 69, (2006) 797.

[11] J. B. Elemans, B. V. Laar, K. V. D. Veen and B. Loopstra, J. Solid State Chem. 3, (1971) 238-242.

[12] J. Hemberger, M. Brando, R. Wehn, V. Yu. Ivanov, A. A. Mukhin, A. M. Balbashov, and A. Loidl, Phys. Rev. B. 69, (2004) 064418.

[13] H. W. Brinks, J. Rodriguez-Carvajal, H. Fjellvag, A. Kjekshus, and B. C. Hauback, Phys. Rev. B. 63, (2001) 094411.

[14] O. Chmaissem, R. Kruk, B. Dabrowski, D. E. Brown, X. Xiong, S. Kolesnik, J. D. Jorgensen, and C. W. Kimball1. Phys. Rev. B. 62, (2000) 14197.

[15] A. Gupta, G. Q. Gong, G. Xiao, P. R. Duncombe, P. Lecoeur, P. Trouilloud, Y. Y. Wang, V. P. Dravid, and J. Z. Sun, Phys. Rev. B. 54, (1996) R15629.

[16] T. Sugahara, M. Ohtaki, Appl. Phys. Lett. 99, (2011) 62103.

[17] J. A. Alonso, J. L. Garcia-Mu-noz, M. T. Fernandez-Diaz, M. A. G. Aranda, M. J. Martinez- Lope, M. T. Casais. Phys. Rev. Lett. 82, (1999) 3871.

[18] A. Poddar, S. Das, A.Chattopadhyay, J. Appl. Phys. 95, (2004) 6261.

[19] K. I. Kobayashi, T. Kimura, H. Sawada, K. Terakura, Y. Tokura, Nature. 395, (1998) 677.

[20] D. Serrate, J. M. D. Teresa and M. R. Ibarra, J. Phys. Condns. Matter. 19, (2007) 023201.

[21] O. Chmaissem, B. Dabrowski, S. Kolesnik, S. Short and J.D. Jorgensen. Phys. Rev. B. 71, (2005) 174421.

[22] M. Takata, K. Kageyama, J. Am. Ceram. Soc. 72, (1989) 1955.

[23] F. Zhao, Z. Yue, Z. Gui, L. Li, Jpn. J. Appl. Phys. 44, (2005) 8066.

[24] W. Z. Yang, M. M. Mao, X. Q. Liu, X. M. Chen, J. Appl. Phys. 107, (2010) 124102.

[25] K. Yoshii, N. Ikeda, M. Mizumaki, Phys. Stat. Sol. 203, (2006) 2812.

[26] Y. Q. Lin and X. M. Chen, Appl. Phys. Lett. 96, (2010) 142902.

[27] Y. Q. Lin, X. M. Chen, and X. Q. Liu. Solid. State. Commun. 149, (2009) 784.

[28] Y. Q. Lin and X. M. Chen, J. Am. Ceram. Soc. 94, (2011) 782.

[29] J. S. Zhou, H. Q. Yin, J. B. Goodenough, Phys. Rev. B. 63, (2001) 184423.

[30] M. H. Aguirre, D. Logvinovich, L. Bocher, R. Robert, S. G. Ebbinghaus, A. Weidenkaff, Acta. Mater. 57, (2009) 108.

[31] T. Sugahara, M. Ohtaki, T. Souma, Jpn. J. Ceram. Soc. 116, (2008) 1278.

[32] Y. H. Huang, R. I. Dass, Z. L. Xing, J. B. Goodenough, Science. 312, (2006) 254.

[33] S. Vasala, M. Lehtimaki, Y. H. Huang, H. Yamauchi, J. B. Goodenough and M. Karppinen, J. Solid. State. Chem. 183, (2010) 1007.

[34] Z. Wang, Y. Tian, Y. Li, J. Power. Sources. 196, (2011) 6104.

[35] Q. Zhang, T. Wei, Y. H. Huang, J. Power. Sources. 198, (2012) 59.

[36] Y. H. Huang, G. Liang, M. Croft, M. Lehtimaki, M. Karppinen and J. B. Goodenough, Chem. Mater. 21, (2009) 2319.

[37] R. I. Dass, J. Q. Yan and J. B. Goodenough, Phys. Rev. B. 68, (2003) 64415.

[38] J. B. Goodenough, Phys. Rev. 100, (1955) 564-573.

[39] J. Kanamori, J. Phys. Chem. Solids. 10, (1959) 87-98.

[40] R. I. Dass and J. B. Goodenough, Phys. Rev. B. 67, (2003) 14401.

[41] M. Azuma, K. Takata, T. Saito, S. Ishiwata, Y. Shimakawa and M. Takano, J. Am. Chem. Soc. 127, (2005) 8889.

[42] R. Pradheesh, H.S. Nair, V. S. Narayanan, K. Sethupathi, Appl. Phys. Lett. 101, (2012) 142401.

[43] R. C. Sahoo, Y. Takeuchi, A. Ohtomo and Z. Hossain, Phys. Rev. B. 100, (2019) 214436.

[44] Y. Jia, Q. Wang, P. Wang, and L. Li, Ceram. Int. 43, (2017) 15856-15861.

[45] J. K. Murthy, K D. Chandrasekhar, S. Mahana, D. Topwal and A. Venimadhav, J. Phys. D. Appl. Phys. 48, (2015) 355001.

[46] J. K. Murthy and A. Venimadhav, J. Phys. D. Appl. Phys. 47, (2014) 445002.

[47] S. Ju and G. Yu. Guo, Appl. Phys. Lett. 92, (2008) 202504.

[48] R. Nechache, F. Rosei, Journal of Solid State Chemistry. 189, (2012) 13-20.

[49] L. Sha, J. Miao, S. Z. Wu, X. G. Xu, Y. Jiang, L. J. Qiao, J. Alloys. Compd. 554, (2013) 299-303.

[50] M. Nasir, S. Kumar, N. Patra, D. Bhattacharya, S. N. Jha, D. R. Basaula, S. Bhatt, M. Khan, S. W. Liu, S. Biring and S. Sen, ACS Appl. Electron. Mater. 1, (2019) 141-153.

[51] A. K. Singh, S. Chauhan, S. K. Srivastava and R. Chandra, Solid State Communications. 242, (2016) 74 - 78.

[52] J. Su, Z. Z. Yang, X. M. Lu, J. T. Zhang, L. Gu, C. J. Lu, Q. C. Li, J. M. Liu and J. S. Zhu, J. Am. Ceram. Soc. 7, (2015) 13260-13265.

[53] D. Choudhury, P. Mandal, R. Mathieu, A. Hazarika, S. Rajan, A. Sundaresan, U. V. Waghmare, R. Knut, O. Karis, P. Nordblad, and D. D. Sarma, Phys. Rev. Lett. 108, (2012) 127201.

[54] R. I. Dass and J. B. Goodenough, Phys. Rev. B. 67, (2003) 014401.

[55] S. Y. Vilar, E. D. Mun, V. S. Zapf, B. G. Ueland, J. S. Gardner, J. D. Thompson, J. Singleton, M. S. Andujar, J. Mira, N. Biskup, M. A. S. Rodrıguez, and C. D. Batista, Phys. Rev. B. 84, (2011) 134427.

[56] Y. Q. Lin and X. M. Chen, J. Am. Ceramic Soc. 94, (2011) 782-787.

[57] J. Blasco, J. L. G. Munoz, J. Garcia, G. Subias, J. Stankiewicz, J. A. R. Velamazan and C. Ritter, Phys. Rev. B. 96, (2017) 024409.

[58] H. Z. Guo, A. Gupta, T. G. Calvarese and M. A. Subramanian, Appl. Phys. Lett. 89, (2006) 262503.

References

[59] R. C. Sahoo, S. K. Giri, P. Dasgupta, A. Poddar and T.K. Nath, J. Alloys and Comp. 658, (2016) 1003-1009.

[60] J. K. Murthy, K. D. Chandrasekhar, S. Murugavelc and A. Venimadhava, J. Mater. Chem. C. 3, (2015) 836.

[61] H. S. Nair, T. Chatterji and A. M. Strydom, Appl. Phys. Lett. 106, (2015) 022407.

[62] H. S. Nair, R. Pradheesh, Y. Xiao, D. Cherian, S. Elizabeth, T. Hansen, T. Chatterji and T. Brückel, J. Appl. Phys. 116, (2014) 123907.

[63] M. K. Kim, J. Y. Moon, H. Y. Choi, S. H. Oh, N. Lee and Y. J. Choi, J. Phys. Condens. Matter. 27, (2015) 426002.

[64] J. Y. Moon, M. K. Kim, D. G. Oh, J. H. Kim, H. J. Shin, Y. J. Choi and N. Lee, Phys. Rev. B. 98, (2018) 174424.

[65] A. Banerjee, J. Sannigrahi, S. Giri and S. Majumdar, Phys. Rev. B. 98, (2018) 104414.

[66] R. C. Sahoo, S. Das and T. K. Nath, J. Magn. Magn. Mater. 460, (2018) 409-417.

[67] G. Sharma, J. Saha, S. D. Koushik, V. Siruguri and S. Patnaik, Appl. Phys. Lett. 103, (2013) 012903.

[68] R. R. Zhang, G.L. Kuang, L.H. Yin and Y.P. Sun, J. Alloys Compd. 519, (2012) 92-96.

[69] W. Liu, L. Shi, S. Zhou, J. Zhao, Y. Li and Y. Guo, J. Appl. Phys. 116, (2014) 193901.

[70] L. Wang, W. Zhou, D. Wang, Q. Cao, Q. Xu and Y. Du, J. Appl. Phys. 117, (2015) 17D914.

[71] D. Majumdar and I. Das, J. Appl. Phys. 129, (2021) 063901.

[72] Y.Ren, T.Palstra, D.Khomskii, E.Pellegrin, A.Nugroho, A.Menovsky, G.Sawatzky, Nature 396, (1998) 441.

[73] Y. Ren, T. T. M. Palstra, D. I. Khomskii, A. A. Nugroho, A. A. Menovsky and G. A. Sawatzky, Phys. Rev. B, 62, (2000) 6577-6586.

[74] S. M. Yusuf, A. Kumar and J. V. Yakhmi, Appl. Phys. Lett. 95, (2009) 182506.

[75] M. Fiebig, J. Phys. D. Appl. Phys. 38, (2005) R123-R124.

[76] B.Rajeswaran, D.I.Khomskii, A.K.Zvezdin, C.N.R.Rao and A.Sundaresan, Phys. Rev. B. 86, (2012) 214409.

[77] S. Biswas and S. Pal, Rev. Adv. Mater. Sci. 53, (2018) 206-217.

[78] A. Kumar and S.M. Yusuf, Phys. Rep. 556, (2015) 1-34.

[79] K. Yoshii, Mater. Res. Bull. 47, (2012) 3243-3248.

[80] H. J. Zhao, J. Iniguez, X.M. Chen and L. Bellaiche, Phys. Rev. B. 93, (2016) 014417.

[81] J.H.Lee, Y.K.Jeong, J.H.Park, M.Oak, H.M.Jang, J.Y.Son, J.F.Scott, Phys. Rev. Lett. 107, (2011) 117201.

[82] L. G. Marshall, J. G. Cheng, J. S. Zhou, J. B. Goodenough, J. Q. Yan and D. G. Mandrus, Phys. Rev. B. Condens. Matter. 86, (2012) 064417.

[83] A. V. Kimel, A. Kirilyuk, A. Tsvetkov, R.V. Pisarev and T. Rasing, Nature. 429, (6994), (2004) 850-853.

[84] J. A. de Jong, A. V. Kimel, R. V. Pisarev, A. Kirilyuk and T. Rasing, Phys. Rev. B. 84, (10), (2011) 10442.

[85] A. V. Kimel, A. Kirilyuk, P. A. Usachev, R. V. Pisarev, A. M. Balbashov and T. Rasing, Nature. 435 (7042), (2005) 655-657.

[86] S. Ju and G. Y. Guo, Appl. Phys. Lett. 92, (2008) 202504.

[87] L. Sha, J. Miao, S. Z. Wu, X. G. Xu, Y. Jiang and L. J. Qiao, J. Alloy. Comp. 554, (2013) 299-303.

[88] R. Nechache and F. Rosei, J. Solid. State. Chem. 189, (2012) 13-20.

[89] R. Nechache, C. V. Cojocaru, C. Harnagea, C. Nauenheim, M. Nicklaus, A. Ruediger, F. Rosei and A. Pignolet, Adv. Mater. 23, (2011) 1724-9.

[90] D. Mazumdar and I. Das, Phys. Chem. Chem. Phys., 23, (2021) 5596.

[91] R. P. Maiti, S. Dutta, M. K. Mitra and D. Chakravorty, Journal of Physics D: Appl. Phy. 46, (2013) 415303.

[92] M. T. Anderson, K. B. Greenwood, G. A. Taylor and K. R. Poeppelmeier. Prog. Solid. State. Chem. 22, (1993) 197.

[93] G. King and P. M. Woodward. J. Mater. Chem. 20, (2010) 5785.

[94] V. M. Goldschmidt and Geochemistry, Oxford University Press, London. (1958).

[95] W. T. Fu, S. Akerboom, D. J. W. IJdo, J. Solid. State. Chem. 180, (2007) 1547.

[96] P. J. Saines, B. J. Kennedy, M. M. Elcombe, J. Solid. State. Chem. 180, (2007) 401.

[97] E. Reynolds, B. J. Kennedy, G.J. Thorogood, D.J. Gregg and J. A. Kimpton. J. Nucl. Mater. 433, (2013) 37.

[98] A. W. Sleight, J. Longo and R. Ward, Inorg. Chem. 1, (1962) 245.

[99] H. L. Feng, C. I. Sathish, J. Li, X. Wang and K. Yamaura, Phys. Procedia. 45, (2013) 117.

[100] S. H. Byeon, T. Nakamura, M. Itoh and M. Matsuo, Mater. Res. Bull. 27, (1992) 1065.

[101] P. C. Donohue and E. L. Mc. Cann, Mater. Res. Bull. 12, (1977) 519.

[102] J. B. Goodenough, J. A. Kafalas, J. M. Longo In: Hagenmuller P, editor. New York: Academic Press, Inc. (1972) 1-69.

[103] K. Ramesha, L. Sebastian, B. Eichhorn and J. Gopalakrishnan, Chem. Mater. 15, (2003) 668.

[104] C. Meneghini, S.Ray, F.Liscio, F.Bardelli, S.Mobilio and D. D. Sarma, Phys. Rev. Lett. 103, (2009) 46403.

[105] M. Wakeshima, D. Harada and Y. Hinatsu, J. Mater. Chem. 10, (2000) 419.

[106] M. Wakeshima, D. Harada and Y. Hinatsu, J. Alloys. Compd. 287, (1999) 130.

[107] W. T. Fu and D. J. W. IJdo, J. Alloys. Compd. 394, (2005) L5.

[108] Q. Zhou, B. J. Kennedy, M. Avdeev, L. Giachini and J. A. Kimpton, J. Solid. State. Chem. 182, (2009) 3195.

[109] W. T. Fu, R. J. Gotz, D. J. W. IJdo, J. Solid. State. Chem. 183, (2010) 419.

[110] P. D. Battle, J. B. Goodenough and R. Price, J. Solid. State. Chem. 46, (1983) 234.

[111] P. D. Battle, Mater. Res. Bull. 16, (1981) 397.

[112] W. T. Fu and D. J. W. IJdo, Solid State Commun. 136, (2005) 456.

[113] C. J. Howard, B. J. Kennedy and P. M. Woodward, Acta Crystallogr Sect B Struct Sci. 59, (2003) 463.

[114] P. J. Saines, J. R. Spencer, B. J. Kennedy, M. Avdeev, J. Solid. State. Chem. 180, (2007) 2991.

[115] P. M. Woodward, Acta Crystallogr Sect B Struct Sci. 53, (1997) 32.

[116] M. Gateshki, J. M. M. Igartua and E. H. Bocanegra, J. Phys. Condens. Matter. 15, (2003) 6199.

[117] P. M. Woodward, Acta Crystallogr Sect B Struct Sci. 53, (1997) 44.

[118] Zhou Q, Blanchard P, Kennedy BJ, Reynolds E, Zhang Z, Miiller W, et al. Chem. Mater. 24, (2012) 2978.

[119] W. T. Fu and D. J. W. IJdo, J. Solid. State. Chem. 179, (2006) 1022.

[120] Q. Zhou, T. Y. Tan, B. J. Kennedy, J. R. Hester. J. Solid. State. Chem. 206, (2013) 122.

[121] C. D. Ling, B. J. Kennedy, Q. Zhou, J. R. Spencer, M. Avdeev, J. Solid. State. Chem. 183, (2010) 727.

[122] Q. Zhou, B. J. Kennedy and M. M. Elcombe, J. Solid. State. Chem. 180, (2007) 541.

[123] Q. Zhou, B. J. Kennedy and M. M. Elcombe, Phys. B. Condens. Matter.190, (2006) 385-386.

[124] J. Blasco, J. Garcia, M. C. Sanchez, J. Campo, G. Subias, J. P. Cacho, Eur. Phys J. B. 30, (2002) 469.

[125] J. Blasco, J. Garcia, G. Subias, M. C. Sanchez, Phys. Rev. B. 70, (2004) 94426.

[126] D. Sanchez, J. A. Alonso, M. G. Hernandez, M. J. M. Lope, J. L. Martinez, A. Mellergard, Phys. Rev. B. 65, (2002) 104426.

[127] J. M. Michalik, J. M. De Teresa, J. Blasco, P. A. Algarabel, M. R. Ibarra, C. Kapusta and U. Zeitler, J. Phys. Condens. Matter. 19, (2007) 506206.

[128] R. Pradheesh, H. Nair, V.Sankaranarayanan, K.Sethupathi. Eur. Phys. J. B. Condens. Matter. 85, (2012) 1.

[129] Q. Zhou, B. J. Kennedy, M. Avdeev, J. Solid. State. Chem. 183, (2010) 1741.

[130] T. Kyomen, R. Yamazaki, M. Itoh, Chem. Mater. 15, (2003) 4798.

[131] D. Mikhailova, N. Narayanan, W. Gruner, A. Voss, A. Senyshyn, D. M. Trots, H. Fuess, and H. Ehrenberg, Inorg. Chem. 49, (2010) 10348.

[132] V. P. Martin, M. Jansen, J. Solid. State. Chem. 157, (2001) 76.

[133] M. K. Sharma, K. Singh, K. Mukherjee, J. Magn. Magn. Mater. 414, (2016) 116 - 121.

[134] G. V. Nair, A. Das, V. Subramanian, and P. N. Santhosh, J. Appl. Phys. 113, (2013) 213907.

[135] V. M. Gaikwad, M. Brahma, R. Borah and S. Ravi, J. Solid. State. Chem. 278, (2019) 120903.

[136] S. Blundell, Magnetism in condensed matter, Oxford University Press, (2001).

[137] R. G. Burns, Geochim. Cosmochim. Acta. 39 (1975) 857.

[138] B. J. Kennedy, Q. Zhou, J. Solid. State. Chem.181, (2008), 2227.

[139] C. Zener, Phys. Rev. 82 (1951) 403.

[140] I. Dzyaloshinsky, J. Phys. Chem. Soilds 4, (1958), 241.

[141] T. Moriya, Phys. Rev. 120, (1960), 91.

[142] C. Kittel, Wiley Press, Singapore (2004).

[143] T. Chakraborty, H. S Nair, H. Nhalil, K. R. Kumar, A. M. Strydom and S. Elizabeth, J. Phys. Condens. Matter. 29, (2017) 025804.

[144] L. Neel, Ann. Phys. 12 (1948) 137.

[145] E. Winkler, S.B. Canosa, F. Rivadulla, M.A. López-Quintela, J. Rivas, A. Caneiro, M.T. Causa, M. Tovar, Phys. Rev. B. 80, (2009) 104418.

[146] E. O. Wollan and W. C. Koehler, Phys. Rev. 100 (1955) 545.

[147] A. P. Ramirez, P. Schiffer, S. W. Cheong, C. H. Chen, W. Bao, T. T. M. Palstra, P. L. Gammel, D. J. Bishop, and B. Zegarski, Phys. Rev. Lett. 76, (1996) 3188.

[148] C. H. Chen and S. W. Cheong, Phys. Rev. Lett. 76 (1996) 4042.

[149] Z. Jirak, S. Krupicka, Z. Simsa, M. Dlouha, and S. Vratislav, J. Magn. Magn. Mater. 53 (1985) 153.

[150] K. Knizek, Z. Jirák, E. Pollert, F. Zounová, and S. Vratislav, J. Solid. State. Chem. 100 (1992) 292.

[151] H. Kawano, R. Kajimoto, H. Yoshizawa, Y. Tomioka, H. Kuwahara, and Y. Tokura, Phys. Rev. Lett. 78 (1997) 4253.

[152] H. Kuwahara, Y. Tomioka, A. Asamitsu, Y. Moritomo, and Y. Tokura, Science. 270 (1995) 961.

[153] Y. Tomioka, A. Asamitsu, Y. Moritomo, H. Kuwahara, and Y. Tokura, Phys. Rev. Lett. 74 (1995) 5108.

[154] G. Xiao, E. J. McNiff, Jr., G. Q. Gong, A. Gupta, C. L. Canedy, and J. Z.Sun, Phys. Rev. B 54 (1996) 6073.

[155] Q. Huang, J. W. Lynn, R. W. Erwin, A. Santoro, D. C. Dender, V. N. Smolyaninova, K. Ghosh, and R. L. Greene, Phys. Rev. B 61 (2000) 8895.

[156] Y. Moritomo, H. Kiwahara, Y. Tomioka, and Y. Tokura, Phys. Rev. B 55 (1997) 7549.

[157] V. Kiryukhin, D. Casa, J. P. Hill, B. Keimer, A. Vigliante, Y. Tomioka, Y. Tokura, Nature 386 (1997) 813.

[158] S. Parashar, E. E. Ebenso, A. R. Raju, and C. N. R. Rao, Solid State Commun. 114 (2000) 295.

[159] K. Miyano, T. Tanaka, Y. Tomioka, and Y. Tokura, Phys. Rev. Lett. 78 (1997) 4257.

[160] C. N. R. Rao, A. Arulraj, A. K. Cheetham, and B. Raveau, J. Phys.: Condens. Matter 12 (2000) R83.

[161] Y. Tomioka, T. Okuda, Y. Okimoto, A. Asamitsu, H. Kuwahara, Y. Tokura, Journal of Alloys and Compounds. 326, (2001) 27–35.

[162] J. E. Greedan, J. Mater. Chem. 11, (2001) 37.

[163] P. D. Battle, T. C. Gibb, C. W. Jones, F. Studer, J. Solid. State. Chem. 78, (1989) 281.

[164] C. Schinzer, J. Alloys. Compd. 288, (1999) 65.

[165] P. D. Battle, T. C. Gibb, A. J. Herod, J. P. Hodges, J. Mater. Chem. 5, (1995) 75.

[166] V. Cannella, J. A. Mydosh, J. I. Budnick, *J. Appl. Phys.* 42, (1971) 1689.

[167] H. T. Diep, World Scientific. (2004).

[168] K. Binder and A. P. Young, Rev. Mod. Phys. 58, (1986) 801.

[169] S. Nagata, P. H. Keesom, and H. R. Harrison, Phys. Rev. B. 19, (1979) 1633.

[170] J. L. van Hemmen, Phys. Rev. A 34, (1986) 3435.

[171] T. Roy, J. Math. Phys. 42, (2001), 4283.

[172] A. M. Samarakoon, K. Barros, Y. W. Li, M. Eisenbach, Q. Zhang, F. Ye, V. Sharma, Z. L. Dun, H. Zhou, S. A. Grigera, C. D. Batista, D. A. Tennant 11, (2020), 892.

[173] J. Inoue, Phys. Rev. E. 63, (2001), 046114.

[174] A. Chakravarti, R. Ranganathan, and S. Chatterjee, J. Magn. Magn. Mater. 138, (1994) 329.

[175] S. Mukherjee, R. Ranganathan, and S. B.Roy, Phys. Rev. B. 50, (1994) 1084.

[176] T. Taniyama and I. Nakatani, J. Appl. Phys. 83, (1998) 6323.

[177] H. Maletta and P. Convert, Phys. Rev. Lett. 42, (1979) 108.

[178] A. Chakravarti, R. Ranganathan, A. K. Raychaudhury, J. T. T. Kumaran, and C. Bansal, Solid State Commun. 77, (1991) 17.

[179] R. V. Helmolt, L. Haupt, K. Bärner, and U. Sondermann, Solid State Commun. 82, (1992) 693.

[180] J. Dho, W. S. Kim, and N. H. Hur, Phy. Rev. Lett. 89, (2002) 027202.

[181] S. K. Hasanain, W. H. Shah, A. Mumtaz, M. Nadeem, M. J.Akhtar, J. Magn. Magn. Mater. 271, (2004) 79.

[182] P. Chaddah, K. Kumar, and A. Banerjee, Phys. Rev. B. 77, (2008) R100402.

[183] R. Mathieu, A. Asamistu, Y. Kaneko, J. P. He, and Y. Tokura, Phys. Rev. B. 72, (2005) 014436.

[184] S. Nair and A. K. Nigam, Phys. Rev. B. 75, (2007) 214415.

[185] Y. G. Joh, R. Orbach, G.G Wood, J. Hammann and E. Vincent, Phys. Rev. Lett. 82, (1999) 438.

[186] G. G. Kenning, Y. G. Joh, D. Chu, and R. Orbach, Phys. Rev. B. 52, (1995) 3479.

[187] L. Lundgren, P. Svedlindh, P. Nordblad, O. Beckman, Phys. Rev. Lett. 51, (1983) 911.

[188] N. Khan, P. Mandal, D. Prabhakaran, Phys. Rev. B. 90, (2014) 024421.

[189] R. C. Sahoo, S.K. Giri, D. Paladhi, A. Das, T. K. Nath, J. Appl. Phys. 120, (2016) 033906.

[190] K. Yoshii, J. Solid State Chem. 159, (2001) 204-208.

[191] H. C. Nguyen, J. B. Goodenough, Phys. Rev. B, 52, (1995) 324.

[192] K. Yoshii, A. Nakamura, Y. Ishii, Y. Morii, J. Solid. State. Chem.162, (2001) 84.

[193] V. A. Khomchenko, I. O. Troyanchuk, R. Szymczak, H. Szymczak, J. Mater. Sci., 43, (2008) 5662.

[194] I. L. Prejbeanu, M. Kerekes, R. C. Sousa, H. Sibuet, O. Redon, B. Dieny, and J. P. Nozieres, J. Phys. Condens. Matter. 19, (2007) 165218.

[195] N. Menyuk, K. Dwight, D.G. Wickham, Phys. Rev. Lett. 4, (1960) 119.

[196] J. Kondo *Prog. Theor. Phys.* 32, (1964), 37.

[197] W. Kinzel, Phys. Rev. B. 19, (1979), 4595.

[198] R. V. Chamberlin, G. Mozurkewich, and R. Orbach, Phys. Rev. Lett. *52*, (1984), 867.

[199] A.V. Mahajan, D. C. Johnston, D. R. Torgeson, F. Borsa, Phys. Rev. B. 46, (1992) 10966.

[200] O. Pen, M. Guilloux-viry, A. B. Antunes, W. Peng, Y. Ma, Z. Gao, C. Moure, J. Magn. Magn. Mater. 321, (2009) 1723–1726.

[201] Y. Su, J. Zhang, Z. Feng, L. Li, B. Li, Y. Zhou, Z. Chen, S. Cao, J. Appl. Phys. 108, (2010) 013905.

[202] A. H. Cooke, D. M. Martin, and M. R. Wells, J. Phys. C Solid State Phys. 7, 3133 (1974).

[203] T. Bora and S. Ravi, J. Appl. Phys.114, (2013) 183902.

[204] N. Dasari, P. Mandal, A. Sundaresan, N. S. Vidhyadhiraja, Eur. Phys. Lett. 99, (2012) 17008.

[205] P. Mandal, A. Sundaresan, C. N. R. Rao, A. Iyo, P. M. Shirage, Y. Tanaka, C. Simon, V. Pralong, O. I. Lebedev, V. Caignaert, B. Raveau, Phys. Rev. B. 82, (2010) 100416.

[206] T. Bora, S. Ravi, J. Appl. Phys. 114, (2013) 033906.

[207] A. K. Azad, A. Mellergard, S. G. Eriksson, S. A. Ivanov, S. M. Yunus, F. Lindberg, G. Svensson, and R. Mathieu, Mater. Res. Bull. 40, (2005) 1633.

[208] B. B. Dash, S. Ravi, J. Magn and Magn Materials. 429, (2017) 281-286.

[209] J. Nogues, and I. K. Schuller, J. Magn. Magn. Mater. 192, (1999) 203.

[210] W. H. Meiklejohn, C. P. Bean, Phys. Rev. 105, (1957) 904.

[211] R. L. Stamps, J. Phys. D: Appl. Phys. 33, (2000) R247.

[212] S. Giri, M. Patra, S. Majumdar, J. Phys.: Condens. Matter. 23, (2011) 073201.

[213] W. H. Meiklejohn and C. P. Bean, Phys. Rev. 102, (1956) 1413.

[214] D. Niebieskikwiat, M. B. Salamon, Phys. Rev. B. 72, (2005) 174422.

[215] T. Qian, G. Li, T. Zhang, T. F. Zhou, X. Q. Xiang, X. W.Kang, X.G.Li, Appl. Phys. Lett. 90, (2007) 012503.

[216] X. H. Huang, J. F. Ding, G. Q. Zhang, Y. Hou, Y. P. Yao, X. G. Li, Phys. Rev. B. 78, (2008) 224408.

[217] S. K. Giri, A. Poddar, T. K. Nath, J. Appl. Phys. 112, (2012) 113903.

[218] S. Karmakar, S. Taran, E. Bose, B. K. Chaudhuri, C. P. Sun, C. L. Huang, H. D. Yang, Phys. Rev. B. 77, (2008) 144409.

[219] Y. K. Tang, Y. Sun, Z. H. Cheng, Phys. Rev. B. 73, (2006) 174419.

[220] K. Tomiyasu, J. Fukunaga, H. Suzuki, Phys. Rev. B. 70, (2004) 214434.

[221] Z. M. Tian, S. L. Yuan, L. Liu, S. Y. Yin, L. C. Jia, P. Li, S. X. Huo, J. Q. Li, J. Phys. D: Appl. Phys. 42, (2009), 035008.

[222] A. Harres, M. Mikhov, V. Skumryev, A. M. H. Andrade, J. E. Schmidt, and J. Geshev, J. Magn. Magn. Mater. 402, (2016) 76.

[223] J. Saha and R. H. Victora, Phys. Rev. B. 76, (2007) 100405(R).

[224] B. M. Wang, Y. Liu, P. Ren, B. Xia, K. B. Ruan, J. B. Yi, J. Ding, X. G. Li, and L. Wang, Phys. Rev. Lett. 106, (2011) 077203.

[225] A. K. Nayak, M. Nicklas, S. Chadov, C. Shekhar, Y. Skourski, J. Winterlik, and C. Felser, Phys. Rev. Lett. 110, (2013) 127204.

[226] T. Maity, S. Goswami, D. Bhattacharya, and S. Roy, Phys. Rev. Lett. 110, (2013) 107201.

[227] L.G.Wang, C.M.Zhu, Z.M.Tian, H.Luo, D.L.G.C.Bao, and S.L.Yuan, Appl.Phys. Lett. 107, (2015) 152406.

[228] H. J. Mao, C. Song, B. Cui, G. Y. Wang, L. R. Xiao and F. Pan, J. Appl. Phys. 114, (2013) 043904.

[229] L. T. Coutrim, D. Rigitano, C. Macchiutti, T. J. A. Mori, R. Lora-Serrano, E. Granado, E. Sadrollahi, F. J. Litterst, M. B. Fontes, E. Baggio-Saitovitch, E. M. Bittar, and L. Bufaiçal1, Phys. Rev. B. 100, (2019) 054428.

[230] S. K. Giri, R. C. Sahoo, P. Dasgupta, A. Poddar, and T. K. Nath, J. Phys. D. 49, (2016) 165002.

[231] Z. P. Li, J. Eisenmenger, C. W. Miller, I. K. Schuller, Phys. Rev. Lett. 96, (2006) 137201.

[232] J. Nogues, D. Lederman, T. J. Moran, I. K. Schuller, Phys. Rev. Lett. 76, (1996) 4624.

[233] T. Bora, S. Ravi, J. Magn. Magn. Mater. 386, (2015) 85.

[234] P. D. Kulkarni, A. Thamizhavel, V. C. Rakhecha, A. K. Nigam, P. L. Paulose, S. Ramakrishnan, A. K. Grover, EPL. 86, (2009) 47003.

[235] S.Venkatesh, V.Ulhas, R.V.Chand, S.Ramakrishnan, A.K.Grover, J. Phys.: Condens. Matter. 22, (2010) 496002.

[236] P. D. Kulkarni, S. K. Dhar, A. Provino, P. Manfrinetti, A. K. Grover, Phys. Rev. B. 82 (2010) 144411.

[237] R. P. Singh, C. V. Tomy, and A. K. Grover, Appl. Phys. Lett. 97, (2010) 182505.

[238] J. Mao, Y. Sui, X. Zhang, X. Wang, Y. Su, Z. Liu, Y. Wang, R. Zhu, Y. Wang, W. Liu, X. Liu, Solid State Commun. 151, (2011) 1982.

[239] K. Yoshii, Appl. Phys. Lett. 99, (2011) 142501.

[240] F. Hong, Z. Cheng, J. Wang, X. Wang, S. Dou, Appl. Phys. Lett. 101, (2012) 102411.

[241] A. A. Belik, Inorg. Chem. 52, (2013) 2015.

[242] J. Yang, Y. P. Lee, Y. Li, J. Appl. Phys. 102, (2007), 033913.

[243] J. K. Murthy, K. D. Chandrasekhar, S. Mahana, D. Topwal, and A. Venimadhav, J. Phys. D: Appl. Phys. 48, (2015) 355001.

[244] S. Pakhira, C. Mazumdar, R. Ranganathan, S. Giri, and M. Avdeev, Phys. Rev. B. 94, (2016) 104414.

[245] V. Franco, J. S. Blazquez & Conde, Appl. Phys. Lett. 89, (2006) 222512.

[246] V. Franco, J. S. Blazquez, B. Ingale, A. Conde, Annu. Rev. Mater. Res. 42, (2012) 305.

[247] D. Choudhury, P. Mandal, R. Mathieu, A. Hazarika, S. Rajan, A. Sundaresan, U. V. Waghmare, R. Knut, O. Karis, P. Nordblad, and D. D. Sarma, Phys. Rev. Lett. 108, (2012) 127201.

[248] R. R. Das, P. N. Lekshmi, S. C. Das and P. N. Santhosh, J. Alloys and Comp. 773, (2019) 770.

[249] Y. J. Choi, H. T. Yi, S. Lee, Q. Huang, V. Kiryukhin, S. W. Cheong, Phys. Rev. Lett. 100, (2008) 047601.

[250] L. Wang, W. Zhou, D. Wang, Q. Cao, Q. Xu, and Y. Du, J. Appl. Phys. 117, (2015) 17D914.

[251] M. Viswanathan, P. S. A. Kumar, V. S. Bhadram, C. Narayana, A. K. Bera, S. M. Yusuf, J. Phys. Condens. Matter. 22, (2010) 346006.

[252] J. Mao, Y. Sui, X. Zhang, Y. Su, X. Wang, Z. Liu, Y. Wang, R. Zhu, W. Liu, Appl. Phys. Lett. 98, (2011) 192510.

[253] S. Ravi, J. Rare Earths. 36, (2018) 1175.

[254] M. R. Suchomel, C. I. Thomas, M. Allix, M. J. Rosseinsky, A. M. Fogg, M. F. Thomas, Appl. Phys. Lett. 90, (2007) 1- 4.

[255] N. Das, S. Singh, A. G. Joshi, M. Thirumal, V. R. Reddy, L. C. Gupta, A. K. Ganguli, Inorg. Chem. 56, (2017), 12712 - 8.

[256] K. Ueda, H. Tabata, T. Kawai, Science, 280, (1998) 1064.

[257] B.D. Cullity, Elements of X-ray diffraction: a practical approach, (1956).

[258] C.N. Banwell, E.M. McCash, Fundamentals of molecular spectroscopy, McGraw-Hill New York, (1994).

[259] G. K. Williamson and W. H. Hall, Acta Metall. Mater. 1, (1953) 22.

[260] Z. Fan, T. Wu, and X. Xu, Scientific Reports, 7, (2017) 1-15.

[261] B.T. Sone, E. Manikandan, A. Gurib-Fakim, and M. Maaza, 650, (2015) 357-362.

[262] M. A. Stranick, Surf. Sci. Spectra, 6, (1999) 39.

[263] M. Jahan, S. Tominaka and J. Henzie, Dalton Trans., 45, (2016) 18494-18501.

[264] M. Oku and K. Hirokawa, J. Electron Spectrosc. Relat. Phenom., 8, (1976) 475-481.

[265] P. W. Menezes, A. Indra, D. G. Flores, N. R. Sahraie, I. Zaharieva, M. Schwarze, P. Strasser, H. Dau and M. Driess, ACS Catal., 5, (2015) 2017-2027.

[266] A. Indra, P. W. Menezes, C. Das, C. Go¨bel, M. Tallarida, D. Schmeisser and M. Driess, J. Mater. Chem. A, 5, (2017) 5171-5177.

[267] S. Chakrabarty, A. Dutta, M. Pal, J. Alloys and Comp. 625, (2015) 216.

[268] R. Pandey, L. K. Pradhan, S. Kumari, M. K. Manglam, S. Kumar and M. Kar, J. Magn. Magn. Mater. 508, (2020) 166862.

[269] S. A. Ivanov, M. S. Andersson, J. Cedervall, E. Lewin, M. Sahlberg, G. V. Bazuev, P. Nordblad and R. Mathieu, J. Materials Science: Materials in Electronics. 29, (2018) 18581-18592.

[270] J. F. Ding, O. I. Lebedev, S. Turner, Y. F. Tian, W. J. Hu, J. W. Seo, C. Panagopoulos, W. Prellier, G. V. Tendeloo and T. Wu, Phys. Rev. B. 87, (2013) 054428.

[271] N. S. E. Osman and T. Moyo, J. Supercond. Nov. Magn. 29, (2016) 361-366.

[272] F. Bert, V. Dupuis, E. Vincent, J. Hammann, and J.P. Bouchaud, Phys. Rev. Lett. 92 (2004) 167203.

[273] S. K. Banerjee, Phys. Lett. 12, 16 (1964).

[274] B. Andrzejewski, A. Kowalczyk, J.E. Frackowiak, T. Tolinski, A. Szlaferek, S. Pal, C. Simon, Phys. Stat. Sol. 243, (2006) 295–298.

[275] A.B. Antunes, V. Gil, C. Moure, O. Pe, J. Eur. Ceram. Soc. 27, (2007) 3927–3930.

[276] T. Bora and S. Ravi, J. Appl. Phys. 116, (2014) 063901.

[277] H. Huang, Y. Zhao, Y. Bai, F. Li, Y. Zhang, and Y. Chen, Adv. Sci. 7, (2020) 1-9.

[278] K. Aswathi, J. P. Palakkal, R. Revathy, M. R. Varma, Journal of Magnetism and Magnetic Materials 483 (2019) 89–94.

[279] L. Capogna, A. Martinelli, M. G. Francesconi, P. G. Radaelli, R. Carvajal, O. Cabeza, M. Ferretti, C. Castellano, T. Corridoni, and N. Pompeo, Phys. Rev. B. 77, (2008) 104438.

[280] M. N. Iliev, M. V. Abrashev, H.-G. Lee, V. N. Popov, Y. Y. Sun, C. Thomsen, R. L. Meng and C. W. Chu, Phys. Rev. B. 57, (1998) 5.

[281] V. Bondarenka, S. Grebinskij, S. Kaciulis, G. Mattogno, S. Mickevicius, H. Tvardauskas, V. Volkov, G. Zakharova, Journal of Electron Spectroscopy and Related Phenomena 120 (2001) 131–135.

[282] K. P. Thiruppathi and D. Nataraj, Materials Advances. 1 (2020) 2971-2982.

[283] Y. Chen, D. An, S. Sun, J. Gao and L. Qian, Materials. 11, (2018) 269.

[284] K.Vijayanandhini, C. Simon, V. Pralong, Y. Breard, V. Caignaert, B. Raveau, P. Mandal, A. Sundaresan, C. N. Rao, J. Phys.: Condens. Matter, 21, (2009) 486002.

[285] R. Padam, S. Pandya, S. Ravi, A.K. Nigam, S. Ramakrishnan, A.K. Grover, D. Pal, Appl. Phys. Lett., 102 (2013) 112412.

[286] A.S.B. Madiligama, P. Ari-Gur, Y. Ren, V.V. Koledov, E.T. Dilmieva, A.P. Kamantsev, A.V. Mashirov, V.G. Shavrov, L. Gonzalez-Legarreta, B.H. Grande, Journal of Magnetism and Magnetic Materials 442 (2017) 25- 35.

[287] Y. Bai, Y.Xia, H.Li, L.Han, Z.Wang, X.Wu, S.Lv, X.Liu, and J.Meng, J. Phys. Chem. C 116, (2012) 16841.

[288] L. H. Yin, J. Yang, P. Tong, X. Luo, W. H. Song, J. M. Dai, X. B. Zhu and Y. P. Sun, Appl. Phys. Lett. 110, (2017) 192904.

[289] M. Yadav, P. Tiwari, C. Rath, Journal of Solid State Chemistry 303 (2021) 122537.

Publications

From Thesis Work:

1. K Pushpanjali Patra and S. Ravi, Magnetic Properties and Exchange Bias Behavior in Nanocrystalline $(Ho_{1-x}Sm_x)_2CoMnO_6$ (x = 0 - 0.5) Double Perovskite, Journal of Magnetism and Magnetic Material. 540, (2021), 168476.
2. K Pushpanjali Patra and S. Ravi, Re-entrant Spin Glass and Magnetocaloric Effect in Frustrated Double Perovskite Ho_2CoMnO_6 Flat Nanorod, Journal of Magnetism and Magnetic Materials, 559 (2022) 169537.
3. K Pushpanjali Patra and S. Ravi, Negative Magnetization and Exchange Bias Behavior in Nanocrystalline $Ho_2CoMn_{1-x}Ni_xO_6$ (x = 0 - 0.4) Double Perovskite, Journal of Alloys and Compounds, 921, (2022) 166090.
4. K Pushpanjali Patra and S. Ravi, Sign Reversal of both Spontaneous and Conventional Exchange Bias in Double Perovskite Y_2FeCrO_6 Nanoparticles, Journal of Applied Physics, 132 (2022) 213903.
5. K Pushpanjali Patra and S. Ravi, Effect of Partial Replacement of Mn with Cr on Exchange Bias Behavior and Negative Magnetization in Nanocrystalline Ho_2CoMnO_6 Double Perovskite, Journal of Magnetism and Magnetic Materials, 582 (2023) 171008.
6. K Pushpanjali Patra and S. Ravi, Magnetization Reversal in Double Perovskite Y_2FeCrO_6 Nanoparticles, Proceedings of the DAE solid state physics symposium. V. 55, (2021), ISBN No: 81-8372-085-4.

Out of Thesis Work:

1. K Pushpanjali Patra and S. Ravi, Effect of Chromium in Magnetic and Dielectric Properties of Inverse Spinel $FeMn_2O_4$, Applied Physics A, 128, (2022) 289.
2. Sikha Sarmah, K Pushpanjali Patra, P.K. Maji, S. Ravi, Tribedi Bora, A comparative study on the structural, magnetic and dielectric properties of magnesium substituted cobalt ferrites, Ceramics International, 49 (2023) 1444–1463.

Publications

Papers presented in International and National Conferences/ Symposium:

1. "Structural and Magnetic Properties of $FeMn_2O_4$", International Conference on advanced nanomaterials and nanotechnology 2019 (ICANN – 2019) held at IIT Guwahati during December 18 - 21- 2019.
2. "Structural and Magnetic Properties of $(Ho_{1-x}Sm_x)_2CoMnO_6$ (x = 0 - 0.5)", 6th International Conference on Nanoscience and Nanotechnology (ICONN – 2021) organized by Department of Physics and Nanotechnology, SRM IST, India during February 01 – 03, 2021.
3. "Negative Magnetization and Sign Reversal Exchange Bias Behavior in Nanocrystalline $Ho_2CoMn_{1-x}Ni_xO_6$ (x = 0 - 0.4) Double Perovskite", 7th International Conference on Advanced nanomaterials and Nanotechnology (ICANN-2021) organized by the Centre for Nanotechnology, IIT Guwahati, Assam, India, during 14-17 December 2021.
4. "Magnetization Reversal in Double Perovskite Y_2FeCrO_6 Nanoparticles", 65th DAE Solid State Physics Symposium (DAE-SSPS 2021) held at Bhabha Atomic Research Centre, Mumbai, during 15 - 19 December 2021.
5. "Re-entrant Spin Glass Behavior in Frustrated Double Perovskite Ho_2CoMnO_6 Nanorod", Symposium on Magnetism and Spintronics (SMS 2021) at NISER Bhubaneswar, India during 25th–27th November, 2021.

Webinar /Workshop Attended

1. Workshop on Rietveld Refinement Method organized by UGC-DAE Consortium for Scientific Research, Mumbai Centre in association with Indore Centre from 22 - 24 September 2020.
2. International webinar on "Exploring the World of Matter, Materials and Machines" organized by Department of Physics, Dhenkanal Autonomous College, Dhenkanal held on 21 December 2020.
3. National Webinar on "A Footstep towards Commercialization of Research work" organized by Research cell, Dr. Ambedkar college, Deekshabhoomi, Nagpur, India on January - 29 - 2021.
4. Hands - On Training on Characterization Tools and Techniques for Materials Sciences by NIT Meghalaya (2022).
5. Unlocking the Secrets of Research: Effective Strategies for Searching and Reading Academic Articles by IIT Guwahati, Speaker Dr. Sparsh Johari (2023).